Title
Aeroelasticity in axial flow: Balakrishnan continuum theory and a semi-continuum approach

Author
DeMoulin, George

Publication Date
2019

Peer reviewed|Thesis/dissertation

UNIVERSITY OF CALIFORNIA

Los Angeles

Aeroelasticity in Axial Flow: Balakrishnan Continuum Theory and a Semi-Continuum Approach

A dissertation submitted in partial satisfaction

of the requirements for the degree

Doctor of Philosophy in Mechanical Engineering

by

George William DeMoulin

2019

ABSTRACT OF THE DISSERTATION

Aeroelasticity in axial flow:

Balakrishnan continuum theory and

a semi-continuum approach

by

George William DeMoulin

Doctor of Philosophy in Mechanical Engineering

University of California,Los Angeles, 2019

Professor Ivan Catton, Chair

This work begins by presenting the mathematical development of the Balakrishnan Continuum Theory (BCT) of aeroelasticity in axial flow, which was left unpublished by Professor Balakrishnan in 2015. While the mathematics and solution had been fully described, the BCT was left incomplete in the sense that it had not been implemented for engineering calculations. The methods developed as part of this dissertation for implementing the BCT are presented. To make improvements to the BCT, and to extend it, a new solution method was developed, implemented, and validated with experimental data. This method, referred to as the semi-continuum approach, combines the BCT continuum solution with a Galerkin method solution. The semi-continuum approach was applied to the fully linear problem solved by the BCT, and was consequently extended to account for nonlinear structure effects.

Experiments were performed to obtain flutter speed data, which was used to make comparisons with theoretical predictions. These comparisons demonstrate the validity of the semi-continuum approach, and the BCT that serves as its foundation. Experiments were also performed to study Limit Cycle Oscillation (LCO) in axial flow, where the dependence of the amplitude and frequencies of the oscillations on air speed was analyzed. These experiments also provide information about the shape of the structure during LCO, which was compared to the eigenfunctions produced by the semi-continuum calculations.

The dissertation of George William DeMoulin is approved.

Oddvar O Bendiksen

Jeffrey D Eldredge

Gregory Eskin

Ivan Catton, Committee Chair

University of California, Los Angeles

2019

This is dedicated to two men I love and miss very much: My dad, Bill DeMoulin, and Professor A.V. Balakrishnan.

Table of Contents

List of Figures **ix**

List of Tables **xiv**

Nomenclature **xvi**

1 Introduction **1**

2 Flutter of structures in axial flow: Balakrishnan continuum theory **8**

2.1 Fluid-structure model 8

2.2 Small perturbation theory/linearization 17

2.3 Generalized Possio Integral Equation 25

2.4 Aeroelastic torsion dynamics 43

2.5 Aeroelastic bending dynamics 56

2.6 Stability of torsional motion in axial flow 75

2.7 Divergence speed 83

3 Modifications to Balakrishnan continuum theory and methods for determining the flutter speed **85**

3.1 Modification to the root locus stability method 85

3.2 Evaluation of bending flutter determinant 89

3.3 Treatment of singular integrals 107

3.4 Flutter speed calculation using Balakrishnan continuum theory 121

4 The semi-continuum approach: Combined approximate and continuum solution **124**

4.1 Semi-continuum method for linear structure and fluid dynamics 124

4.2 Flutter speed calculation based on linear fluid and linear structure dynamics 135

4.3 Semi-continuum method for nonlinear structure and linear fluid dynamics . . 141

4.4 Flutter speed calculation based on linear fluid and nonlinear structure dynamics 158

5 Flutter speed and limit cycle oscillation by experiment **163**

5.1 Description of wind tunnel and instrumentation 163

5.2 Experimental results 166

5.2.1 Flutter speed 166

5.2.2 Limit cycle oscillation: Modal analysis 169

5.2.3 Limit cycle oscillation: Image processing 182

5.3 Scaling and data 193

6 Discussion of results **204**

6.1 Flutter speed 204

6.2 Limit cycle oscillation 207

6.3 Scaling 209

7 Conclusions **210**

A Numerical methods **213**

A.1 Composite Simpson's Rule. 213

A.2 Newton Raphson method for a system of equations 214

A.3 Gaussian elimination 217

A.4 Determinant of a matrix 221

A.5 Inverse of a matrix 222

A.6 Calculation of eigenvectors 224

B Experimental data **227**

B.1 Modal analysis data for 2024-T3 aluminum. 227

B.2 Modal analysis data for ABS plastic. 231

B.3 Modal analysis data for PETG plastic. 234

B.4 Image processing data for 2024-T3 aluminum. 238

B.5 Image processing data for ABS plastic. 244

B.6 Image processing data for PETG plastic. 250

B.7 Uncertainty in measured frequencies for 2024-T3 aluminum. 254

B.8 Uncertainty in measured frequencies for ABS plastic. 255

B.9 Uncertainty in measured frequencies for PETG plastic. 256

C Galerkin coefficients from semi-continuum method. **257**

C.1 Galerkin coefficients for linear fluid and structure dynamics. 257

C.2 Galerkin coefficients for linear fluid and nonlinear structure dynamics. 260

References **263**

List of Figures

1.1 The Collar triangle of aeroelasticity. 1

1.2 Bending and torsional motion of a cantilever beam. 2

1.3 Normal flow vs. axial flow. 3

2.1 Cantilever beam and coordinate system. 9

2.2 Structure as seen in the x-y plane. 11

3.1 The function $\eta'(t)$ from Equation (3.108). 112

3.2 Integrand of $\bar{\mathrm{T}}_{R,1}[\psi(i\omega,\phi)]$: Original (left) and transformed (right). 115

3.3 Integrand of $\bar{\mathrm{T}}_{R,2}[\psi(i\omega,\phi)]$: Original (left) and transformed (right).. 116

3.4 Convergence of ω (left) and U (right) with number of iterations for 2024-T3 aluminum case. 123

4.1 First three eigenfunctions. 131

4.2 Convergence of flutter speed with number of terms used in the Galerkin method. 136

4.3 Eigenfunctions from the real (left) and imaginary (right) flutter determinant for 2024-T3 aluminum. 137

4.4 Convergence of flutter speed with number of terms used in the Galerkin method for PETG case. 138

4.5 Eigenfunctions from the real (left) and imaginary (right) flutter determinant for PETG plastic. 138

4.6 Convergence of flutter speed with number of terms used in the Galerkin method for the ABS case. 139

4.7 Eigenfunctions from the real (left) and imaginary (right) flutter determinant for PETG plastic. 140
4.8 Beam and coordinate system with three modes of motion. 141
4.9 Solution procedure for nonlinear model. 157
4.10 Convergence of flutter speed with number of Galerkin terms for 2024-T3 aluminum. 159
4.11 Eigenfunctions from the real (left) and imaginary (right) flutter determinant for 2024-T3 aluminum. 160
4.12 Convergence of flutter speed with number of Galerkin terms for PETG. . . . 160
4.13 Eigenfunctions from the real (left) and imaginary (right) flutter determinant for PETG plastic. 161
4.14 Convergence of flutter speed with number of Galerkin terms for ABS plastic. 161
4.15 Eigenfunctions from the real (left) and imaginary (right) flutter determinant for ABS plastic. 162
5.1 a)Aerolab wind tunnel used for LCO experiments; b) Wind tunnel test section. 164
5.2 Aerolab Pitot-Static Probe. 164
5.3 Measured pressure difference versus fan speed. 167
5.4 Air velocity versus fan speed. 168
5.5 Sample 2 with accelerometer attached. 170
5.6 Accelerometer time domain signal for Sample 1 at the flutter speed. 171
5.7 FFT of Sample 1 at the flutter speed. 172
5.8 FFT for Sample 2 at the flutter speed. 175
5.9 FFT for Sample 3 at the flutter speed. 177

5.10 Wind tunnel with halogen lamps and camera mounting structure. 184

5.11 Image of Sample 1 in LCO at the Flutter Speed. Original (left) and enhanced for visibility (right). 186

5.12 Image of Sample 2 in LCO at the Flutter Speed. Original (left) and enhanced for visibility (right). 186

5.13 Image of Sample 3 in LCO at the Flutter Speed. Original (left) and enhanced for visibility (right). 186

5.14 Midpoint displacement versus time for Sample 1 at the flutter speed. 188

5.15 Midpoint displacement versus time for Sample 2 at the flutter speed. 189

5.16 Midpoint displacement versus time for Sample 3 at the flutter speed. 191

5.17 Dimensionless frequency versus air speed for 2024-T3 aluminum. 200

5.18 Dimensionless frequency versus air speed for PETG plastic. 202

5.19 Dimensionless frequency versus air speed for ABS plastic. 203

B.1 FFT for 2024-T3 aluminum at U = 36.7 m/s. 227

B.2 FFT for 2024-T3 aluminum at U = 37.5 m/s. 228

B.3 FFT for 2024-T3 aluminum at U = 38.3 m/s. 228

B.4 FFT for 2024-T3 aluminum at U = 39.1 m/s. 229

B.5 FFT for 2024-T3 aluminum at U = 39.8 m/s. 229

B.6 FFT for 2024-T3 aluminum at U = 40.6 m/s. 230

B.7 FFT for ABS plastic at U = 17.3 m/s. 231

B.8 FFT for ABS plastic at U = 18.0 m/s. 231

B.9 FFT for ABS plastic at U = 18.8 m/s. 232

B.10 FFT for ABS plastic at U = 19.6 m/s. 232

B.11 FFT for ABS plastic at U = 20.4 m/s. 233

B.12 FFT for ABS plastic at U = 21.2 m/s. 233

B.13 FFT for PETG plastic at U = 25.9 m/s. 234

B.14 FFT for PETG plastic at U = 25.9 m/s. 234

B.15 FFT for PETG plastic at U = 26.7 m/s. 235

B.16 FFT for PETG plastic at U = 27.5 m/s. 235

B.17 FFT for PETG plastic at U = 28.3 m/s. 236

B.18 FFT for PETG plastic at U = 29.1 m/s. 236

B.19 FFT for PETG plastic at U = 29.8 m/s. 237

B.20 Midpoint displacement versus time for U = 36.7 m/s for 0.5 seconds duration. 238

B.21 Midpoint displacement versus time for U = 36.7 m/s for 5.4 seconds duration. 238

B.22 Midpoint displacement versus time for U = 37.5 m/s for 0.5 seconds duration. 239

B.23 Midpoint displacement versus time for U = 37.5 m/s for 5.0 seconds duration. 239

B.24 Midpoint displacement versus time for U = 38.3 m/s for 0.5 seconds duration. 240

B.25 Midpoint displacement versus time for U = 38.3 m/s for 5.0 seconds duration. 240

B.26 Midpoint displacement versus time for U = 39.0 m/s for 0.5 seconds duration. 241

B.27 Midpoint displacement versus time for U = 39.0 m/s for 5.0 seconds duration. 241

B.28 Midpoint displacement versus time for U = 39.8 m/s for 0.5 seconds duration. 242

B.29 Midpoint displacement versus time for U = 39.8 m/s for 5.0 seconds duration. 242

B.30 Midpoint displacement versus time for U = 40.6 m/s for 0.5 seconds duration. 243

B.31 Midpoint displacement versus time for U = 40.6 m/s for 5.0 seconds duration. 243

B.32 Midpoint displacement versus time for U = 17.3 m/s for 0.5 seconds duration. 244

B.33 Midpoint displacement versus time for U = 17.3 m/s for 5.0 seconds duration. 244

B.34 Midpoint displacement versus time for U = 18.0 m/s for 0.5 seconds duration. 245

B.35 Midpoint displacement versus time for U = 18.0 m/s for 5.0 seconds duration. 245

B.36 Midpoint displacement versus time for U = 18.8 m/s for 0.5 seconds duration. 246

B.37 Midpoint displacement versus time for U = 18.8 m/s for 5.0 seconds duration. 246

B.38 Midpoint displacement versus time for U = 19.6 m/s for 0.5 seconds duration. 247

B.39 Midpoint displacement versus time for U = 19.6 m/s for 5.0 seconds duration. 247

B.40 Midpoint displacement versus time for U = 20.4 m/s for 0.5 seconds duration. 248

B.41 Midpoint displacement versus time for U = 20.4 m/s for 5.0 seconds duration. 248

B.42 Midpoint displacement versus time for U = 21.2 m/s for 0.5 seconds duration. 249

B.43 Midpoint displacement versus time for U = 21.2 m/s for 5.0 seconds duration. 249

B.44 Midpoint displacement versus time for U = 26.7 m/s for 0.5 seconds duration. 250

B.45 Midpoint displacement versus time for U = 26.7 m/s for 5.0 seconds duration. 250

B.46 Midpoint displacement versus time for U = 27.5 m/s for 0.5 seconds duration. 251

B.47 Midpoint displacement versus time for U = 27.5 m/s for 5.0 seconds duration. 251

B.48 Midpoint displacement versus time for U = 28.3 m/s for 0.5 seconds duration. 252

B.49 Midpoint displacement versus time for U = 28.3 m/s for 5.0 seconds duration. 252

B.50 Midpoint displacement versus time for U = 29.1 m/s for 0.5 seconds duration. 253

B.51 Midpoint displacement versus time for U = 29.1 m/s for 5.4 seconds duration. 253

B.52 Uncertainty values for 2024-T3 aluminum. 254

B.53 Uncertainty values for ABS plastic. 255

B.54 Uncertainty values for PETG plastic. 256

List of Tables

2.1 First five roots to Equation (2.273). 72

3.1 Numerical Integration of Equation (3.95) using Simpson's Rule. 108

3.2 Number of Integration Points Required for Integrals in the Flutter Determinant. 119

3.3 Material Properties and Dimensions for Three Structures. 121

3.4 Newton-Rapshon Convergence for 2024-T3 Aluminum Case. 122

4.1 Material properties and dimensions for three configurations. 135

4.2 Material properties and dimensions for three configurations. 158

5.1 Parameters and Measured Flutter Speed for Three Structures. 169

5.2 Experimental and Theoretical Frequencies of Sample 1 at the Flutter Speed. 173

5.3 Experimental and Theoretical Frequencies of Sample 1 at the Flutter Speed. 174

5.4 Peak Frequencies for Sample 2 At and Above the Flutter Speed 176

5.5 Peak Frequencies for Sample 2 At and Above the Flutter Speed. 177

5.6 Uncertainty in Measured Frequencies for Sample 1. 181

5.7 Uncertainty in Measured Frequencies for Sample 2. 181

5.8 Uncertainty in Measured Frequencies for Sample 3. 182

5.9 High-Speed Camera Record and Display Settings. 183

5.10 Parameters and Measured Flutter Speed for Three configurations. 185

5.11 Maximum Midpoint Displacement for Sample 1 at Six Air Speeds. 189

5.12 Maximum Midpoint Displacement for Sample 2 at Four Air Speeds. 190

5.13 Maximum Midpoint Displacement for Sample 3 at Six Air Speeds. 191

5.14 Dimensional and Nondimensional Flutter Speed. 197

5.15 Dimensional and Nondimensional Frequencies for 2024-T3 Aluminum. 199

5.16 Dimensional and Nondimensional Frequencies for PETG Plastic. 201

5.17 Dimensional and Nondimensional Frequencies for ABS Plastic. 202

C.1 Galerkin Coefficients for 2024-T3 Aluminum. 257

C.2 Galerkin Coefficients for PETG Plastic. 258

C.3 Galerkin Coefficients for ABS Plastic. 259

C.4 Galerkin Coefficients for 2024-T3 Aluminum. 260

C.5 Galerkin Coefficients for PETG Plastic. 261

C.6 Galerkin Coefficients for ABS Plastic. 262

Nomenclature

A Kussner doublet function, or defined matrix, or defined function

b Beam half-width

B Galerkin coefficient

C Galerkin coefficient

d Flutter determinant

D Defined funciton, or Galerkin coefficient

E Modulus of elasticity

f Defined function

g Accerleration due to gravity

G Shear modulus, or defined function

h Bending displacement, or defined function

H Trial function, or defined function

I Area moment of inertia

I_θ Polar mass moment of inertia

J Polar area moment of inertia

K Modified Bessel function of the second kind

l Beam half-length

L) Aerodynamic lift per unit length, or defined function, or Laplace transform

m mass per unit length, or moment per unit length, or complex number

M Aerodynamic moment per unit length, or defined function

N Defined function

p	Pressure
P	Pressure
Q	Defined function, or defined constant
r	Distance
s	Laplace transform of time independent variable
S	Defined function
T	Defined function
U	Velocity
u	Defined functions
u, v, w	Velocity components
W	Defined operator, or trial function
x	Defined function
y	Defined function
z	Defined function
Z	Total displacement

GREEK

β Defined parameter

δ Difference operator

η Defined function

γ Defined parameter

κ Defined parameter

λ Real part of s

ν Defined function

ϕ Velocity potential

ρ Fluid density

σ Integration variable

θ Torsion angle

Θ Torsion angle

ν Trial function

ω frequency, or imaginary part of s

Ω Defined operator or defined constant$s$

ζ Integration variable

SPECIAL CHARACTERS

$\mathcal{L}$ Defined operator

$\mathcal{T}$ Defined operator

$\mathcal{P}$ Defined operator

$\mathcal{X}$ Defined operator

ACCENTS

$\dot{}$ Time derivative

$'$ spatial derivative

$\hat{}$ Laplace transform

$\tilde{}$ Fourier transform

ACKNOWLEDGEMENTS

I would like to thank my advisor, Professor Ivan Catton, for his immeasurable technical guidance and tireless support. And his wife, Susan Catton, for the many dinners, stories, and for always making me feel comfortable in their home.

A special thank you to Mrs. Sonya Balakrishnan for her friendship, the many fascinating conversations, and for introducing an engineer to the arts.

I would like to thank my lab mates, for the good times we had together, including Sean Reilly, David Geb, Qi Yao, Krsto Sbutega, Jake Supowit, Mike Stubblebine, Matevž Frajnkovič, Eylül Şimşek, Ampol Likitchatchawankun, Sun Baek, Sara Valleo Castano, and Zachary Wong.

Finally, I could not have done this without my mom, Debee, my brother, Billy, and my sister, Jessica. I am lucky to have them by my side.

VITA

2004

High School Diploma

Tracy High School

Tracy, CA

2009

B.S., Mechanical Engineering

San Jose State University

San Jose, CA

2012

M.S., Mechanical Engineering

University of California Los Angeles

Los Angeles, CA

1 Introduction

Aeroelasticity is the field of study that examines the response of a structure to dynamic forces exerted on it by a moving fluid. In such systems the dynamics of an elastic structure are directly coupled to the dynamics of the fluid at the fluid-structure boundary. As a result, this subject is inherently interdisciplinary, and from the very beginning has attracted the interest of mechanical engineers, aerospace engineers, structural engineers, and mathematicians. The rich history of aeroelasticity, which begins in the first half of the twentieth century, covers several fascinating applications. Perhaps the most interesting historical event to point to is the catastrophic failure of the (first) Tacoma Narrows Bridge in 1940.

From a technical standpoint, the field of aeroelasticity can be described by the Collar triangle [10], shown in Figure 1.1.

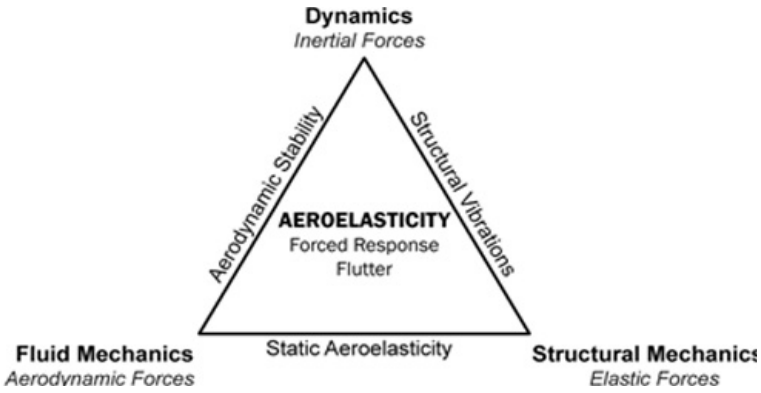

Figure 1.1: The Collar triangle of aeroelasticity.

In aeroelasticity we are primarily interested in the stability of the structure when subjected to aerodynamic loading. While static aeroelasticity has great importance in laying the foun-

dation for aeroelasticity, much of the modern research is devoted to dynamic aeroelasticity. In fact, it is the dynamic instability of the structure, known as flutter, that is of utmost importance to the aeroelastician. When flutter occurs the motion of the structure may be bounded, in which case we call the motion Limit Cycle Oscillation (LCO). In cases where flutter causes violent motion of the structure, the result is almost always catastrophic failure. It is not hard to see why avoiding flutter is critically important in the design of aircraft.

In beam-like structures, e.g. the wing of an airplane, there are two modes of motion that can be excited by flutter: bending motion, or "plunge", and torsional motion, or "pitch". Using a cantilever beam as an example, Figure 1.2 illustrates bending and torsional motion.

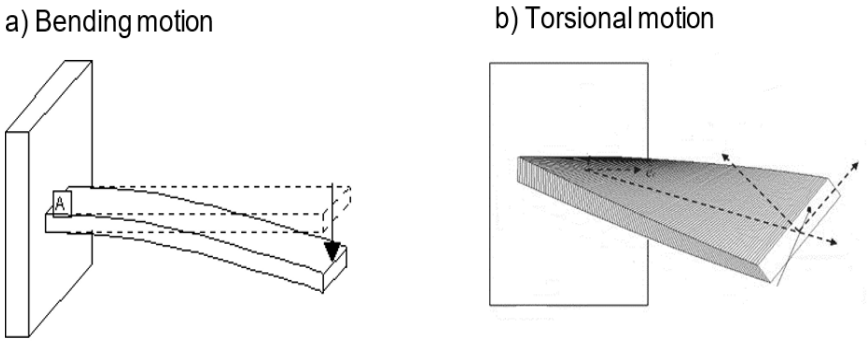

Figure 1.2: Bending and torsional motion of a cantilever beam.

Another important distinction that should be made is the difference between "normal" flow and "axial" flow aeroelasticity. In beam-like structures, the term normal flow is used to describe systems where the fluid velocity in the free stream is normal to the longitudinal axis of the beam. This is the configuration used to investigate the flutter of wings of an

airplane. Axial flow is somewhat less common, and exists when the fluid velocity is parallel to the beam's longitudinal axis. Flutter in axial flow is sometimes referred to as "flag" flutter because a flag fluttering in the wind resembles axial flow. Figure 1.3 shows the difference between normal and axial flow.

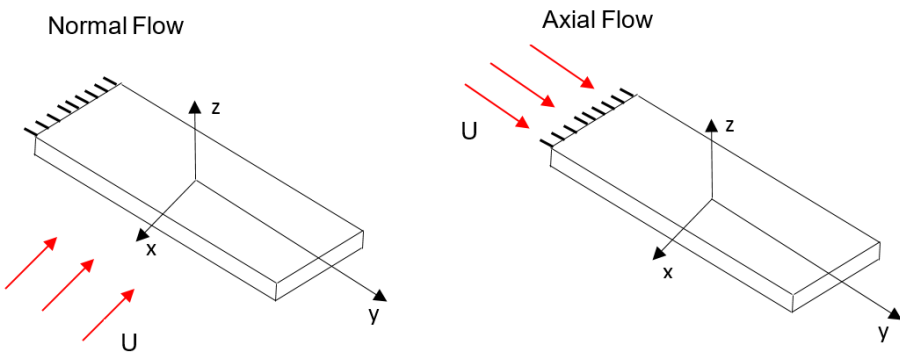

Figure 1.3: Normal flow vs. axial flow.

The key difference between modeling normal and axial flow involves modeling the fluid. In normal flow, if the beam's aspect ratio is assumed to be large, the dependence of the fluid velocity on the y-direction can be neglected. That is, normal flow systems can be well represented by a 2-D unsteady flow model. The counterpart of this assumption in axial flow would be to neglect the x-direction dependence, but due to the torsional motion of the structure this assumption cannot be made without a significant loss in accuracy. The added complexity in modeling axial flow is that it requires a 3-D unsteady flow model for the fluid. Like many fields of engineering, the nature of the research in aeroelasticity can be classified as either: theoretical/analytical, experimental, or computational. Much of the effort in this dissertation belongs to the first category, and therefore this will be the emphasis of this literature reveiw . For a review of experimental aeroelasticity reference can be made to [23],

and for a more recent discussion see Dowell[13]. For a commanding review of computational aeroelasticity see Bendiksen [6].

Most relevant to this work is aeroelastic modeling of beam-like structures, but aeroelastic modeling in general has been used to solve a wide variety of problems. For example, vibration of tubes in heat exchangers can lead to a fluid-elastic instability; for an example on modeling this phenomenon see Marn and Catton [22] and the review by Khushnood et al. [19]. In aerospace engineering, a great deal of work has been done in analyzing turbomachinery; see Bendiksen [5]. If we narrow our attention to beam-like structures, the majority of the literature is focused on normal flow applications, e.g. the wings of aircraft. A natural extension of modeling is the modeling of axial flow aeroelasticity, which in the last decade has gained the attention of researchers aiming to develop piezoelectric energy harvesters [14].

The earliest work of consequence in modeling dynamic aeroelasticity was published in 1934 by Theodorsen [27] in the context of analyzing flutter of aircraft wings. One of the most cited works in aeroelasticity, the classic paper by Theodorsen reduces a 3-D wing to a "typical section" whose structural stiffness is represented by springs with constants K_h for bending motion and K_α for torsional motion. This model proceeds by assuming simple harmonic motion for the bending and torsional displacements, and represents the fluid forces in terms of lift and moment coefficients which depend on these simple harmonic motion displacements. Neither steady nor unsteady, this type of aerodynamic modeling has been termed "quasi-steady". The resulting stability analyses lead to what is known as the flutter determinant, which then gives rise to a flutter parameter that can be used to determine at which air speed

the structure becomes unstable. This approach played an important role in developing a technical understanding of flutter, and the validity of using quasi-steady aerodynamics was confirmed in the classic work of Bisplinghoff and Ashley [7]. It should also be noted that Theodorsen [27, 28] employed unsteady aerodynamics to use a flutter determinant approach for thin plates.

The next significant improvement to the typical section model involves using more accurate methods to model the structure. To avoid using empirical coefficients for the structural stiffness, as was the case in the typical section model, governing differential equations are derived using expressions for the strain energy of the structure. Perhaps the most widely used models based on this approach use Euler-Bernoulli beam theory for bending deformation and St. Venant's theory for torsional deformation. Assuming small displacements for bending and torsion, the resulting set of partial differential equations usually takes the form:

$$EI\frac{\partial^4 h(t,y)}{\partial y^4} + m\frac{\partial^2 h(t,y)}{\partial t^2} = L(t,y) \tag{1.1}$$

$$-GJ\frac{\partial^2 \theta(t,y)}{\partial y^2} + I_\theta\frac{\partial^2 \theta(t,y)}{\partial t^2} = M(t,y) \tag{1.2}$$

Where $h(t,y)$ and $\theta(t,y)$ are the bending and torsional displacements, and $L(t,y)$ and $M(t,y)$ are the aerodynamic lift and moment forces. Equations (1.1) and (1.2) are in fact the Goland beam model [16], which form the basis for the linear continuum theory presented here. For a

complete treatment of the structural dynamics used to derive these equations reference can be made to Hodges [17] or Donaldson [11], and for the aeroelastic modeling see Goland [16] or Runyan and Watkins [24]. It should be noted that this type of structure modeling gives rise to the concept of structural modes for bending and torsional motion, which is a result of the linear equations resembling an eigenvalue problem. Coupled with Theodorsen-like aerodynamics, stability of the structure has been studied using several methods: U-g method, p-k method, flutter eigenvalue analysis, assumed modes etc. For a detailed discussion on these stability techniques see Hodges [17] or Dowell [12].

The theoretical efforts described so far remained very popular until the 1970s and 1980s, and as a whole have been categorized as "classical aeroelasticity". It is not a coincidence that the analytical methods for aeroelasticity began to decline during this time period, which is of course the era when numerical and computational methods began to dominate many areas of mechanics. However, analytical, or continuum, methods have continued to be of great importance. In an engineering setting, a commonly made argument is that such approaches can be used to obtain simplified governing equations that can be solved numerically with a fraction of the computational cost associated with Direct Numerical Simulation (DNS). This is the argument made here, along with the argument that continuum methods can provide physical insight unattainable by numerical computation. For example, through a mathematical proof we can demonstrate that the divergence speed in axial flow is undefined. Such a result cannot be extracted from discretized governing equations.

We will narrow our attention to recent advances in developing continuum methods for aeroe-

lasticity. The methods of interest here use Euler-Bernoulli beam theory to model bending and torsional displacement of the structure, and unsteady aerodynamics for the fluid. Modeling the fluid as unsteady potential flow, and using the Goland beam model [16] , all governing equations are linear. While this methodology is restricted to small displacements of the structure, it is all that is needed to study the stability characteristics. Nonlinear terms only appear in the fluid-structure boundary condition, but because it is assumed that structural displacements are small, these terms are easily discarded. In the case of normal flow, this problem has been solved without any numerics by A.V. Balakrishnan and is summarized in his 2012 book [2]. Because it does not use numerical approximation, it has been termed the "continuum" theory of aeroelasticity. Central to its development is the solution of the fluid governing equations with a dynamic boundary condition at the fluid-structure interface. This gives rise to an integral equation, often referred to as the Possio integral equation [3], whose solution requires techniques found in functional analysis. In the past decade the mathematical aspects of solving this problem have been studied by many authors; for examples see Chueshov [9, 8] , Lasiecka [21] and Shubov [26].

In recent years an effort to extend the aeroelastic continuum theory to axial flow was begun by A.V. Balakrishnan. This work involves using the Goland beam model, as is done for normal flow, but requires the use of a fluid model where the velocity is a function of two spatial coordinates instead of one. The resulting integral equation now contains a double integral, instead of a single integral, and thus can be appropriately termed the Generalized Possio Integral Equation. The completion and implementation of the axial flow continuum theory, most of which was done by Balakrishnan, is an important aspect of this dissertation.

2 Flutter of structures in axial flow: Balakrishnan continuum theory

In this chapter the continuum theory of aeroelasticity in axial flow developed by Balakrishnan [4] is presented, although some changes have been made throughout. For example, the linearization technique has been reformulated: here a small perturbation method with scaling arguments is used in place of the more abstract power series formulation. While both methods are mathematically correct, and produce the same set of linearized equations, the approach taken here is more physically intuitive. The other changes are mostly notation changes, and filling in extra steps in the development. The stability of the system is analyzed for bending and torsional motion, where a proof shows that torsion is unconditionally stable in axial flow. This chapter concludes by proving that the divergence speed is undefined in axial flow.

2.1 Fluid-structure model

The fluid-structure model is based on the Goland beam model [16], with the aerodynamics represented by an unsteady three-dimensional potential flow model. The most restrictive assumptions limit the model to cases where the structure displacements are small, which is perfectly acceptable if the purpose is only to analyze the stability of the system.

Consider a cantilever beam, as shown in Figure 2.1, exposed to uniform airflow with velocity U parallel to the y-axis. The coordinate system is located at the center of the beam so that

the length is $2l$ and the width is $2b$.

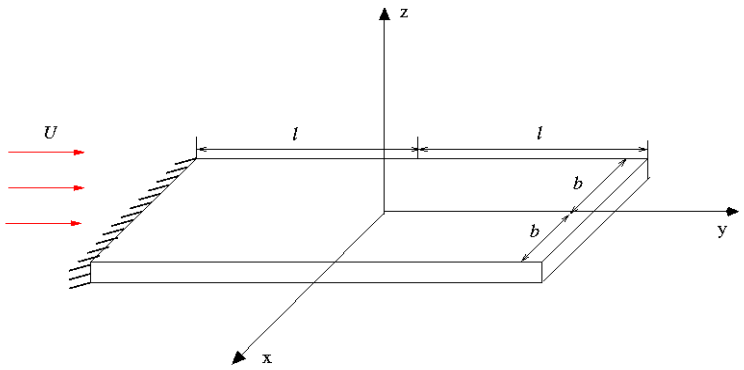

Figure 2.1: Cantilever beam and coordinate system.

For homogeneous structures of uniform cross-section, the torsion pitch axis coincides with the beam's elastic axis, and it is safe to neglect structural coupling between bending and torsional motion. Letting $h(t, y)$ denote the bending displacement in the negative z-direction and $\theta(t, y)$ denote the torsion angle corresponding to rotation about the y-axis, the Goland beam model is:

$$EI\frac{\partial^4 h(t,y)}{\partial y^4} + m\frac{\partial^2 h(t,y)}{\partial t^2} = L(t,y) \tag{2.1}$$

and

$$-GJ\frac{\partial^2 \theta(t,y)}{\partial y^2} + I_\theta\frac{\partial^2 \theta(t,y)}{\partial t^2} = M(t,y) \tag{2.2}$$

where

E	is the modulus of elasticity
I	is the moment of inertia of the cross section
m	is the mass per unit length of the beam
$L(t, y)$	is the aerodynamic lift per unit length of the beam
G	is the shear modulus
J	is the torsional constant
I_θ	is the polar mass moment of inertia
$M(t, y)$	is the aerodynamic moment per unit length of the beam

In the BCT, the torsional constant is approximated as the polar area moment of inertia, which would be exact if it were a circular cross section. At the clamped end of the beam, $y = -l$, no displacements are allowed and the slope of the bending displacement is zero. These boundary conditions are:

$$h(t, -l) = h'(t, -l) = \theta(t, -l) = 0 \tag{2.3}$$

Because the free end of the beam cannot support forces or moments, the boundary conditions for $y = l$ are:

$$h''(t, l) = h'''(t, l) = \theta'(t, l) = 0 \tag{2.4}$$

To obtain expressions for the aerodynamic lift and moment, the beam is treated as being infinitely thin in the flow field, with a jump discontinuity at $z = 0$. Figure 2.2 shows a side

view of the beam, which lies in the x-y plane, where $z = 0^+$ and $z = 0^-$ denote the top and bottom surfaces of the beam, respectively.

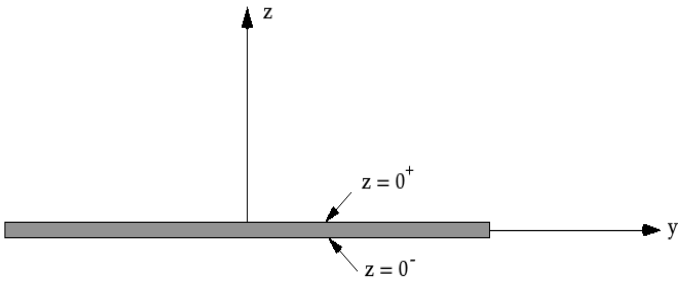

Figure 2.2: Structure as seen in the x-y plane.

For inviscid flow, the lift force per unit length at any location y along the beam can be obtained by integrating the pressure difference across the beam over the beam's width. Denoting the difference of a quantity between the top and bottom surfaces of the beam by the operator $\delta()$, the pressure jump can be written as:

$$\delta p\left(t, x, y\right) = p\left(t, x, y, 0^+\right) - p\left(t, x, y, 0^-\right) \tag{2.5}$$

The expression for $L(t, y)$ in terms of the pressure jump is:

$$L\left(t, y\right) = \int_{-b}^{b} \delta p\left(t, x, y\right) dx \tag{2.6}$$

At any point on the beam, the moment per unit length (due to pressure forces) about the y-axis can be written as:

$$m(t,x,y) = \delta p\,(t,x,y)\,x \tag{2.7}$$

Integrating $m(t,x,y)$ over x, the expression for the moment becomes:

$$M\,(t,y) = \int_{-b}^{b} \delta p\,(t,x,y) x dx \tag{2.8}$$

For unsteady, inviscid, incompressible flow, the aerodynamics can be represented using a potential flow model:

$$\nabla^2 \phi\,(t,x,y,z) = 0 \tag{2.9}$$

where the velocity potential is defined by:

$$\nabla \phi = \vec{u} \tag{2.10}$$

and $\vec{u}$ is the velocity vector:

$$\vec{u} = u\vec{i} + v\vec{j} + w\vec{k} \tag{2.11}$$

The next step is to relate the pressure difference across the beam to the velocity poten-

tial. Because the flow is assumed to be incompressible and inviscid, the unsteady Bernoulli equation is applicable:

$$\frac{\partial \phi}{\partial t} + \frac{\nabla \phi \cdot \nabla \phi}{2} + \frac{p}{\rho} + gz = f(t) \tag{2.12}$$

Neglecting body forces due to gravity, and rearranging Equation (2.12), the pressure difference can be written as:

$$\delta p(t, x, y) = -\rho \left[\delta \left(\frac{\partial \phi}{\partial t} \right) + \delta \left(\frac{\nabla \phi \cdot \nabla \phi}{2} \right) \right] \tag{2.13}$$

Using Equation (2.13), the governing equations for the structure become:

$$EI \frac{\partial^4 h(t,y)}{\partial y^4} + m \frac{\partial^2 h(t,y)}{\partial t^2} = -\rho \int_{-b}^{b} \left[\delta \left(\frac{\partial \phi}{\partial t} \right) + \delta \left(\frac{\nabla \phi \cdot \nabla \phi}{2} \right) \right] dx \tag{2.14}$$

$$-GJ \frac{\partial^2 \theta(t,y)}{\partial y^2} + I_\theta \frac{\partial^2 \theta(t,y)}{\partial t^2} = -\rho \int_{-b}^{b} \left[\delta \left(\frac{\partial \phi}{\partial t} \right) + \delta \left(\frac{\nabla \phi \cdot \nabla \phi}{2} \right) \right] x dx \tag{2.15}$$

To complete the development of the fluid-structure model, the boundary conditions for the velocity potential $\phi(t, x, y, z)$ as it relates to the structure are constructed. The first condition is that the velocity field must return to uniform flow very far away from the structure. With the distance away from the structure denoted by,

$$r = \sqrt{x^2 + y^2 + z^2} \tag{2.16}$$

This condition can be expressed as:

$$\lim_{r \to \infty} \phi\left(t, x, y, z\right) = Uy \tag{2.17}$$

The boundary condition for $\phi(t, x, y, z)$ at the structure surface presents a fundamental challenge to the modeling approach used so far. Euler-Bernoulli beam theory has been used to describe the motion of the structure, which is formulated in the Lagrangian perspective, along with a potential flow model for the fluid which is is based on the Eulerian perspective. That is, the structure variables $h(t, y)$ and $\theta(t, y)$ provide information about a material point on the structure whereas the fluid model conserves mass and momentum at a point in the field.

While it may seem that this discrepancy would make the model inherently invalid, it can be shown through basic kinematics that the Lagrangian and Eulerian perspectives can be connected using the material derivative for the structure's velocity. At the surface of the structure, the condition imposed is:

Normal velocity of the structure = Normal velocity of the fluid at the structure

Because the torsion angle $\theta(t, y)$ is assumed to be small, the total displacement of the structure can be written as:

$$Z\left(t,x,y\right)=h\left(t,y\right)+x\theta\left(t,y\right) \tag{2.18}$$

The normal velocity of the structure can be obtained by taking the material derivative of $Z(t,x,y)$. Noting that the normal velocity of the fluid is the z-derivative of the velocity potential, the condition becomes:

$$\frac{DZ\left(t,x,y\right)}{Dt}=-\frac{\partial}{\partial z}\phi(t,x,y,z=0^{+})=-\frac{\partial}{\partial z}\phi(t,x,y,z=0^{-}) \tag{2.19}$$

Where the negative sign appears because $h(t,y)$ is in the negative z-direction. Evaluating the material derivative in Equation (2.19), the condition becomes:

$$\begin{aligned}\nabla\phi\left(t,x,y,0^{\pm}\right)\cdot\vec{k}=&-\dot{h}\left(t,y\right)-x\dot{\theta}\left(t,y\right)-\left(\nabla\phi(t,x,y,0^{\pm})\cdot\vec{i}\right)\theta\left(t,y\right)\\&-\left(\nabla\phi(t,x,y,0^{\pm})\cdot\vec{j}\right)\left(h'\left(t,y\right)+x\theta'\left(t,y\right)\right)\end{aligned} \tag{2.20}$$

Equation (2.20) is often referred to as the "flow tangency" or "attached flow" condition. The remaining conditions, the Kutta-Joukowski conditions, ensure that the flow field is continuous away from the structure. For the beam shown in Figure 2.1, the Kutta-Joukowski conditions are:

$$\delta p\left(t,|x|>2b,y>2l\right)=0 \tag{2.21}$$

and

$$\delta p\left(t, x, y = l\right) = 0 \tag{2.22}$$

Equation (2.22), the Kutta condition, ensures uniqueness of the solution. The development so far has produced a closed set of governing equations for the fluid and the structure, along with all appropriate boundary conditions. The potential flow model and the homogeneous part of the Goland beam model are linear differential equations, but the flow tangency condition and the pressure jump terms in the structure model contain nonlinear terms. Because the fluid-structure model assumes small structural displacements, the nonlinear terms can be linearized using a small perturbation technique.

2.2 Small perturbation theory/linearization

The first step to linearize the problem is to consider the "static" solution", which is defined as the solution corresponding to the beam at rest and parallel uniform flow, $\vec{u}\,(t,x,y,z) = U\vec{j}$. The static solution can be expressed as:

$$h_0\,(t,y) = 0 \tag{2.23}$$

$$\theta_0\,(t,y) = 0 \tag{2.24}$$

For the fluid:

$$\vec{u}_0\,(t,x,y,z) = U\vec{j} \tag{2.25}$$

$$\phi_0\,(t,x,y,z) = Uy \tag{2.26}$$

It can be shown through direct substitution that the static solution satisfies the governing equations. The structure is now perturbed from the static solution by a small bending displacement $h^*(t,y)$ and small torsion angle $\theta^*(t,y)$:

$$h\,(t,y) = h_0\,(t,y) + h^*\,(t,y) \tag{2.27}$$

$$\theta\,(t,y) = \theta_0\,(t,y) + \theta^*\,(t,y) \tag{2.28}$$

From the definition of the static solution, it is evident that:

$$h\left(t,y\right)=h^{*}\left(t,y\right) \tag{2.29}$$

and

$$\theta\left(t,y\right)=\theta^{*}\left(t,y\right) \tag{2.30}$$

The perturbations in the structure will affect the flow field, but perturbations in any of the flow quantities are assumed to be small and are assuemd to satisfy the conservation equations in the potential flow model. Letting $\phi^{*}\left(t,x,y,z\right)$ denote the perturbation in the velocity potential, the velocity potential can be written as:

$$\phi\left(t,x,y,z\right)=Uy+\phi^{*}\left(t,x,y,z\right) \tag{2.31}$$

The far field condition, Equation (2.17), can be applied to the velocity potential in Equation (2.31) to obtain:

$$\lim_{r\to\infty}\phi^{*}\left(t,x,y,z\right)=0 \tag{2.32}$$

Denoting the perturbation in the pressure jump by $\delta p^{*}\left(t,x,y\right)$, the pressure jump can be written as:

$$\delta p\left(t,x,y\right)=\delta p_{0}\left(t,x,y\right)+\delta p^{*}\left(t,x,y\right) \tag{2.33}$$

Because $\delta p_{0}\left(t,x,y\right)=0$ from the static solution, the Kutta-Joukowski and Kutta conditions apply to the perturbation:

$$\delta p^{*}\left(t,|x|>2b,y>2l\right)=0 \tag{2.34}$$

$$\delta p^{*}\left(t,x,y=-l\right)=0 \tag{2.35}$$

Now that it has been shown that the perturbations in the flow quantities satisfy the boundary conditions, the model can be linearized by assuming the perturbations are small. Recall the flow tangency condition:

$$\begin{aligned}\nabla\phi\left(t,x,y,0^{\pm}\right)\cdot\vec{k}=&-\dot{h}\left(t,y\right)-x\dot{\theta}\left(t,y\right)-\left(\nabla\phi(t,x,y,0^{\pm})\cdot\vec{i}\right)\theta\left(t,y\right)\\&-\left(\nabla\phi(t,x,y,0^{\pm})\cdot\vec{j}\right)\left(h'\left(t,y\right)+x\theta'\left(t,y\right)\right)\end{aligned} \tag{2.36}$$

The velocity vector can be written as:

$$\vec{u}=\left[0+u^{*}\left(t,x,y,z\right)\right]\vec{i}+\left[U+v^{*}\left(t,x,y,z\right)\right]\vec{j}+\left[0+w^{*}\left(t,x,y,z\right)\right]\vec{k} \tag{2.37}$$

Here the starred quantities denote perturbations from the static solution. Thus,

$$\nabla\phi\left(t,x,y,0^{\pm}\right)\cdot\vec{i}=u^{*}\left(t,x,y,0^{\pm}\right) \tag{2.38}$$

$$\nabla\phi\left(t,x,y,0^{\pm}\right)\cdot\vec{j}=U+v^{*}\left(t,x,y,0^{\pm}\right) \tag{2.39}$$

$$\nabla\phi\left(t,x,y,0^{\pm}\right)\cdot\vec{k}=w^{*}\left(t,x,y,0^{\pm}\right) \tag{2.40}$$

Substituting these expressions, along with the expressions for $h(t,y)$ and $\theta(t,y)$, the flow tangency condition becomes:

$$\begin{aligned} w^{*}\left(t,x,y,0^{\pm}\right)=&-\frac{\partial}{\partial t}h^{*}\left(t,y\right)-x\frac{\partial}{\partial t}\theta^{*}\left(t,y\right)-u^{*}\left(t,x,y,0^{\pm}\right)\theta^{*}\left(t,y\right)\\ &-\left(U+v^{*}\left(t,x,y,0^{\pm}\right)\right)\left(\frac{\partial}{\partial y}h^{*}\left(t,y\right)+x\frac{\partial}{\partial y}\theta^{*}\left(t,y\right)\right) \end{aligned} \tag{2.41}$$

The last term can be simplified by noting that:

$$v^{*}\left(t,x,y,0^{\pm}\right)\ll U \tag{2.42}$$

Equation (2.41) becomes:

$$w^*\left(t,x,y,0^{\pm}\right) = -\frac{\partial}{\partial t}h^*\left(t,y\right) - x\frac{\partial}{\partial t}\theta^*\left(t,y\right) - u^*\left(t,x,y,0^{\pm}\right)\theta^*\left(t,y\right) - U\left(\frac{\partial}{\partial y}h^*\left(t,y\right) + x\frac{\partial}{\partial y}\theta^*\left(t,y\right)\right) \tag{2.43}$$

Because the starred quantities are assumed to be small,

$$\left|u^*\left(t,x,y,0^{\pm}\right)\theta^*\left(t,y\right)\right| \ll \left|w^*\left(t,x,y,0^{\pm}\right)\right| \tag{2.44}$$

This eliminates the third term on the RHS of Equation (2.43), and the equation becomes:

$$w^*\left(t,x,y,0^{\pm}\right) = -\frac{\partial}{\partial t}h^*\left(t,y\right) - x\frac{\partial}{\partial t}\theta^*\left(t,y\right) - U\left(\frac{\partial}{\partial y}h^*\left(t,y\right) + x\frac{\partial}{\partial y}\theta^*\left(t,y\right)\right) \tag{2.45}$$

Because $h\left(t,y\right) = h^*\left(t,y\right)$ and $\theta\left(t,y\right) = \theta^*\left(t,y\right)$, and using Equation (2.40), the linearized flow tangency condition is:

$$\nabla\phi\left(t,x,y,0^{\pm}\right)\cdot\vec{k} = -\frac{\partial}{\partial t}h\left(t,y\right) - x\frac{\partial}{\partial t}\theta\left(t,y\right) - U\left(\frac{\partial}{\partial y}h\left(t,y\right) + x\frac{\partial}{\partial y}\theta\left(t,y\right)\right) \tag{2.46}$$

For the pressure jump, recall the expression:

$$\delta p\left(t,x,y\right) = -\rho\left[\delta\left(\frac{\partial\phi}{\partial t}\right) + \delta\left(\frac{\nabla\phi\cdot\nabla\phi}{2}\right)\right] \tag{2.47}$$

The derivative in the first bracketed term becomes:

$$\frac{\partial \phi}{\partial t} = \frac{\partial}{\partial t}\left(Uy + \phi^*\left(t, x, y, z\right)\right) = \frac{\partial}{\partial t}\phi^*\left(t, x, y, z\right) \tag{2.48}$$

The second bracketed term in Equation (2.47) can be simplified by noting that:

$$\nabla\phi \cdot \nabla\phi = u^*u^* + \left(U + v^*\right)\left(U + v^*\right) + w^*w^* \tag{2.49}$$

Or,

$$\nabla\phi \cdot \nabla\phi = u^*u^* + 2Uv^* + U^2 + v^*v^* + w^*w^* \tag{2.50}$$

The second bracketed term in Equation (2.47) becomes:

$$\delta\left(\frac{\nabla\phi \cdot \nabla\phi}{2}\right) = \frac{1}{2}\delta\left(u^*u^* + 2Uv^* + U^2 + v^*v^* + w^*w^*\right) \tag{2.51}$$

Because $\delta\left(U^2\right) = 0$,

$$\delta\left(\frac{\nabla\phi \cdot \nabla\phi}{2}\right) = \frac{1}{2}\delta\left(u^*u^* + 2Uv^* + v^*v^* + w^*w^*\right) \tag{2.52}$$

Comparing the magnitude of each term,

$$u^*u^*, v^*v^*, w^*w^* \ll Uv^* \tag{2.53}$$

The second bracketed term in Equation (2.47) is:

$$\delta\left(\frac{\nabla\phi\cdot\nabla\phi}{2}\right) = \delta\left(Uv^*\right) = U\delta\left(v^*\right) \tag{2.54}$$

Or, in terms of the velocity potential:

$$\delta\left(\frac{\nabla\phi\cdot\nabla\phi}{2}\right) = U\delta\left(\frac{\partial\phi^*}{\partial y}\right) \tag{2.55}$$

Using the definition of the static solution:

$$\frac{\partial\phi^*}{\partial y} = -U + \frac{\partial\phi}{\partial y} \tag{2.56}$$

Equation (2.55) becomes:

$$\delta\left(\frac{\nabla\phi\cdot\nabla\phi}{2}\right) = \delta\left(\frac{\partial\phi}{\partial y}\right) \tag{2.57}$$

The pressure jump, Equation (2.47), can now be written as:

$$\delta p\left(t,x,y\right) = -\rho\left[\delta\left(\frac{\partial\phi}{\partial t}\right) + U\delta\left(\frac{\partial\phi}{\partial y}\right)\right] \tag{2.58}$$

Which contains only linear terms in ϕ. The governing equations for the structure become:

$$EI\frac{\partial^4 h(t,y)}{\partial y^4} + m\frac{\partial^2 h(t,y)}{\partial t^2} = -\rho \int_{-b}^{b} \left[\delta\left(\frac{\partial \phi}{\partial t}\right) + U\delta\left(\frac{\partial \phi}{\partial y}\right)\right] dx \tag{2.59}$$

and

$$-GJ\frac{\partial^2 \theta(t,y)}{\partial y^2} + I_\theta \frac{\partial^2 \theta(t,y)}{\partial t^2} = -\rho \int_{-b}^{b} \left[\delta\left(\frac{\partial \phi}{\partial t}\right) + U\delta\left(\frac{\partial \phi}{\partial y}\right)\right] x dx \tag{2.60}$$

Along with the linearized flow tangency condition:

$$\frac{\partial}{\partial z}\phi\left(t,x,y,0^{\pm}\right) = -\frac{\partial}{\partial t}h\left(t,y\right) - x\frac{\partial}{\partial t}\theta\left(t,y\right) - U\left(\frac{\partial}{\partial y}h\left(t,y\right) + x\frac{\partial}{\partial y}\theta\left(t,y\right)\right) \tag{2.61}$$

Equations (2.59)-(2.61) show that the problem has successfully been linearized, where the simplified set of equations are valid for small $h(t,y)$ and $\theta(t,y)$. These equations will be solved in the coming sections, with the understanding that any solutions should be used only when the structure displacements are small. Because flutter is a very abrupt, self-excited phenomenon, these assumptions are reasonable for air speeds up to the onset of instability. The goal now is to use the linearized set of equations to determine the largest value of U for which the system is stable, and define this U to be the flutter speed.

2.3 Generalized Possio Integral Equation

At the heart of the Balakrishnan continuum theory is the development and solution of the Generalized Possio Integral Equation (GPIE), a two dimensional form of the Possio Integral Equation encountered in normal flow aeroelasticity. The first step in the development is to define the Kussner doublet function, $A\left(t,x,y\right)$, which is defined only on the structure:

$$A\left(t,x,y\right)=-\frac{\delta p\left(t,x,y\right)}{\rho U} \tag{2.62}$$

Using the linearized pressure jump, the linearized Kussner doublet function can be written as:

$$A\left(t,x,y\right)=-\frac{1}{U}\delta\left(\frac{\partial\phi}{\partial t}\right)-\delta\left(\frac{\partial\phi}{\partial y}\right) \tag{2.63}$$

With this definition the structure governing equations, Equations (2.59) and (2.60), can be written as:

$$EI\frac{\partial^4 h(t,y)}{\partial y^4}+m\frac{\partial^2 h(t,y)}{\partial t^2}=\rho U\int_{-b}^{b}A\left(t,x,y\right)dx \tag{2.64}$$

and

$$-GJ\frac{\partial^2\theta(t,y)}{\partial y^2}+I_\theta\frac{\partial^2\theta(t,y)}{\partial t^2}=\rho U\int_{-b}^{b}A\left(t,x,y\right)xdx \tag{2.65}$$

The approach to solving Equations (2.64) and (2.65) can be summarized as using the fluid

model and boundary conditions to write $A(t,x,y)$ in terms of the structure displacements and their derivatives only, which will result in a set of differential equations for $h(t,y)$ and $\theta(t,y)$. The flow tangency condition, Equation (2.61), suggests that $A(t,x,y)$ should be written as a function of $\frac{\partial}{\partial z}\phi(t,x,y,0^{\pm})$. This approach does not carry the burden of obtaining an analytical solution for the velocity potential $\phi(t,x,y,z)$, but will require several manipulations of $\phi(t,x,y,z)$, and thus $A(t,x,y)$, while satisfying the potential flow equation and boundary conditions.

Following the approach in [2], the Laplace transform in the time variable and the spatial Fourier transforms in x and y of the velocity potential are taken to obtain:

$$\tilde{\hat{\phi}}(s,\omega_1,\omega_2,z) = \int_{-\infty}^{\infty}\int_{-\infty}^{\infty}\int_{0}^{\infty} e^{-ix\omega_1}e^{-iy\omega_2}e^{-st}\phi(t,x,y,z)dtdxdy \tag{2.66}$$

where

$$0 \leq s \leq \infty, -\infty \leq \omega_1 \leq \infty, -\infty \leq \omega_2 \leq \infty$$

In Equation (2.66) the Laplace transform is denoted by $\hat{}$ and each Fourier transform is denoted by $\tilde{}$. The next step is to obtain an equivalent form of the fluid governing equation in terms of the transformed velocity potential. It can be shown that the Fourier transform of a derivative is:

$$\int_{-\infty}^{\infty}\int_{-\infty}^{\infty}\int_{0}^{\infty} e^{-i(x\omega_1+y\omega_2)}e^{-st}\frac{\partial\phi}{\partial x}(t,x,y,z)dtdxdy = i\omega_1\tilde{\hat{\phi}}(s,\omega_1,\omega_2,z) \tag{2.67}$$

For the Fourier transform of a second derivative, it follows that:

$$\int_{-\infty}^{\infty}\int_{-\infty}^{\infty}\int_{0}^{\infty} e^{-i(x\omega_1+y\omega_2)}e^{-st}\frac{\partial^2\phi}{\partial x^2}(t,x,y,z)dtdxdy = -{\omega_1}^2\tilde{\hat{\phi}}(s,\omega_1,\omega_2,z) \tag{2.68}$$

Similarly, for the second derivative with respect to y,

$$\int_{-\infty}^{\infty}\int_{-\infty}^{\infty}\int_{0}^{\infty} e^{-i(x\omega_1+y\omega_2)}e^{-st}\frac{\partial^2\phi}{\partial y^2}(t,x,y,z)dtdxdy = -{\omega_2}^2\tilde{\hat{\phi}}(s,\omega_1,\omega_2,z) \tag{2.69}$$

For the z-derivative, note that:

$$\int_{-\infty}^{\infty}\int_{-\infty}^{\infty}\int_{0}^{\infty} e^{-i(x\omega_1+y\omega_2)}e^{-st}\frac{\partial^2\phi}{\partial z^2}(t,x,y,z)dtdxdy = \frac{\partial^2\tilde{\hat{\phi}}}{\partial z^2}(s,\omega_1,\omega_2,z) \tag{2.70}$$

Combining Equations (2.68)-(2.70),

$$\int_{-\infty}^{\infty}\int_{-\infty}^{\infty}\int_{0}^{\infty} e^{-i(x\omega_1+y\omega_2)}e^{-st}\left(\frac{\partial^2\phi}{\partial x^2}+\frac{\partial^2\phi}{\partial y^2}+\frac{\partial^2\phi}{\partial z^2}\right)dtdxdy = -{\omega_1}^2\tilde{\hat{\phi}} - {\omega_2}^2\tilde{\hat{\phi}} + \frac{\partial^2\tilde{\hat{\phi}}}{\partial z^2} \tag{2.71}$$

Recall the fluid governing equation:

$$\frac{\partial^2\phi}{\partial x^2}+\frac{\partial^2\phi}{\partial y^2}+\frac{\partial^2\phi}{\partial z^2} = 0 \tag{2.72}$$

Equation (2.71) becomes:

$$-{\omega_1}^2\tilde{\tilde{\hat{\phi}}} - {\omega_2}^2\tilde{\tilde{\hat{\phi}}} + \frac{\partial^2\tilde{\tilde{\hat{\phi}}}}{\partial z^2} = 0 \tag{2.73}$$

Equation(2.73) can be rearranged to obtain the differential equation:

$$\frac{\partial^2\tilde{\tilde{\hat{\phi}}}}{\partial z^2} = \left({\omega_1}^2 + {\omega_2}^2\right)\tilde{\tilde{\hat{\phi}}} \tag{2.74}$$

Equation (2.74) is a relatively simple differential equation, but because there is a jump discontinuity at $z = 0$, it must be solved in separate regions for $z < 0$ and $z > 0$. For a 2^{nd} order homogeneous equation it follows that:

$$\tilde{\tilde{\hat{\phi}}}\left(s, \omega_1, \omega_2, z\right) = b_1\left(s, \omega_1, \omega_2\right) e^{\sqrt{\omega_1^2+\omega_2^2}z} + b_2\left(s, \omega_1, \omega_2\right) e^{-\sqrt{\omega_1^2+\omega_2^2}z} \tag{2.75}$$

Here $b_1\left(s, \omega_1, \omega_2\right)$ and $b_2\left(s, \omega_1, \omega_2\right)$ are functions to be determined from the boundary conditions. The case where $z < 0$ is treated first. Recall that $\tilde{\tilde{\hat{\phi}}}$ vanishes in the far field, so that:

$$\tilde{\tilde{\hat{\phi}}}\left(s, \omega_1, \omega_2, z \to -\infty\right) = 0 \tag{2.76}$$

For $\tilde{\tilde{\hat{\phi}}}$ to be finite, $b_2\left(s, \omega_1, \omega_2\right) = 0$ for $z < 0$. $\tilde{\tilde{\hat{\phi}}}$ can now be written as:

$$\tilde{\tilde{\hat{\phi}}}(s,\omega_1,\omega_2,z) = b_1(s,\omega_1,\omega_2)\, e^{\sqrt{\omega_1^2+\omega_2^2}z} \quad \text{for} \quad z<0 \tag{2.77}$$

The function $b_1(s,\omega_1,\omega_2)$ can be obtained by evaluating $\tilde{\tilde{\hat{\phi}}}$ at the structure boundary, $z=0^-$:

$$\tilde{\tilde{\hat{\phi}}}(s,\omega_1,\omega_2,z) = \tilde{\tilde{\hat{\phi}}}_k\left(s,\omega_1,\omega_2,0^-\right) e^{z\sqrt{\omega_1^2+\omega_2^2}} \quad \text{for} \quad z<0 \tag{2.78}$$

Similarly, for $z>0$:

$$\tilde{\tilde{\hat{\phi}}}(s,\omega_1,\omega_2,z) = \tilde{\tilde{\hat{\phi}}}_k\left(s,\omega_1,\omega_2,0^+\right) e^{-z\sqrt{\omega_1^2+\omega_2^2}} \quad \text{for} \quad z>0 \tag{2.79}$$

Differentiating Equations (2.78) and (2.79), the following expressions are obtained:

$$\frac{\partial}{\partial z}\tilde{\tilde{\hat{\phi}}}(s,\omega_1,\omega_2,z) = \tilde{\tilde{\hat{\phi}}}_k\left(s,\omega_1,\omega_2,0^-\right)\sqrt{\omega_1^2+\omega_2^2}e^{z\sqrt{\omega_1^2+\omega_2^2}} \quad \text{for} \quad z<0 \tag{2.80}$$

and

$$\frac{\partial}{\partial z}\tilde{\tilde{\hat{\phi}}}(s,\omega_1,\omega_2,z) = -\tilde{\tilde{\hat{\phi}}}_k\left(s,\omega_1,\omega_2,0^+\right)\sqrt{\omega_1^2+\omega_2^2}e^{z\sqrt{\omega_1^2+\omega_2^2}} \quad \text{for} \quad z>0 \tag{2.81}$$

Equations (2.80) and (2.81) can be evaluated at the structure boundaries to obtain:

$$\frac{\partial}{\partial z}\tilde{\tilde{\hat{\phi}}}\left(s,\omega_1,\omega_2,0^-\right) = \tilde{\tilde{\hat{\phi}}}\left(s,\omega_1,\omega_2,0^-\right)\sqrt{\omega_1^2+\omega_2^2} \tag{2.82}$$

and

$$\frac{\partial}{\partial z}\tilde{\tilde{\hat{\phi}}}\left(s,\omega_1,\omega_2,0^+\right)=-\tilde{\tilde{\hat{\phi}}}\left(s,\omega_1,\omega_2,0^+\right)\sqrt{\omega_1^2+\omega_2^2} \tag{2.83}$$

With expressions for the z-derivative of the velocity potential, recall the flow tangency condition:

$$\nabla\phi\left(t,x,y,0\pm\right)\cdot\vec{k}=-\frac{\partial}{\partial t}h\left(t,y\right)-x\frac{\partial}{\partial t}\theta\left(t,y\right)-U\left[\frac{\partial}{\partial y}h\left(t,y\right)+x\frac{\partial}{\partial y}\theta\left(t,y\right)\right] \tag{2.84}$$

Because the RHS of Equation (2.84) does not depend on z, it is evident that:

$$\frac{\partial}{\partial z}\tilde{\tilde{\hat{\phi}}}\left(s,\omega_1,\omega_2,0^+\right)=\frac{\partial}{\partial z}\tilde{\tilde{\hat{\phi}}}\left(s,\omega_1,\omega_2,0^-\right) \tag{2.85}$$

Therefore, using Equations (2.82) and (2.83), the velocity potential at the upper and lower surfaces of the beam are related by:

$$\tilde{\tilde{\hat{\phi}}}\left(s,\omega_1,\omega_2,0^+\right)=-\tilde{\tilde{\hat{\phi}}}\left(s,\omega_1,\omega_2,0^-\right) \tag{2.86}$$

The jump in the transformed velocity potential becomes:

$$\delta\tilde{\tilde{\hat{\phi}}}=2\tilde{\tilde{\hat{\phi}}}\left(s,\omega_1,\omega_2,0^+\right)=2\tilde{\tilde{\hat{\phi}}}\left(s,\omega_1,\omega_2,0^-\right) \tag{2.87}$$

The jump in the transformed velocity potential can now be substituted into the expression for the Kussner doublet function. From its linearized form, Equation (2.63), and noting that $\delta(.)$ is commutative with differentiation, $A(t,x,y)$ can be written as:

$$A\left(t,x,y\right)=-\frac{1}{U}\frac{\partial\left(\delta\phi\right)}{\partial t}-\frac{\partial\left(\delta\phi\right)}{\partial y} \tag{2.88}$$

Taking the Laplace and double Fourier transforms of $A(t,x,y)$,

$$\tilde{\tilde{\hat{A}}}\left(s,\omega_1,\omega_2\right)=\int_{-\infty}^{\infty}\int_{-\infty}^{\infty}\int_{0}^{\infty}e^{-i(x\omega_1+y\omega_2)}e^{-st}\left[-\frac{1}{U}\frac{\partial}{\partial t}\delta\phi\left(t,x,y,z\right)-\frac{\partial}{\partial y}\delta\phi\left(t,x,y,z\right)\right]dtdxdy \tag{2.89}$$

Evaluating the Laplace transform of the first bracketed term in Equation (2.89), this term becomes:

$$\int_{-\infty}^{\infty}\int_{-\infty}^{\infty}\int_{0}^{\infty}e^{-i(x\omega_1+y\omega_2)}e^{-st}\left[-\frac{1}{U}\frac{\partial}{\partial t}\delta\phi\left(t,x,y,z\right)\right]dtdxdy=-\frac{1}{U}s\int_{-\infty}^{\infty}\int_{-\infty}^{\infty}e^{-i(x\omega_1+y\omega_2)}\delta\hat{\phi}\left(t,x,y,z\right)dxdy \tag{2.90}$$

Or, using the notation for Fourier transforms, this term can be written as:

$$\int_{-\infty}^{\infty}\int_{-\infty}^{\infty}\int_{0}^{\infty}e^{-i(x\omega_1+y\omega_2)}e^{-st}\left[-\frac{1}{U}\frac{\partial}{\partial t}\delta\phi\left(t,x,y,z\right)\right]dtdxdy=-\frac{s}{U}\delta\tilde{\tilde{\hat{\phi}}}\left(s,\omega_1,\omega_2,z\right) \tag{2.91}$$

The second bracketed term of Equation (2.89), from the property of Fourier transforms used previously, becomes:

$$\int_{-\infty}^{\infty}\int_{-\infty}^{\infty}\int_{0}^{\infty} e^{-i(x\omega_1+y\omega_2)}e^{-st}\left[-\frac{\partial}{\partial y}\delta\phi\left(t,x,y,z\right)\right]dtdxdy = -i\omega_2\delta\tilde{\tilde{\hat{\phi}}}\left(s,\omega_1,\omega_2,z\right) \tag{2.92}$$

Equation (2.89) becomes:

$$\tilde{\tilde{\hat{A}}}\left(s,\omega_1,\omega_2\right) = -\left(\frac{s}{U}+i\omega_2\right)\delta\tilde{\tilde{\hat{\phi}}}\left(s,\omega_1,\omega_2,z\right) \tag{2.93}$$

It is convenient to define the symbol:

$$\kappa \equiv \frac{s}{U} \tag{2.94}$$

Equation (2.93) can now be written in terms of κ:

$$\tilde{\tilde{\hat{A}}}\left(s,\omega_1,\omega_2\right) = -\left(\kappa+i\omega_2\right)\delta\tilde{\tilde{\hat{\phi}}}\left(s,\omega_1,\omega_2,z\right) \tag{2.95}$$

Using the expression for $\delta\tilde{\tilde{\hat{\phi}}}$ obtained in Equation (2.87), the Kussner doublet function becomes:

$$\tilde{\tilde{\hat{A}}}\left(s,\omega_1,\omega_2\right) = -2\left(\kappa+i\omega_2\right)\tilde{\tilde{\hat{\phi}}}\left(s,\omega_1,\omega_2,0^+\right) \tag{2.96}$$

Using Equation (2.83), $\hat{\tilde{\tilde{\phi}}}$ can be written in a slightly different form:

$$\hat{\tilde{\tilde{\phi}}}\left(s,\omega_1,\omega_2,0^+\right) = -\frac{1}{\sqrt{\omega_1^2+\omega_2^2}}\frac{\partial}{\partial z}\hat{\tilde{\tilde{\phi}}}\left(s,\omega_1,\omega_2,0^+\right) \tag{2.97}$$

Equation (2.96) becomes:

$$\hat{\tilde{\tilde{A}}}\left(s,\omega_1,\omega_2\right) = 2\frac{(\kappa+i\omega_2)}{\sqrt{\omega_1^2+\omega_2^2}}\frac{\partial}{\partial z}\hat{\tilde{\tilde{\phi}}}\left(s,\omega_1,\omega_2,0^+\right) \tag{2.98}$$

Rearranging Equation (2.98),

$$\frac{\partial}{\partial z}\hat{\tilde{\tilde{\phi}}}\left(s,\omega_1,\omega_2,0^+\right) = \frac{1}{2}\frac{\sqrt{\omega_1^2+\omega_2^2}}{(\kappa+i\omega_2)}\hat{\tilde{\tilde{A}}}\left(s,\omega_1,\omega_2\right) \tag{2.99}$$

Equation (2.99) is close to being in the form where the Kussner doublet function, $\hat{\tilde{\tilde{A}}}\left(s,\omega_1,\omega_2\right)$, can be related to the structural displacements via the flow tangency condition. First, both Fourier transforms are inverted to obtain:

$$\frac{\partial}{\partial z}\hat{\phi}\left(s,\omega_1,\omega_2,0^+\right) = \frac{1}{4\pi^2}\int_{-\infty}^{\infty}\int_{-\infty}^{\infty} e^{i(x\omega_1+y\omega_2)}\frac{\sqrt{\omega_1^2+\omega_2^2}}{2\left(\kappa+i\omega_2\right)}\hat{\tilde{\tilde{A}}}\left(s,\omega_1,\omega_2\right)d\omega_1 d\omega_2 \tag{2.100}$$

There is no need to invert the Laplace transform because the stability analysis will be performed in the Laplace domain. The Laplace transform of the flow tangency condition, Equation (2.61), is:

$$\frac{\partial}{\partial z}\hat{\phi}\left(s,\omega_1,\omega_2,0^+\right)=s\hat{h}\left(s,y\right)+sx\hat{\theta}\left(s,y\right)+U\left(\hat{h}'\left(s,y\right)+x\hat{\theta}'\left(s,y\right)\right) \tag{2.101}$$

In Equation (2.101), the prime denotes differentiation with respect to y. This expression can be substituted into Equation (2.100) to obtain:

$$\frac{1}{4\pi^2}\int_{-\infty}^{\infty}\int_{-\infty}^{\infty}e^{i(x\omega_1+y\omega_2)}\frac{\sqrt{\omega_1^2+\omega_2^2}}{2\left(\kappa+i\omega_2\right)}\tilde{\hat{A}}\left(s,\omega_1,\omega_2\right)d\omega_1 d\omega_2=s\hat{h}\left(s,y\right)+sx\hat{\theta}\left(s,y\right)$$
$$+U\left(\hat{h}'\left(s,y\right)+x\hat{\theta}'\left(s,y\right)\right) \tag{2.102}$$

Equation (2.102) is the Generalized Possio Integral Equation (GPIE), an integral equation where the function to be solved for is $\hat{A}\left(s,x,y\right)$. With $\hat{A}\left(s,x,y\right)$ representing the pressure jump across the structure, this equation connects the aerodynamics to the structural motion, which was the original goal. Possessing the solution of $A\left(s,\hat{x},y\right)$ from the GPIE will provide the aerodynamic loading in terms of the structure state variables, which will lead to a stability analysis in the Laplace domain to determine if the structure will flutter for a given air speed U. Equation (2.102) will be solved by treating the right hand side as being known. In other words, the structure state variables will be thought of as "inputs", with $\hat{A}\left(s,x,y\right)$ being the corresponding output.

The approach used here is to take advantage of the similarities between the GPIE and the Possio integral equation of normal flow aeroelasticity, which has a known solution [3].

The first difference between the two equations is that the GPIE contains a double integral, whereas the normal flow Possio equation contains only a single integral. Both equations have the Kussner doublet function as the kernel, with the structure variables on the right hand side, but a key difference is that the multiplier in the GPIE is not a Mikhlin multiplier. The GPIE can be manipulated to where it contains a Mikhlin multiplier, at which point it can be compared to the known solution of the 1-D Possio equation.

The first step is to decompose the RHS of Equation (2.102) by recognizing that it is of the form:

$$x\left(s\hat{\theta}\left(s,y\right)+U\hat{\theta}'\left(s,y\right)\right)+s\hat{h}\left(s,y\right)+U\hat{h}'\left(s,y\right)=x\hat{f}_1\left(s,y\right)+\hat{f}_2\left(s,y\right) \tag{2.103}$$

where

$$\hat{f}_1\left(s,y\right)=s\hat{\theta}\left(s,y\right)+U\hat{\theta}'\left(s,y\right) \tag{2.104}$$

and

$$\hat{f}_2\left(s,y\right)=s\hat{h}\left(s,y\right)+U\hat{h}'\left(s,y\right) \tag{2.105}$$

To decompose the LHS of Equation (2.102), let:

$$\hat{A}(s,x,y) = ix\hat{A}_1(s,y) + \hat{A}_2(s,y) \tag{2.106}$$

Taking the Fourier transforms in x and y, Equation (2.106) becomes:

$$\hat{\tilde{\tilde{A}}}(s,\omega_1,\omega_2) = \int_{-\infty}^{\infty}\int_{-\infty}^{\infty} e^{-i(x\omega_1+y\omega_2)} ix\hat{A}_1(s,y)\,dxdy + \int_{-\infty}^{\infty}\int_{-\infty}^{\infty} e^{-i(x\omega_1+y\omega_2)}\hat{A}_2(s,y)\,dxdy \tag{2.107}$$

To simplify Equation (2.107), the integrals can be rearranged to obtain:

$$\hat{\tilde{\tilde{A}}}(s,\omega_1,\omega_2) = \int_{-\infty}^{\infty} e^{-iy\omega_2}\hat{A}_1(s,y)\,dy \int_{-\infty}^{\infty} e^{-ix\omega_1} ixdx + \int_{-\infty}^{\infty} e^{-iy\omega_2}\hat{A}_2(s,y)\,dy \int_{-\infty}^{\infty} e^{-ix\omega_1} dx \tag{2.108}$$

Noticing that the integrals over y are Fourier transforms of $\hat{A}(s,x,y)$, Equation (2.108) becomes:

$$\hat{\tilde{\tilde{A}}}(s,\omega_1,\omega_2) = \tilde{\hat{A}}_1(s,\omega_2) \int_{-\infty}^{\infty} e^{-ix\omega_1} ixdx + \tilde{\hat{A}}_2(s,\omega_2) \int_{-\infty}^{\infty} e^{-ix\omega_1} dx \tag{2.109}$$

The second term in Equation (2.109) is the Fourier transform of 1, which gives the Dirac delta function. Equation (2.109) becomes:

$$\hat{\tilde{\tilde{A}}}(s,\omega_1,\omega_2) = \tilde{\hat{A}}_1(s,\omega_2) \int_{-\infty}^{\infty} e^{-ix\omega_1} ixdx + \tilde{\hat{A}}_2(s,\omega_2)\,\delta(\omega_1) \tag{2.110}$$

To simplify the first term in Equation (2.110), note that:

$$e^{-ix\omega_1} ix = -\frac{\partial}{\partial \omega_1}\left(e^{-ix\omega_1}\right) \tag{2.111}$$

Thus, Equation (2.110) becomes:

$$\tilde{\tilde{\hat{A}}}\left(s, \omega_1, \omega_2\right) = -\tilde{\hat{A}}_1\left(s, \omega_2\right) \frac{\partial}{\partial \omega_1} \int_{-\infty}^{\infty} e^{-ix\omega_1} dx + \tilde{\hat{A}}_2\left(s, \omega_2\right) \delta\left(\omega_1\right) \tag{2.112}$$

Noticing that the integral in Equation (2.112) is the Dirac delta function, the equation becomes:

$$\tilde{\tilde{\hat{A}}}\left(s, \omega_1, \omega_2\right) = -\delta'\left(\omega_1\right) \tilde{\hat{A}}_1\left(s, \omega_2\right) + \tilde{\hat{A}}_2\left(s, \omega_2\right) \delta\left(\omega_1\right) \tag{2.113}$$

Where $\delta'\left(\omega_1\right)$ is the distributional derivative, which has the following property:

$$\int_{-\infty}^{\infty} \delta'\left(\omega_1\right) g\left(\omega_1\right) d\omega_1 = -\int_{-\infty}^{\infty} \delta\left(\omega_1\right) g'\left(\omega_1\right) d\omega_1 \tag{2.114}$$

The expression for $\tilde{\tilde{\hat{A}}}\left(s, \omega_1, \omega_2\right)$ can now be substituted into the GPIE, Equation (2.102), to obtain:

$$\frac{1}{4\pi^2}\int_{-\infty}^{\infty}\int_{-\infty}^{\infty} -\delta'(\omega_1)\, e^{i(x\omega_1+y\omega_2)}\frac{\sqrt{\omega_1^2+\omega_2^2}}{2(\kappa+i\omega_2)}\tilde{\hat{A}}_1(s,\omega_2)\, d\omega_1 d\omega_2$$
$$+\frac{1}{4\pi^2}\int_{-\infty}^{\infty}\int_{-\infty}^{\infty}\delta(\omega_1)\, e^{i(x\omega_1+y\omega_2)}\frac{\sqrt{\omega_1^2+\omega_2^2}}{2(\kappa+i\omega_2)}\tilde{\hat{A}}_2(s,\omega_2)\, d\omega_1 d\omega_2 = x\hat{f}_1(s,y)+\hat{f}_2(s,y) \quad (2.115)$$

Using the property of the distributional derivative to simplify the first term, Equation (2.115) becomes:

$$\frac{1}{4\pi^2}\int_{-\infty}^{\infty}\int_{-\infty}^{\infty}\delta(\omega_1)\, e^{i(x\omega_1+y\omega_2)}\frac{ix\sqrt{\omega_1^2+\omega_2^2}+\omega_1(\omega_1^2+\omega_2^2)^{-\frac{1}{2}}}{2(\kappa+i\omega_2)}\tilde{\hat{A}}_1(s,\omega_2)\, d\omega_1 d\omega_2$$
$$+\frac{1}{4\pi^2}\int_{-\infty}^{\infty}\int_{-\infty}^{\infty}\delta(\omega_1)\, e^{i(x\omega_1+y\omega_2)}\frac{\sqrt{\omega_1^2+\omega_2^2}}{2(\kappa+i\omega_2)}\tilde{\hat{A}}_2(s,\omega_2)\, d\omega_1 d\omega_2 = x\hat{f}_1(s,y)+\hat{f}_2(s,y) \quad (2.116)$$

The Dirac delta function has the following property:

$$\int_{-\infty}^{\infty}\delta(\omega_1)\, g(\omega_1,\cdot)d\omega_1 = g(0,\cdot) \quad (2.117)$$

Thus, performing the integration over ω_1, Equation (2.116) becomes:

$$\frac{1}{4\pi^2}\int_{-\infty}^{\infty} e^{iy\omega_2}\frac{ix\,|\omega_2|}{2\,(\kappa+i\omega_2)}\tilde{\hat{A}}_1\,(s,\omega_2)\,d\omega_2$$
$$+\frac{1}{4\pi^2}\int_{-\infty}^{\infty} e^{iy\omega_2}\frac{|\omega_2|}{2\,(\kappa+i\omega_2)}\tilde{\hat{A}}_2\,(s,\omega_2)\,d\omega_2 = x\hat{f}_1(s,y)+\hat{f}_2\,(s,y) \tag{2.118}$$

Equating coefficients of like powers of x produces the set of integral equations:

$$\frac{1}{4\pi^2}\int_{-\infty}^{\infty} e^{iy\omega_2}\frac{|\omega_2|}{2\,(\kappa+i\omega_2)}i\tilde{\hat{A}}_1\,(s,\omega_2)\,d\omega_2 = \hat{f}_1(s,y) \tag{2.119}$$

$$\frac{1}{4\pi^2}\int_{-\infty}^{\infty} e^{iy\omega_2}\frac{|\omega_2|}{2\,(\kappa+i\omega_2)}\tilde{\hat{A}}_2\,(s,\omega_2)\,d\omega_2 = \hat{f}_2\,(s,y) \tag{2.120}$$

Equations (2.119) and (2.120) each have the same form as the 1-D Possio equation, which has a known solution [3]. The solution of the Possio equation will not be repeated here because of its length and complexity; see Balakrishnan [3] for the full solution. Instead, the solution will be used and adapted to $i\tilde{\hat{A}}_1\,(s,\omega_2)$ and $\tilde{\hat{A}}_2\,(s,\omega_2)$. The solutions in their most compact form are:

$$i\hat{A}_1\,(s,y) = (I+\kappa\mathcal{L}\,(0))\left[\hat{\nu}_1\,(s,\cdot)+h\,(\kappa,\cdot)\,\frac{L\,(\kappa,(I+\kappa\mathcal{L}\,(0))\,\hat{\nu}_1\,(s,\cdot))}{l\kappa\,(K_0\,(l\kappa)+K_1\,(l\kappa))\,e^{l\kappa}}\right] \tag{2.121}$$

and

$$\hat{A}_2(s,y) = (I + \kappa\mathcal{L}(0)) \left[\hat{\nu}_2(s,\cdot) + h(\kappa,\cdot) \frac{L(\kappa, (I + \kappa\mathcal{L}(0)) \hat{\nu}_2(s,\cdot))}{\ell\kappa (K_0(l\kappa) + K_1(l\kappa)) e^{l\kappa}} \right] \tag{2.122}$$

In Equation (2.122) I is the identity operator and dots have been used in the place of the y independent variable to ensure that the y dependence does not get integrated out by the operators. The operators ν_i are given by:

$$\hat{\nu}_1(s,\cdot) = 2\mathrm{T}\hat{f}_1(s,\cdot) \tag{2.123}$$

and

$$\hat{\nu}_2(s,\cdot) = 2\mathrm{T}\hat{f}_2(s,\cdot) \tag{2.124}$$

where T is the linear bounded operator defined by:

$$\mathrm{T}f = g \tag{2.125}$$

$$g(s,y) = \frac{1}{\pi}\sqrt{\frac{l-y}{l+y}} \int_{-l}^{l} \sqrt{\frac{l+\zeta}{l-\zeta}} \frac{f(s,\zeta)}{\zeta - y} d\zeta \tag{2.126}$$

The operator $\mathcal{L}(0)$ is given by:

$$\mathcal{L}(0) f = \bar{g} \tag{2.127}$$

where

$$\bar{g}(s, y) = \int_{-l}^{y} f(s, \zeta)\, d\zeta \tag{2.128}$$

The operator $L(\kappa, f)$ is defined as:

$$L(\kappa, f) = \int_{-l}^{l} e^{-\kappa(l-\zeta)} f(s, \zeta)\, d\zeta \tag{2.129}$$

The function $h(\kappa, y)$ is given by:

$$h(\kappa, y) = \frac{1}{\pi}\sqrt{\frac{l-y}{l+y}} \int_{0}^{\infty} e^{-\kappa\zeta} \sqrt{\frac{2l+\zeta}{\zeta}} \frac{1}{y-l-\zeta} d\zeta \tag{2.130}$$

$K_0(l\kappa)$ and $K_1(l\kappa)$ are the Bessel K functions:

$$K_0(l\kappa) = \int_{1}^{\infty} \frac{e^{-l\kappa t}}{\sqrt{t^2-1}} dt \tag{2.131}$$

$$K_1(l\kappa) = -K'_0(l\kappa) = \int_{1}^{\infty} \frac{t e^{-l\kappa t}}{\sqrt{t^2-1}} dt \tag{2.132}$$

Recall the decomposed form of the Kussner doublet function:

$$\hat{A}(s,x,y) = ix\hat{A}_1(s,y) + \hat{A}_2(s,y) \tag{2.133}$$

Using the solution to the GPIE, Equations (2.121) and (2.122), the Kussner doublet function can be written as:

$$\hat{A}(s,x,y) = (I + \kappa\mathcal{L}(0)) \left[x\hat{\nu}_1(s,\cdot) + xh(\kappa,\cdot) \frac{L(\kappa,(I+\kappa\mathcal{L}(0))\hat{\nu}_1(s,\cdot))}{l\kappa(K_0(l\kappa)+K_1(l\kappa))e^{l\kappa}} \right.$$

$$\left. + \hat{\upsilon}_2(s,\cdot) + h(\kappa,\cdot) \frac{L(\kappa,(I+\kappa\mathcal{L}(0))\hat{\nu}_2(s,\cdot))}{l\kappa(K_0(l\kappa)+K_1(l\kappa))e^{l\kappa}} \right] \tag{2.134}$$

Equation (2.134) is the solution for the Kussner doublet function, in the Laplace domain, as a function of integrals of the structure variables $\hat{h}(s,y)$ and $\hat{\theta}(s,y)$. The procedure so far has not produced a closed form expression for $\phi(t,x,y,z)$, and therefore does not contain a detailed description of the flow field off the structure, but this is not needed to analyze the stability of the structure. Having the solution for $\hat{A}(s,x,y)$, which represents the aerodynamic loading on the structure, the next step is to solve the structure governing equations.

2.4 Aeroelastic torsion dynamics

In this section the governing equation for the torsion angle, $\hat{\theta}(s,y)$, will be solved using the solution of the GPIE in the aerodynamic loading term. Because the goal is to perform a stability analysis, and not to obtain a time domain solution, the equation will be solved in the Laplace domain. Taking the Laplace transform of Equation (2.2), the governing equation for the torsion angle becomes:

$$-GJ\hat{\theta}''(s,y) + s^2 I_\theta \hat{\theta}(s,y) = \rho U \int_{-b}^{b} x\hat{A}(s,x,y)dx \tag{2.135}$$

The boundary conditions, unaffected by the Laplace transform, are:

$$\hat{\theta}(s,-l) = \hat{\theta}'(s,l) = 0 \tag{2.136}$$

Substituting in the decomposed form of $\hat{A}(s,x,y)$, the equation becomes:

$$-GJ\hat{\theta}''(s,y) + s^2 I_\theta \hat{\theta}(s,y) = \rho U \int_{-b}^{b} x^2 i\hat{A}_1(s,y)\,dx + \rho U \int_{-b}^{b} x\hat{A}_2(s,y)\,dx \tag{2.137}$$

The second integral, whose integrand is an odd function of x, evaluates to zero upon integrating from $-b$ to b. Evaluating the first integral, Equation (2.137) becomes:

$$-GJ\hat{\theta}''(s,y) + s^2 I_\theta \hat{\theta}(s,y) = \frac{2b^3}{3}\rho U i\hat{A}_1(s,y) \tag{2.138}$$

Substituting the expression for $i\hat{A}_1(s,y)$ from Equation (2.121) and rearranging, the equation becomes:

$$GJ\hat{\theta}''(s,y) = s^2 I_\theta \hat{\theta}(s,y) - \frac{2b^3}{3}\rho U\left(I+\kappa\mathcal{L}(0)\right)\left[\hat{\nu}_1(s,\cdot) + h(\kappa,\cdot)\frac{L\left(\kappa,\left(I+\kappa\mathcal{L}(0)\right)\hat{\nu}_1(s,\cdot)\right)}{l\kappa\left(K_0(l\kappa)+K_1(l\kappa)\right)e^{l\kappa}}\right] \tag{2.139}$$

Because there is no need to invert the Laplace transforms in Equation (2.139), and thus no need for initial conditions, the equation represents a two-point boundary value problem. It is convenient to solve Equation (2.139) by writing it in state-space form. Let:

$$\vec{x}(s,y) = \begin{bmatrix} \hat{\theta}(s,y) \\ \hat{\theta}'(s,y) \end{bmatrix} \tag{2.140}$$

Differentiating Equation (2.140),

$$\vec{x}'(s,y) = \begin{bmatrix} \hat{\theta}'(s,y) \\ \hat{\theta}''(s,y) \end{bmatrix} \tag{2.141}$$

The boundary condition vectors are:

$$\vec{x}(s,-l) = \begin{bmatrix} 0 \\ \hat{\theta}'(s,-l) \end{bmatrix} \tag{2.142}$$

And

$$\vec{x}\,(s,l) = \begin{bmatrix} \hat{\theta}\,(s,l) \\ \\ 0 \end{bmatrix} \tag{2.143}$$

The $\hat{\theta}\,(s,l)$ and $\hat{\theta}'\,(s,-l)$ are unspecified by the problem and are left arbitrary. The governing equation, Equation (2.139), can now be expressed as:

$$\vec{x}'\,(s,y) = A\,(s,U)\,\vec{x}\,(s,y) \tag{2.144}$$

The matrix A should not be confused with the Kussner doublet function. $A\,(s,U)$ can be decomposed into two parts as follows:

$$A\,(s,U) = A_0\,(s,0) + A_U\,(s,U) \tag{2.145}$$

where

$$A_0\,(s,0) = \begin{bmatrix} 0 & 1 \\ \\ \frac{s^2 I_\theta}{GJ} & 0 \end{bmatrix} \tag{2.146}$$

$$A_U\,(s,U) = \begin{bmatrix} 0 & 0 \\ \\ -W_1\,(s,U) & -W_2\,(s,U) \end{bmatrix} \tag{2.147}$$

The nonzero elements of the matrix in Equation (2.147) are linear bounded operators defined by:

$$W_1(s,U)\,x_1 = g_1 \tag{2.148}$$

with

$$g_1 = \frac{4b^3\rho U s}{3GJ}\left(I+\kappa\mathcal{L}(0)\right)\left[\mathrm{T}x_1(s,\cdot)+h(\kappa,\cdot)\,\frac{L\left(\kappa,\left(I+\kappa\mathcal{L}(0)\right)\mathrm{T}x_1(s,\cdot)\right)}{l\kappa\left(K_0(l\kappa)+K_1(l\kappa)\right)e^{l\kappa}}\right] \tag{2.149}$$

The following substitution for $\hat{\nu}_1(s,y)$ has been used:

$$\hat{\nu}_1(s,y) = 2\mathrm{T}\hat{f}_1(s,\cdot) = 2\mathrm{T}\left[sx_1(s,\cdot)+Ux_2(s,\cdot)\right] \tag{2.150}$$

Similarly, $W_2(s,U)$ is given by:

$$W_2(s,U)\,x_1 = g_2 \tag{2.151}$$

with

$$g_2 = \frac{4b^3\rho U^2}{3GJ}\left(I+\kappa\mathcal{L}(0)\right)\left[\mathrm{T}x_2(s,\cdot)+h(\kappa,\cdot)\,\frac{L\left(\kappa,\left(I+\kappa\mathcal{L}(0)\right)\mathrm{T}x_2(s,\cdot)\right)}{l\kappa\left(K_0(l\kappa)+K_1(l\kappa)\right)e^{l\kappa}}\right] \tag{2.152}$$

The state-space representation of the equation for $\hat{\theta}(s,y)$ can be written in a slightly different form:

$$\vec{x}'(s,y) = A_0(s,0)\,\vec{x} + \vec{b}(s,y) \tag{2.153}$$

where

$$\vec{b}(s,y) = \begin{bmatrix} -W_1(s,U)\,x_1 \\ -W_2(s,U)\,x_2 \end{bmatrix} \tag{2.154}$$

Here $\vec{b}(s,y)$ contains x_1 and x_2, but is not an explicit function of x_1 and x_2 due to the operators W. Therefore, Equation (2.153) can be treated as a nonhomogeneous set of linear differential equations with $\vec{b}(s,y)$ representing the nonhomogeneous part. For a two-point boundary value problem on $[-l,l]$, application of Duhamel's theorem yields the solution:

$$\vec{x}(s,y) = e^{A_0(s,0)(y+l)}\vec{x}(s,-l) + \int_{-l}^{y} e^{A_0(s,0)(y-\sigma)}\vec{z}(s,\sigma)d\sigma \tag{2.155}$$

where

$$\vec{z}(s,\sigma) = \begin{bmatrix} 0 \\ z_1(s,\sigma) \end{bmatrix} \tag{2.156}$$

where

$$z_1(s,\sigma) = -\frac{4b^3\rho U s}{3GJ}\left(I+\kappa\mathcal{L}(0)\right)\left[\mathrm{T}\hat{\theta}(s,\cdot) + h(\kappa,\cdot)\frac{L\left(\kappa,\left(I+\kappa\mathcal{L}(0)\right)\mathrm{T}\hat{\theta}(s,\cdot)\right)}{l\kappa\left(K_0(l\kappa)+K_1(l\kappa)\right)e^{l\kappa}}\right]$$
$$-\frac{4b^3\rho U^2}{3GJ}\left(I+\kappa\mathcal{L}(0)\right)\left[\mathrm{T}\hat{\theta}'(s,\cdot) + h(\kappa,\cdot)\frac{L\left(\kappa,\left(I+\kappa\mathcal{L}(0)\right)\mathrm{T}\hat{\theta}'(s,\cdot)\right)}{l\kappa\left(K_0(l\kappa)+K_1(l\kappa)\right)e^{l\kappa}}\right] \tag{2.157}$$

It should be noted that the σ-dependence in Equations (2.155) and (2.157) is found in the operators, which will integrate to σ instead of y. Equations (2.155)-(2.157) provide a general solution for the torsion angle, but they need to be simplified before applying the boundary conditions. First, $z_1(s,\sigma)$ can be written more compactly as:

$$z_1(s,\sigma) = -\frac{4b^3\rho U}{3GJ}\left(I+\kappa\mathcal{L}(0)\right)\left[\mathrm{T}\left(s\hat{\theta}(s,\cdot)+U\hat{\theta}'(s,\cdot)\right)\right.$$
$$\left.+h(\kappa,\cdot)\frac{L\left(\kappa,\left(I+\kappa\mathcal{L}(0)\right)\mathrm{T}\left(s\hat{\theta}(s,\cdot)+U\hat{\theta}'(s,\cdot)\right)\right)}{l\kappa\left(K_0(l\kappa)+K_1(l\kappa)\right)e^{l\kappa}}\right] \tag{2.158}$$

To evaluate the matrix exponential, let:

$$\beta = \sqrt{\frac{I_\theta}{GJ}} \tag{2.159}$$

$A_0(s,0)$ becomes:

$$A_0(s,0) = \begin{bmatrix} 0 & 1 \\ (s\beta)^2 & 0 \end{bmatrix} \tag{2.160}$$

The matrix exponential is defined by:

$$e^{A} = \sum_{n=0}^{\infty} \frac{1}{n!} A^{n} \tag{2.161}$$

Evaluating a few terms, the matrix exponential can be written as:

$$e^{A_0(s,0)} = \begin{bmatrix} \left(1 + \frac{1}{2!}(s\beta)^2 + \frac{1}{4!}(s\beta)^4 + ...\right) & \left(1 + \frac{1}{3!}(s\beta)^2 + \frac{1}{5!}(s\beta)^4 + ...\right) \\ \left((s\beta)^2 + \frac{1}{3!}(s\beta)^4 + ...\right) & \left(1 + \frac{1}{2!}(s\beta)^2 + \frac{1}{4!}(s\beta)^4 + ...\right) \end{bmatrix} \tag{2.162}$$

Comparing the elements of Equation(2.162) to Taylor series expansions of common functions, it can be shown that:

$$e^{A(s,0)y} = \begin{bmatrix} \cosh(s\beta y) & \frac{1}{s\beta}\sinh(s\beta y) \\ s\beta \sinh(\beta s y) & \cosh(s\beta y) \end{bmatrix} \tag{2.163}$$

The expression for the matrix exponential can now be substituted into the solution given by Equations (2.155)-(2.157), along with the expression for the clamped end boundary condition vector $\vec{x}(s,-l)$, to obtain:

$$\vec{x}(s,y) = \begin{bmatrix} \frac{1}{s\beta}\sinh(s\beta(y+l)) \\ \cosh(s\beta(y+l)) \end{bmatrix} + \int_{-l}^{y} \begin{bmatrix} \frac{1}{s\beta}\sinh(s\beta(y-\sigma)) \\ \cosh(s\beta(y-\sigma)) \end{bmatrix} z_1(s,\sigma)\, d\sigma \tag{2.164}$$

The arbitrary condition $\hat{\theta}'(-l)$ from earlier has been set to 1 for convenience. Equation

(2.164) is not a solution in closed form because the second term on the right hand side is an implicit function of $\vec{x}(s,y)$. It is convenient to define the vector:

$$\vec{x}_0(s,y) = \begin{bmatrix} \frac{1}{s\beta}\sinh(s\beta(y+l)) \\ \cosh(s\beta(y+l)) \end{bmatrix} \tag{2.165}$$

And the linear bounded operator:

$$J(s,U)\,\vec{x} = \vec{y} \tag{2.166}$$

with

$$\vec{y} = \int_{-l}^{y} \begin{bmatrix} \frac{1}{s\beta}\sinh(s\beta(y-\sigma)) \\ \cosh(s\beta(y-\sigma)) \end{bmatrix} z_1(s,\sigma)\,d\sigma \tag{2.167}$$

Equation (2.164) can be written as:

$$[I - J(s,U)]\,\vec{x}(s,y) = \vec{x}_0(s,y) \tag{2.168}$$

Thus,

$$\vec{x}(s,y) = [I - J(s,U)]^{-1}\,\vec{x}_0(s,y) \tag{2.169}$$

The inverse in Equation (2.169) can be expressed as a Neumann expansion:

$$[I - J(s,U)]^{-1} = \sum_{n=0}^{\infty} [J(s,U)]^n \tag{2.170}$$

For the linear stability problem, the series is truncated at $n = 1$. Thus,

$$\vec{x}(s,y) = [I + J(s,U)]\,\vec{x}_0(s,y) \tag{2.171}$$

Equation (2.171) is a closed form solution, but the boundary condition at $y = l$ still needs to be enforced. Before applying this boundary condition, it is convenient to expand the solution given by Equation (2.171) as follows:

$$\hat{\theta}(s,y) = \frac{1}{s\beta}\sinh(2s\beta l) + \int_{-l}^{y} \frac{1}{s\beta}\sinh(s\beta(y-\sigma))\, z_0(s,\sigma)\, d\sigma \tag{2.172}$$

$$\hat{\theta}'(s,y) = \cosh(2s\beta l) + \int_{-l}^{y} \cosh(s\beta(y-\sigma))\, z_0(s,\sigma)\, d\sigma \tag{2.173}$$

where

$$\begin{aligned} z_0(s,\sigma) = &-\frac{4b^3\rho U}{3GJ}(I + \kappa\mathcal{L}(0))\Bigg[\mathrm{T}(sx_{0,1}(s,\cdot) + Ux_{0,2}(s,\cdot)) \\ &+h(\kappa,\cdot)\frac{L(\kappa,(I+\kappa\mathcal{L}(0))\,\mathrm{T}(sx_{0,1}(s,\cdot)+Ux_{0,2}(s,\cdot)))}{l\kappa(K_0(l\kappa)+K_1(l\kappa))e^{l\kappa}}\Bigg] \end{aligned} \tag{2.174}$$

Applying the free end boundary condition, $\hat{\theta}'(s,l) = 0$, Equation (2.173) becomes:

$$0 = \cosh(2s\beta l) + \int_{-l}^{l} \cosh(s\beta(l-\sigma))\, z_0(s,\sigma)\, d\sigma \tag{2.175}$$

To satisfy Equation (2.175), let:

$$d(s,U) = \cosh(2s\beta l) + \int_{-l}^{l} \cosh(s\beta(l-\sigma))\, z_0(s,\sigma)\, d\sigma \tag{2.176}$$

To satisfy the boundary conditions it is required that:

$$d(s,U) = 0 \tag{2.177}$$

Equation (2.177) can be satisfied by finding the complex roots s for a given air speed U. Consider the special case of the structure in still air, where $U = 0$. Equation (2.176) becomes:

$$d(s,0) = \cosh(2s\beta l) \tag{2.178}$$

Thus, to satisfy Equation (2.177):

$$\cosh(2s\beta l) = 0 \tag{2.179}$$

The roots to Equation (2.179) are:

$$(2s\beta l)_n = 2\pi i\,(2n-1) \tag{2.180}$$

Using the definition of β and solving for s_n, note that:

$$s_n = \frac{i\pi}{l}\,(2n-1)\sqrt{\frac{GJ}{I_\theta}} \tag{2.181}$$

It is interesting to note that the torsional natural frequencies of the structure in still air are given by:

$$\omega_{T,n} = \frac{\pi}{l}\,(2n-1)\sqrt{\frac{GJ}{I_\theta}} \tag{2.182}$$

Defining the real and imaginary parts of s_n to be:

$$s_n\,(U) = \lambda_n\,(U) + i\omega_n\,(U) \tag{2.183}$$

It is clear that:

$$\omega_n\,(0) = \omega_{T,n} \tag{2.184}$$

Equations (2.183) and (2.184) show that the imaginary part of s_n is equal to the torsional

natural frequencies when $U = 0$. Therefore, the $\omega_n(U)$ for $U > 0$ can be thought of as "aeroelastic modes". Extending this concept to the real part of s_n, the $\lambda_n(U)$ can be thought of as aeroelastic damping of the structure. With this in mind, it should be expected for $\lambda_n(U)$ to play an important role in determining the stability of the system.

A common way to determine the stability of a system is to assume that the time domain solution can be written in the form:

$$\theta(t, y) = f(y)e^{mt} \tag{2.185}$$

In Equation (2.185) m is a complex number. It is evident from Equation (2.185) that $\theta(t, y)$ will exhibit exponential growth for $\mathrm{Re}(m) > 0$ and exponential decay for $\mathrm{Re}(m) < 0$. Taking the time derivative of $\theta(t, y)$, Equation (2.185) becomes:

$$\dot{\theta}(t, y) = mf(y)e^{mt} \tag{2.186}$$

Note that:

$$\dot{\theta}(t, y) = m\theta(t, y) \tag{2.187}$$

Taking the Laplace transform, Equation (2.187) becomes:

$$s\hat{\theta}\left(s,y\right)=m\hat{\theta}\left(t,y\right) \tag{2.188}$$

And thus $s=m$ for the form of the solution assumed in Equation (2.185). This shows that for a given U, the system is stable for $\mathrm{Re}\left[s\left(U\right)\right]<0$ and unstable for $\mathrm{Re}\left[s\left(U\right)\right]>0$. The results obtained for the case of $U=0$ suggest that there are a countable number of roots for each U, each corresponding to an aeroelastic mode. This makes the "Root Locus" technique a natural choice for determining if an individual mode is stable for a given U.

A Root Locus stability plot is a plot of $\lambda_n(U)$ versus U, where each mode n will produce its own curve. This leads to the definition of the modal flutter speed $U_{F,n}$ of mode n as the smallest value of U for which λ_n is non-negative. The flutter speed is defined as the smallest U in the set of modal flutter speeds $U_{F,n}$. This can be expressed mathematically using the infimum:

$$U_F=\inf_n\{U_{F,n}\} \tag{2.189}$$

where the infimum is taken over all modes.

2.5 Aeroelastic bending dynamics

The bending dynamics of the structure in axial flow is analyzed in the same manner as was done for torsion. The governing equation will be solved in the Laplace domain, using state-space representation, where the goal is to determine the minimum air speed U which will cause the structure to become unstable. The governing equation for bending in the Laplace domain is:

$$ms^2\hat{h}(s,y) + EI\hat{h}''''(s,y) = \rho U \int_{-b}^{b} \hat{A}(s,x,y)dx \tag{2.190}$$

where the prime denotes differentiation with respect to y. Using the solution for $\hat{A}(s,x,y)$, Equation (2.190) becomes:

$$ms^2\hat{h}(s,y) + EI\hat{h}''''(s,y) = \rho U \int_{-b}^{b} ix\hat{A}_1(s,y)dx + \rho U \int_{-b}^{b} \hat{A}_2(s,y)dx \tag{2.191}$$

Evaluating the integrals on the right hand side, and rearranging, the Equation (2.191) becomes:

$$\hat{h}''''(s,y) = -\frac{ms^2}{EI}\hat{h}(s,y) + \frac{2b\rho U}{EI}\hat{A}_2(s,y) \tag{2.192}$$

To write Equation(2.192) in state-space form, let:

$$\vec{x}\,(s,y) = \begin{bmatrix} \hat{h}\,(s,y) \\ \hat{h}'\,(s,y) \\ \hat{h}''\,(s,y) \\ \hat{h}'''\,(s,y) \end{bmatrix} \tag{2.193}$$

Taking the derivative,

$$\vec{x}\,'\,(s,y) = \begin{bmatrix} \hat{h}'\,(s,y) \\ \hat{h}''\,(s,y) \\ \hat{h}'''\,(s,y) \\ \hat{h}''''\,(s,y) \end{bmatrix} \tag{2.194}$$

The boundary condition vectors are:

$$\vec{x}\,(s,-l) = \begin{bmatrix} 0 \\ 0 \\ \hat{h}''\,(s,-l) \\ \hat{h}'''\,(s,-l) \end{bmatrix} \tag{2.195}$$

and

$$\vec{x}(s,l) = \begin{bmatrix} \hat{h}(s,l) \\ \hat{h}'(s,l) \\ 0 \\ 0 \end{bmatrix} \tag{2.196}$$

The non-zero entries in the boundary condition vectors are understood to be arbitrary because they are not specified by the physics of the problem; in fact they can safely be set to 1. Equation (2.192) can now be written as:

$$\vec{x}'(s,y) = A(s,U)\,\vec{x}(s,y) \tag{2.197}$$

The coefficient matrix $A(s,U)$ can be decomposed as follows:

$$A(s,U) = A_0(s,0) + A_U(s,U) \tag{2.198}$$

where

$$A_0(s,0) = \begin{bmatrix} 0 & 1 & 0 & 0 \\ 0 & 0 & 1 & 0 \\ 0 & 0 & 0 & 1 \\ -\frac{ms^2}{EI} & 0 & 0 & 0 \end{bmatrix} \tag{2.199}$$

and

$$A_U(s,U) = \begin{bmatrix} 0 & 0 & 0 & 0 \\ 0 & 0 & 0 & 0 \\ 0 & 0 & 0 & 0 \\ W_1 & W_2 & 0 & 0 \end{bmatrix} \tag{2.200}$$

where the operators W_1 and W_2 are defined as:

$$W_1(s,U)\, x_1 = g_1 \tag{2.201}$$

$$W_2(s,U)\, x_2 = g_2 \tag{2.202}$$

where

$$g_1 = \frac{4b\rho U s}{EI}\left(I + \kappa\mathcal{L}(0)\right)\left[\mathrm{T}x_1(s,\cdot) + h(\kappa,\cdot)\,\frac{L\left(\kappa,\left(I+\kappa\mathcal{L}(0)\right)\mathrm{T}x_1(s,\cdot)\right)}{l\kappa\left(K_0(l\kappa)+K_1(l\kappa)\right)e^{l\kappa}}\right] \tag{2.203}$$

$$g_2 = \frac{4b\rho U^2}{EI}\left(I + \kappa\mathcal{L}(0)\right)\left[\mathrm{T}x_2(s,\cdot) + h(\kappa,\cdot)\,\frac{L\left(\kappa,\left(I+\kappa\mathcal{L}(0)\right)\mathrm{T}x_2(s,\cdot)\right)}{l\kappa\left(K_0(l\kappa)+K_2(l\kappa)\right)e^{l\kappa}}\right] \tag{2.204}$$

The linear system can now be written as:

$$\vec{x}'(s,y) = A_0(s,0)\,\vec{x}(s,y) + \vec{b}(s,y) \tag{2.205}$$

where

$$\vec{b}\left(s,y\right)=\begin{bmatrix} g_1 \\ \\ g_2 \end{bmatrix} \tag{2.206}$$

Recognizing that Equation (2.205), along with the boundary conditions in Equations (2.195) and (2.196), represents a two-point boundary value problem, the solution can be written as:

$$\vec{x}\left(s,y\right)=e^{A_0(s,0)(y+l)}\vec{x}\left(s,-l\right)+\int_{-l}^{y}e^{A_0(s,0)(y-\sigma)}\vec{z}\left(s,\sigma\right)d\sigma \tag{2.207}$$

where

$$\vec{z}\left(s,\sigma\right)=\begin{bmatrix} 0 \\ \\ 0 \\ \\ 0 \\ \\ z_1\left(s,\sigma\right) \end{bmatrix} \tag{2.208}$$

where

$$\begin{aligned} z_1\left(s,\sigma\right)=&-\frac{2b\rho U}{EI}\left(I+\kappa\mathcal{L}\left(0\right)\right)\Bigg[\mathrm{T}\left(s\hat{h}\left(s,\cdot\right)+U\hat{h}'\left(s,\cdot\right)\right) \\ &+h\left(\kappa,\cdot\right)\frac{L\left(\kappa,\left(I+\kappa\mathcal{L}\left(0\right)\right)\mathrm{T}\left(s\hat{h}\left(s,\cdot\right)+U\hat{h}'\left(s,\cdot\right)\right)\right)}{l\kappa\left(K_0\left(l\kappa\right)+K_1\left(l\kappa\right)\right)e^{l\kappa}}\Bigg] \end{aligned} \tag{2.209}$$

To evaluate the matrix exponential of $A_0(s,0)$, let:

$$A_0(s,0) = \begin{bmatrix} 0 & 1 & 0 & 0 \\ 0 & 0 & 1 & 0 \\ 0 & 0 & 0 & 1 \\ \gamma^4 & 0 & 0 & 0 \end{bmatrix} \tag{2.210}$$

where

$$\gamma^4 = -\frac{ms^2}{EI} \tag{2.211}$$

The definition of the matrix exponential can be written as a power series:

$$e^A = \sum_{n=0}^{\infty} \frac{A^n}{n!} = 1 + A + \frac{AA}{2!} + \frac{AAA}{3!} + ... \tag{2.212}$$

The matrix exponential is then determined by expanding a few terms of the power series, and comparing the expressions in each element to Taylor series of common functions. To write the matrix exponential, let:

$$a_{ij}(s,y) = e^{A_{ij}(s,0)(y)} \tag{2.213}$$

The sixteen elements of $e^{A_{ij}(s,0)(y)}$ are:

$$a_{11}(s,y) = \frac{1}{2}\left[\cos(\gamma y) + \cosh(\gamma y)\right] \tag{2.214}$$

$$a_{12}(s,y) = \frac{1}{2\gamma}\left[\sin(\gamma y) + \sinh(\gamma y)\right] \tag{2.215}$$

$$a_{13}(s,y) = \frac{1}{2\gamma^2}\left[-\cos(\gamma y) + \cosh(\gamma y)\right] \tag{2.216}$$

$$a_{14}(s,y) = \frac{1}{2\gamma^3}\left[-\sin(\gamma y) + \sinh(\gamma y)\right] \tag{2.217}$$

$$a_{21}(s,y) = \frac{1}{2}\gamma\left[-\sin(\gamma y) + \sinh(\gamma y)\right] \tag{2.218}$$

$$a_{22}(s,y) = \frac{1}{2}\left[\cos(\gamma y) + \cosh(\gamma y)\right] \tag{2.219}$$

$$a_{23}(s,y) = \frac{1}{2\gamma}\left[\sin(\gamma y) + \sinh(\gamma y)\right] \tag{2.220}$$

$$a_{24}(s,y) = \frac{1}{2\gamma^2}\left[-\cos(\gamma y) + \cosh(\gamma y)\right] \tag{2.221}$$

$$a_{31}(s,y) = \frac{1}{2}\gamma^2\left[-\cos(\gamma y) + \cosh(\gamma y)\right] \tag{2.222}$$

$$a_{32}(s,y) = \frac{1}{2}\gamma\left[-\sin(\gamma y) + \sinh(\gamma y)\right] \tag{2.223}$$

$$a_{33}(s,y) = \frac{1}{2}\left[\cos(\gamma y) + \cosh(\gamma y)\right] \tag{2.224}$$

$$a_{34}(s,y) = \frac{1}{2\gamma}\left[\sin(\gamma y) + \sinh(\gamma y)\right] \tag{2.225}$$

$$a_{41}(s,y) = \frac{1}{2}\gamma^3\left[\sin(\gamma y) + \sinh(\gamma y)\right] \tag{2.226}$$

$$a_{42}(s,y) = \frac{1}{2}\gamma^2\left[-\cos(\gamma y) + \cosh(\gamma y)\right] \tag{2.227}$$

$$a_{43}(s,y) = \frac{1}{2}\gamma\left[-\sin(\gamma y) + \sinh(\gamma y)\right] \tag{2.228}$$

$$a_{44}(s,y) = \frac{1}{2}\left[\cos(\gamma y) + \cosh(\gamma y)\right] \tag{2.229}$$

The solution to Equation (2.205) can now be written as:

$$x_1(s,y) = a_{13}(s,y+l) + a_{14}(s,y+l) + \int_{-l}^{y} a_{14}(s,y-\sigma)\, z_1(s,\sigma)\, d\sigma \tag{2.230}$$

$$x_2(s,y) = a_{23}(s,y+l) + a_{24}(s,y+l) + \int_{-l}^{y} a_{24}(s,y-\sigma)\, z_1(s,\sigma)\, d\sigma \tag{2.231}$$

$$x_3(s,y) = a_{33}(s,y+l) + a_{34}(s,y+l) + \int_{-l}^{y} a_{34}(s,y-\sigma)\, z_1(s,\sigma)\, d\sigma \tag{2.232}$$

$$x_4(s,y) = a_{43}(s,y+l) + a_{44}(s,y+l) + \int_{-l}^{y} a_{44}(s,y-\sigma)\, z_1(s,\sigma)\, d\sigma \tag{2.233}$$

Before applying the free end boundary conditions, Equations (2.230)-(2.233) need to be simplified. First, let:

$$\vec{q}(s,y) = \begin{bmatrix} a_{13}(s,y) + a_{14}(s,y) \\ a_{23}(s,y) + a_{24}(s,y) \\ a_{33}(s,y) + a_{34}(s,y) \\ a_{43}(s,y) + a_{44}(s,y) \end{bmatrix} \tag{2.234}$$

Note that $z_1(s,U,\sigma)$ can be written as:

$$z_1(s,U,\sigma) = W_1 x_1(s,\sigma) + W_2 x_2(s,\sigma) \tag{2.235}$$

The solution becomes:

$$x_1(s,y) = q_1(s,y+l) + \int_{-l}^{y} a_{14}(s,y-\sigma)\left[W_1 x_1(s,\sigma) + W_2 x_2(s,\sigma)\right] d\sigma \tag{2.236}$$

$$x_2(s,y) = q_2(s,y+l) + \int_{-l}^{y} a_{24}(s,y-\sigma)\left[W_1 x_1(s,\sigma) + W_2 x_2(s,\sigma)\right] d\sigma \tag{2.237}$$

$$x_3(s,y) = q_3(s,y+l) + \int_{-l}^{y} a_{34}(s,y-\sigma)\left[W_1 x_1(s,\sigma) + W_2 x_2(s,\sigma)\right] d\sigma \tag{2.238}$$

$$x_4(s,y) = q_4(s,y+l) + \int_{-l}^{y} a_{44}(s,y-\sigma)\left[W_1 x_1(s,\sigma) + W_2 x_2(s,\sigma)\right] d\sigma \tag{2.239}$$

To simplify further, let:

$$\vec{\chi} = \begin{bmatrix} x_1 \\ \\ x_2 \end{bmatrix} \tag{2.240}$$

It is convenient to define the operator:

$$\mathcal{P}_1\vec{\chi} = \begin{bmatrix} \int_{l}^{y} a_{14}(s,y-\sigma)\left[W_1 x_1(s,\sigma) + W_2 x_2(s,\sigma)\right] d\sigma \\ \int_{l}^{y} a_{24}(s,y-\sigma)\left[W_1 x_1(s,\sigma) + W_2 x_2(s,\sigma)\right] d\sigma \end{bmatrix} \tag{2.241}$$

Equations (2.236) and (2.237) become:

$$\vec{\chi} - \mathcal{P}_1\vec{\chi} = \begin{bmatrix} q_1 \\ \\ q_2 \end{bmatrix} \tag{2.242}$$

Solving for $\vec{\chi}$,

$$\vec{\chi} = (I - \mathcal{P}_1)^{-1} \begin{bmatrix} q_1 \\ \\ q_2 \end{bmatrix} \tag{2.243}$$

Applying the Neumann expansion in the same manner as was done for torsion, Equation (2.243) becomes:

$$\vec{\chi} = (I + \mathcal{P}_1) \begin{bmatrix} q_1 \\ \\ q_2 \end{bmatrix} \tag{2.244}$$

The operator $\mathcal{P}_3$ is defined as:

$$\mathcal{P}_3 \vec{\chi} = \begin{bmatrix} \int_l^y a_{34}(s, y-\sigma) \left[W_1 x_1(s,\sigma) + W_2 x_2(s,\sigma) \right] d\sigma \\ \int_l^y a_{44}(s, y-\sigma) \left[W_1 x_1(s,\sigma) + W_2 x_2(s,\sigma) \right] d\sigma \end{bmatrix} \tag{2.245}$$

The second half of the solution, Equations (2.238) and (2.239), can be expressed as:

$$\begin{bmatrix} x_3 \\ \\ x_4 \end{bmatrix} = \mathcal{P}_3 \vec{\chi} + \begin{bmatrix} q_3 \\ \\ q_4 \end{bmatrix} \tag{2.246}$$

Substituting the expression for $\vec{\chi}$ from Equation (2.244),

$$\begin{bmatrix} x_3 \\ \\ x_4 \end{bmatrix} = \mathcal{P}_3 (I + \mathcal{P}_1) \begin{bmatrix} q_1 \\ \\ q_2 \end{bmatrix} + \begin{bmatrix} q_3 \\ \\ q_4 \end{bmatrix} \tag{2.247}$$

As an approximation the product of the operators, $\mathcal{P}_3 \mathcal{P}_1$, can be neglected to obtain:

$$\begin{bmatrix} x_3 \\ \\ x_4 \end{bmatrix} = \mathcal{P}_3 \begin{bmatrix} q_1 \\ \\ q_2 \end{bmatrix} + \begin{bmatrix} q_3 \\ \\ q_4 \end{bmatrix} \tag{2.248}$$

Equations (2.245) and (2.248) provide a simplified form of the solution for the structure state variables, $\vec{x}$, where the right hand side no longer depends on $\vec{x}$. The full solution can now be written as:

$$x_1(s,y) = q_1(s,y+l) + \int_{-l}^{y} a_{14}(s,y-\sigma)\left[W_1 q_1(s,\sigma) + W_2 q_2(s,\sigma)\right] d\sigma \tag{2.249}$$

$$x_2(s,y) = q_2(s,y+l) + \int_{-l}^{y} a_{24}(s,y-\sigma)\left[W_1 q_1(s,\sigma) + W_2 q_2(s,\sigma)\right] d\sigma \tag{2.250}$$

$$x_3(s,y) = q_3(s,y+l) + \int_{-l}^{y} a_{34}(s,y-\sigma)\left[W_1 q_1(s,\sigma) + W_2 q_2(s,\sigma)\right] d\sigma \tag{2.251}$$

$$x_4(s,y) = q_4(s,y+l) + \int_{-l}^{y} a_{44}(s,y-\sigma)\left[W_1 q_1(s,\sigma) + W_2 q_2(s,\sigma)\right] d\sigma \tag{2.252}$$

Equations (2.249)-(2.252) are now in the form where the free end boundary conditions can be applied. Recall:

$$x_3(s,l) = x_4(s,l) = 0 \tag{2.253}$$

From Equations (2.251) and (2.252), the boundary conditions are enforced by:

$$0 = q_3(s, 2l) + \int_{-l}^{l} a_{34}\left(s, l-\sigma\right)\left[W_1 q_1\left(s,\sigma\right) + W_2 q_2\left(s,\sigma\right)\right] d\sigma \tag{2.254}$$

$$0 = q_4(s, 2l) + \int_{-l}^{l} a_{44}\left(s, l-\sigma\right)\left[W_1 q_1\left(s,\sigma\right) + W_2 q_2\left(s,\sigma\right)\right] d\sigma \tag{2.255}$$

Using the expressions from the matrix exponential $e^{A_{ij}(s,0)(\cdot)}$, the quantities $q_i\left(s,\cdot\right)$ and $a_{ij}\left(s,\cdot\right)$ in Equations (2.254) and (2.255) can be written as:

$$q_1(s,\sigma) = \frac{1}{2\gamma^2}\left[-\cos\left(\sigma\gamma\right) + \cosh\left(\sigma\gamma\right)\right] + \frac{1}{2\gamma^3}\left[-\sin\left(\sigma\gamma\right) + \sinh\left(\sigma\gamma\right)\right] \tag{2.256}$$

$$q_2(s,\sigma) = \frac{1}{2\gamma}\left[\sin\left(\sigma\gamma\right) + \sinh\left(\sigma\gamma\right)\right] + \frac{1}{2\gamma^2}\left[-\cos\left(\sigma\gamma\right) + \cosh\left(\sigma\gamma\right)\right] \tag{2.257}$$

$$q_3(s,2l) = \frac{1}{2}\left[\cos\left(2l\gamma\right) + \cosh\left(2l\gamma\right)\right] + \frac{1}{2\gamma}\left[\sin\left(2l\gamma\right) + \sinh\left(2l\gamma\right)\right] \tag{2.258}$$

$$q_4(s,2l) = \frac{1}{2}\gamma\left[-\sin\left(2l\gamma\right) + \sinh\left(2l\gamma\right)\right] + \frac{1}{2}\left[\cos\left(2l\gamma\right) + \cosh\left(2l\gamma\right)\right] \tag{2.259}$$

$$a_{34}(s, l-\sigma) = \frac{1}{2\gamma}\left[\sin\left(\left(l-\sigma\right)\gamma\right) + \sinh\left(\left(l-\sigma\right)\gamma\right)\right] \tag{2.260}$$

$$a_{44}(s, l-\sigma) = \frac{1}{2}\left[\cos\left(\left(l-\sigma\right)\gamma\right) + \cosh\left(\left(l-\sigma\right)\gamma\right)\right] \tag{2.261}$$

To satisfy Equations (2.254) and (2.255), they are written in the form:

$$0 = D_0\left(s, 0\right)\vec{\alpha} + D_U\left(s, U\right)\vec{\alpha} \tag{2.262}$$

where each equation has been multiplied by scalar α. That is,

$$\vec{\alpha} = \begin{bmatrix} \alpha \\ \\ \alpha \end{bmatrix} \tag{2.263}$$

The matrices in Equation (2.262) are given by:

$$D_0\left(s, 0\right) = \begin{bmatrix} \frac{1}{2}\left[\cos\left(2l\gamma\right) + \cosh\left(2l\gamma\right)\right] & \frac{1}{2\gamma}\left[\sin\left(2l\gamma\right) + \sinh\left(2l\gamma\right)\right] \\ \\ \frac{1}{2}\gamma\left[-\sin\left(2l\gamma\right) + \sinh\left(2l\gamma\right)\right] & \frac{1}{2}\left[\cos\left(2l\gamma\right) + \cosh\left(2l\gamma\right)\right] \end{bmatrix} \tag{2.264}$$

and

$$D_U\left(s, U\right) = \begin{bmatrix} \int\limits_{-l}^{l} \frac{1}{2\gamma}\sin\left(\left(l-\sigma\right)\gamma\right) z_q\left(s, \sigma\right) d\sigma & \int\limits_{-l}^{l} \frac{1}{2\gamma}\sinh\left(\left(l-\sigma\right)\gamma\right) z_q\left(s, \sigma\right) d\sigma \\ \\ \int\limits_{-l}^{l} \frac{1}{2}\cos\left(\left(l-\sigma\right)\gamma\right) z_q\left(s, \sigma\right) d\sigma & \int\limits_{-l}^{l} \frac{1}{2}\cosh\left(\left(l-\sigma\right)\gamma\right) z_q\left(s, \sigma\right) d\sigma \end{bmatrix} \tag{2.265}$$

where

$$z_q(s,\sigma) = W_1 q_1(s,\sigma) + W_2 q_2(s,\sigma) \tag{2.266}$$

and γ is defined by:

$$\gamma^4 = -\frac{ms^2}{EI} \tag{2.267}$$

Equation (2.261) can be written as:

$$0 = \left[D_0(s,0) + D_U(s,U)\right]\vec{\alpha} \tag{2.268}$$

Using the definition:

$$d(s,U) = \det\left[D_0(s,0) + D_U(s,U)\right] \tag{2.269}$$

Equation (2.268) is satisfied if:

$$d(s,U) = 0 \tag{2.270}$$

The free end boundary conditions can be satisfied by finding the roots s that satisfy Equation (2.270) for a given air speed U. As was done for torsion, the special case of $U = 0$ is considered. For $U = 0$:

$$d(s,0) = \det\left[D_0(s,0)\right] \tag{2.271}$$

Evaluating the determinant, and setting it to zero, Equation (2.271) becomes:

$$0 = \frac{1}{4}\left[\cos(2l\gamma) + \cosh(2l\gamma)\right]^2 - \frac{1}{4}\left[\sin(2l\gamma) + \sinh(2l\gamma)\right]\left[-\sin(2l\gamma) + \sinh(2l\gamma)\right] \tag{2.272}$$

Expanding the terms in Equation (2.272), and simplifying, the equation becomes:

$$1 + \cos(2l\gamma)\cosh(2l\gamma) = 0 \tag{2.273}$$

Equation (2.273) is a transcendental equation of the form:

$$1 + \cos(\beta)\cosh(\beta) = 0 \tag{2.274}$$

The roots in Equation (2.274) can found through numerical solution. The first five roots are given in Table 2.1.

Table 2.1: First five roots to Equation (2.273).

n	β_n
1	1.875
2	4.694
3	7.855
4	11.00
5	14.14

It is evident that the roots β_n are positive and real. The β_n are related to γ_n by:

$$2l\gamma_n = \beta_n \tag{2.275}$$

The terms in Equation (2.275) can be squared to obtain:

$$\gamma_n^2 = \frac{\beta_n^2}{4l^2} \tag{2.276}$$

Using the definition of γ from Equation (2.267),

$$\pm\sqrt{\frac{m}{EI}}is_n = \frac{\beta_n^2}{4l^2} \tag{2.277}$$

Or,

$$s_n = i\sqrt{\frac{EI}{m}}\frac{1}{4l^2}{\beta_n}^2 \tag{2.278}$$

where the negative root of s_n has been discarded. The real and imaginary parts of s_n are denoted by:

$$s_n = \sigma_n + i\omega_n \tag{2.279}$$

Comparison of Equations (2.278) and (2.279) yields:

$$\omega_n = \sqrt{\frac{EI}{m}}\frac{1}{4l^2}{\beta_n}^2 \tag{2.280}$$

As was the case for torsion, Equation (2.280) shows that the ω_n are the bending natural frequencies of the structure. Therefore, the $\omega_n(U)$ for nonzero U represent "aeroelastic modes" and the $\lambda_n(U)$ corresponds to aeroelastic damping of the structure. By virtue of the Laplace transform, $\mathrm{Re}\,[d(s,U)] < 0$ indicates that the system is stable and $\mathrm{Re}\,[d(s,U)] > 0$ indicates that the system is unstable.

The key observation, which was also made in the torsion case, is that there are a countable set of roots s_n to $d(s,U) = 0$ for a given U. Hence, the root locus method is a natural choice to determine if a given aeroelastic mode is stable by starting at the structure mode $s_n(0) = i\omega_n(0)$. For each n a stability curve can be constructed showing $\lambda_n(U)$ as a function

of U, and the modal flutter speed is defined as the smallest value of U_n for which $\lambda_n(U)$ is non-negative. Then flutter speed of the system is defined as the smallest $U_{F,n}$, for all n:

$$U_F = \inf_n \{U_{F,n}\} \tag{2.281}$$

Once again, the infimum is taken over all modes.

2.6 Stability of torsional motion in axial flow

In this section it will be shown that torsional motion is unconditionally stable in axial flow, at least when modelled using linear structure and fluid dynamics. This is done simply by proving that the flutter determinant, $d(s,U)$, has no zeros for all $U > 0$. To begin, recall the flutter determinant for torsion:

$$d(i\omega,U) = \cosh(2i\omega\beta l) - \frac{4b^3\rho U}{3GJ}\int_{-l}^{y}\cosh(i\omega\beta(y-\sigma))z_0(i\omega,\sigma)\,d\sigma \tag{2.282}$$

where

$$\begin{aligned} z_0(i\omega,\sigma) = (U + i\omega\mathcal{L}(0))\Bigg[&\mathrm{T}(i\omega x_{0,1}(s,\cdot) + Ux_{0,2}(s,\cdot)) \\ &+h(\kappa,\cdot)\frac{L(\kappa,(I+\kappa\mathcal{L}(0))\,\mathrm{T}(i\omega x_{0,1}(i\omega,\cdot)+Ux_{0,2}(i\omega,\cdot)))}{l\kappa(K_0(l\kappa)+K_1(l\kappa))e^{l\kappa}}\Bigg] \end{aligned} \tag{2.283}$$

where

$$\kappa = \frac{i\omega}{U} \tag{2.284}$$

The first observation is that as $U \to \infty$,the function $z_0 \to -\infty$.In this limit, note that:

$$\lim_{U\to\infty}|d(s,U)| \to -\infty \tag{2.285}$$

With U appearing in the denominator of κ, the approach now is to investigate the behavior of $d(i\omega, U)$ for some very small U , which is denoted by U_0 :

$$0 < U_0 \ll 1 \tag{2.286}$$

Several of the terms in Equation (2.283) can be compared, noting that $U_0 \ll 1$. First, notice that with U_0 very small:

$$U_0 + i\omega\mathcal{L}(0) \cong i\omega\mathcal{L}(0) \tag{2.287}$$

Similarly,

$$\mathrm{T}\left(i\omega x_{0,1}(i\omega, \cdot) + U_0 x_{0,2}(i\omega, \cdot)\right) \cong \mathrm{T}\left(i\omega x_{0,1}(i\omega, \cdot)\right) \tag{2.288}$$

Equation (2.283) reduces to:

$$z_0(i\omega, \sigma) = i\omega\mathcal{L}(0)\left[\mathrm{T}\left(i\omega x_{0,1}(s, \cdot)\right) + H(\kappa, \cdot) L\left(\kappa, \left(I + \kappa\mathcal{L}(0)\right)\mathrm{T}\left(i\omega x_{0,1}(i\omega, \cdot)\right)\right)\right] \tag{2.289}$$

$H(\kappa, \cdot)$ is defined as:

$$H(\kappa, \cdot) = \frac{h(\kappa, \cdot)}{l\kappa\left(K_0(l\kappa) + K_1(l\kappa)\right)e^{l\kappa}} \tag{2.290}$$

The denominator in Equation (2.290) is the Sears formula [25]:

$$S\left(l\kappa\right)=l\kappa\left(K_0\left(l\kappa\right)+K_1\left(l\kappa\right)\right)e^{l\kappa} \tag{2.291}$$

The Sears formula, $S\left(\kappa\right)$, which appears in the normal flow continuum solution, has already been analyzed in [4]. For brevity, the analysis will not be repeated here. The result is:

$$S\left(l\kappa\right)=O\left(U^{-\frac{4}{3}}\right) \tag{2.292}$$

Recall the function $h\left(\kappa,y\right)$, now written using $\kappa=\frac{i\omega}{U_0}$:

$$h\left(\kappa,y\right)=\frac{1}{\pi}\sqrt{\frac{l-y}{l+y}}\int_0^\infty e^{-\frac{i\omega}{U_0}\zeta}\sqrt{\frac{2l+\zeta}{\zeta}}\frac{1}{y-l-\zeta}d\zeta \tag{2.293}$$

Note that for U_0 very small:

$$e^{-\frac{i\omega}{U_0}\zeta}=\cos\left(\frac{i\omega}{U_0}\zeta\right)-i\sin\left(\frac{i\omega}{U_0}\zeta\right)=O\left(1\right) \tag{2.294}$$

Thus,

$$H\left(\kappa,\cdot\right)=O\left({U_0}^{\frac{4}{3}}\right) \tag{2.295}$$

Furthermore, note that with no further dependence of U_0 on the second bracketed term of Equation (2.289), that:

$$H(\kappa,\cdot)\,\mathcal{L}\left[\kappa,\left(I+\kappa\mathcal{L}(0)\right)\mathrm{T}\left(i\omega x_{0,1}(i\omega,\cdot)\right)\right]=O\left({U_0}^{\frac{4}{3}}\right) \tag{2.296}$$

Noting that:

$$\mathrm{T}\left(i\omega x_{0,1}(i\omega,\cdot)\right)\gg O\left({U_0}^{\frac{4}{3}}\right) \tag{2.297}$$

Equation (2.289) reduces to, for small U:

$$z_0(i\omega,\sigma)=-\frac{4b^3\rho}{3GJ}i\omega\mathcal{L}(0)\,\mathrm{T}\left(i\omega x_{0,1}(i\omega,\cdot)\right) \tag{2.298}$$

Thus,

$$\lim_{U\to 0} z_0(i\omega,\sigma)=-\frac{4b^3\rho}{3GJ}i\omega\mathcal{L}(0)\,\mathrm{T}\left(i\omega x_{0,1}(i\omega,\cdot)\right) \tag{2.299}$$

Thus, for small U, $d(i\omega,U)$ becomes:

$$\lim_{U\to 0} d(i\omega,U)=\cosh(2i\omega\beta l)-\frac{4b^3\rho}{3GJ}i\omega\int_{-l}^{y}\cosh\left(i\omega\beta(y-\sigma)\right)\mathcal{L}(0)\,\mathrm{T}\left(i\omega x_{0,1}(i\omega,\cdot)\right)d\sigma \tag{2.300}$$

Or,

$$d\left(i\omega,0\right)=\cosh\left(2i\omega\beta l\right)-\frac{4b^{3}\rho}{3GJ}i\omega\int_{-l}^{y}\cosh\left(i\omega\beta\left(y-\sigma\right)\right)\mathcal{L}\left(0\right)\mathrm{T}\left(i\omega x_{0,1}\left(i\omega,\cdot\right)\right)d\sigma \tag{2.301}$$

The next step is to consider the behavior of the derivative of $d\left(i\omega,U\right)$ as $U\rightarrow 0$. From Equation (2.299), note that $z_{0}\left(i\omega,\sigma\right)$ approaches a constant as $U\rightarrow 0$. Taking the derivative, Equation (2.300) becomes:

$$\frac{\partial}{\partial U}d\left(i\omega,U\right)=\frac{\partial}{\partial U}\left[-\frac{4b^{3}\rho U}{3GJ}\int_{-l}^{y}\cosh\left(i\omega\beta\left(y-\sigma\right)\right)\mathcal{L}\left(0\right)\mathrm{T}\left(i\omega x_{0,1}\left(i\omega,\cdot\right)\right)d\sigma\right] \tag{2.302}$$

In the limit of $U\rightarrow 0$ the integrand in Equation (2.302) is a constant, hence:

$$\frac{\partial}{\partial U}d\left(i\omega,U\right)=-\frac{4b^{3}\rho}{3GJ}\int_{-l}^{y}\cosh\left(i\omega\beta\left(y-\sigma\right)\right)\mathcal{L}\left(0\right)\mathrm{T}\left(i\omega x_{0,1}\left(i\omega,\cdot\right)\right)d\sigma \tag{2.303}$$

Note that:

$$\frac{\partial^{2}}{\partial U^{2}}d\left(i\omega,U\right)=0 \tag{2.304}$$

From Equation (2.303), the first derivative is a negative constant, indicating a negative slope near $U=0$, and therefore $d\left(i\omega\right)$ is expected to monotonically decrease with U . To investigate this further, consider the absolute square of the function, which is defined as:

$$\left\|z\right\|^{2}=z\bar{z} \tag{2.305}$$

where $\bar{z}$ is the complex conjugate of z . The absolute square of $d(i\omega, U)$ is:

$$\|d(i\omega, U)\|^2 = d(i\omega, U)\, d(-i\omega, U) \tag{2.306}$$

The first derivative of $\|d(i\omega, U)\|^2$ is:

$$\frac{\partial}{\partial U}\|d(i\omega, U)\|^2 = \frac{\partial}{\partial U}d(i\omega, U)\, d(-i\omega, U) + d(i\omega, U)\, \frac{\partial}{\partial U}d(-i\omega, U) \tag{2.307}$$

And the second derivative,

$$\begin{aligned}\frac{\partial^2}{\partial U^2}\|d(i\omega, U)\|^2 =& d(-i\omega, U)\, \frac{\partial^2}{\partial U^2}d(i\omega, U) + \frac{\partial}{\partial U}d(i\omega, U)\, \frac{\partial}{\partial U}d(-i\omega, U) \\ &+ d(-i\omega, U)\, \frac{\partial^2}{\partial U^2}d(i\omega, U) + \frac{\partial}{\partial U}d(i\omega, U)\, \frac{\partial}{\partial U}d(-i\omega, U)\end{aligned} \tag{2.308}$$

Noting that the second derivative of $d(i\omega, U)$ is zero, Equation (2.308) reduces to:

$$\frac{\partial^2}{\partial U^2}\|d(i\omega, U)\|^2 = \frac{\partial}{\partial U}d(i\omega, U)\, \frac{\partial}{\partial U}d(-i\omega, U) + \frac{\partial}{\partial U}d(-i\omega, U)\, \frac{\partial}{\partial U}d(i\omega, U) \tag{2.309}$$

The next step is to consider the complex conjugate of $d(i\omega, U)$. First, using properties of $\cosh(z)$, Equation (2.303) can be written as:

$$\frac{\partial}{\partial U} d\left(i\omega, U\right) = -\frac{4b^3\rho}{3GJ} \int_{-l}^{y} \cos\left(\omega\beta\left(y-\sigma\right)\right) \mathcal{L}\left(0\right) \mathrm{T}\left(i\omega x_{0,1}\left(i\omega, \cdot\right)\right) d\sigma \tag{2.310}$$

Noting that $i\omega$ can be treated as a constant in the integral in $\mathrm{T}\left(i\omega x_{0,1}\left(i\omega, \cdot\right)\right)$, the complex conjugate is:

$$\frac{\partial}{\partial U} d\left(-i\omega, U\right) = -\frac{\partial}{\partial U} d\left(i\omega, U\right) \tag{2.311}$$

Thus,

$$\frac{\partial^2}{\partial U^2} \left\| d\left(i\omega, U\right) \right\|^2 = -\left[\frac{\partial}{\partial U} d\left(i\omega, U\right)\right]^2 \tag{2.312}$$

Using Equation (2.303), it is concluded that for small U , the function $d\left(i\omega, U\right)$ will be concave downward, indicating that it will decrease monotonically. The analysis so far can be summarized as:

1. For $U = 0$, $d\left(i\omega, U\right)$ is a nonzero, negative constant.

2. For small U, $d\left(i\omega, U\right)$ has negative slope.

3. For small U, the absolute square of $d\left(i\omega, U\right)$ shows that it is concave downward.

4. As $U \to \infty$, $d\left(i\omega, U\right)$ approaches $-\infty$.

Having proven the statements above, it has been shown that $d(i\omega, U)$ is negative for all $U > 0$, and therefore there is no $U > 0$ that will produce zeroes of $d(i\omega, U)$, and therefore there is no flutter speed. This concludes the proof that torsional motion is unconditionally stable in axial flow.

2.7 Divergence speed

The divergence speed is defined as an air speed that produces an unstable structure, with a frequency of zero. While the divergence speed is a construct of static aeroelasticity, it can be detected by a flutter analysis which is of course based on dynamic aeroelasticity. For example, it has been proven to exist in normal flow aeroelasticity [12]. Its existence can be investigated by determining if the flutter determinant has zeroes for $\omega = 0$:

$$d\left(0, U_D\right) = 0 \tag{2.313}$$

where U_D is the divergence speed if Equation (2.313) is satisfied. A key finding of the Balakrishnan continuum theory is that the divergence speed is undefined in axial flow. To prove this, consider the integral:

$$\bar{h}\left(\frac{i\omega}{U}, y\right) = \int_0^\infty e^{-\frac{i\omega}{U}\zeta} \sqrt{\frac{2l+\zeta}{\zeta}} \frac{1}{y-l-\zeta} d\zeta \tag{2.314}$$

The integral in Equation (2.314) appears in the flutter determinant for both bending and torsion. Setting $\omega = 0$, the integral becomes:

$$\bar{h}\left(0, y\right) = \int_0^\infty \sqrt{\frac{2l+\zeta}{\zeta}} \frac{1}{y-l-\zeta} d\zeta \tag{2.315}$$

Simplifying the square root, and changing the sign, Equation (2.315) becomes:

$$\bar{h}(0,y) = -\int_0^\infty \sqrt{1+\frac{2l}{\zeta}}\frac{1}{-y+l+\zeta}d\zeta \tag{2.316}$$

Because the upper bound on the integral is infinity, ζ can be treated as being large. Notice that the square root simplifies to:

$$\lim_{\zeta\to\infty}\sqrt{1+\frac{2l}{\zeta}} = 1 \tag{2.317}$$

The integral is now in a form where it can be evaluated analytically. Equation (2.317) becomes:

$$\bar{h}(0,y) = -\lim_{M\to\infty}\ln(-y+l+\zeta) = -\infty \tag{2.318}$$

It is clear that the integral $\bar{h}(0,y)$, and thus $d(i\omega,U)$, is undefined for both bending and torsional motion. This concludes the proof that the divergence speed is undefined in axial flow.

3 Modifications to Balakrishnan continuum theory and methods for determining the flutter speed

This chapter presents the techniques developed to compute the flutter speed using the Balakrishnan continuum theory. First, the root locus stability method is modified so that all of the functions resulting from the axial flow solution are defined. The solution of the GPIE for bending motion, $\hat{A}_2(s,y)$, is then decomposed so that it can be evaluated for calculation of the flutter determinant. The functions composing $\hat{A}_2(s,y)$ contain integrals that are singular at the endpoints and within the domain of integration. In this chapter two methods for handling singular integrals numerically are presented: the IMT method [18] and the Tanh transformation [15]. Finally, this chapter concludes with calculated results for a rectangular beam-like structure.

3.1 Modification to the root locus stability method

In the normal flow continuum theory developed by Balakrishnan [2], a root locus method was employed to determine the minimum air speed at which the structure becomes unstable. This method is based on assuming a general form for $h(t,y)$:

$$h(t,y) = f(y)\, e^{mt} \tag{3.1}$$

The Laplace domain $h(t,y)$ takes the form:

$$\hat{h}(s,y) = e^{(\lambda+i\omega)t} f(y) \tag{3.2}$$

with

$$s = \lambda + i\omega \tag{3.3}$$

There are a countable number of ω_n , each corresponding to an "aeroelastic" mode; the ω_n are the natural frequencies of the structure when $U = 0$. The root locus method evaluates the flutter determinant for a given ω_n , and finds the roots λ and U that make it zero. That is, for a given ω_n :

$$\mathrm{Re}\left[d(\lambda + i\omega_n, U)\right] = 0 \tag{3.4}$$

$$\mathrm{Im}\left[d(\lambda + i\omega_n, U)\right] = 0 \tag{3.5}$$

It is evident that if $\lambda < 0$, the structure is stable for that U , and if $\lambda > 0$ the structure is unstable at the corresponding air speed U . A stability curve, with λ vs U , is plotted starting at $U = 0$. As U is increased beyond zero, λ is negative, and if λ reaches zero and becomes positive, there is a U for that aeroelastic mode ω_n that will cause the structure to become unstable. The minimum U for which λ is non-negative is the modal flutter speed for the given ω_n . However, it is also possible that for a given ω_n the λ will remain negative

and never cross the λ - axis. In this scenario, the structure is unconditionally stable for that ω_n .

The root locus method is successfully used in the continuum theory for normal flow aeroelasticity [2], but when applying it to the axial flow case an inherent issue arises. Consider one of the integrals present in the Kussner doublet function $\hat{A}_2(s, y)$:

$$h(\kappa, y) = \frac{1}{\pi}\sqrt{\frac{l-y}{l+y}}\int_0^\infty e^{-\kappa\zeta}\sqrt{\frac{2l+\zeta}{\zeta}}\frac{1}{y-l-\zeta}d\zeta \tag{3.6}$$

where

$$\kappa = \frac{s}{U} = \frac{\sigma + i\omega}{U} \tag{3.7}$$

so that,

$$e^{-\kappa\zeta} = e^{-\sigma\zeta}\left[\cos(\omega\zeta) - \sin(\omega\zeta)\right] \tag{3.8}$$

Equations (3.6) and (3.8) show that the function $h(\kappa, y)$ is undefined for $\lambda < 0$. This is not consistent with the root locus stability method, i.e. finding the points (λ, U) starting with $U = 0$ and determining at which U the λ becomes non-negative for a given ω_n . However, the stability of the system can be analyzed by setting λ to zero, and finding the roots ω and U that drive the real and imaginary parts of the flutter determinant to zero:

$$\mathrm{Re}\left[d\left(\lambda = 0, i\omega, U\right)\right] = 0 \tag{3.9}$$

$$\mathrm{Im}\left[d\left(\lambda = 0, i\omega, U\right)\right] = 0 \tag{3.10}$$

This approach does not produce a stability curve, but instead finds sets of roots (ω_i, U_i) that drive the flutter determinant to zero. The minimum U_i is the flutter speed,U_f , and the ω_i corresponding to it is the aeroelastic mode present at the onset of flutter. Equations (3.9) and (3.10) are solved using the Newton-Raphson method shown in Appendix B.

3.2 Evaluation of bending flutter determinant

To calculate the flutter speed, the flutter determinant for bending motion must be decomposed into its real and imaginary parts. Due to the amount of algebra involved, this section is written so that it can be skipped by the reader without loss in continuity with the rest of the chapter. The flutter determinant is:

$$d(s,U) = \det \begin{bmatrix} D_{11}(s,U) & D_{12}(s,U) \\ D_{21}(s,U) & D_{22}(s,U) \end{bmatrix} \tag{3.11}$$

Or,

$$d(s,U) = D_{11}(s,U) D_{22}(s,U) - D_{12}(s,U) D_{21}(s,U) \tag{3.12}$$

Setting $s = i\omega$, it is clear that $d(i\omega,U)$ is complex. Letting the subscript R denote the real part of a function, and the subscript I denote the imaginary part, $d(i\omega,U)$ can be decomposed as follows:

$$d(i\omega,U) = d_R(\omega,U) + i d_I(\omega,U) \tag{3.13}$$

Keeping the same notation, Equation (3.13) is expanded to separate the real and imaginary

parts. The real part of $d(i\omega, U)$ is:

$$\begin{aligned} d_R(\omega, U) =& D_{11,R}(\omega, U) D_{22,R}(\omega, U) - D_{11,I}(\omega, U) D_{22,I}(\omega, U) \\ & - D_{12,R}(\omega, U) D_{21,R}(\omega, U) + D_{12,I}(\omega, U) D_{21,I}(\omega, U) \end{aligned} \tag{3.14}$$

And the imaginary part is:

$$\begin{aligned} d_R(\omega, U) =& D_{11,R}(\omega, U) D_{22,I}(\omega, U) + D_{11,I}(\omega, U) D_{22,R}(\omega, U) \\ & - D_{12,R}(\omega, U) D_{21,I}(\omega, U) - D_{12,I}(\omega, U) D_{21,R}(\omega, U) \end{aligned} \tag{3.15}$$

The functions $D_{ij}(\omega, U)$ are defined as:

$$D_{ij}(i\omega, U) = D_{0,ij}(\omega) + \int_{-l}^{l} Q_{ij}(\omega, \phi) z_q(i\omega, \phi) d\phi \tag{3.16}$$

Because the functions $D_{0,ij}(\omega)$ and $Q_{ij}(\omega, \phi)$ are purely real, Equation (3.16) can be separated into its real and imaginary parts by:

$$D_{ij,R}(i\omega, U) = D_{0,ij}(\omega) + \int_{-l}^{l} Q_{ij}(\omega, \phi) z_{q,R}(i\omega, \phi) d\phi \tag{3.17}$$

and

$$D_{ij,I}(i\omega, U) = \int_{-l}^{l} Q_{ij}(\omega, \phi) z_{q,I}(i\omega, \phi) d\phi \tag{3.18}$$

The $D_{0,ij}(\omega)$ are given by:

$$D_{0,11}(\omega) = \frac{1}{2}\left[\cos\left(2l\beta\sqrt{\omega}\right) + \cosh\left(2l\beta\sqrt{\omega}\right)\right] \tag{3.19}$$

$$D_{0,12}(\omega) = \frac{1}{2\beta\sqrt{\omega}}\left[\sin\left(2l\beta\sqrt{\omega}\right) + \sinh\left(2l\beta\sqrt{\omega}\right)\right] \tag{3.20}$$

$$D_{0,21}(\omega) = \frac{1}{2}\beta\sqrt{\omega}\left[-\sin\left(2l\beta\sqrt{\omega}\right) + \sinh\left(2l\beta\sqrt{\omega}\right)\right] \tag{3.21}$$

$$D_{0,22}(\omega) = \frac{1}{2}\left[\cos\left(2l\beta\sqrt{\omega}\right) + \cosh\left(2l\beta\sqrt{\omega}\right)\right] \tag{3.22}$$

The $Q_{ij}(\omega,\phi)$ are given by:

$$Q_{11}(\omega,\phi) = \frac{1}{2\beta\sqrt{\omega}}\sin\left[(l-\phi)\beta\sqrt{\omega}\right] \tag{3.23}$$

$$Q_{12}(\omega,\phi) = \frac{1}{2\beta\sqrt{\omega}}\sinh\left[(l-\phi)\beta\sqrt{\omega}\right] \tag{3.24}$$

$$Q_{21}(\omega,\phi) = \frac{1}{2}\cos\left[(l-\phi)\beta\sqrt{\omega}\right] \tag{3.25}$$

$$Q_{22}(\omega,\phi) = \frac{1}{2}\cosh\left[(l-\phi)\beta\sqrt{\omega}\right] \tag{3.26}$$

The function $z_q(i\omega, \phi)$ is complex, and defined as:

$$z_q(i\omega, \phi) = \frac{2b\rho}{EI}\left(U + i\omega\Omega(0)\right)\bar{z}_q(i\omega, \phi) \tag{3.27}$$

where

$$\begin{aligned}\bar{z}_q(i\omega, \phi) &= \mathrm{T}\left(i\omega q_1(\omega, \phi) + Uq_2(\omega, \phi)\right) \\ &\quad + H(i\omega, \phi)\, L\left[\kappa_\omega, \left(I + \kappa_\omega\Omega(0)\right)\mathrm{T}\left(i\omega q_1(\omega, \phi) + Uq_2(\omega, \phi)\right)\right]\end{aligned} \tag{3.28}$$

In Equation (3.28), κ has been replaced with κ_ω, which is defined as:

$$\kappa_\omega = \frac{i\omega}{U} \tag{3.29}$$

Recall the definition of the operator $\Omega(0)$:

$$\Omega(0)\, f = \bar{g} \tag{3.30}$$

where

$$\bar{g}(s, y) = \int_{-l}^{y} f(s, \zeta)\, d\zeta \tag{3.31}$$

Thus, it is convenient to spit $z_q(i\omega,\phi)$ into two functions:

$$z_q(i\omega,\phi) = x(i\omega,\phi) + y(i\omega,\phi) \tag{3.32}$$

The function $x(i\omega,\phi)$ is defined as:

$$x(i\omega,\phi) = \frac{2b\rho U}{EI}\left[x_1(i\omega,\phi) + x_2(i\omega,\phi)\right] \tag{3.33}$$

where

$$x_1(i\omega,\phi) = \mathrm{T}\left(i\omega q_1(\omega,\phi) + U q_2(\omega,\phi)\right) \tag{3.34}$$

and

$$x_2(i\omega,\phi) = H(i\omega,\phi)\, L\left[\kappa_\omega, \left(I + \kappa_\omega \Omega(0)\right)\mathrm{T}\left(i\omega q_1(\omega,\phi) + U q_2(\omega,\phi)\right)\right] \tag{3.35}$$

The function $y(i\omega,\phi)$ is defined by:

$$y(i\omega,\phi) = i\omega \int_{-l}^{\phi} x(i\omega,\zeta)\, d\zeta \tag{3.36}$$

The real and imaginary parts of $z_q(i\omega,\phi)$ are:

$$z_{q,R}(\omega,\phi) = x_R(\omega,\phi) + y_R(\omega,\phi) \tag{3.37}$$

and

$$z_{q,I}(\omega,\phi) = x_I(\omega,\phi) + y_I(\omega,\phi) \tag{3.38}$$

From Equation (3.36), it can be shown that the real and imaginary parts of $y(i\omega,\phi)$ are:

$$y_R(\omega,\phi) = -\omega \int_{-l}^{\phi} x_I(\omega,\zeta)\, d\zeta \tag{3.39}$$

and

$$y_I(\omega,\phi) = \omega \int_{-l}^{\phi} x_R(\omega,\zeta)\, d\zeta \tag{3.40}$$

Due to its complexity, several simplifications will be made before decomposing $x(i\omega,\phi)$. The function $H(i\omega,\phi)$ is defined by:

$$H(i\omega,\phi) = S(\kappa_\omega)\, h(\kappa_\omega,\phi) \tag{3.41}$$

where

$$S(\kappa_\omega) = \frac{1}{l\kappa_\omega \left[K_0(l\kappa_\omega) + K_1(l\kappa_\omega)\right] e^{l\kappa_\omega}} \tag{3.42}$$

The functions $K_0(l\kappa_\omega)$ and $K_1(l\kappa_\omega)$ are the Bessel K functions. The function $h(\kappa_\omega, \phi)$ is defined by Equation (3.6), but replacing κ with κ_ω . It is convenient to write $h(\kappa_\omega, \phi)$ as:

$$h(\kappa_\omega, \phi) = \frac{1}{\pi}\sqrt{\frac{l-\phi}{l+\phi}}\bar{h}(\kappa_\omega, \phi) \tag{3.43}$$

where

$$\bar{h}(\kappa_\omega, \phi) = \int_0^\infty e^{-\kappa_\omega \zeta}\sqrt{\frac{2l+\zeta}{\zeta}}\frac{1}{\phi - l - \zeta}d\zeta \tag{3.44}$$

$H(i\omega, \phi)$ can now be written as:

$$H(i\omega, \phi) = \frac{1}{\pi}\sqrt{\frac{l-\phi}{l+\phi}}S(\kappa_\omega)\bar{h}(\kappa_\omega, \phi) \tag{3.45}$$

It will be convenient to rewrite the function $\mathrm{T}(\cdot)$ in a similar fashion. Recall its definition:

$$\mathrm{T}[\psi(i\omega, \phi)] = \frac{1}{\pi}\sqrt{\frac{l-\phi}{l+\phi}}\int_{-l}^{l}\sqrt{\frac{l+\zeta}{l-\zeta}}\frac{\psi(i\omega, \zeta)}{\zeta - \phi}d\zeta \tag{3.46}$$

where, from Equation (3.28),

$$\psi\left(i\omega,\phi\right)=i\omega q_1\left(\omega,\phi\right)+Uq_2\left(\omega,\phi\right) \tag{3.47}$$

Equation (3.46) can be written as:

$$\mathrm{T}\left[\psi\left(i\omega,\phi\right)\right]=\frac{1}{\pi}\sqrt{\frac{l-\phi}{l+\phi}}\bar{\mathrm{T}}\left[\psi\left(i\omega,\phi\right)\right] \tag{3.48}$$

where

$$\bar{\mathrm{T}}\left[\psi\left(i\omega,\phi\right)\right]=\int_{-l}^{l}\sqrt{\frac{l+\zeta}{l-\zeta}}\frac{\psi\left(i\omega,\zeta\right)}{\zeta-\phi}d\zeta \tag{3.49}$$

Equations (3.45) and (3.48) show that there is a common factor in the bracketed terms of Equation (3.35). The function $x\left(i\omega,\phi\right)$ can be written in terms of the barred quantities to obtain:

$$x\left(i\omega,\phi\right)=\frac{2b\rho U}{EI}\frac{1}{\pi}\sqrt{\frac{l-\phi}{l+\phi}}\left\{\bar{\mathrm{T}}\left(\psi\left(i\omega,\phi\right)\right)+S\left(\kappa_\omega\right)\bar{h}\left(\kappa_\omega,\phi\right)L\left[\kappa_\omega,\left(I+\kappa_\omega\Omega\left(0\right)\right)\mathrm{T}\psi\left(i\omega,\phi\right)\right]\right\} \tag{3.50}$$

For simplicity, the following shorthand notation is used for the function $L\left[\cdot\right]$ in Equation (3.50):

$$\tilde{L}\left(\kappa_\omega\right)=L\left[\kappa_\omega,\left(I+\kappa_\omega\Omega\left(0\right)\right)\mathrm{T}\psi\left(i\omega,\phi\right)\right] \tag{3.51}$$

Equation (3.50) becomes:

$$x\left(i\omega,\phi\right)=\frac{2b\rho U}{EI}\frac{1}{\pi}\sqrt{\frac{l-\phi}{l+\phi}}\left[\bar{\mathrm{T}}\left(\psi\left(i\omega,\phi\right)\right)+S\left(\kappa_{\omega}\right)\bar{h}\left(\kappa_{\omega},\phi\right)\tilde{L}\left(\kappa_{\omega}\right)\right] \tag{3.52}$$

Equation (3.52) can be written as:

$$x\left(i\omega,\phi\right)=\frac{2b\rho U}{EI}\frac{1}{\pi}\sqrt{\frac{l-\phi}{l+\phi}}\bar{x}\left(i\omega,\phi\right) \tag{3.53}$$

where

$$\bar{x}\left(i\omega,\phi\right)=\bar{\mathrm{T}}\left(\psi\left(i\omega,\phi\right)\right)+S\left(\kappa_{\omega}\right)\bar{h}\left(\kappa_{\omega},\phi\right)\tilde{L}\left(\kappa_{\omega}\right) \tag{3.54}$$

The real and imaginary parts of $x\left(i\omega,\phi\right)$ are:

$$x_{R}\left(\omega,\phi\right)=\frac{2b\rho U}{EI}\frac{1}{\pi}\sqrt{\frac{l-\phi}{l+\phi}}\bar{x}_{R}\left(\omega,\phi\right) \tag{3.55}$$

and

$$x_{I}\left(\omega,\phi\right)=\frac{2b\rho U}{EI}\frac{1}{\pi}\sqrt{\frac{l-\phi}{l+\phi}}\bar{x}_{I}\left(\omega,\phi\right) \tag{3.56}$$

The task now is to decompose $\bar{x}\left(i\omega,\phi\right)$ into its real and imaginary parts. For clarity, this

will be done in two steps for each part. The real part can be written as:

$$\bar{x}_R(\omega,\phi) = \bar{\mathrm{T}}_R(\psi(i\omega,\phi)) + \mathrm{Re}\left[S(\kappa_\omega)\tilde{L}(\kappa_\omega)\right]\bar{h}_R(\kappa_\omega,\phi) - \mathrm{Im}\left[S(\kappa_\omega)\tilde{L}(\kappa_\omega)\right]\bar{h}_I(\kappa_\omega,\phi) \tag{3.57}$$

Continuing to separate the real and imaginary parts, Equation (3.57) becomes:

$$\begin{aligned}\bar{x}_R(\omega,\phi) = \bar{\mathrm{T}}_R(\psi(i\omega,\phi)) &+ \left[S_R(\omega)\tilde{L}_R(\omega) - S_I(\omega)\tilde{L}_I(\omega)\right]\bar{h}_R(\kappa_\omega,\phi) \\ &- \left[S_R(\omega)\tilde{L}_I(\omega) + S_I(\omega)\tilde{L}_R(\omega)\right]\bar{h}_I(\kappa_\omega,\phi)\end{aligned} \tag{3.58}$$

The imaginary part of $x(i\omega,\phi)$ is:

$$\bar{x}_I(\omega,\phi) = \bar{\mathrm{T}}_I(\psi(i\omega,\phi)) + \mathrm{Re}\left[S(\kappa_\omega)\tilde{L}(\kappa_\omega)\right]\bar{h}_I(\kappa_\omega,\phi) + \mathrm{Im}\left[S(\kappa_\omega)\tilde{L}(\kappa_\omega)\right]\bar{h}_R(\kappa_\omega,\phi) \tag{3.59}$$

Or,

$$\begin{aligned}\bar{x}_I(\omega,\phi) = \bar{\mathrm{T}}_R(\psi(i\omega,\phi)) &+ \left[S_R(\omega)\tilde{L}_R(\omega) - S_I(\omega)\tilde{L}_I(\omega)\right]\bar{h}_I(\kappa_\omega,\phi) \\ &+ \left[S_R(\omega)\tilde{L}_I(\omega) + S_I(\omega)\tilde{L}_R(\omega)\right]\bar{h}_R(\kappa_\omega,\phi)\end{aligned} \tag{3.60}$$

The next step is to find the real and imaginary parts of $\bar{\mathrm{T}}\left[\psi\left(i\omega,\phi\right)\right]$. First, recall:

$$\psi\left(i\omega,\phi\right)=i\omega q_1\left(\omega,\phi\right)+Uq_2\left(\omega,\phi\right) \tag{3.61}$$

Because $q_1\left(\omega,\phi\right)$ and $q_2\left(\omega,\phi\right)$ are purely real, note that:

$$\psi_R\left(\omega,\phi\right)=Uq_2\left(\omega,\phi\right) \tag{3.62}$$

and

$$\psi_I\left(\omega,\phi\right)=\omega q_1\left(\omega,\phi\right) \tag{3.63}$$

From the definition of $\bar{\mathrm{T}}\left[\psi\left(i\omega,\phi\right)\right]$, it follows that:

$$\bar{\mathrm{T}}_R\left[\psi\left(i\omega,\phi\right)\right]=\int_{-l}^{l}\sqrt{\frac{l+\zeta}{l-\zeta}}\frac{\psi_R\left(\omega,\zeta\right)}{\zeta-\phi}d\zeta \tag{3.64}$$

and

$$\bar{\mathrm{T}}_I\left[\psi\left(i\omega,\phi\right)\right]=\int_{-l}^{l}\sqrt{\frac{l+\zeta}{l-\zeta}}\frac{\psi_I\left(\omega,\zeta\right)}{\zeta-\phi}d\zeta \tag{3.65}$$

Next, the function $\tilde{L}\left(\kappa_\omega\right)$ will be decomposed into its real and imaginary parts . Recall the

undecomposed form:

$$\tilde{L}\left(\kappa_{\omega}\right)=L\left[\kappa_{\omega},\left(I+\kappa_{\omega}\Omega\left(0\right)\right)\mathrm{T}\psi\left(i\omega,\phi\right)\right] \tag{3.66}$$

The operator $L\left[\kappa_{\omega},f\right]$ is defined by:

$$L\left[\kappa_{\omega},f\right]=\int_{-l}^{l}e^{-\kappa_{\omega}\left(l-\zeta\right)}f\left(s,\zeta\right)d\zeta \tag{3.67}$$

The second argument in $L\left[\kappa_{\omega},f\right]$, from Equation (1.63), can be expanded to obtain:

$$\left(I+\kappa_{\omega}\Omega\left(0\right)\right)\mathrm{T}\psi\left(i\omega,\phi\right)=\mathrm{T}\psi\left(i\omega,\phi\right)+\kappa_{\omega}\Omega\left(0\right)\mathrm{T}\psi\left(i\omega,\phi\right) \tag{3.68}$$

Using the definition of $\Omega\left(0\right)$, Equation (3.68) becomes:

$$\left(I+\kappa_{\omega}\Omega\left(0\right)\right)\mathrm{T}\psi\left(i\omega,\phi\right)=\mathrm{T}\psi\left(i\omega,\phi\right)+\kappa_{\omega}\int_{-l}^{\phi}\mathrm{T}\psi\left(i\omega,\zeta\right)d\zeta \tag{3.69}$$

It is convenient to define:

$$G\left(i\omega,\phi\right)=\int_{-l}^{\phi}\mathrm{T}\left[\psi\left(i\omega,\zeta\right)\right]d\zeta \tag{3.70}$$

so that:

$$\left(I+\kappa_{\omega}\Omega\left(0\right)\right)\mathrm{T}\psi\left(i\omega,\phi\right)=\mathrm{T}\psi\left(i\omega,\phi\right)+\kappa_{\omega}G\left(i\omega,\phi\right) \tag{3.71}$$

Or, in terms of the barred quantities:

$$\left(I+\kappa_{\omega}\Omega\left(0\right)\right)\mathrm{T}\psi\left(i\omega,\phi\right)=\frac{1}{\pi}\sqrt{\frac{l-\phi}{l+\phi}}\bar{\mathrm{T}}\left[\psi\left(i\omega,\phi\right)\right]+\kappa_{\omega}G\left(i\omega,\phi\right) \tag{3.72}$$

Where $G\left(i\omega,\phi\right)$ can be written as:

$$G\left(i\omega,\phi\right)=\frac{1}{\pi}\int_{-l}^{\phi}\sqrt{\frac{l-\zeta}{l+\zeta}}\bar{\mathrm{T}}\left[\psi\left(i\omega,\zeta\right)\right]d\zeta \tag{3.73}$$

The real and imaginary parts of $G\left(i\omega,\phi\right)$ are:

$$G_{R}\left(\omega,\phi\right)=\frac{1}{\pi}\int_{-l}^{\phi}\sqrt{\frac{l-\zeta}{l+\zeta}}\bar{\mathrm{T}}_{R}\left[\psi\left(i\omega,\zeta\right)\right]d\zeta \tag{3.74}$$

and

$$G_{I}\left(\omega,\phi\right)=\frac{1}{\pi}\int_{-l}^{\phi}\sqrt{\frac{l-\zeta}{l+\zeta}}\bar{\mathrm{T}}_{I}\left[\psi\left(i\omega,\zeta\right)\right]d\zeta \tag{3.75}$$

Returning to $\tilde{L}\left(\kappa_{\omega}\right)$, Equations (3.66), (3.67), and (3.71) can be used to obtain:

$$\tilde{L}(\kappa_\omega) = \frac{1}{\pi}\int_{-l}^{l}\sqrt{\frac{l-\zeta}{l+\zeta}}e^{-\kappa_\omega(l-\zeta)}\bar{\mathrm{T}}\left[\psi(i\omega,\zeta)\right]d\zeta + \kappa_\omega\int_{-l}^{l}e^{-\kappa_\omega(l-\zeta)}G(i\omega,\zeta)\,d\zeta \tag{3.76}$$

To decompose Equation (3.76), note that:

$$e^{-\kappa_\omega(l-\zeta)} = e^{-\frac{i\omega}{U}(l-\zeta)} = \cos\left[\frac{\omega}{U}(l-\zeta)\right] - i\sin\left[\frac{\omega}{U}(l-\zeta)\right] \tag{3.77}$$

From Equations (3.76) and (3.77), it can be shown that the real part of $\tilde{L}(\kappa_\omega)$ is:

$$\begin{aligned}\tilde{L}_R(\omega) = {} & \frac{1}{\pi}\int_{-l}^{l}\sqrt{\frac{l-\zeta}{l+\zeta}}\cos\left[\frac{\omega}{U}(l-\zeta)\right]\bar{\mathrm{T}}_R\left[\psi(i\omega,\zeta)\right]d\zeta \\ & + \frac{1}{\pi}\int_{-l}^{l}\sqrt{\frac{l-\zeta}{l+\zeta}}\sin\left[\frac{\omega}{U}(l-\zeta)\right]\bar{\mathrm{T}}_I\left[\psi(i\omega,\zeta)\right]d\zeta \\ & - \frac{\omega}{U}\int_{-l}^{l}\cos\left[\frac{\omega}{U}(l-\zeta)\right]G_I(\omega,\zeta)\,d\zeta + \frac{\omega}{U}\int_{-l}^{l}\sin\left[\frac{\omega}{U}(l-\zeta)\right]G_R(\omega,\zeta)\,d\zeta\end{aligned} \tag{3.78}$$

The imaginary part is:

$$\tilde{L}_I(\omega) = \frac{1}{\pi}\int_{-l}^{l}\sqrt{\frac{l-\zeta}{l+\zeta}}\cos\left[\frac{\omega}{U}(l-\zeta)\right]\bar{\mathrm{T}}_I\left[\psi(i\omega,\zeta)\right]d\zeta$$
$$-\frac{1}{\pi}\int_{-l}^{l}\sqrt{\frac{l-\zeta}{l+\zeta}}\sin\left[\frac{\omega}{U}(l-\zeta)\right]\bar{\mathrm{T}}_R\left[\psi(i\omega,\zeta)\right]d\zeta$$
$$+\frac{\omega}{U}\int_{-l}^{l}\cos\left[\frac{\omega}{U}(l-\zeta)\right]G_R(\omega,\zeta)\,d\zeta+\frac{\omega}{U}\int_{-l}^{l}\sin\left[\frac{\omega}{U}(l-\zeta)\right]G_I(\omega,\zeta)\,d\zeta \tag{3.79}$$

The next step is to decompose the function $S(\kappa_\omega)$. First, let:

$$S(\kappa_\omega) = \frac{1}{M(\omega)+iN(\omega)} \tag{3.80}$$

where

$$M(\omega) = \mathrm{Re}\left\{l\kappa_\omega\left[K_0(l\kappa_\omega)+K_1(l\kappa_\omega)\right]e^{l\kappa_\omega}\right\} \tag{3.81}$$

and

$$N(\omega) = \mathrm{Im}\left\{l\kappa_\omega\left[K_0(l\kappa_\omega)+K_1(l\kappa_\omega)\right]e^{l\kappa_\omega}\right\} \tag{3.82}$$

The real and imaginary parts of Equation (3.80) can be separated by multiplying it by one:

$$S(\kappa_\omega) = \frac{1}{M(\omega)+iN(\omega)}\frac{M(\omega)-iN(\omega)}{M(\omega)-iN(\omega)} \tag{3.83}$$

Equation (3.83) becomes:

$$S\left(\kappa_{\omega}\right)=\frac{M\left(\omega\right)}{\left[M\left(\omega\right)\right]^{2}+\left[N\left(\omega\right)\right]^{2}}-i\frac{N\left(\omega\right)}{\left[M\left(\omega\right)\right]^{2}+\left[N\left(\omega\right)\right]^{2}} \tag{3.84}$$

The real and imaginary parts are:

$$S_{R}\left(\omega\right)=\frac{M\left(\omega\right)}{\left[M\left(\omega\right)\right]^{2}+\left[N\left(\omega\right)\right]^{2}} \tag{3.85}$$

and

$$S_{I}\left(\omega\right)=-\frac{N\left(\omega\right)}{\left[M\left(\omega\right)\right]^{2}+\left[N\left(\omega\right)\right]^{2}} \tag{3.86}$$

The functions $M\left(\omega\right)$ and $N\left(\omega\right)$ from Equations (3.81) and (3.82) still need to be evaluated. First, let:

$$\tilde{K}\left(l\kappa_{\omega}\right)=K_{0}\left(l\kappa_{\omega}\right)+K_{1}\left(l\kappa_{\omega}\right) \tag{3.87}$$

Equation (3.81) can now be written as:

$$M\left(\omega\right)=\mathrm{Re}\left\{l\frac{i\omega}{U}\tilde{K}\left(l\kappa_{\omega}\right)\left[\cos\left(\frac{l\omega}{U}\right)+i\sin\left(\frac{l\omega}{U}\right)\right]\right\} \tag{3.88}$$

Or,

$$M(\omega) = \mathrm{Re}\left[l\frac{i\omega}{U}\tilde{K}(l\kappa_\omega)\right]\cos\left(\frac{l\omega}{U}\right) - \mathrm{Im}\left[l\frac{i\omega}{U}\tilde{K}(l\kappa_\omega)\right]\sin\left(\frac{l\omega}{U}\right) \tag{3.89}$$

Finally, $M(\omega)$ becomes:

$$M(\omega) = -l\frac{\omega}{U}\tilde{K}_I(l\kappa_\omega)\cos\left(\frac{l\omega}{U}\right) - l\frac{\omega}{U}\tilde{K}_R(l\kappa_\omega)\sin\left(\frac{l\omega}{U}\right) \tag{3.90}$$

The function $N(\omega)$ is evaluated in the same manner. Without showing the algebra, the function can be written as:

$$N(\omega) = -l\frac{\omega}{U}\tilde{K}_I(l\kappa_\omega)\sin\left(\frac{l\omega}{U}\right) + l\frac{\omega}{U}\tilde{K}_R(l\kappa_\omega)\cos\left(\frac{l\omega}{U}\right) \tag{3.91}$$

Further treatment of the Bessel functions $\tilde{K}_R(l\kappa_\omega)$ and $\tilde{K}_I(l\kappa_\omega)$ is deferred to the next section. The last function that needs to be decomposed is $\bar{h}(\kappa_\omega, \phi)$. Recall its definition:

$$\bar{h}(\kappa_\omega, \phi) = \int_0^\infty e^{-\kappa_\omega \zeta}\sqrt{\frac{2l+\zeta}{\zeta}}\frac{1}{\phi - l - \zeta}d\zeta \tag{3.92}$$

Euler's formula can be applied to Equation (3.92) to obtain:

$$\bar{h}_R(\omega, \phi) = \int_0^\infty \cos\left(\frac{\omega}{U}\zeta\right)\sqrt{\frac{2l+\zeta}{\zeta}}\frac{1}{\phi - l - \zeta}d\zeta \tag{3.93}$$

The bending flutter determinant, $d(i\omega, U)$, has been decomposed into its real and imaginary parts completely. Some of the integrals in $d(i\omega, U)$ can be evaluated using routine numerical integration methods, but the integrals that are singular must be treated with care.

3.3 Treatment of singular integrals

It has been shown that some of the integrals present in the flutter determinant are singular, where the integrand goes to infinity within the domain of integration. It may be tempting to use traditional numerical integration methods, and do nothing more than increase the number of subdivisions near the singular point, but this would result in catastrophic error. The best way to demonstrate this is with a simple example. Consider the definite integral:

$$I = \int_0^1 \frac{1}{\sqrt{x}} dx \tag{3.94}$$

Where it is clear that this integral is singular because $\frac{1}{\sqrt{x}} \to \infty$ as $x \to 0$. However, it is known that I is finite, because the integral can be evaluated analytically and results in $I = 2$. Consider a scenario where the integral is evaluated numerically by setting the lower bound to a very small number ϵ , where the intent is for it to converge if ϵ is sufficiently small. That is, the following integral is computed using standard numerical methods.

$$I = \int_\varepsilon^1 \frac{1}{\sqrt{x}} dx \tag{3.95}$$

Table 3.1 shows the result of applying Simpson's Rule to Equation (3.95), using 1000 subdivisions, for ϵ ranging from 0.1 to 1×10^{-13}.

Table 3.1: Numerical Integration of Equation (3.95) using Simpson's Rule.

ϵ	I
1×10^{-1}	1.36754
1×10^{-2}	1.8
1×10^{-3}	1.9369
1×10^{-4}	1.98917
1×10^{-5}	2.06515
1×10^{-6}	2.29348
1×10^{-7}	3.01428
1×10^{-8}	5.29353
1×10^{-9}	12.5011
1×10^{-10}	35.2935
1×10^{-11}	107.369
1×10^{-12}	335.294
1×10^{-13}	1056.05

It is clear from Table 3.1 that the integral in Equation (3.95) will not converge, no matter how small the ϵ. The easiest way to treat singular integrals, whenever possible, is to use a variable substitution to eliminate the singularity. For example, consider the integral $G(i\omega, \phi)$ from the bending flutter determinant.

$$G\left(i\omega,\phi\right)=\frac{1}{\pi}\int_{-l}^{\phi}\sqrt{\frac{l-\zeta}{l+\zeta}}\bar{\mathrm{T}}\left[\psi\left(i\omega,\zeta\right)\right]d\zeta \tag{3.96}$$

In Equation (3.96), $\bar{\mathrm{T}}\left[\psi\left(i\omega,\zeta\right)\right]$ is finite. Here it is evident that the integral is singular at $\zeta=-l$. However, this can be avoided with a variable substitution. Let:

$$u=\sqrt{l+\zeta} \tag{3.97}$$

so that:

$$du=\frac{1}{2\sqrt{l+\zeta}}d\zeta \tag{3.98}$$

and

$$\zeta=u^2-l \tag{3.99}$$

The bounds in terms of the new integration variable are $0\leq u\leq\sqrt{l+\phi}$ for $-l\leq\zeta\leq\phi$. Substituting these expressions into Equation (3.96), the integral becomes:

$$G\left(i\omega,\phi\right)=\frac{2}{\pi}\int_{0}^{\sqrt{l+\phi}}\sqrt{2l-u^2}\bar{\mathrm{T}}\left[\psi\left(i\omega,u^2-l\right)\right]du \tag{3.100}$$

The integrand in Equation (3.100) is finite throughout the entire integration domain. This

type of variable substitution can be applied to several of the integrals in $d(i\omega, U)$, including $\tilde{L}(\kappa_\omega)$ and $y(i\omega, \phi)$. However, this type of substitution cannot eliminate singularities that are not in the form of a square root. For example, consider the integral $\bar{\mathrm{T}}(\kappa_\omega, \phi)$:

$$\bar{\mathrm{T}}[\psi(i\omega, \phi)] = \int_{-l}^{l} \sqrt{\frac{l+\zeta}{l-\zeta}} \frac{\psi(i\omega, \zeta)}{\zeta - \phi} d\zeta \tag{3.101}$$

This integral is singular at two points within the domain, $\zeta = l$ and $\zeta = \phi$. The singularity at $\zeta = l$ can be eliminated using a variable substitution. Let:

$$u = \sqrt{l - \zeta} \tag{3.102}$$

so that:

$$du = -\frac{1}{2\sqrt{l-\zeta}} d\zeta \tag{3.103}$$

The lower and upper bounds become $u = \sqrt{2l}$ and $u = 0$, respectively. Performing the substitution, and reversing the bounds, the integral in Equation (3.101) becomes:

$$\bar{\mathrm{T}}[\psi(i\omega, \phi)] = 2 \int_{0}^{\sqrt{2l}} \sqrt{2l - u^2} \frac{\psi(i\omega, l - u^2)}{l - u^2 - \phi} du \tag{3.104}$$

Or, rearranging,

$$\bar{\mathrm{T}}\left[\psi\left(i\omega,\phi\right)\right]=-2\int_{0}^{\sqrt{2l}}\sqrt{2l-u^{2}}\frac{\psi\left(i\omega,l-u^{2}\right)}{u^{2}-\left(\phi-l\right)}du \tag{3.105}$$

One singular point has been eliminated, but there is no such variable substitution that can eliminate the singularity at $u^2 = \phi - l$. However, the IMT method provides a variable transformation that eliminates singularities given that they are at the endpoints of the integration. Because $-l \leq \phi \leq l$ in Equation (1.102), the singularity at $u^2 = \phi - l$ is not located at an endpoint, but the integral can be split at $u = \sqrt{\phi - l}$ to force this to be the case. Consider the integral of a function $f\left(x\right)$from 0 to 1, where $f\left(x\right)$ can approach infinity as $x \to 0$, $x \to 1$, or both. For an integral in this form, the IMT method is:

$$\int_{0}^{1}f\left(x\right)dx=\int_{0}^{1}g\left(t\right)dt \tag{3.106}$$

where

$$g\left(t\right)=f\left[\eta\left(t\right)\right]\eta'\left(t\right) \tag{3.107}$$

where

$$\eta'\left(t\right)=\frac{1}{Q}\exp\left(-\frac{1}{t}-\frac{1}{1-t}\right) \tag{3.108}$$

where

$$Q = \int_0^1 \exp\left(-\frac{1}{\tau} - \frac{1}{1-\tau}\right) d\tau \cong 0.007043 \tag{3.109}$$

where it is evident that:

$$\eta(t) = \int_0^t \eta'(\tau)\, d\tau \tag{3.110}$$

The integral in Equation (3.110) cannot be evaluated analytically, but its numerical computation is straightforward. The IMT method accomplishes the task of eliminating the endpoint singularities by the choice of $\eta'(t)$. This function is plotted in Figure 3.1.

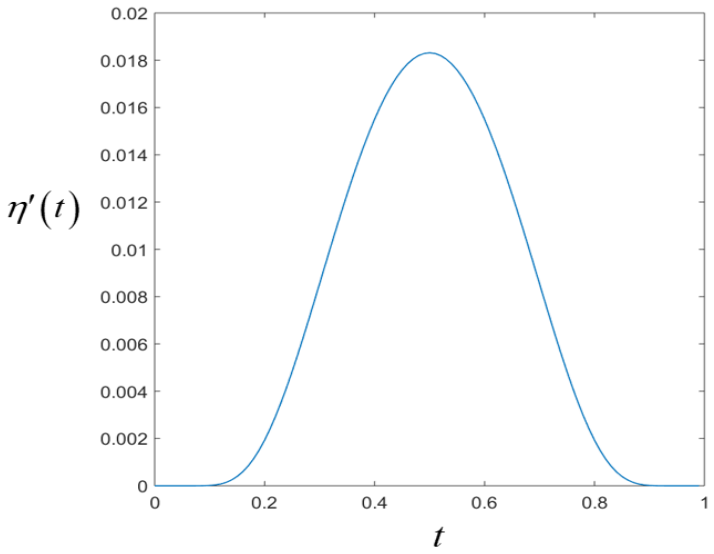

Figure 3.1: The function $\eta'(t)$ from Equation (3.108).

Figure 3.1 shows that $\eta'(t)$ sharply approaches zero at $t = 0$ and $t = 1$, which will prevent a singular integrand from being very large near the endpoints. To demonstrate the IMT

method, it will be applied to the real part of $\bar{\mathrm{T}}\left[\psi\left(i\omega,\phi\right)\right]$:

$$\bar{\mathrm{T}}_R\left[\psi\left(i\omega,\phi\right)\right] = -2\int_0^{\sqrt{2l}} \sqrt{2l-u^2}\frac{\psi_R\left(\omega, l-u^2\right)}{u^2-(\phi-l)}du \tag{3.111}$$

The integral in Equation (3.111) can be split at the singular point as follows. Let:

$$\bar{\mathrm{T}}_R\left[\psi\left(i\omega,\phi\right)\right] = \bar{\mathrm{T}}_{R,1}\left[\psi\left(i\omega,\phi\right)\right] + \bar{\mathrm{T}}_{R,2}\left[\psi\left(i\omega,\phi\right)\right] \tag{3.112}$$

where

$$\bar{\mathrm{T}}_{R,1}\left[\psi\left(i\omega,\phi\right)\right] = -2\int_0^{\lambda} \sqrt{2l-u^2}\frac{\psi_R\left(\omega, l-u^2\right)}{u^2-(\phi-l)}du \tag{3.113}$$

and

$$\bar{\mathrm{T}}_{R,2}\left[\psi\left(i\omega,\phi\right)\right] = -2\int_{\lambda}^{\sqrt{2l}} \sqrt{2l-u^2}\frac{\psi_R\left(\omega, l-u^2\right)}{u^2-(\phi-l)}du \tag{3.114}$$

where $\lambda \equiv \sqrt{l-\phi}$. The next step is to make a variable substitution so that the bounds on each of the integrals are 0 and 1. For the first integral, let:

$$v = \frac{u}{\lambda} \Rightarrow du = \lambda dv \tag{3.115}$$

For the second integral, let:

$$v = \frac{u - \lambda}{\sqrt{2l} - \lambda} \Rightarrow du = \left(\sqrt{2l} - \lambda\right) dv \tag{3.116}$$

Performing the substitutions, the integrals become:

$$\bar{\mathrm{T}}_{R,1}\left[\psi\left(i\omega, \phi\right)\right] = -2\lambda \int_0^1 \sqrt{2l - \left(\lambda v\right)^2} \frac{\psi_R\left(\omega, l - \left(\lambda v\right)^2\right)}{\left(\lambda v\right)^2 - \left(\phi - l\right)} dv \tag{3.117}$$

and

$$\bar{\mathrm{T}}_{R,2}\left[\psi\left(i\omega, \phi\right)\right] = -2\left(\sqrt{2l} - \lambda\right) \int_0^1 \sqrt{2l - \gamma^2} \frac{\psi_R\left(\omega, l - \gamma^2\right)}{\gamma^2 - \left(\phi - l\right)} dv \tag{3.118}$$

where

$$\gamma \equiv \lambda + \left(\sqrt{2l} - \lambda\right) v \tag{3.119}$$

Applying the IMT method to Equation (3.117), the integral becomes:

$$\bar{\mathrm{T}}_{R,1}\left[\psi\left(i\omega, \phi\right)\right] = -2\lambda \int_0^1 \sqrt{2l - \left(\lambda \eta\left(t\right)\right)^2} \frac{\psi_R\left(\omega, l - \left(\lambda \eta\left(t\right)\right)^2\right)}{\left(\lambda \eta\left(t\right)\right)^2 - \left(\phi - l\right)} \eta'\left(t\right) dt \tag{3.120}$$

To verify that $\bar{\mathrm{T}}_{R,1}\left[\psi\left(i\omega, \phi\right)\right]$ is no longer singular, the integrand in Equation (3.120) is plotted for $L = 0.15$, $\phi = 0$, and $\omega = 1$. Figure 3.2 shows the original integrand (left) and the

transformed integrand (right) of Equation (3.120).

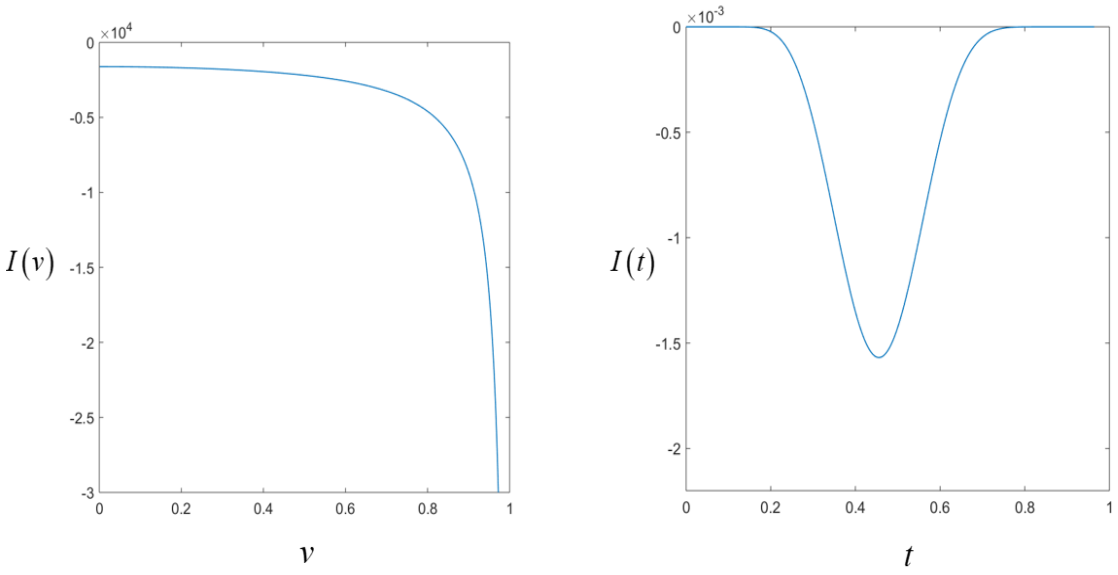

Figure 3.2: Integrand of $\bar{\mathrm{T}}_{R,1}\left[\psi\left(i\omega,\phi\right)\right]$: Original (left) and transformed (right).

Figure 3.2 demonstrates that the IMT method was successful in transforming $\bar{\mathrm{T}}_{R,1}\left[\psi\left(i\omega,\phi\right)\right]$ to a nonsingular integral. It was observed, when implementing the IMT method, that while it is successful on $\bar{\mathrm{T}}_{R,1}\left[\psi\left(i\omega,\phi\right)\right]$, it did not convert $\bar{\mathrm{T}}_{R,2}\left[\psi\left(i\omega,\phi\right)\right]$to a nonsingular integral. Since the original publication of the IMT method, several subsequent methods based on this approach have been developed. The method that works best for $\bar{\mathrm{T}}_{R,2}\left[\psi\left(i\omega,\phi\right)\right]$ is the so-called Tanh transformation, which drives the integrand to zero at the endpoints via the function $\mathrm{sech}^2\left(t\right)$. The Tanh transformation is given by:

$$\int_a^b f\left(x\right)dx=\frac{1}{2}\left(b-a\right)\int_{-\infty}^{\infty}f\left[\frac{1}{2}\left(b+a\right)+\frac{1}{2}\left(b-a\right)\tanh\left(t\right)\right]\mathrm{sech}^2\left(t\right)dt \tag{3.121}$$

Here $f\left(x\right)$ can be singular at $x=a$, $x=b$, or both. Implementing the Tanh transformation

for $\bar{\mathrm{T}}_{R,2}\left[\psi\left(i\omega,\phi\right)\right]$, the integral becomes:

$$\bar{\mathrm{T}}_{R,2}\left[\psi\left(i\omega,\phi\right)\right]=-\left(\sqrt{2l}-\lambda\right)\int_{-M}^{M}\sqrt{2l-\tilde{\gamma}^{2}}\frac{\psi_{R}\left(\omega,l-\tilde{\gamma}^{2}\right)}{\tilde{\gamma}^{2}-\left(\phi-l\right)}\mathrm{sech}^{2}\left(t\right)dt \tag{3.122}$$

where

$$\tilde{\gamma}=\lambda+\left(\sqrt{2l}-\lambda\right)\left[\frac{1}{2}+\frac{1}{2}\tanh\left(t\right)\right] \tag{3.123}$$

It was found that $M=5$ is sufficiently large for the integral $\bar{\mathrm{T}}_{R,2}\left[\psi\left(i\omega,\phi\right)\right]$to converge. Once again, the transformed integrand of $\bar{\mathrm{T}}_{R,2}\left[\psi\left(i\omega,\phi\right)\right]$ is plotted to ensure that the integral is no longer singular. Figure 3.3 shows the original and transformed integrands of $\bar{\mathrm{T}}_{R,2}\left[\psi\left(i\omega,\phi\right)\right]$, for $L=0.15$, $\phi=0$, and $\omega=1$.

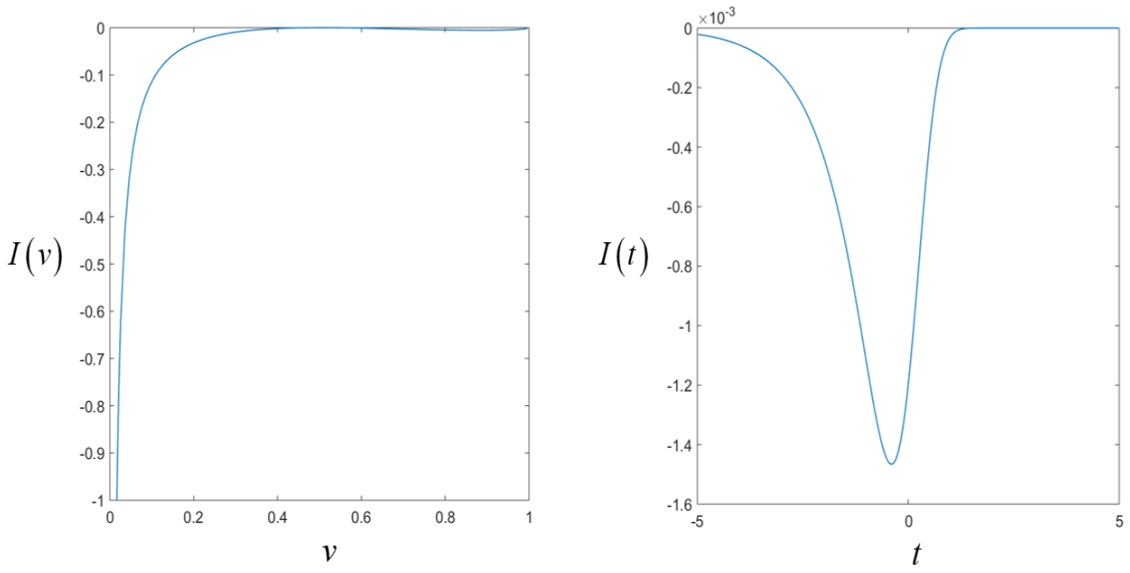

Figure 3.3: Integrand of $\bar{\mathrm{T}}_{R,2}\left[\psi\left(i\omega,\phi\right)\right]$: Original (left) and transformed (right)..

Another integral that is singular is $\bar{h}(\kappa_\omega, \phi)$:

$$\bar{h}(\kappa_\omega, \phi) = \int_0^\infty e^{-\kappa_\omega \zeta} \sqrt{\frac{2l+\zeta}{\zeta}} \frac{1}{\phi - l - \zeta} d\zeta \tag{3.124}$$

This integral is singular at two points within the domain, $\zeta = 0$ and $\zeta = \phi - l$. The singularity at $\zeta = 0$ can be eliminated using a variable substitution. Let:

$$u = \sqrt{\zeta} \tag{3.125}$$

so that:

$$du = \frac{1}{2\sqrt{\zeta}} d\zeta \tag{3.126}$$

The bounds of integration remain unchanged. The integral in Equation (3.124) becomes:

$$\bar{h}(\kappa_\omega, \phi) = 2 \int_0^\infty e^{-\kappa_\omega u^2} \sqrt{2l + u^2} \frac{1}{\phi - l - u^2} du \tag{3.127}$$

One singular point has been eliminated, but there is no variable substitution that can eliminate the singularity at $u^2 = \phi - l$. However, with $-l \leq \phi \leq l$, note that $(\phi - l) \leq 0$. With $u^2 \geq 0$, the integral in Equation (1.124) can only be singular when $(\phi - l) = 0$, or $\phi = l$. Recall the form of $h(\kappa_\omega, \phi)$ from Equation (3.43) :

$$h\left(\kappa_\omega, \phi\right) = \frac{1}{\pi}\sqrt{\frac{l-\phi}{l+\phi}}\bar{h}\left(\kappa_\omega, \phi\right) \tag{3.128}$$

Note that in Equation (3.128) $h\left(\kappa_\omega, \phi\right)$ is identically zero when $\phi = l$, and with $\bar{h}\left(\kappa_\omega, \phi\right)$ finite, there is no need to evaluate the function $\bar{h}\left(\kappa_\omega, \phi\right)$ when $\phi = l$. While the IMT method or the Tanh transformation can be applied to $\bar{h}\left(\kappa_\omega, \phi\right)$ in a straightforward manner, it is not necessary.

With the variable substitutions and the IMT and Tanh transformations applied to the singular integrals, the task at hand now involves numerical integration of relatively smooth functions. There are many methods to choose from, but it was determined that Simpson's Rule – a Newton-Cotes formula of order 3 – provides sufficient accuracy. The Composite Simpson's Rule is shown in Appendix B.1. For each of the integrals in $d\left(i\omega, U\right)$, the number of integration points was increased until the result of the numerical integration was independent of the number of points. The minimum number of points for each of these integrals is shown in Table 2.

Table 3.2: Number of Integration Points Required for Integrals in the Flutter Determinant.

Integral	N
$\bar{\mathrm{T}}\left[\psi\left(i\omega,\phi\right)\right]$	26
$G\left(i\omega,\phi\right)$	12
$\bar{h}\left(\kappa_{\omega},\phi\right)$	14
$\tilde{L}\left(\kappa_{\omega}\right)$	22
$\bar{y}\left(\omega,\phi\right)$	10

While it may seem that the number of points required for these integrals is not excessive, due to the nature of the integrals being nested up to three times, the calculation of $d\left(i\omega,U\right)$ can be computationally expensive. To reduce the computational time, any integrals that are functions of one variable only can be integrated only once and reused in subsequent instances of it. An example of such an integral is $\eta\left(t\right)$ from the IMT method:

$$\eta\left(t\right)=\frac{1}{Q}\int_{0}^{t}\exp\left(-\frac{1}{\tau}-\frac{1}{1-\tau}\right)dt \tag{3.129}$$

Where $0\leq t\leq 1$. Using object-oriented programming techniques, the values of $\eta\left(t\right)$ can be stored in a data structure and retrieved by the main computer program computing $d\left(i\omega,U\right)$. In this work, $\eta\left(t\right)$ was calculated for 10,000 values of t , where each integration was performed using Simpson's Rule with 1000 points. For values of t that fall between the tabulated values, for example t_k and t_{k+1} , linear interpolation is used to more accurately determine the corresponding value of $\eta\left(t\right)$.

$$\eta(t) \cong \eta(t_k) + \frac{t - t_k}{t_{k+1} - t_k} \left[\eta(t_{k+1}) - \eta(t_k)\right] \tag{3.130}$$

This approach is also applicable for evaluating the Bessel K functions $K_0(l\kappa_\omega)$and $K_1(l\kappa_\omega)$. The results of these functions are stored as a function of the variable $l\kappa_\omega$, where it is understood that new values would have to be computed if the constant l is to be changed. For a complex argument z , the Bessel K functions are:

$$K_0(z) = \frac{2^{-\frac{1}{4}}}{(2\pi)^{-\frac{3}{2}}} e^{-z} z^{-\frac{1}{4}} \int_{-\infty}^{\infty} \Gamma\left(\frac{1}{4} + it\right) \Gamma^2\left(\frac{1}{4} - it\right) (2z)^{it} dt \tag{3.131}$$

And

$$K_1(z) = e^{-z} z^{-1} - \frac{2^{-\frac{1}{4}}}{(2\pi)^{-\frac{3}{2}}} e^{-z} z^{-\frac{1}{4}} \int_{-\infty}^{\infty} \Gamma\left(\frac{1}{4} + it\right) \Gamma^2\left(\frac{1}{4} - it\right) (2z)^{it} dt \tag{3.132}$$

The function $\Gamma(\cdot)$ is the gamma function, for a complex argument, given by:

$$\Gamma(z) = \int_0^{\infty} x^{z-1} e^{-x} dx \tag{3.133}$$

Due to the complexity of $K_0(l\kappa_\omega)$ and $K_1(l\kappa_\omega)$, the results for 10,000 values of $l\kappa_\omega$ were obtained from the software Mathematica. These values were then used to calculate the functions $S_R(\kappa_\omega)$and $S_I(\kappa_\omega)$ for 10,000 $l\kappa_\omega$ values, for a given value of l .

3.4 Flutter speed calculation using Balakrishnan continuum theory

Using the methods for determining the flutter speed presented in this chapter, along with the Balakrishnan continuum theory of Chapter 2, flutter speed calculations were performed for three rectangular, beam-like structures. The three structures were made of 2024-T3 aluminum, PETG plastic, and ABS plastic. The dimensions and material properties of each structure are shown in Table 3.3.

Table 3.3: Material Properties and Dimensions for Three Structures.

	2024-T3 Aluminum	PETG	ABS
Young's Modulus (GPa)	73.1	2.83	2.10
Length (cm)	30.5	20.32	20.32
Width (cm)	10.2	10.2	10.2
Thickness (cm)	3.81×10^{-4}	0.075	0.05

The calculations were performed in a C++ computer program, consisting of a source file accompanied by header files which stored the tabulated data for some integrals. The Newton-Raphson routine for finding the roots ω and U to the real and imaginary parts of the flutter determinant converged rapidly using a reasonable initial guess. For the 2024 aluminum case, using an initial guess of $\omega = 122$ rad/s and $U = 45$ m/s, the Newton-Rapshon method converged after 9 iterations with an error of 1.06×10^{-8}. Table 3.4 shows the error for this case, defined using the 2-norm, for each iteration.

Table 3.4: Newton-Rapshon Convergence for 2024-T3 Aluminum Case.

Iteration	Error
1	3.58×10^{13}
2	2.75×10^{8}
3	3.06×10^{5}
4	9.06×10^{4}
5	2.29×10^{4}
6	2.23×10^{3}
7	12.5
8	1.27×10^{-3}
9	1.06×10^{-8}

The roots ω and U also converged rapidly. Figure 3.4 shows the convergence of ω (left) and U (right) for the 2024-T3 aluminum case.

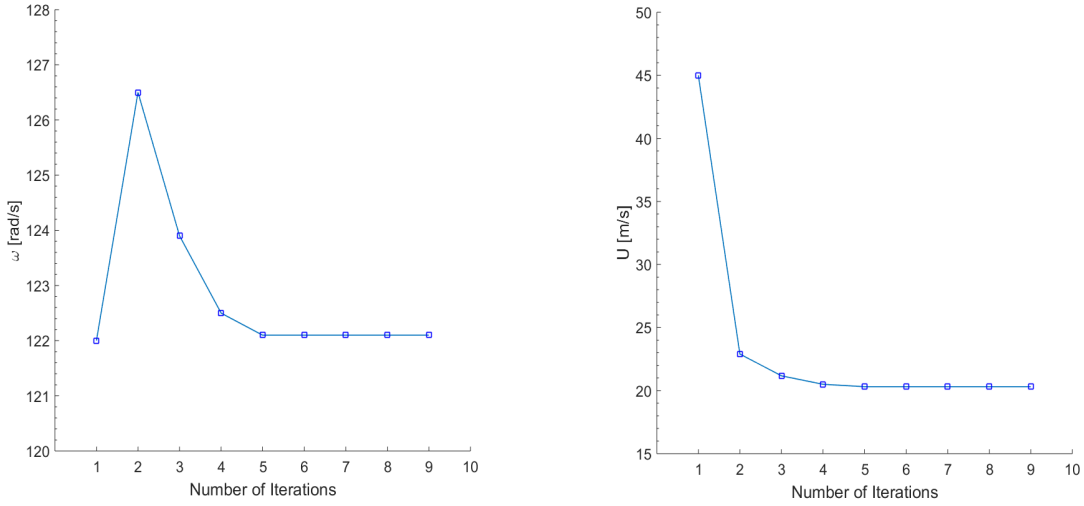

Figure 3.4: Convergence of ω (left) and U (right) with number of iterations for 2024-T3 aluminum case.

The flutter speed obtained from these calculations was 20.3 m/s. The calculated value for the aeroelastic mode frequency, ω, was 122 rad/s, which is near the second bending natural frequency of 133.5 rad/s. The convergence behavior was similar for the PETG and ABS plastic cases. For PETG, the calculated flutter speed was 32.4 m/s and the ω was 34.4 rad/s. The U and ω for the ABS case were 23.1 m/s and 94.3 rad/s, respectively.

4 The semi-continuum approach: Combined approximate and continuum solution

When the linear continuum theory is extended to account for nonlinear structure effects, the problem that arises is that the structure side of the problem can no longer be solved analytically. It will be shown that allowing for lateral motion of the structure, which produces a set of coupled nonlinear equations for the dynamics of the structure, does not prohibit the use of the continuum solution for the aerodynamics if the flow is treated as inviscid. Thus, the approach presented here uses the continuum solution developed previously for the aerodynamic lift and moment, and uses approximate methods to solve the nonlinear structure equations.

4.1 Semi-continuum method for linear structure and fluid dynamics

In this section the semi-continuum method is developed to solve the governing equations for the case where the fluid and structure dynamics are both linear. This is the same set of equations used in the Balakrishnan continuum theory (BCT), but the use of an approximate solution for the structure side allows for a key simplifying assumption in the solution to be relieved. To begin, recall the governing equation for the bending displacement in the Laplace domain, $\hat{h}(s,y)$:

$$EI\hat{h}^{(4)}(s,y) + m_s s^2 \hat{h}(s,y) = 2b\rho U \hat{A}_2\left(s, y, \hat{h}, \hat{h}'\right) \tag{4.1}$$

Where $\hat{A}_2\left(s, \bar{y}, \hat{h}, \hat{h}'\right)$ is the Kussner doublet function representing the lift on the structure, which is solved for using the BCT. In the solution method presented in this chapter, the continuum solution for $\hat{A}_2\left(s, \bar{y}, \hat{h}, \hat{h}'\right)$ is used for the fluid side of the problem, and the structure side of the problem is solved using the Galerkin method.

The boundary conditions for the structure in the cantilever configuration, with $-l \leq y \leq l$, are:

$$\hat{h}(s,-l) = \hat{h}'(s,-l) = \hat{h}''(s,l) = \hat{h}'''(s,l) = 0 \tag{4.2}$$

For the Galerkin method, it is convenient to nondimensionalize the y variable as follows:

$$\bar{y} = \frac{y+l}{2l} \tag{4.3}$$

where $0 \leq \bar{y} \leq 1$. The governing equation becomes:

$$\frac{EI}{16l^4}\hat{h}^{(4)}(s,\bar{y}) + m_s s^2 \hat{h}(s,\bar{y}) = 2b\rho U \hat{A}_2\left(s, \bar{y}, \hat{h}, \hat{h}'\right) \tag{4.4}$$

The boundary conditions in terms of $\bar{y}$ are:

$$\hat{h}(s,0) = \hat{h}'(s,0) = \hat{h}''(s,1) = \hat{h}'''(s,1) = 0 \tag{4.5}$$

To analyze the stability of the system for a given air speed U , a disturbance is applied to the structure from rest:

$$h\left(t,\bar{y}\right)=0+f\left(t\right)H\left(\bar{y}\right) \tag{4.6}$$

The function for the time dependence of $h\left(t,y\right)$ is chosen to be purely real in the time domain so that the bending displacement $h\left(t,y\right)$ is purely real, but complex in the Laplace domain to perform a stability analysis. The function $f\left(t\right)$ can be written in terms of two independent parameters σ and ω :

$$f\left(t\right)=e^{\sigma t}\left[cos\left(\omega t\right)+\sin\left(\omega t\right)\right] \tag{4.7}$$

It can be shown, using Euler's Formula, that $f\left(t\right)$ can be written as:

$$f\left(t\right)=e^{\sigma t}\left[cos\left(\omega t\right)+\sin\left(\omega t\right)\right]=e^{\sigma t}\left[\frac{1}{2i}e^{i\omega t}-\frac{1}{2i}e^{-i\omega t}+\frac{1}{2}e^{i\omega t}+\frac{1}{2}e^{-i\omega t}\right] \tag{4.8}$$

In Equation (4.8), $f\left(t\right)$ is the sum of four linearly independent functions:

$$u_{1}\left(t\right)=\frac{1}{2i}e^{(\sigma+i\omega)t} \tag{4.9}$$

$$u_{1}\left(t\right)=-\frac{1}{2i}e^{(\sigma-i\omega)t} \tag{4.10}$$

$$u_1(t) = \frac{1}{2} e^{(\sigma + i\omega)t} \tag{4.11}$$

$$u_1(t) = \frac{1}{2} e^{(\sigma - i\omega)t} \tag{4.12}$$

Before taking the Laplace transform, it is useful to look at the derivatives:

$$\dot{u}_1(t) = \frac{1}{2i} (\sigma + i\omega) e^{(\sigma + i\omega)t} = (\sigma + i\omega) u_1(t) \tag{4.13}$$

Similarly,

$$\dot{u}_2(t) = (\sigma - i\omega) u_2(t) \tag{4.14}$$

$$\dot{u}_3(t) = (\sigma + i\omega) u_3(t) \tag{4.15}$$

$$\dot{u}_4(t) = (\sigma - i\omega) u_4(t) \tag{4.16}$$

By taking the Laplace transform of $\dot{u}_1(t)$ from Equation (4.13), note that:

$$sL[u_1(t)] = (\sigma + i\omega) L[u_1(t)] \tag{4.17}$$

It evident that for $u_1(t)$ and $u_3(t)$:

$$s = \sigma + i\omega \tag{4.18}$$

Whereas for $u_2(t)$ and $u_4(t)$:

$$s = \sigma - i\omega \tag{4.19}$$

For the $f(t)$ chosen for the disturbance, s comes as a complex conjugate pair $s = \sigma \pm i\omega$, where the negative root can be discarded. The Laplace transform of $h(t, y)$ is:

$$\hat{h}(s, \bar{y}) = \left[\frac{s - \sigma}{(s - \sigma)^2 + \omega^2} + \frac{\omega}{(s - \sigma)^2 + \omega^2} \right] H(\bar{y}) \tag{4.20}$$

Substituting the expression for $\hat{h}(s, \bar{y})$ from Equation (4.20) into the governing equation, Equation (4.1), and canceling the denominator, the governing equation becomes:

$$\frac{EI}{16l^4}(s - \sigma + \omega) H^{(4)}(\bar{y}) + m_s s^2 (s - \sigma + \omega) H(\bar{y}) = 2b\rho U (s - \sigma + \omega) \hat{A}_2 [s, y, U, H(\bar{y})] \tag{4.21}$$

As demonstrated in Chapter 3, the sign of σ determines whether or not the structure is stable for a given U, where $\sigma = 0$ corresponds to the onset of flutter. As before, σ will be set to zero and the roots ω and U will be calculated to determine the onset of instability. For $\sigma = 0$ and $s = i\omega$, Equation (4.21) becomes:

$$\frac{EI}{16l^4}(1+i)H^{(4)}(\bar{y}) - m_s\omega^2(1+i)H(\bar{y}) = 2b\rho U(1+i)\hat{A}_2[i\omega, \bar{y}, U, H(\bar{y})] \tag{4.22}$$

Because Equation (4.22) has real and imaginary parts, they must be separated and each equation must be satisfied simultaneously. The real equation is:

$$\frac{EI}{16l^4}H^{(4)}(\bar{y}) - m_s\omega^2 H(\bar{y}) = 2b\rho U\left[\mathrm{Re}\left(\hat{A}_2[i\omega, \bar{y}, U, H(\bar{y})]\right) - \mathrm{Im}\left(\hat{A}_2[i\omega, \bar{y}, U, H(\bar{y})]\right)\right] \tag{4.23}$$

And the imaginary equation is:

$$\frac{EI}{16l^4}H^{(4)}(\bar{y}) - m_s\omega^2 H(\bar{y}) = 2b\rho U\left[\mathrm{Re}\left(\hat{A}_2[i\omega, \bar{y}, U, H(\bar{y})]\right) + \mathrm{Im}\left(\hat{A}_2[i\omega, \bar{y}, U, H(\bar{y})]\right)\right] \tag{4.24}$$

The task now is to find the roots ω and U that satisfy Equations (4.23) and (4.24). Because σ has been set to zero, which corresponds to a marginally stable structure, this U is the flutter speed.

The Galerkin method approximates a function as a series with a finite number of terms. Each term is a trial function multiplied by a coefficient, as shown in Equation (4.25).

$$H(\bar{y}) = \sum_{n=1}^{N} B_n H_n(\bar{y}) \tag{4.25}$$

The trial functions, $H_n(\bar{y})$, must satisfy the boundary conditions, and for the Galerkin method to be useful they must also be orthogonal. A natural choice for the trial functions is the solution for a beam vibrating without the presence of air. This is an eigenvalue problem, where the solution for the spatial dependence comes in the form of the following eigenfunctions:

$$H_n(\bar{y}) = \cosh(\mu_n \bar{y}) - \cos(\mu_n \bar{y}) + \frac{\cosh(\mu_n) + \cos(\mu_n)}{\sinh(\mu_n) + \sin(\mu_n)} (\sin(\mu_n \bar{y}) - \sinh(\mu_n \bar{y})) \tag{4.26}$$

The μ_n are calculated to satisfy the boundary conditions using the transcendental equation:

$$\cosh(\mu_n)\cos(\mu_n) + 1 = 0 \tag{4.27}$$

The functions in Equation (4.10) are orthogonal, and represent the mode shapes for each natural frequency ω_n. The first three eigenfunctions, $H_n(\bar{y})$, are shown in Figure 4.1.

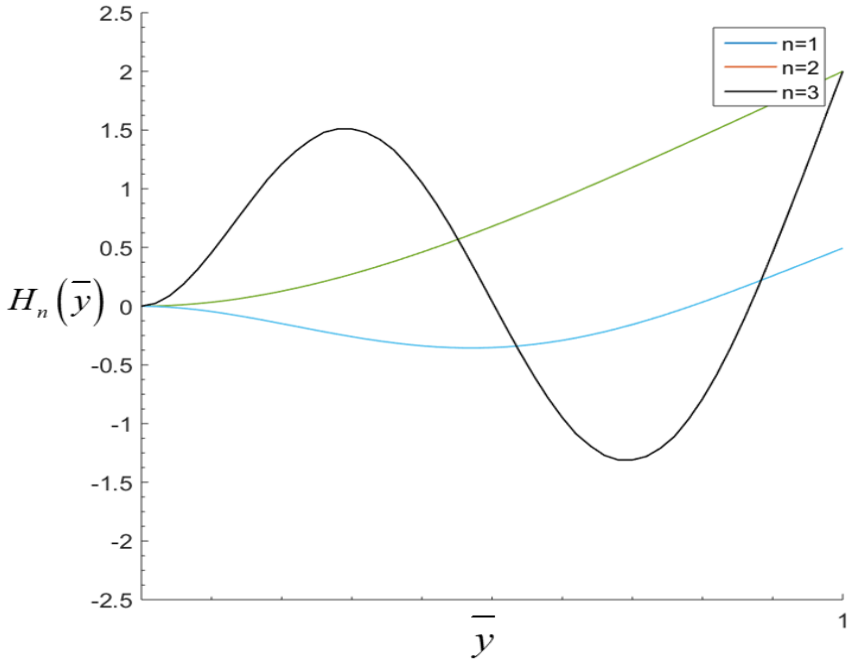

Figure 4.1: First three eigenfunctions.

The functions $H_n(\bar{y})$ have the following orthogonality property:

$$\int_0^1 H_n(\bar{y}) H_m(\bar{y}) \, d\bar{y} = \delta_{mn} \tag{4.28}$$

The fourth derivative of $H_n(\bar{y})$ is:

$$H_n^{(4)}(\bar{y}) = \mu_n^4 H_n(\bar{y}) \tag{4.29}$$

Thus,

$$H^{(4)}(\bar{y}) = \sum_{n=1}^{N} \mu_n^4 B_n H_n(\bar{y}) \tag{4.30}$$

Substituting Equations (4.25) and (4.30), the governing equation becomes:

$$\frac{EI}{16l^4}(1+i)\sum_{n=1}^{N}\mu_n^4 B_n H_n(\bar{y}) - m_s\omega^2(1+i)\sum_{n=1}^{N}B_n H_n(\bar{y}) = 2b\rho U(1+i)\sum_{n=1}^{N}B_n\hat{A}_{2n}\left[i\omega,\bar{y},U,H_n(\bar{y})\right] \tag{4.31}$$

The next step is to multiply through by $H_m(\bar{y})$ and integrate over $\bar{y}$ to obtain:

$$\frac{EI}{16l^4}(1+i)\sum_{n=1}^{N}\mu_n^4 B_n\int_0^1 H_n(\bar{y})H_m(\bar{y})\,d\bar{y} - m_s\omega^2(1+i)\sum_{n=1}^{N}B_n\int_0^1 H_n(\bar{y})H_m(\bar{y})\,d\bar{y} = 2b\rho U(1+i)\sum_{n=1}^{N}B_n\int_0^1 H_m(\bar{y})\hat{A}_{2n}\left[i\omega,\bar{y},U,H_n(\bar{y})\right]d\bar{y} \tag{4.32}$$

For $n = 1, 2, ..., N$ and $m = 1, 2, ..., N$. For each m , there is one equation containing the coefficients $B_1, B_2, ..., B_N$. Applying the orthogonality property, Equation (4.32) becomes:

$$\frac{EI}{16l^4}(1+i)\sum_{n=1}^{N}\mu_n^4 B_n - m_s\omega^2(1+i)\sum_{n=1}^{N}B_n = 2b\rho U(1+i)\sum_{n=1}^{N}B_n\int_0^1 H_m(\bar{y})\hat{A}_{2n}\left[i\omega,\bar{y},U,H_n(\bar{y})\right]d\bar{y} \tag{4.33}$$

Rearranging,

$$(1+i)\sum_{n=1}^{N}\left(\mu_n^4\frac{EI}{16l^4}-m_s\omega^2\right)B_n-2b\rho U\,(1+i)\sum_{n=1}^{N}B_n\int_0^1 H_m\left(\bar{y}\right)\hat{A}_{2n}\left[i\omega,\bar{y},U,H_n\left(\bar{y}\right)\right]d\bar{y}=0 \tag{4.34}$$

Equation (4.36) can be written in matrix form, to isolate U and obtain:

$$\sum_{n=1}^{N}B_nM_{nn}^1-U\sum_{n=1}^{N}B_nM_{nm}^2=0 \tag{4.35}$$

where

$$M_{nn}^1=(1+i)\left(\frac{EI}{16l^4}\mu_n^4-m_s\omega^2\right) \tag{4.36}$$

and

$$M_{nm}^2=2b\rho\,(1+i)\int_0^1 H_m\left(\bar{y}\right)\hat{A}_{2n}\left[i\omega,\bar{y},U,H_n\left(\bar{y}\right)\right]d\bar{y} \tag{4.37}$$

Multiplying through by $\left(M_{nm}^2\right)^{-1}$ and rearranging,

$$\sum_{n=1}^{N}B_nM_{nn}^1\left(M_{nm}^2\right)^{-1}-U\sum_{n=1}^{N}B_nI_{nn}=0 \tag{4.38}$$

For $m=1,2,...,N$. Equation (4.38) expressed in block matrix form:

$$\left|\overline{\overline{M}} - U\bar{\bar{I}}\right| \left|\bar{B}\right| = 0 \tag{4.39}$$

where $\bar{\bar{I}}$ is the identity matrix, and:

$$\overline{\overline{M}} = M^1_{nn}\left(M^2_{nm}\right)^{-1} \tag{4.40}$$

Equation (4.40) is satisfied if:

$$\det\left(\overline{\overline{M}} - U\bar{\bar{I}}\right) = 0 \tag{4.41}$$

Because the matrix $\bar{\bar{M}}$ in Equation (4.41) is complex, the real and imaginary parts of the determinant must be set to zero simultaneously. Thus,

$$\det\left[\mathrm{Re}\left(\overline{\overline{M}}\left(\omega\right) - U\bar{\bar{I}}\right)\right] = 0 \tag{4.42}$$

$$\det\left[\mathrm{Im}\left(\overline{\overline{M}}\left(\omega\right) - U\bar{\bar{I}}\right)\right] = 0 \tag{4.43}$$

By finding the roots ω and U to Equations (4.42) and (4.43), it is evident that U is a repeated eigenvalue of the matrix $\bar{\bar{M}}$. As a result, the coefficients B_n can be determined because they are the elements of the eigenvector corresponding to the eigenvalue U .

4.2 Flutter speed calculation based on linear fluid and linear structure dynamics

Using the numerical methods described in Chapter 3 and Appendix A, calculations were performed for three different structures. The benchmark case was a 2024-T3 Aluminum beam, where aluminum was chosen because the material properties are precisely known. The two additional cases were of different materials, ABS and PETG plastic, each with different dimensions. The flutter speed was measured in a wind tunnel for each sample; see Chapter 5.2. The material properties and dimensions for each configuration is shown in in Table 4.1.

Table 4.1: Material properties and dimensions for three configurations.

Material	2024-T3 Aluminum	PETG	ABS
Density (kg/m^3)	2780	1270	1070
Young's Modulus (GPa)	73.1	2.83	2.10
Shear Modulus (GPa)	28.0	0.0385	0.0827
Length (cm)	30.5	20.32	20.32
Width (cm)	10.2	10.2	10.2
Thickness (cm)	3.81^{-4}	0.075	0.05

For each case, the number of terms used in the Galerkin method was increased until sufficient convergence was obtained. The plot in Figure 4.2 shows that the flutter speed convergence for the 2024-T3 aluminum case, where it converges reasonably well using 17 terms.

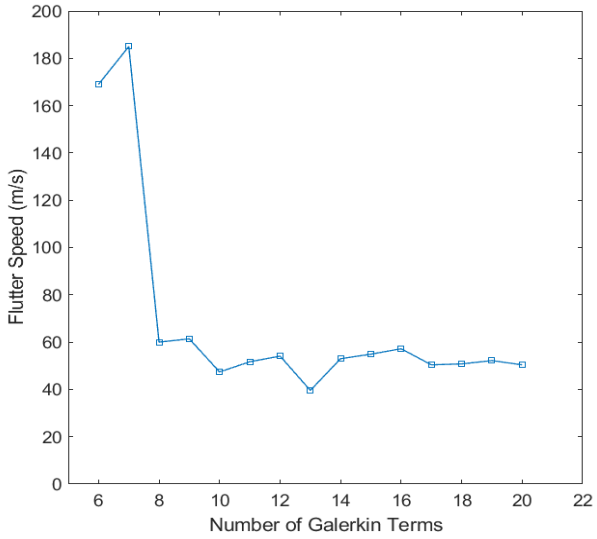

Figure 4.2: Convergence of flutter speed with number of terms used in the Galerkin method.

The flutter speed obtained for the 2024-T3 aluminum case using 20 terms is 50.4 m/s, and the corresponding ω is 122 rad/s. The Galerkin coefficients obtained from the calculation at the flutter speed can be used to construct the eigenfunctions associated with the approximation of $h(t, y)$. The eigenfunctions from the real and imaginary parts of the flutter determinant were plotted to inspect the shape of the structure associated with the approximation of $h(t, y)$, as shown in Figure 4.3. The coefficients are tabulated in Appendix C.

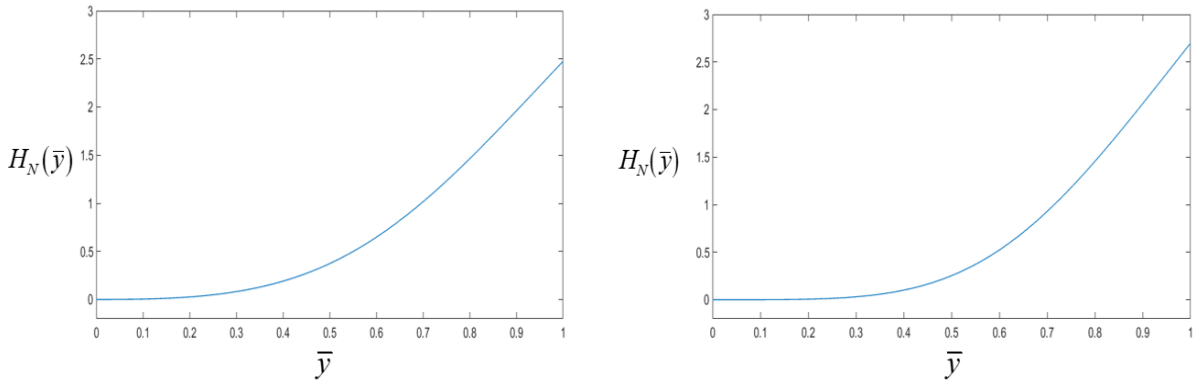

Figure 4.3: Eigenfunctions from the real (left) and imaginary (right) flutter determinant for 2024-T3 aluminum.

The eigenfunctions in Figure 4.3 are primarily a combination of the first and second bending mode shapes. For experimental visualization of the mode shapes of a structure fluttering in axial flow see Chapter 5.3. Figure 4.4 shows the convergence of flutter speed with number of Galerkin terms for the second configuration, PETG plastic.

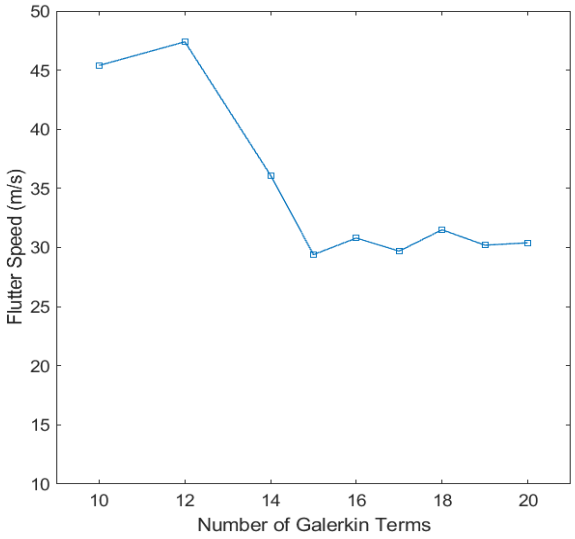

Figure 4.4: Convergence of flutter speed with number of terms used in the Galerkin method for PETG case.

The flutter speed obtained for the PETG case is 30.4 m/s, and the corresponding ω is 99.9 rad/s. The eigenfunctions determined from the solution at the flutter speed are shown in Figure 4.5.

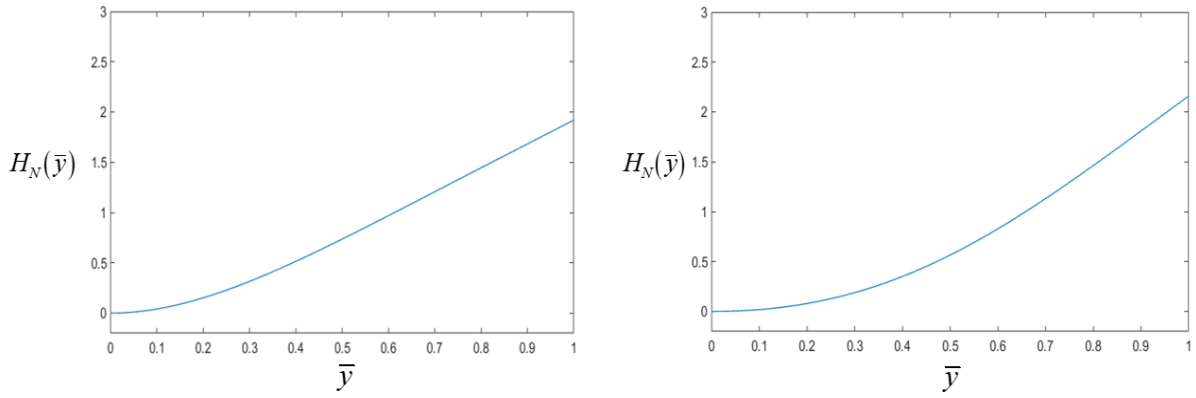

Figure 4.5: Eigenfunctions from the real (left) and imaginary (right) flutter determinant for PETG plastic.

The solution produced for the PETG plastic configuration is a combination of the first and second bending modes, where the first bending mode is dominant. Note that the eigenfunction from the imaginary part of the flutter determinant has more influence from the second bending mode as compared to the eigenfunction from the real part. Figure 4.6 shows the flutter speed versus number of Galerkin terms for the third configuration, ABS plastic.

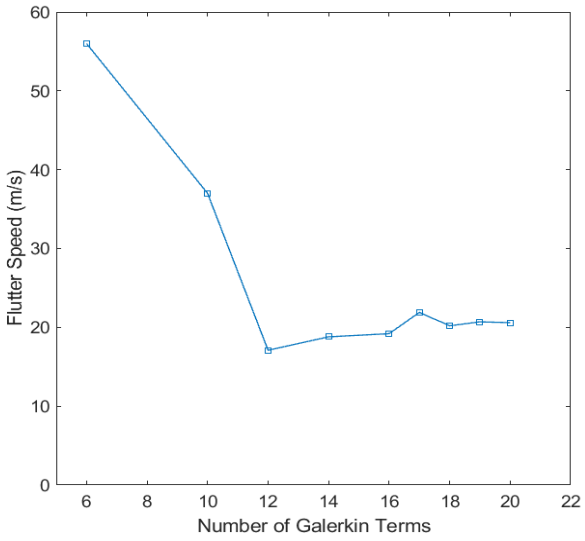

Figure 4.6: Convergence of flutter speed with number of terms used in the Galerkin method for the ABS case.

The flutter speed obtained for the ABS case is 20.6 m/s using 20 Galerkin terms, and the ω is 130 rad/s. The eigenfunctions for this case are shown in Figure 4.7.

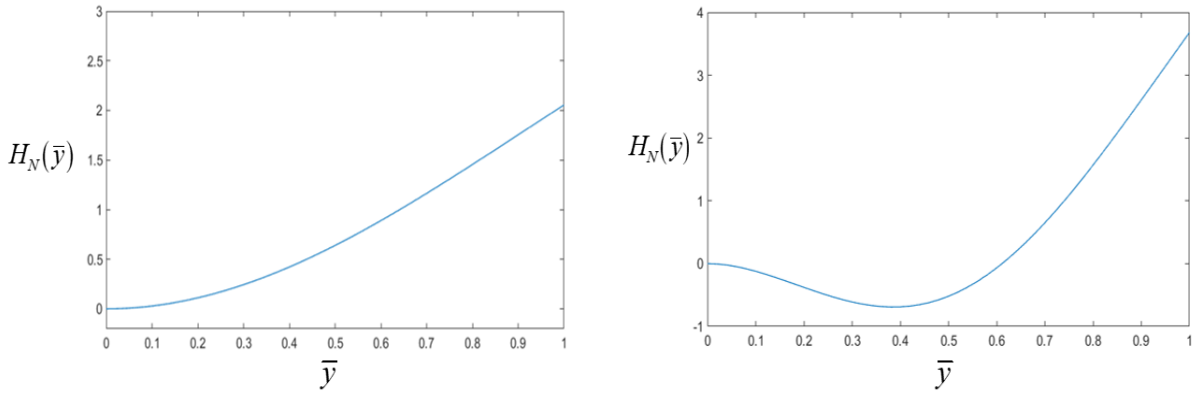

Figure 4.7: Eigenfunctions from the real (left) and imaginary (right) flutter determinant for PETG plastic.

The eigenfunctions obtained for the ABS plastic case show that they are composed primarily of the first and second mode shapes. As was the case for the PETG plastic configuration, the eigenfunction from the imaginary part of the solution has a greater influence from the second bending mode.

4.3 Semi-continuum method for nonlinear structure and linear fluid dynamics

The Galerkin method, combined with the continuum solution for the aerodynamics, produced a reasonably accurate result in the linear case and eliminated a simplifying assumption. However, the true usefulness of the semi-continuum approach is that it can be used to extend the model to account for nonlinear structure dynamics – something a purely continuum approach cannot do. The nonlinear effects investigated here, using the Dowell-Hodges model [**DH**], arise from allowing lateral motion of the structure. This motion, perpendicular to the air velocity as shown in Figure 4.8, will have no effect on the flow field if the flow is assumed to be inviscid because the beam is very thin.

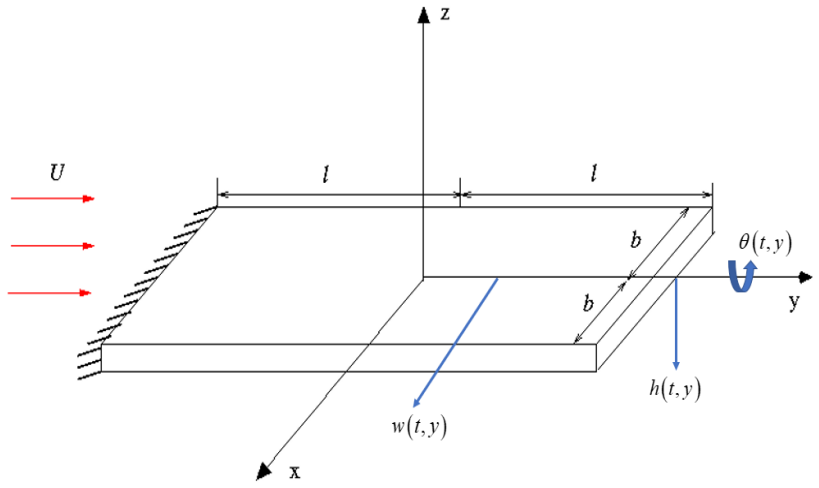

Figure 4.8: Beam and coordinate system with three modes of motion.

The governing equations for the Dowell-Hodges model, using the nondimensional coordinate, $0 \leq \bar{y} \leq 1$, are:

$$\frac{EI_{xx}}{16l^4}h^{(4)}(t,\bar{y})+m_s\ddot{h}(t,\bar{y})+\frac{\Delta EI}{16l^4}[\theta(t,\bar{y})\,w''(t,\bar{y})]''=2b\rho UL^{-1}\left[\hat{A}_2\left(s,\bar{y},\hat{h},\hat{h}'\right)\right] \quad (4.44)$$

and

$$-\frac{GJ}{2l^2}\theta''(t,\bar{y})+I_\theta\ddot{\theta}(t,\bar{y})+\frac{\Delta EI}{16l^4}h''(t,\bar{y})\,w''(t,\bar{y})=\frac{2}{3}b^3\rho UL^{-1}\left[i\hat{A}_1\left(s,\bar{y},\hat{\theta},\hat{\theta}'\right)\right] \quad (4.45)$$

and

$$\frac{EI_{zz}}{16l^4}w^{(4)}(t,\bar{y})+m_s\ddot{w}(t,\bar{y})+\frac{\Delta EI}{16l^4}[\theta(t,\bar{y})\,h''(t,\bar{y})]''=0 \quad (4.46)$$

where $\Delta EI=EI_{zz}-EI_{xx}$. Note that the Kussner doublet functions, where $L^{-1}[\cdot]$ denotes the inverse Laplace transform, have been used for the lift and moment on the right hand sides of Equations (4.44) and (4.45). The boundary conditions for Equations (4.44)-(4.46) are:

$$h(t,0)=h'(t,0)=h''(t,1)=h'''(t,1)=0 \quad (4.47)$$

$$\theta(t,0)=\theta'(t,1)=0 \quad (4.48)$$

$$w(t,0)=w'(t,0)=w''(t,1)=w'''(t,1)=0 \quad (4.49)$$

For the Galerkin method, the independent variables are assumed to have the form:

$$h(t,y) = f(t)\, H(\bar{y}) \tag{4.50}$$

$$\theta(t,y) = f(t)\, \Theta(\bar{y}) \tag{4.51}$$

$$w(t,y) = f(t)\, W(\bar{y}) \tag{4.52}$$

The time dependence in the trial functions, $f(t)$, is chosen to be the same as before:

$$f(t) = e^{\sigma t}\left[cos(\omega t) + \sin(\omega t)\right] \tag{4.53}$$

The trial functions for the bending displacements, $H(\bar{y})$ and $W(\bar{y})$, are the solutions to the beam vibration without the presence of air:

$$H(\bar{y}) = \sum_{n=1}^{N} B_n H_n(\bar{y}) \tag{4.54}$$

where

$$H_n(\bar{y}) = \cosh(\mu_n \bar{y}) - \cos(\mu_n \bar{y}) + \frac{\cosh(\mu_n) + \cos(\mu_n)}{\sinh(\mu_n) + \sin(\mu_n)} \left(\sin(\mu_n \bar{y}) - \sinh(\mu_n \bar{y})\right) \tag{4.55}$$

and

$$W\left(\bar{y}\right) = \sum_{n=1}^{N} D_n W_n\left(\bar{y}\right) \tag{4.56}$$

where

$$W_n\left(\bar{y}\right) = \cosh\left(\mu_n \bar{y}\right) - \cos\left(\mu_n \bar{y}\right) + \frac{\cosh\left(\mu_n\right) + \cos\left(\mu_n\right)}{\sinh\left(\mu_n\right) + \sin\left(\mu_n\right)} \left(\sin\left(\mu_n \bar{y}\right) - \sinh\left(\mu_n \bar{y}\right)\right) \tag{4.57}$$

The μ_n remain unchanged because both functions satisfy the same boundary conditions. The trial functions for $\Theta\left(\bar{y}\right)$ are:

$$\Theta\left(\bar{y}\right) = \sum_{n=1}^{N} C_n \Theta_n\left(\bar{y}\right) \tag{4.58}$$

where

$$\Theta_n\left(\bar{y}\right) = \sin\left(\lambda_n \bar{y}\right) \tag{4.59}$$

where, from the boundary conditions, λ_n is given by:

$$\lambda_n = \left(\frac{2n-1}{2}\right)\pi \tag{4.60}$$

Beginning with the governing equation for $h(t,y)$, the assumed forms from Equations (4.50)-(4.52) are substituted to obtain:

$$\frac{EI_{xx}}{16l^4} f(t) H^{(4)}(\bar{y}) + m_s \ddot{f}(t) H(\bar{y}) + \frac{\Delta EI}{16l^4} [f(t)]^2 [\Theta(\bar{y}) W''(\bar{y})]'' = 2b\rho U f(t) L^{-1} \left[\hat{A}_2(s, \bar{y}, H, H')\right] \tag{4.61}$$

The challenge presented here is that the nonlinear term contains a factor of $[f(t)]^2$, which would prevent the use of the stability analysis developed for the linear case. In order to preserve the linear stability analysis, $[f(t)]^2$ is linearized using a power series expansion. $[f(t)]^2$ is given by:

$$[[f(t)]^2 = [\cos(\omega t) + \sin(\omega t)]^2 = 1 + 2\cos(\omega t)\sin(\omega t) \tag{4.62}$$

The first few terms of the power series for $\sin x$ and $\cos x$ are:

$$\cos x = 1 - \frac{x^2}{2!} + \frac{x^4}{4!} + ... \tag{4.63}$$

$$\sin x = x - \frac{x^3}{3!} + \frac{x^5}{5!} + ... \tag{4.64}$$

Thus,

$$1 + 2\cos(\omega t)\sin(\omega t) = 1 + 2\omega t - 2\frac{(\omega t)^3}{3!} + ... \tag{4.65}$$

All terms of order $(\omega t)^3$ and higher are discarded to obtain:

$$1 + 2\cos(\omega t)\sin(\omega t) \cong 1 + 2\omega t \tag{4.66}$$

Comparing this to the power series expansions in Equations (4.63) and (4.64), $[f(t)]^2$ becomes:

$$[f(t)]^2 \cong \cos(\omega t) + 2\sin(\omega t) \tag{4.67}$$

With $[f(t)]^2$ linearized, the stability analysis detailed previously can be applied, and there is no longer any need to work in the time domain. Taking the Laplace transform of Equation (4.61),

$$\frac{EI_{xx}}{16l^4} L[f(t)] H^{(4)}(\bar{y}) + m_s s^2 L[f(t)] H(\bar{y}) + \frac{\Delta EI}{16l^4} L\left\{[f(t)]^2\right\} [\Theta(\bar{y}) W''(\bar{y})]'' =$$
$$L[f(t)] 2b\rho U \hat{A}_2(s, \bar{y}, H, H') \tag{4.68}$$

The Laplace transforms of $f(t)$ and $[f(t)]^2$are:

$$L\left[f\left(t\right)\right]=\frac{s-\sigma}{\left(s-\sigma\right)^{2}+\omega^{2}}+\frac{\omega}{\left(s-\sigma\right)^{2}+\omega^{2}} \tag{4.69}$$

and

$$L\left[\left(f\left(t\right)\right)^{2}\right]=\frac{s-\sigma}{\left(s-\sigma\right)^{2}+\omega^{2}}+\frac{2\omega}{\left(s-\sigma\right)^{2}+\omega^{2}} \tag{4.70}$$

Substituting into Equation (4.68),

$$\begin{aligned}&\frac{EI_{xx}}{16l^{4}}\left(s-\sigma+\omega\right)H^{(4)}\left(s,\bar{y}\right)-m_{s}\left(s-\sigma+\omega\right)\omega^{2}H\left(\bar{y}\right)+\frac{\Delta EI}{16l^{4}}\left(s-\sigma+2\omega\right)\left[\Theta\left(\bar{y}\right)W''\left(\bar{y}\right)\right]''\\&=2b\rho U\left(s-\sigma+\omega\right)\hat{A}_{2}\left(s,\bar{y},H,H'\right)\end{aligned} \tag{4.71}$$

For $\sigma=0$ and $s=i\omega$, the equation reduces to:

$$\begin{aligned}&\frac{EI_{xx}}{16l^{4}}\omega\left(1+i\right)H^{(4)}\left(s,\bar{y}\right)-m_{s}\left(1+i\right)\omega^{3}H\left(\bar{y}\right)+\frac{\Delta EI}{16l^{4}}\omega\left(2+i\right)\left[\Theta\left(\bar{y}\right)W''\left(\bar{y}\right)\right]''\\&=2b\rho U\omega\left(1+i\right)\hat{A}_{2}\left(s,\bar{y},H,H'\right)\end{aligned} \tag{4.72}$$

Or,

$$\frac{EI_{xx}}{16l^4}H^{(4)}(s,\bar{y}) - m_s\omega^2 H(\bar{y}) + \frac{\Delta EI}{16l^4}\Omega\left[\hat{\Theta}(\bar{y})\,W''(\bar{y})\right]'' = 2b\rho U\hat{A}_2(s,\bar{y},H,H') \quad (4.73)$$

Where $\Omega = 2$ for the real equation and $\Omega = 1$ for the imaginary equation The same procedure can be applied to the governing equations for $\hat{\theta}(s,\bar{y})$ and $\hat{w}(s,\bar{y})$. Upon substituting the assumed form, $\hat{\theta}(s,\bar{y}) = f(t)\,\Theta(\bar{y})$, the real and imaginary parts of the governing equation for $\hat{\theta}(s,\bar{y})$ become:

$$-\frac{GJ}{4l^2}\Theta''(s,\bar{y}) - I_\theta\omega^2\Theta(s,\bar{y}) + \frac{\Delta EI}{16l^4}\Omega W''(s,\bar{y})\,H''(s,\bar{y}) = \frac{2}{3}b^3\rho U i\hat{A}_1\left(s,\bar{y},\hat{\theta},\hat{\theta}'\right) \quad (4.74)$$

Similarly, the governing equation for $\hat{w}(s,\bar{y})$ becomes:

$$\frac{EI_{zz}}{16l^4}W^{(4)}(s,\bar{y}) - m_s\omega^2 W(\bar{y}) + \frac{\Delta EI}{16l^4}\Omega[\Theta(\bar{y})\,H''(\bar{y})]'' = 0 \quad (4.75)$$

Returning to the equation for $\hat{h}(s,\bar{y})$, the trial functions for $H(\bar{y})$, $\Theta(\bar{y})$, and $W(\bar{y})$ are substituted into Equation (4.73) to obtain:

$$\frac{EI_{xx}}{16l^4}\mu_n^4\sum_{n=1}^{N}B_nH_n\left(\bar{y}\right)-m_s\omega^2\sum_{n=1}^{N}B_nH_n\left(\bar{y}\right)+\frac{\Delta EI}{16l^4}\Omega\left[\sum_{n=1}^{N}C_n\Theta_n\left(\bar{y}\right)\sum_{k=1}^{N}D_kW_k{}''\left(\bar{y}\right)\right]''$$
$$=2b\rho U\sum_{n=1}^{N}B_n\hat{A}_{2n}\left[i\omega,\bar{y},U,H_n\left(\bar{y}\right)\right] \tag{4.76}$$

Multiplying through by $H_m\left(\bar{y}\right)$, integrating each term over, and applying orthogonality, Equation (4.76) becomes:

$$\left(\frac{EI_{xx}}{16l^4}\mu_n^4-m_s\omega^2\right)B_n\delta_{mn}+\frac{\Delta EI}{16l^4}\Omega\int_0^1 H_m\left(\bar{y}\right)\left[\sum_{n=1}^{N}C_n\Theta_n\left(\bar{y}\right)\sum_{k=1}^{N}D_kW_k{}''\left(\bar{y}\right)\right]''d\bar{y}$$
$$=2b\rho U\int_0^1 H_m\left(\bar{y}\right)\sum_{n=1}^{N}B_n\hat{A}_{2n}\left[i\omega,\bar{y},U,H_n\left(\bar{y}\right)\right]d\bar{y} \tag{4.77}$$

For $n=1,2,...,N$ and $m=1,2,...,N$.Equation (4.77) can be written in matrix form:

$$\sum_{n=1}^{N}B_nM_{nm}^{H,1}+\sum_{n=1}^{N}C_nM_{nm}^{H,2}-U\sum_{n=1}^{N}B_nM_{nm}^{H,3}=0 \tag{4.78}$$

where

$$M_{nm}^{H,1}=\left(\frac{EI_{xx}}{16l^4}\mu_n^4-m_s\omega^2\right)\delta_{mn} \tag{4.79}$$

$$M_{nm}^{H,2}=\frac{\Delta EI}{16l^4}\Omega\int_0^1 H_m\left(\bar{y}\right)\left[\Theta_n\left(\bar{y}\right)\sum_{k=1}^{N}D_kW_k{}''\left(\bar{y}\right)\right]''d\bar{y} \tag{4.80}$$

$$M_{nm}^{H,3} = 2b\rho \int_0^1 H_m(\bar{y})\, \hat{A}_{2n}\left[i\omega, \bar{y}, U, H_n(\bar{y})\right] d\bar{y} \tag{4.81}$$

To construct an eigenvalue problem, Equation (4.81) is multiplied by the inverse of $M_{nm}^{H,3}$ to obtain:

$$\sum_{n=1}^{N} B_n M_{nm}^{H,1}\left[M_{nm}^{H,3}\right]^{-1} + \sum_{n=1}^{N} C_n M_{nm}^{H,2}\left[M_{nm}^{H,3}\right]^{-1} - U\sum_{n=1}^{N} B_n = 0 \tag{4.82}$$

Equation (4.82) can be simplified by defining the following matrices:

$$M_{nm}^{1} = M_{nm}^{H,1}\left[M_{nm}^{H,3}\right]^{-1} \tag{4.83}$$

$$M_{nm}^{2} = M_{nm}^{H,2}\left[M_{nm}^{H,3}\right]^{-1} \tag{4.84}$$

Equation (4.82) becomes:

$$\sum_{n=1}^{N} B_n M_{nm}^{1} + \sum_{n=1}^{N} C_n M_{nm}^{2} - U\sum_{n=1}^{N} B_n = 0 \tag{4.85}$$

Or, in block matrix form,

$$\left|\left(\overline{\overline{M}}^{1} - U\overline{\overline{I}}\right) \quad \overline{\overline{M}}^{2}\right| \left|\begin{matrix}\overline{B} \\ \overline{C}\end{matrix}\right| = 0 \tag{4.86}$$

Here it is important to note that the system in Equation (4.86) is $N \times 2N$, due to the unknowns $\bar{B}$ and $\bar{C}$. By performing the same procedure on the torsion governing equation, another $N \times 2N$ system will be created with the same unknowns. The two systems can be combined to obtain a $2N \times 2N$ system with U as the repeated eigenvalue.

The governing equation for torsion, in the Laplace domain, is:

$$\frac{GJ}{4l^2}\hat{\theta}''(s,\bar{y}) - I_\theta \omega^2 \hat{\theta}(s,\bar{y}) + \frac{\Delta EI}{16l^4}\hat{w}''(s,\bar{y})\,\hat{h}''(s,\bar{y}) = \frac{2}{3}b^3\rho U i \hat{A}_1\left(s,\bar{y},\hat{\theta},\hat{\theta}'\right) \tag{4.87}$$

The second derivative of $\hat{\theta}(s,\bar{y})$ is:

$$\hat{\theta}''(s,\bar{y}) = f(t)\,\Theta''(\bar{y}) = f(t)\,\lambda_n^2 \sin(\lambda_n \bar{y}) \tag{4.88}$$

Or,

$$\hat{\theta}''(s,\bar{y}) = \lambda_n^2 \hat{\theta}(s,\bar{y}) \tag{4.89}$$

Thus,

$$\Theta''(s,\bar{y}) = \lambda_n^2 \Theta(s,\bar{y}) \tag{4.90}$$

Substituting the trial functions,

$$-\frac{GJ}{4l^2}\sum_{n=1}^{N}\lambda_n^2 C_n\Theta_n(\bar{y})-I_\theta\omega^2\sum_{n=1}^{N}C_n\Theta_n(\bar{y})+\frac{\Delta EI}{16l^4}\Omega\sum_{n=1}^{N}B_n H''_n(\bar{y})\sum_{k=1}^{N}D_k W_k(\bar{y})$$
$$=\frac{2}{3}b^3\rho U\sum_{n=1}^{N}C_n i\hat{A}_1(s,\bar{y},\Theta_n) \tag{4.91}$$

Multiplying through by $\Theta_m(\bar{y})$ and integrating over $\bar{y}$, Equation (4.91) becomes,

$$-\frac{GJ}{4l^2}\sum_{n=1}^{N}\lambda_n^2 C_n\int_0^1\Theta_m(\bar{y})\Theta_n(\bar{y})\,d\bar{y}-I_\theta\omega^2\sum_{n=1}^{N}C_n\int_0^1\Theta_m(\bar{y})\Theta_n(\bar{y})\,d\bar{y}$$
$$=\frac{2}{3}b^3\rho U\sum_{n=1}^{N}C_n i\hat{A}_1(s,\bar{y},\Theta_n)$$
$$+\frac{\Delta EI}{16l^4}\Omega\int_0^1\Theta_m(\bar{y})\sum_{n=1}^{N}B_n H''_n(\bar{y})\sum_{k=1}^{N}D_k W_k(\bar{y})d\bar{y}=\frac{2}{3}b^3\rho U\sum_{n=1}^{N}C_n\int_0^1\Theta_m(\bar{y})\,i\hat{A}_{1,n}(s,\bar{y},\Theta_n)\,d\bar{y} \tag{4.92}$$

Applying the orthogonality property to the first two terms, Equation (4.92) becomes:

$$\left(-\frac{GJ}{4l^2}\lambda_n^2-I_\theta\omega^2\right)C_n\delta_{nm}+\frac{\Delta EI}{16l^4}\Omega\int_0^1\Theta_m(\bar{y})\sum_{n=1}^{N}B_n H''_n(\bar{y})\sum_{k=1}^{N}D_k W_k(\bar{y})d\bar{y}=$$
$$\frac{2}{3}b^3\rho U\sum_{n=1}^{N}C_n\int_0^1\Theta_m(\bar{y})\,i\hat{A}_{1,n}(s,\bar{y},\Theta_n)\,d\bar{y} \tag{4.93}$$

Equation (4.93) can be written in matrix form:

$$\sum_{n=1}^{N} C_n M_{nm}^{\Theta,1} + \sum_{n=1}^{N} B_n M_{nm}^{\Theta,2} - U \sum_{n=1}^{N} C_n M_{nm}^{\Theta,3} = 0 \tag{4.94}$$

where

$$M_{nm}^{\Theta,1} = \left(-\frac{GJ}{4l^2} \lambda_n^2 - I_\theta \omega^2 \right) \delta_{nm} \tag{4.95}$$

$$M_{nm}^{\Theta,2} = \frac{\Delta EI}{16l^4} \Omega \int_0^1 \Theta_m(\bar{y}) \, H''_n(\bar{y}) \sum_{k=1}^{N} D_k W_k(\bar{y}) d\bar{y} \tag{4.96}$$

$$M_{nm}^{\Theta,3} = \frac{2}{3} b^3 \rho \int_0^1 \Theta_m(\bar{y}) \, i\hat{A}_{1,n}(s, \bar{y}, \Theta_n) \, d\bar{y} \tag{4.97}$$

As before, U will be isolated to construct an eigenvalue problem. This is done by multiplying through by $\left[M_{nm}^{\Theta,3}\right]^{-1}$:

$$\sum_{n=1}^{N} C_n M_{nm}^{\Theta,1} \left[M_{nm}^{\Theta,3}\right]^{-1} + \sum_{n=1}^{N} B_n M_{nm}^{\Theta,2} \left[M_{nm}^{\Theta,3}\right]^{-1} - U \sum_{n=1}^{N} C_n = 0 \tag{4.98}$$

Equation (4.98) can be simplified as:

$$\sum_{n=1}^{N} B_n M_{nm}^{3} + \sum_{n=1}^{N} C_n M_{nm}^{4} - U \sum_{n=1}^{N} C_n = 0 \tag{4.99}$$

where

$$M_{nm}^{3} = M_{nm}^{\Theta,2}\left[M_{nm}^{\Theta,3}\right]^{-1} \tag{4.100}$$

and

$$M_{nm}^{4} = M_{nm}^{\Theta,1}\left[M_{nm}^{\Theta,3}\right]^{-1} \tag{4.101}$$

Or, in block matrix form,

$$\left|\overline{\overline{M}}^{3} \quad \left(\overline{\overline{M}}^{4} - U\overline{\overline{I}}\right)\right| \left|\begin{matrix}\overline{B} \\ \overline{C}\end{matrix}\right| = 0 \tag{4.102}$$

Recall from the analysis on the equation for $\hat{h}\left(s, \bar{y}\right)$:

$$\left|\left(\overline{\overline{M}}^{1} - U\overline{\overline{I}}\right) \quad \overline{\overline{M}}^{2} \quad\right| \left|\begin{matrix}\overline{B} \\ \overline{C}\end{matrix}\right| = 0 \tag{4.103}$$

Equations (4.102) and (4.103) are combined to obtain:

$$\left|\begin{matrix}\left(\overline{\overline{M}}^{1} - U\overline{\overline{I}}\right) & \overline{\overline{M}}^{2} \\ \overline{\overline{M}}^{3} & \left(\overline{\overline{M}}^{4} - U\overline{\overline{I}}\right)\end{matrix}\right| \left|\begin{matrix}\overline{B} \\ \overline{C}\end{matrix}\right| = 0 \tag{4.104}$$

Equation (4.104) is a $2N \times 2N$ system of equations, with U as an eigenvalue when the determinant of the square matrix is set to zero. Once again, the elements of the corresponding

eigenvector will be the coefficients B_n and C_n . It is important to note that the matrices $\bar{\bar{M}}^2$ and $\bar{\bar{M}}^3$ contain the unknown coefficients D_n . To obtain an equation for these coefficients, and as a result close the system, we turn to the governing equation for $\hat{w}(s,\bar{y})$:

$$\frac{EI_{zz}}{16l^4}\hat{w}^{(4)}(s,\bar{y}) - m_s\omega^2\hat{w}(s,\bar{y}) + \frac{\Delta EI}{16l^4}\left[\hat{\theta}(s,\bar{y})\,\hat{h}''(s,\bar{y})\right]'' = 0 \tag{4.105}$$

Notice that in Equation (4.105) that there is no aerodynamic loading, a result of assuming inviscid flow. Substituting the trial functions for $\hat{w}(s,\bar{y})$, Equation (4.105) becomes:

$$\frac{EI_{zz}}{16l^4}\sum_{n=1}^{N} D_n\mu_n^4 W_n(\bar{y}) - m_s\omega^2\sum_{n=1}^{N} D_n W_n(\bar{y}) + \frac{\Delta EI}{16l^4}\Omega\left[\sum_{n=1}^{N} C_n\Theta_n(\bar{y})\sum_{k=1}^{N} B_k H''_k(\bar{y})\right]'' = 0 \tag{4.106}$$

Multiplying through by $W_m(\bar{y})$ and integrating, Equation (4.106) becomes:

$$\begin{aligned}&\frac{EI_{zz}}{16l^4}\sum_{n=1}^{N} D_n\mu_n^4\int_0^1 W_m(\bar{y})\,W_n(\bar{y})\,d\bar{y} - m_s\omega^2\sum_{n=1}^{N} D_n\int_0^1 W_m(\bar{y})\,W_n(\bar{y})\,d\bar{y}\\ &+\frac{\Delta EI}{16l^4}\Omega\int_0^1 W_m(\bar{y})\left[\sum_{n=1}^{N} C_n\Theta_n(\bar{y})\sum_{k=1}^{N} B_k H''_k(\bar{y})\right]'' d\bar{y} = 0\end{aligned} \tag{4.107}$$

Applying orthogonality, the equation becomes:

$$\left(\frac{EI_{zz}}{16l^4}\mu_n^4 - m_s\omega^2\right)D_n\delta_{nm} + \frac{\Delta EI}{16l^4}\Omega\int_0^1 W_m(\bar{y})\left[\sum_{n=1}^{N} C_n\Theta_n(\bar{y})\sum_{k=1}^{N} B_k H''_k(\bar{y})\right]'' d\bar{y} = 0 \tag{4.108}$$

Writing Equation (4.108) in terms of matrices,

$$\sum_{n=1}^{N} D_n M_{nm}^5 + \sum_{n=1}^{N} C_n M_{nm}^6 = 0 \tag{4.109}$$

where

$$M_{nm}^5 = \left(\frac{EI_{zz}}{16l^4} \mu_n^4 - m_s \omega^2 \right) \delta_{nm} \tag{4.110}$$

and

$$M_{nm}^6 = \frac{\Delta EI}{16l^4} \Omega \int_0^1 W_m(\bar{y}) \left[\Theta_n(\bar{y}) \sum_{k=1}^{N} B_k H''_k(\bar{y}) \right]'' d\bar{y} \tag{4.111}$$

Or,

$$\left| \overline{\overline{M}}^6 \right| \left| \bar{D} \right| + \left| \overline{\overline{M}}^5 \right| \left| \bar{C} \right| = 0 \tag{4.112}$$

Solving for the vector of coefficients $\bar{D}$,

$$\bar{D} = - \left| \overline{\overline{M}}^6 \right|^{-1} \left| \overline{\overline{M}}^5 \right| \left| \bar{C} \right| \tag{4.113}$$

In Equation (4.113), $\bar{C}$ is unknown and the matrix contains the unknown coefficients $\bar{B}$. As

a result, an iterative method will be employed to solve for the three unknowns $\bar{B}$, $\bar{C}$, and $\bar{D}$ using equations (4.104) and (4.113). It will start with an initial guess for $\bar{D}$, then proceed to solve for $\bar{B}$ and $\bar{C}$ from Equation (4.104), then update the values of $\bar{D}$ using Equation (4.113). The process repeats until there is sufficiently small change in $\bar{D}$. This process is illustrated in Figure 4.9.

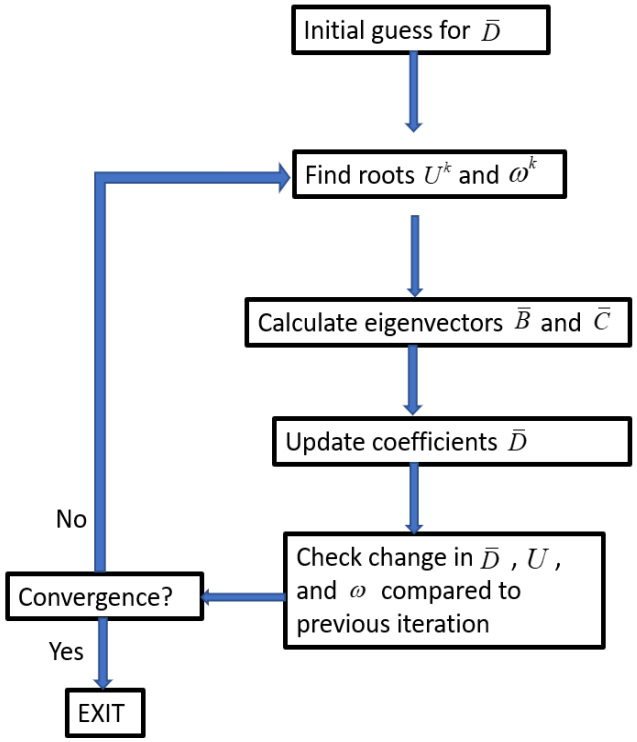

Figure 4.9: Solution procedure for nonlinear model.

The next section implements this solution procedure to calculate the flutter speed for the three configurations.

4.4 Flutter speed calculation based on linear fluid and nonlinear structure dynamics

Using the numerical methods described in Chapter 3 and Appendix B, calculations were performed for three different structures and compared to experimental data. The benchmark case was a 2024-T3 Aluminum beam, where aluminum was chosen because the material properties are precisely known. The two additional cases were of different materials, ABS and PETG plastic, each with different dimensions. The material properties and dimensions for each configuration is shown in in Table 4.2.

Table 4.2: Material properties and dimensions for three configurations.

Material	2024-T3 Aluminum	PETG	ABS
Density (kg/m^3)	2780	1270	1070
Young's Modulus (GPa)	73.1	2.83	2.10
Shear Modulus (GPa)	28.0	0.0385	0.0827
Length (cm)	30.5	20.32	20.32
Width (cm)	10.2	10.2	10.2
Thickness (cm)	3.81×10^{-4}	0.075	0.05

For each case, the number of terms used in the Galerkin method was increased until sufficient convergence was obtained. The plot in Figure 4.10 shows that the flutter speed convergence for the 2024-T3 aluminum case, where it converges reasonably well using 7 terms.

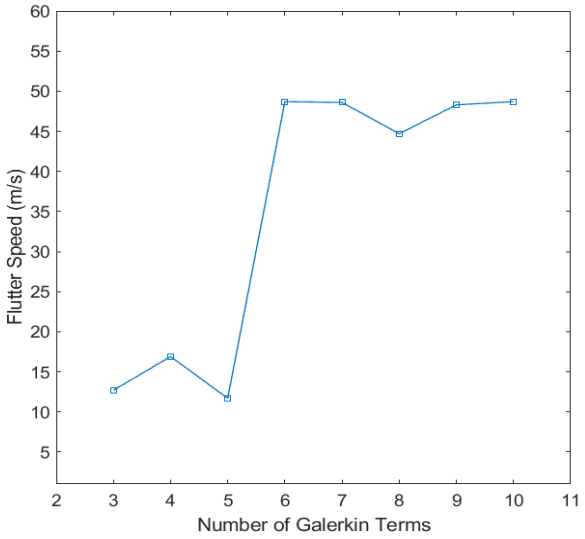

Figure 4.10: Convergence of flutter speed with number of Galerkin terms for 2024-T3 aluminum.

The flutter speed for the 2024-T3 aluminum configuration is 48.7 m/s, and the corresponding ω value is 134 m/s. The eigenfunctions from the real and imaginary parts of the flutter determinant were plotted to inspect the shape of the structure associated with the approximation of $h(t, y)$. In each of the three configurations, there was negligible influence from the torsional and lateral bending coefficients. As a result, only the axial bending eigenfunctions, $H_N(\bar{y})$, have any significance in observing the overall shape of the structure. The eigenfunctions for 2024-T3 aluminum are shown in Figure 4.11. The coefficients are tabulated in Appendix C.

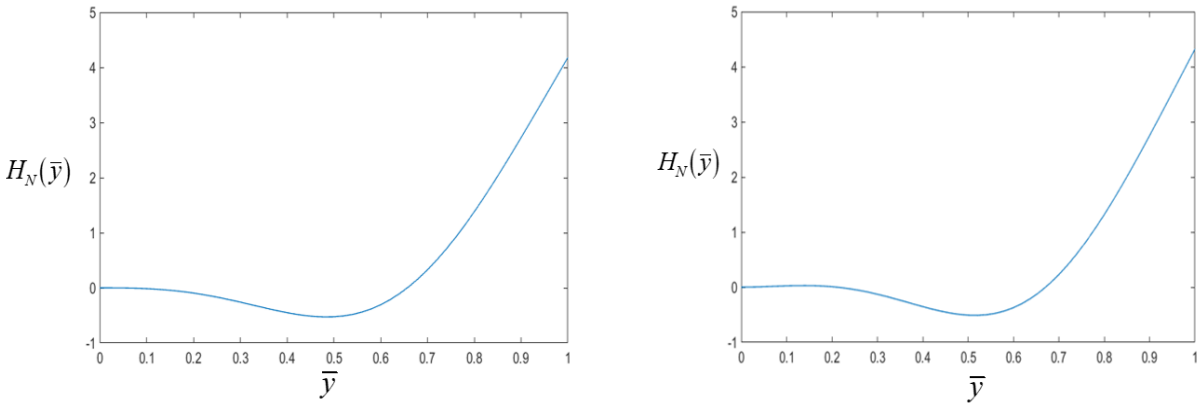

Figure 4.11: Eigenfunctions from the real (left) and imaginary (right) flutter determinant for 2024-T3 aluminum.

The eigenfunctions in Figure 4.11 show the first and bending modes dominating the structure's shape, where the influence of the second bending mode is more present than in the linear case. Figure 4.12 shows the flutter speed convergence for the PETG configuration.

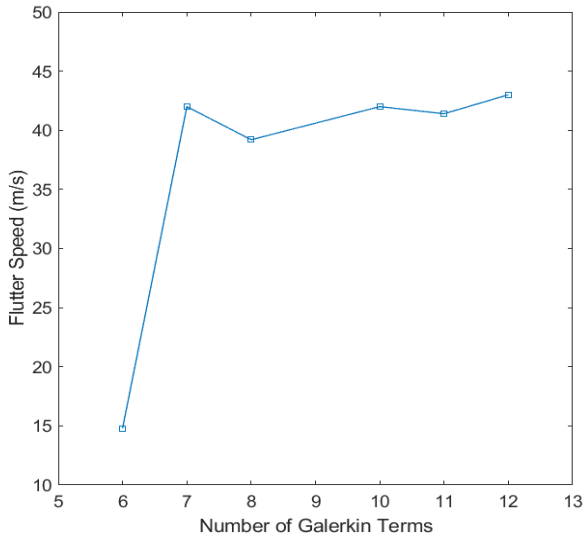

Figure 4.12: Convergence of flutter speed with number of Galerkin terms for PETG.

The calculated flutter speed for the PETG case using 12 terms is 22.6 m/s, and the ω is 104

rad/s . The eigenfunctions for this case are shown in Figure 4.13.

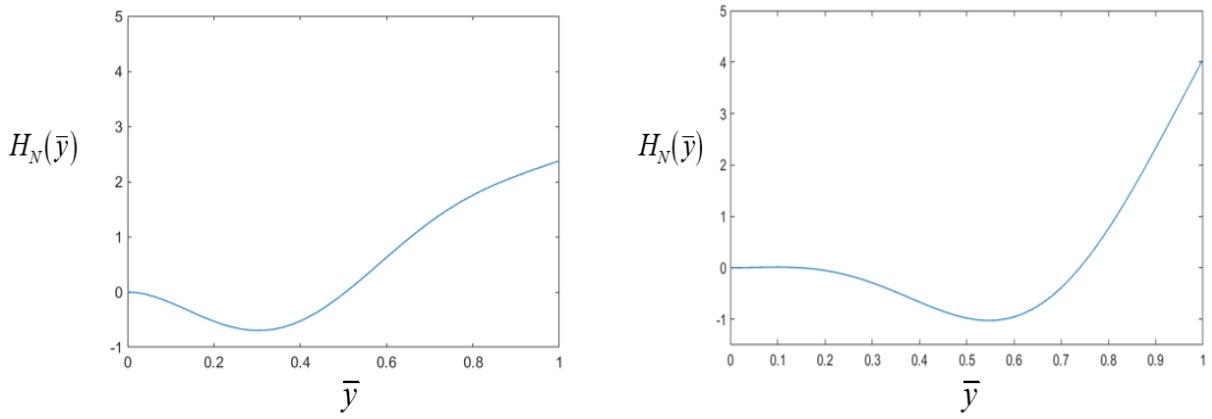

Figure 4.13: Eigenfunctions from the real (left) and imaginary (right) flutter determinant for PETG plastic.

As was the case for 2024-T3 aluminum, the eigenfunctions for the PETG configuration show the shape as being influenced by the first and second bending modes. Figure 4.14 shows the flutter speed versus number of terms for the third sample, ABS plastic.

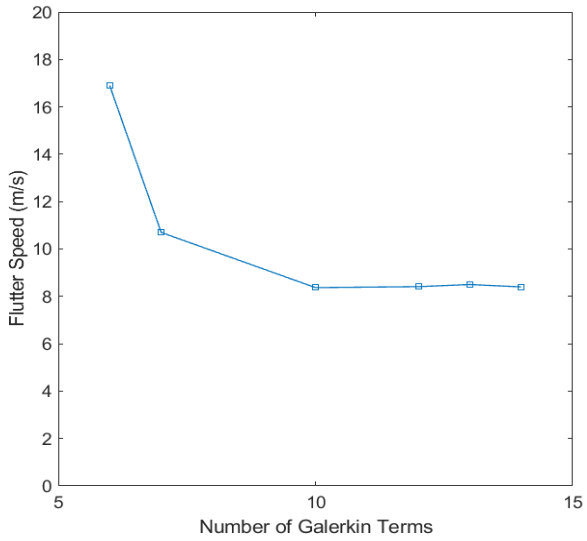

Figure 4.14: Convergence of flutter speed with number of Galerkin terms for ABS plastic.

The calculated flutter speed for the ABS plastic case is 8.5 m/s, and the corresponding ω is 68 rad/s. The eigenfunctions for ABS plastic are shown in Figure 4.15.

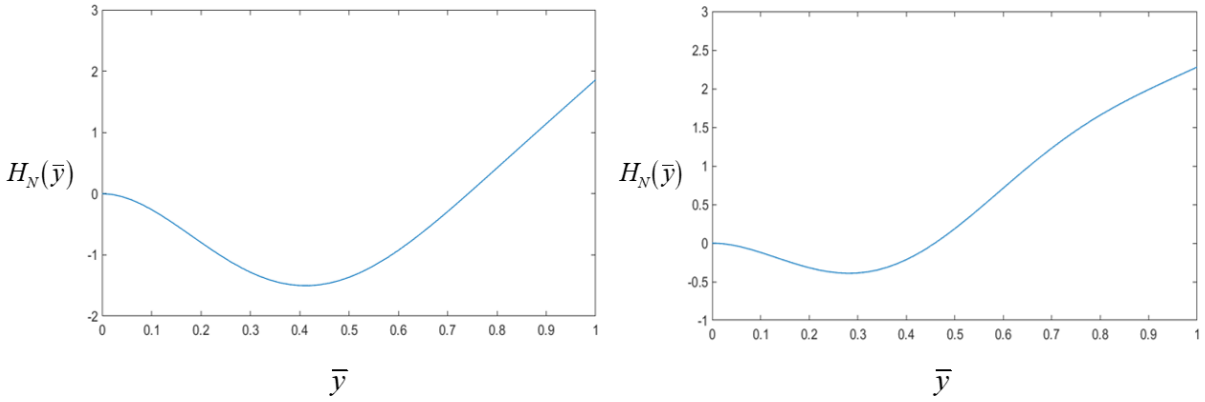

Figure 4.15: Eigenfunctions from the real (left) and imaginary (right) flutter determinant for ABS plastic.

The eigenfunctions for the ABS plastic case once again show that the shape of the structure is influenced primarily by the first and second bending modes.

5 Flutter speed and limit cycle oscillation by experiment

The previous chapters provided an analytical treatment of aeroelasticity in axial flow, but only as it relates to the onset of instability of the structure. The models used are limited to small structural displacements, which is adequate for calculating the flutter speed, but these models fall short in describing the motion of the structure after the flutter speed is reached. When Limit Cycle Oscillation (LCO) occurs, the structure exhibits large displacements in the form of bounded oscillations. This chapter presents observations from wind tunnel experiments, where structures were brought past the flutter speed to undergo LCO. Two sets of experiments were performed. The purpose of the modal analysis experiments was to determine how the frequencies of the oscillations changed with air speeds higher than the flutter speed. The aim of the second set of experiments, which used image processing techniques, was to determine the effect of increasing air speed on the amplitude of the oscillations. Finally, a scaling analysis is used to present the data in nondimensional form and obtain expressions to estimate the flutter speed and LCO frequency.

5.1 Description of wind tunnel and instrumentation

All experiments were performed in an Aerolab open circuit, subsonic wind tunnel. The wind tunnel is constructed of fiberglass, with a steel and aluminum test section measuring 11.5 in.$\times$11.75 in.$\times$22 in. The fan is located on the outlet side of the wind tunnel and draws air through the inlet where honeycomb-style flow straighteners are used to ensure a uniform flow field through the test section. Within the test section, a custom assembly was mounted

to the bottom to cantilever the beam structures, as shown in Figure 5.1. The assembly acts as a clamp, bolting one end of the beams from all sides.

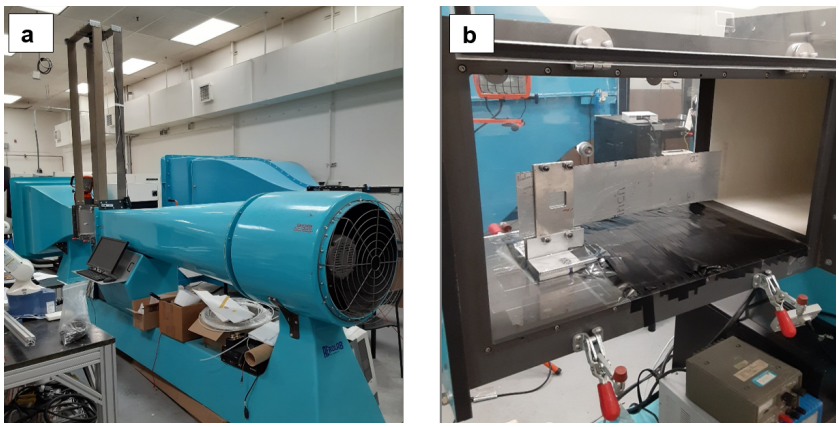

Figure 5.1: a)Aerolab wind tunnel used for LCO experiments; b) Wind tunnel test section.

Air velocity measurements were taken using a Pitot tube, the Aerolab Pitot-Static Probe, which was purchased as an accessory to the wind tunnel. It is an L-shaped probe, as shown in Figure , which is inserted into the air stream through the side of the test section.

Figure 5.2: Aerolab Pitot-Static Probe.

The short segment of the tube is parallel to the air stream, so that the holes along its length measure the static pressure and the hole on the tip measures the stagnation pressure. The

hoses at the other end of the Pitot tube were connected to a Dwyer 616KD-02 temperature-compensated differential pressure transducer. The pressure transducer was calibrated by the manufacturer, with a reported uncertainty of ± 2% full scale for a range of 0-3 in. H_20.

The modal analysis experiments used a PCB Piezotronics 352A71 single axis accelerometer. The accelerometer was calibrated by the manufacturer, with uncertainty of ¡0.4% of the measured value for frequencies between 0 and 100 Hz. The signal from the accelerometer was amplified using a PCB Piezotronics 422B104 sensor signal conditioner, and the amplified signal was sent to a National Instruments USB-6210 data acquisition board. The data was collected and processed in LabView 2012 installed on a Dell Optiplex 790 PC.

The high speed camera used in the image processing experiments was a Fastec-IL4 equipped with a Nikon Micro-NIKKOR 55mm F/2.8 lens. The Fastec-IL4 is capable of frame rates up to 6259 fps at 320×240 resolution, and can provide a resolution of 1280×1024 for frame rates up to 510 fps. The settings used on the high speed camera for these experiments are shown in section 5.2.3.

5.2 Experimental results

5.2.1 Flutter speed

A critical aspect of aeroelasticity analysis is the determination of the flutter speed, which can be measured in a wind tunnel by slowly increasing the air speed until the structure begins to flutter. The onset of flutter in axial flow is very abrupt, with the amplitude of the structure's oscillations increasing visibly within the span of one air speed increment.

The air speed is controlled by increasing the wind tunnel fan speed in increments of 0.1 rotations per second, which correspond to increments of 0.08 m/s in air speed. This linear trend between fan speed and air speed was determined experimentally by calculating the free stream air velocity at different fan speed settings from measurements taken using a Pitot tube. The Pitot tube was inserted into the vacant test section, with one channel measuring the stagnation pressure of the air stream and the other measuring the static pressure. For the range of air speeds required for these experiments, 0-40 m/s, the flow can be treated as incompressible. Thus, the Bernoulli equation can be used to calculate air velocity from the measured pressure difference:

$$U = \sqrt{\frac{2\Delta P}{\rho}} \tag{5.1}$$

where ΔP is the pressure difference measured by the Pitot tube, and ρ is the density of air at the temperature when the measurement was taken. The uncertainty in the pressure transducer provided by the manufacturer is $\pm 2\%$ of the full scale, which corresponds to $\pm$

0.06 in. H_2O. Using Equation (1.1), the uncertainty in the air speed due to the pressure transducer is 4.93 m/s. Because the structure and clamp occupy a large portion of the test section, and to avoid obstruction by the Pitot tube, the air speed was not measured during flutter. However, because the flow is largely incompressible, the structure does not have any influence on the upstream air speed. Therefore, all measurements were taken without the structure and clamp in the test section. Using 45 pressure measurements taken at different fan speeds over the range of the pressure transducer, the plot shown in Figure B.54 was constructed.

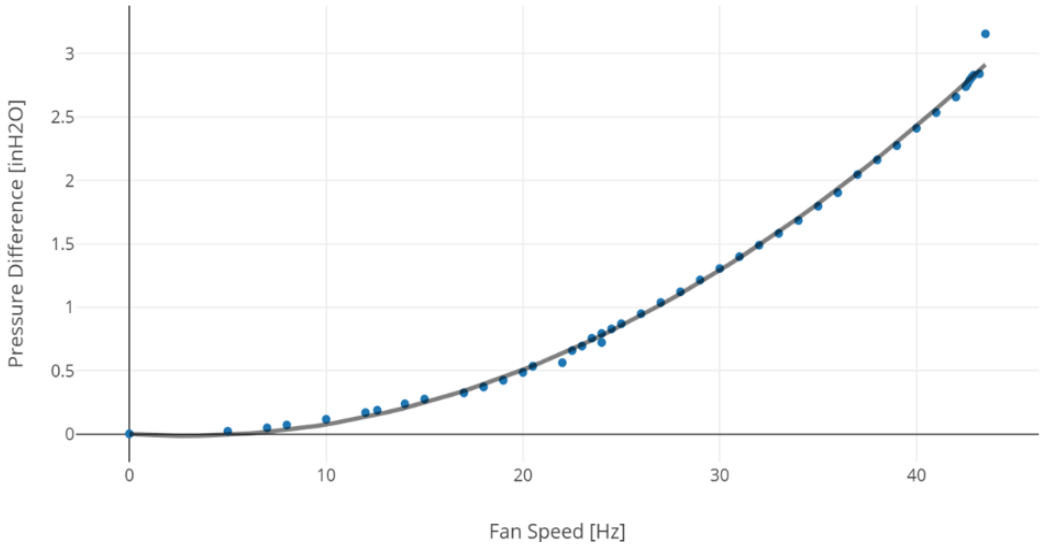

Figure 5.3: Measured pressure difference versus fan speed.

The data fits a quadratic trendline with an R^2 value of 0.998, shown on Figure B.54 as a black line. Observing that the fan speed is proportional to the square root of the pressure difference from the Pitot tube, a comparison can be made between the data and Equation (5.1) and a linear relationship between the velocity and fan speed can be determined. Using

Equation (5.1), the velocity was calculated from the measured pressures and plotted against the fan speed as shown in Figure 5.4.

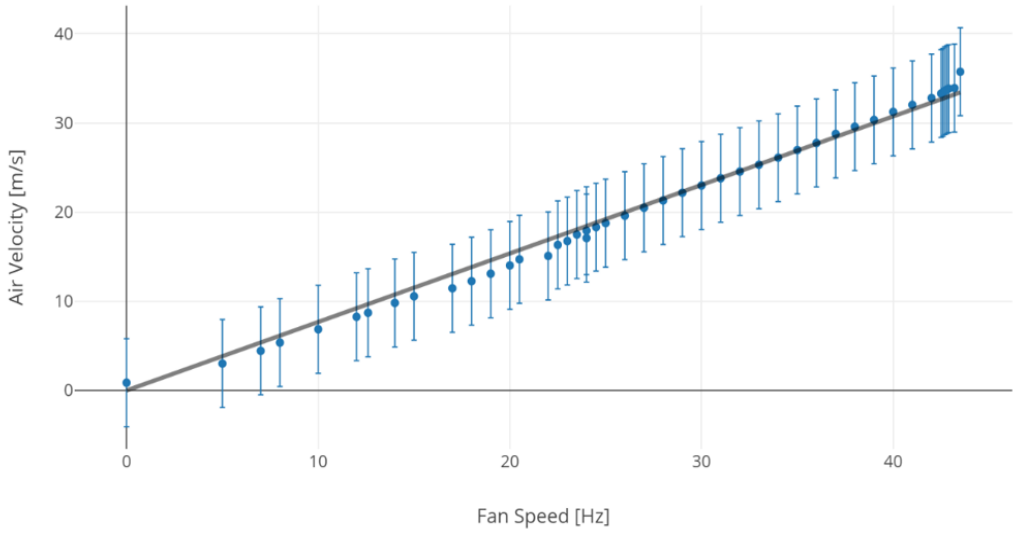

Figure 5.4: Air velocity versus fan speed.

The linear curve fit in Figure 5.4 has an R^2 value of 0.992, indicating a linear relationship between velocity and fan speed . From the linear curve fit, the equation relating velocity to fan speed is:

$$U\,[\text{m/s}] = 0.7811\omega[\text{Hz}] \pm 4.93 \tag{5.2}$$

For one controller increment (0.1 Hz) , the wind tunnel air speed is increased by approximately 0.08 m/s. This air speed increment of 0.08 m/s is the maximum uncertainty that can be present from incrementally increasing the speed. At each increment in air speed, the structure was allowed to reach steady state to avoid the possibility of transient effects.

Three different structures were analyzed for their flutter speed and LCO behavior. The material properties, dimensions, and measured flutter speeds for each structure are shown in

Table 5.1. For the remainder of this chapter, each structure will be referred to by its sample number, as given at the top of Table 5.1.

Table 5.1: Parameters and Measured Flutter Speed for Three Structures.

	Sample 1	Sample 2	Sample 3
Material	2024-T3 Aluminum	PETG	ABS
Young's Modulus (GPa)	73.1	2.83	2.10
Length (cm)	30.5	20.32	20.32
Width (cm)	10.2	10.2	10.2
Thickness (cm)	3.81×10^{-4}	0.075	0.05
Flutter speed (m/s)	38.3	28.0	15.5

Table 5.1 shows that the flutter speed of the aluminum sample is the highest, due to the aluminum being considerably stiffer. The lower flutter speeds of the PETG and ABS plastic samples can be partially attributed to their shorter length but are primarily due to the much lower stiffness.

5.2.2 Limit cycle oscillation: Modal analysis

In these experiments, an accelerometer was attached to the structure near the clamped end. Figure 5.5 shows the accelerometer attached to the structure in the wind tunnel test section for Sample 2.

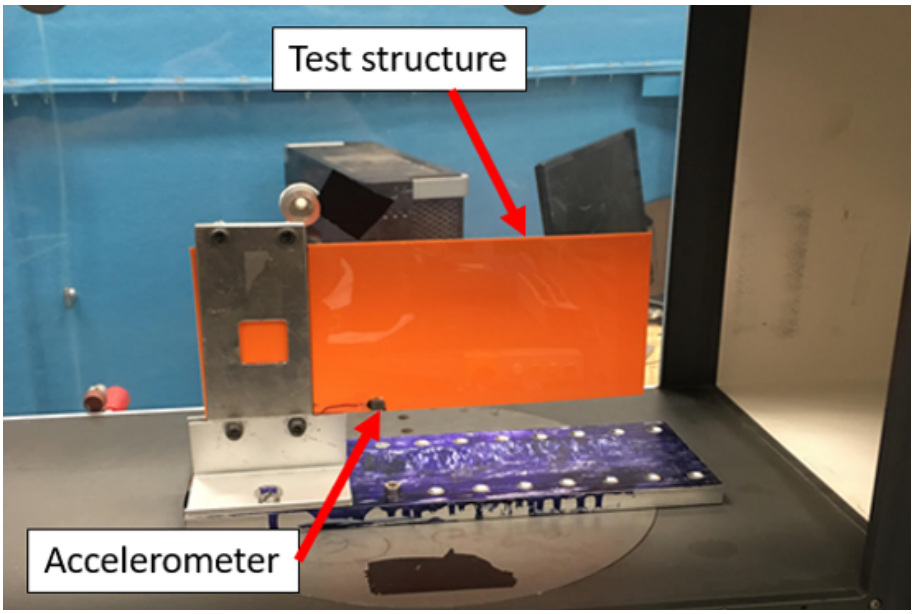

Figure 5.5: Sample 2 with accelerometer attached.

Once the fan speed and thus the air speed is set and the structure undergoes LCO, the signal from the accelerometer was recorded for 10 seconds using a data acquisition system. Figure 5.6 shows the accelerometer time domain signal for Sample 1 at the flutter speed, for 3 seconds duration.

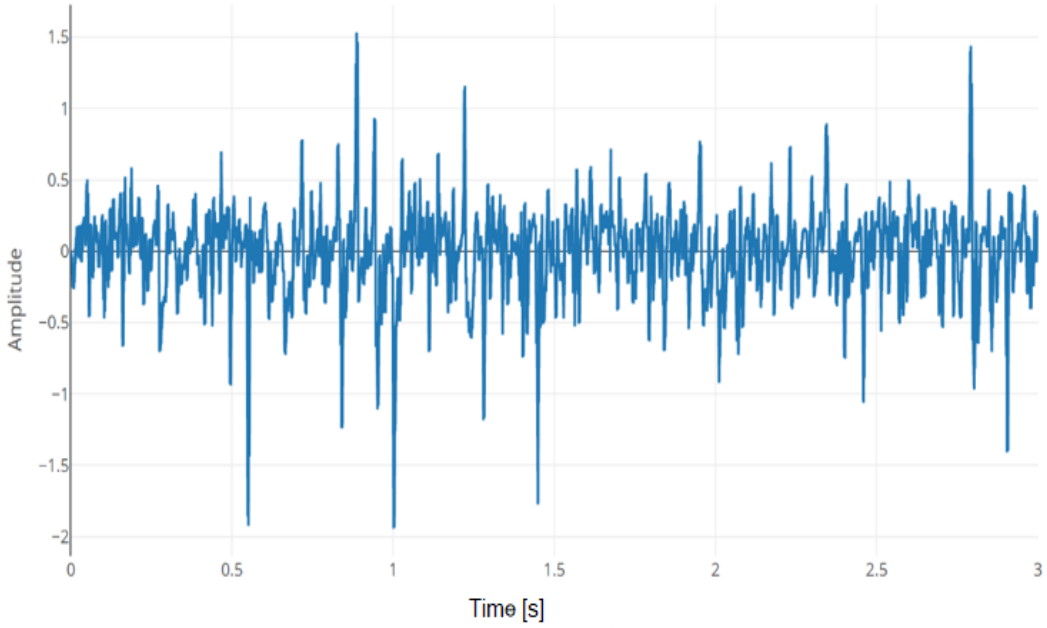

Figure 5.6: Accelerometer time domain signal for Sample 1 at the flutter speed.

Figure 5.6 shows that there are multiple frequencies present in the time domain signal, indicating that more than one mode is present in the LCO. To determine the frequency content of the LCO, a Fast Fourier Transform (FFT) is performed on the time domain signal. The FFT for the case from Figure 5.7 is shown below.

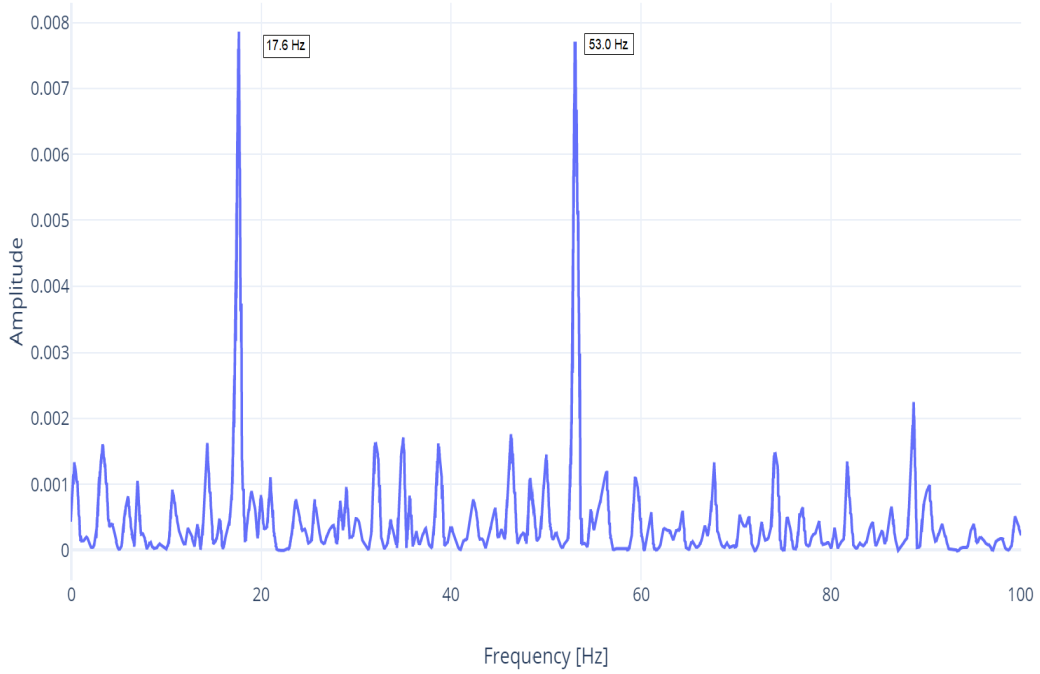

Figure 5.7: FFT of Sample 1 at the flutter speed.

The peaks in the FFT of Figure 5.7 show that that there are two dominant frequencies present, each of which may belong to any structural mode shape. It is expected that the frequencies of the LCO in these experiments will be different from the structure's natural frequencies for several reasons. First, from physical intuition, air flow will dampen the structure's motion. The second reason is that the accelerometer acts as point mass added to the structure, which is expected to have a greater impact on the frequency. Despite these effects, comparison of the measured frequencies to the theoretical natural frequencies can reveal which mode shapes are present in LCO. For bending motion, the theoretical natural frequencies can be obtained from Euler-Bernoulli beam theory:

$$\omega_n = \alpha_n \sqrt{\frac{EI}{mL^4}} \tag{5.3}$$

where L is the length of the beam, I is the moment of inertia of the cross section, and m is the mass of the beam. The coefficients α_n are the roots to the transcendental equation:

$$\cosh(\alpha_n)\cos(\alpha_n) = 1 \tag{5.4}$$

Once the experimental FFT is obtained, the frequency corresponding to each peak is determined. Table 5.2 shows the peak frequencies of Sample 1 at the flutter speed and the theoretical natural frequencies.

Table 5.2: Experimental and Theoretical Frequencies of Sample 1 at the Flutter Speed.

Mode Number	Experimental Frequency (Hz)	Theoretical Frequency (Hz)	Percent Difference (%)
1	-	3.48	-
2	17.6	21.8	19.3
3	53.0	61.0	13.1
4	-	120	-

The values in Table 5.2 show that the measured frequencies are 13.1-19.3% lower than the closest theoretical frequencies, but this difference is far less than the difference between the consecutive modes. Therefore, from Table 2 we can conclude that, at the flutter speed, the 2nd and 3rd bending modes are present in the structure's LCO and are comparable in magnitude as indicated by Figure 5.7. To further investigate the LCO, measurements were taken for five air speeds higher than the flutter speed. These experiments were performed for all three configurations to see if increasing the air speed would either excite higher frequency

modes or shift the existing frequencies higher or lower. Table 5.3 shows the peak frequencies obtained for Sample 1, and the corresponding FFTs for each trial are shown in Appendix B.

Table 5.3: Experimental and Theoretical Frequencies of Sample 1 at the Flutter Speed.

Trial	Air Speed (m/s)	1^{st} Peak	2^{nd} Peak
1	36.7	17.6	53
2	37.5	17.6	53.3
3	38.3	18	54
4	39	18	54.3
5	39.8	18.3	55
6	40.6	18.3	55.3

The data in Table 5.3 shows that there is a slight upward shift in the peak frequencies as the air speed increases past the flutter speed. The FFTs (shown in Appendix C) reveal that no higher frequencies were excited as a result of raising the air speed from 36.7 m/s to 40.6 m/s. The same trend is observed in the PETG plastic structure, Sample 2. Although it has a lower Young's Modulus than Sample 1, the natural frequencies are comparable to Sample 1 due to its shorter length. The modal frequencies were determined for Sample 2 at the flutter speed and at five additional speeds higher than the flutter speed. Figure 5.8 shows the FFT of Sample 2 at the flutter speed.

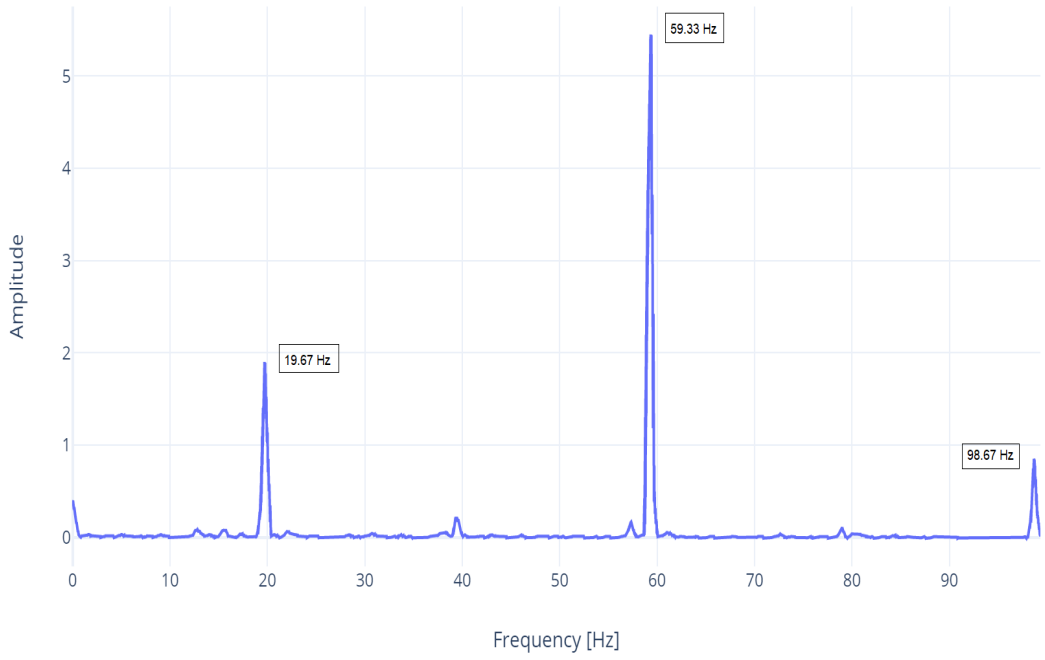

Figure 5.8: FFT for Sample 2 at the flutter speed.

The FFT in Figure 5.8 shows that for Sample 2 a third peak is present at the flutter speed, whereas only two modes were excited in Sample 1. Upon comparison to the theoretical natural frequencies, it was determined that these peaks correspond to the 2^{nd}, 3^{rd}, and 4^{th} bending modes. It is interesting to note that for this material and dimensions the 3rd bending mode is dominant, whereas for the configuration of Sample 1 the 2^{nd} and 3^{rd} bending modes had roughly equal contribution to the overall shape. Table 5.4 lists the frequencies of the peaks for all six speeds tested.

Table 5.4: Peak Frequencies for Sample 2 At and Above the Flutter Speed

Trial	Air Speed (m/s)	1st Peak	2nd Peak	3rd peak
1	25.9	19.67	59.33	98.67
2	26.7	19.67	59.33	98.67
3	27.5	19.67	59.33	98.67
4	28.3	20	59.67	99.33
5	29.1	20	59.67	99.33
6	29.8	20	59.67	99.67

The results in Table 5.4 show that as the speed increases beyond the flutter speed, there is a slight shift in the peak frequencies. This is the same behavior that was observed for Sample 1: a shift in existing frequencies but no excitation of higher modes. Sample 3, which is made of ABS plastic, was chosen to have a lower Young's modulus than Sample 2 and substantially lower natural frequencies than Samples 1 and 2. Performing the same analysis, there are six peak frequencies present at the flutter speed.

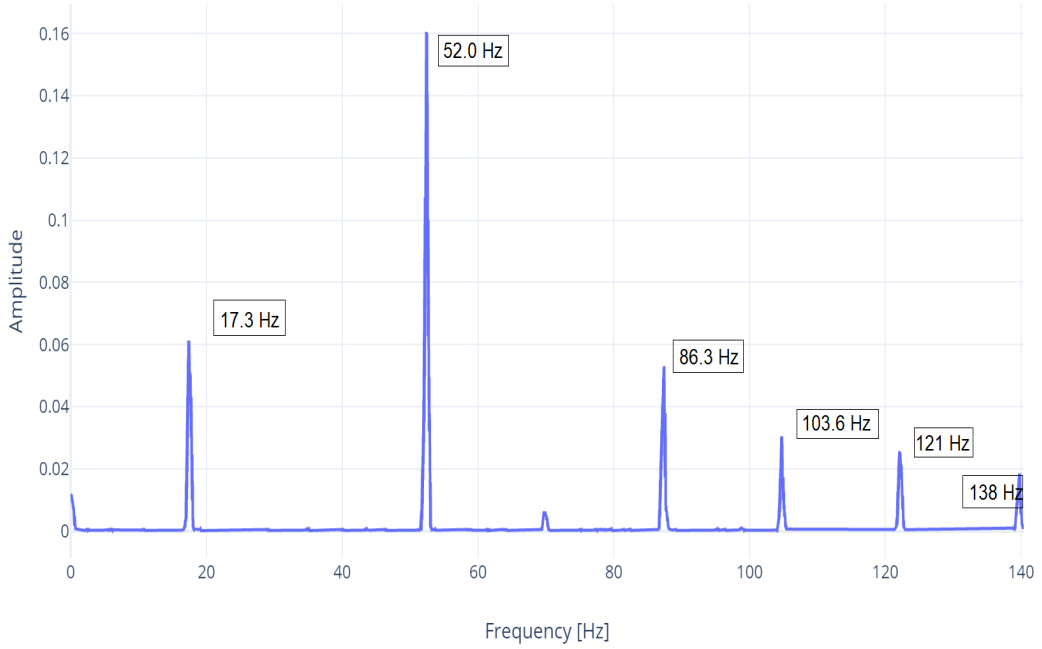

Figure 5.9: FFT for Sample 3 at the flutter speed.

Figure 5.9 shows that the second frequency present is dominant over the other five frequencies. The air speed was increased for five speeds higher than the flutter speed for a total of six air speeds. The peak frequencies for all trials of Sample 3 are shown in Table 5.5.

Table 5.5: Peak Frequencies for Sample 2 At and Above the Flutter Speed.

Trial	Air Speed (m/s)	1st Peak	2nd Peak	3rd Peak	4th Peak	5th Peak	6th peak
1	17.3	17.3	52	86.3	103.6	121	138.3
2	18	17.3	52.3	87.3	104.6	122.3	139.6
3	18.8	17.7	53	88.6	105.8	123.1	141
4	19.6	18	53.7	89.6	107.5	125.6	143.3
5	20.4	18.3	54.7	91	109.1	127.3	145.5
6	21.2	18.3	55.3	92.3	111	129.1	147.7

In the experiments performed on Sample 3, it was observed that the frequencies measured do not correlate well with the theoretical natural frequencies, for bending or torsion modes. This indicates that Sample 3, although it is a rectangular beam of uniform cross-section, does not behave as predicted by Euler-Bernoulli (EB) beam theory when the accelerometer is attached. In Samples 1 and 2, with the accelerometer attached, the frequencies observed in experiments were up to 20% lower than those predicted by EB theory but could still be correlated to one of the mode shapes. This difference indicates that the mass of the accelerometer has a substantial effect on beam-like behavior that became especially prominent due to Sample 3's lower stiffness.

The uncertainty in the observed frequencies in these experiments is partially due to uncertainty in the time domain signal measured by the accelerometer. From the manufacturer, for frequencies between 0 and 100 Hz, the uncertainty is reported to be no more than 0.4% of the measured value. Uncertainty in the peak frequencies also arises from uncertainty in measuring the dimensions of the structure. Measuring the dimensions with a dial caliper, the uncertainty in the measured dimension is:

$$\delta L = \frac{1}{2}\Delta x \tag{5.5}$$

where Δx is the spacing between each increment on the caliper. Following the single sample uncertainty analysis proposed by Kline and McClintock [20], and using Equation (5.3), the uncertainty in the modal frequency can be expressed as:

$$\delta\omega_n = \alpha_n \sqrt{\left(\frac{\partial \omega_n}{\partial L}\delta L\right)^2 + \left(\frac{\partial \omega_n}{\partial I}\delta I\right)^2 + \left(\frac{\partial \omega_n}{\partial m}\delta m\right)^2} \tag{5.6}$$

Before using Equation (5.6) to calculate $\delta\omega_n$, the uncertainties in the mass and moment of inertia must be calculated using uncertainty propagation analysis. Using the density of the structure, the mass can be written as:

$$m = \rho b t L \tag{5.7}$$

where b is the width and t is the thickness. Applying the Kline and McClintock method, the uncertainty in the mass is:

$$\delta m = \sqrt{\left(\frac{\partial m}{\partial L}\delta L\right)^2 + \left(\frac{\partial m}{\partial t}\delta t\right)^2 + \left(\frac{\partial m}{\partial b}\delta b\right)^2} \tag{5.8}$$

Or,

$$\delta m = \sqrt{(bt\delta L)^2 + (bL\delta t)^2 + (tL\delta b)^2} \tag{5.9}$$

For a rectangular cross-section, the moment of inertia is:

$$I = \frac{1}{12} b t^3 \tag{5.10}$$

Therefore, the uncertainty in I due to the measurement of the dimensions is:

$$\delta I = \sqrt{\left(\frac{\partial I}{\partial b}\delta b\right)^2 + \left(\frac{\partial I}{\partial t}\delta t\right)^2} \tag{5.11}$$

Or,

$$\delta I = \frac{1}{12}\sqrt{(t^3\delta b)^2 + (3bt^2\delta t)^2} \tag{5.12}$$

The uncertainty in each modal frequency due to the uncertainty in measuring the dimensions of the structure was calculated using Equations (5.6)-(5.12). The total uncertainty in the frequencies measured is the sum of the uncertainty from measuring the dimensions and the uncertainty due to the accelerometer. The uncertainty due to measuring the dimensions depends on the measured frequency itself, therefore the uncertainty must be calculated for each frequency measured. For each peak frequency, there was only a slight change in the measured value as the air speed was increased, and thus only a slight change in the uncertainty associated with that peak frequency. For brevity, Tables 5.6-5.8 list the range of uncertainties (corresponding to the range of air speeds) for each peak frequency, and the individual uncertainties for each measurement are tabulated in Appendix C. Table 5.6 shows the uncertainties for the peak frequencies in Sample 1.

Table 5.6: Uncertainty in Measured Frequencies for Sample 1.

Peak	Measured Frequency (Hz)	Uncertainty (Hz)
1	17.6-18.3	1.21
2	53.0-55.3	2.12-2.13

Table 5.6 shows that for the first peak frequency in Sample 1, the uncertainty is 1.91 Hz, which is about 10% of the measured value. For the second peak frequency in Sample 1, the uncertainty is 2.13 Hz, which is less than 4% of the measured value for each trial. The uncertainties for Sample 2 are shown in Table 5.7.

Table 5.7: Uncertainty in Measured Frequencies for Sample 2.

Peak	Measured frequency (Hz)	Uncertainty (Hz)
1	19.7-20.0	0.884-0.885
2	59.3-59.7	1.59-1.60
3	98.7-99.7	2.29

Table 5.7 shows that uncertainties in the first, second, and third frequencies of Sample 2 are no more than 0.884, 1.60, and 2.29 Hz, respectively. The challenge in determining the uncertainties for Sample 3 is that the frequencies did not correspond to those predicted by Euler-Bernoulli beam theory. To provide a rough estimate, the same uncertainty analysis used for Samples 1 and 2 was used and the frequencies were treated as Euler-Bernoulli bending frequencies starting with the second mode. The uncertainties for Sample 3 are

shown in Table 5.8.

Table 5.8: Uncertainty in Measured Frequencies for Sample 3.

Peak	Measured Frequency (Hz)	Uncertainty (Hz)
1	17.3-18.3	0.813-0.817
2	52.0-55.3	1.46-1.47
3	86.3-92.3	2.10-2.12
4	103.6-111	2.65-2.68
5	121-129	3.72-3.76
6	138.3-147.7	4.29-4.33

For the Sample 3 uncertainties shown in Table 5.8, the uncertainty ranges from 0.813 Hz to 4.33 Hz for the highest and lowest frequencies, respectively. While the uncertainty in these experiments is noticeable, as high as 10% for some frequencies, it does not undermine the observations made about LCO in axial flow. That is, that increasing the air speed beyond the flutter speed shifts the existing frequencies slightly upward as seen in Samples 1 and 2 and does not excite higher frequency modes.

5.2.3 Limit cycle oscillation: Image processing

While the modal experiments reveal important information about the structure undergoing LCO, i.e. how the frequencies present in the motion change with increasing air speed, they provide no details about the amplitude of the structure's motion. The experiments presented in this section use a high-speed camera to observe the LCO of the structure at and above the

flutter speed. Using image processing techniques with the camera footage, the structure's displacement as a function of time was obtained while it was undergoing LCO. This allows further analysis of how the amplitude changes with increasing air speed. The high-speed camera used is a Fastec-IL4 model equipped with a Nikon Micro-Nikkor 55mm F/2.8 lens. It provides 1280 x 1024 resolution for frame rates up to 510 frames per second (fps) and is capable of frame rates up to 60,000 fps at reduced resolutions. The shutter speed is also variable, but must be low enough to avoid blurring the image of the moving structure. Table 5.9 lists the camera settings used for the three configurations tested in these experiments.

Table 5.9: High-Speed Camera Record and Display Settings.

Setting	Value
Frame Rate (fps)	1022
Resolution	950×650
Shutter speed (μs)	443
Record Time (s)	13.5
Brightness	-7
Contrast	28

Because the highest frequency present in the structure's motion is on the order of 100 Hz, the shutter speed required to capture a clear image was fairly high. Because the images for higher shutter speeds are dark under room lighting, an auxiliary halogen light source was used to illuminate the test section. Figure 10 shows the wind tunnel with the camera mounted from above, along with the halogen light source.

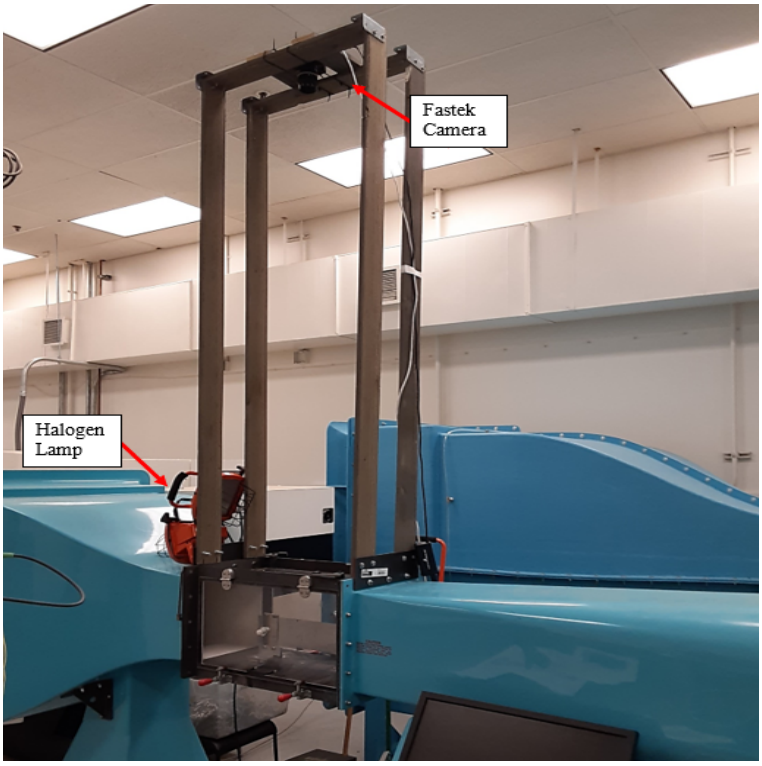

Figure 5.10: Wind tunnel with halogen lamps and camera mounting structure.

The three configurations tested are the same ones used in the accelerometer experiments, as shown in Table 5.10.

Table 5.10: Parameters and Measured Flutter Speed for Three configurations.

	Sample 1	Sample 2	Sample 3
Material	2024-T3 Aluminum	PETG	ABS
Young's Modulus (GPa)	73.1	2.83	2.10
Length (cm)	30.5	20.32	20.32
Width (cm)	10.2	10.2	10.2
Thickness (cm)	0.000381	0.075	0.05
Flutter Speed (m/s)	38.3	28.0	15.5

Observations about the LCO of the structure can be made by visually inspecting the footage, without any image processing. Due to the high shutter speed required to obtain images without blurring, playback of the camera footage is visibly dark. It should be emphasized that this has no effect on the image processing program. Figures 5.11 - 5.13 show still frames of each sample undergoing LCO, where the original image is on the left, and the image on the right side of each figure has been enhanced to make the shape of the structure more visible.

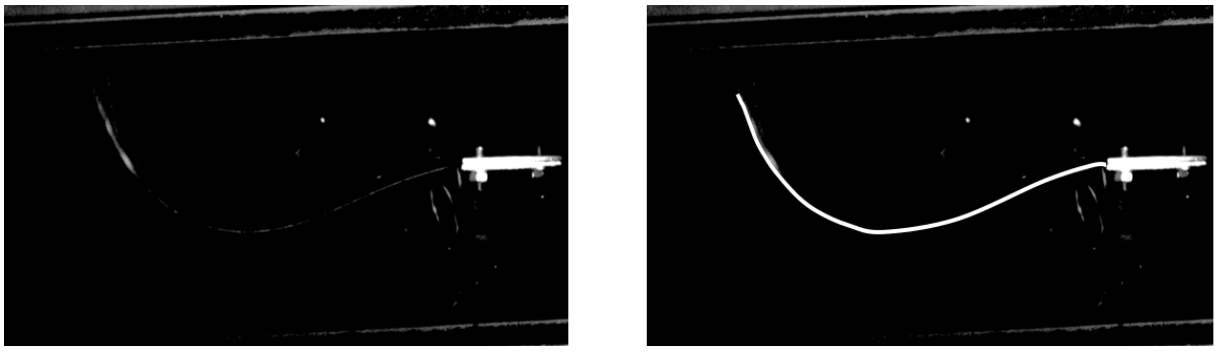

Figure 5.11: Image of Sample 1 in LCO at the Flutter Speed. Original (left) and enhanced for visibility (right).

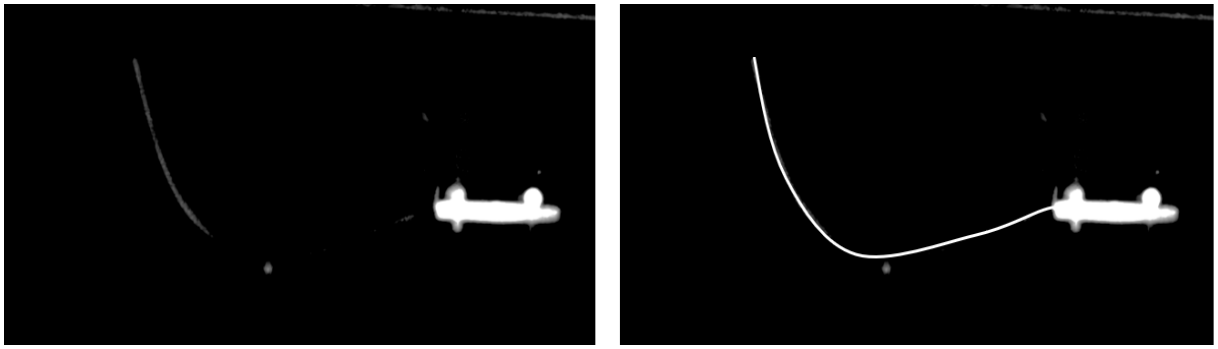

Figure 5.12: Image of Sample 2 in LCO at the Flutter Speed. Original (left) and enhanced for visibility (right).

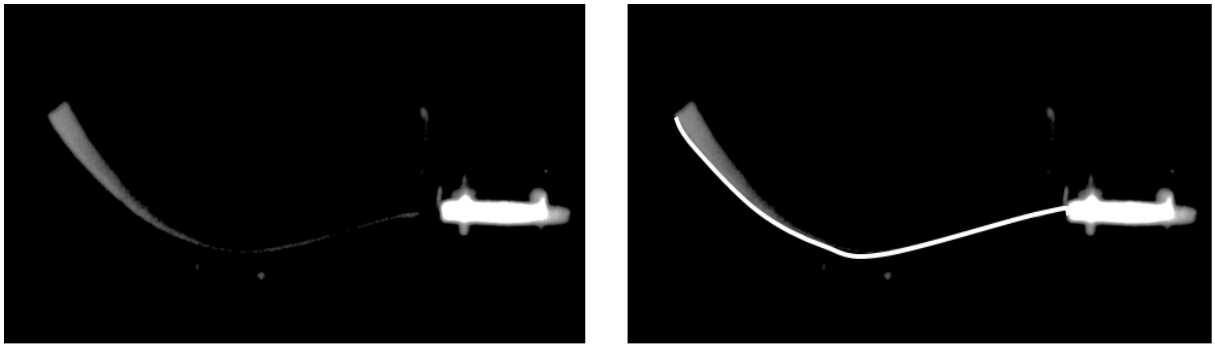

Figure 5.13: Image of Sample 3 in LCO at the Flutter Speed. Original (left) and enhanced for visibility (right).

The still images in Figures 5.11 and 5.12 corresponding to Samples 1 and 2, respectively, show nearly pure bending motion in the structure. However, Figure 5.13 indicates that there is torsion in Sample 3. This can be attributed to a non-uniform air stream, due to the clamp, and possible nonlinear effects in the structure considering it was the most flexible beam.

The image processing technique used to determine the structure's displacement as a function of time is based on tracking the position of a pixel corresponding to a point on the structure for each frame. The image processing program, written in MATLAB, starts by converting a grayscale frame to a binary image – where white is assigned to all pixels on the structure and black is assigned to pixels off the structure. This is done by evaluating the grayscale value for each pixel, which varies from 0 for black and 255 for white, and determining whether it is above or below a specified threshold. The threshold used in these experiments comes from a long-standing method of binarization known as Otsu's method. For this method, all possible thresholds are iterated through and data is collected for the number and intensity of pixels that fall above or below each threshold. The final threshold value is the one that has the lowest variance above and below that threshold.

For these experiments, a pixel located at the midpoint of the beam's length was tracked during LCO for a duration of 4.85 seconds. For each sample, this experiment was performed at the flutter speed, and for five speeds above the flutter speed. Figure 5.14 shows the midpoint displacement versus time for Sample 1 at the flutter speed, between 0 and 0.5 seconds.

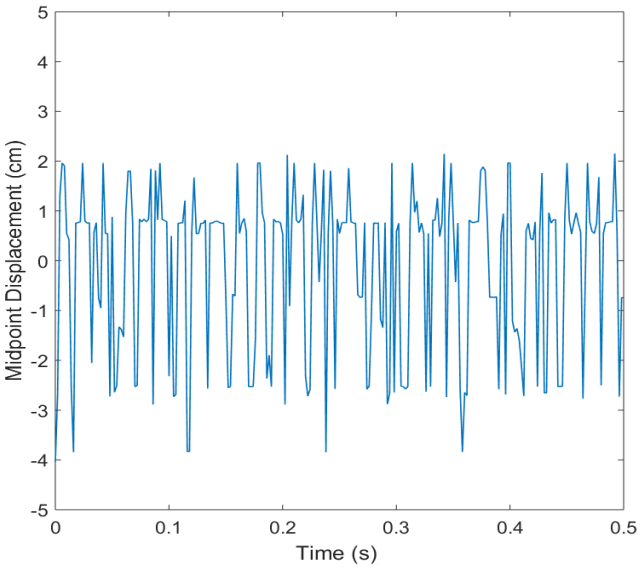

Figure 5.14: Midpoint displacement versus time for Sample 1 at the flutter speed.

For each case, the maximum displacement of the midpoint was obtained from the image processing results. Because the distance from zero is offset in the image processing output, the maximum displacement is defined as the maximum displacement from the mean. Table 5.11 shows the maximum midpoint displacements for Sample 1 at the flutter speed and for five air speeds above the flutter speed. Table 5.11 shows that as air speed increases there is an increase in the maximum displacement.

Table 5.11: Maximum Midpoint Displacement for Sample 1 at Six Air Speeds.

Air Speed (m/s)	Maximum Midpoint Displacement (cm)
38.3	4.80
39.1	4.93
39.8	5.03
40.6	5.08
41.4	5.11
42.2	5.66

These experiments were repeated for Samples 2 and 3 to see if there is a greater effect on structures of lower Young's Modulus. Figure 5.15 shows the maximum midpoint displacement for Sample 2 at the flutter speed for 0.5 seconds duration.

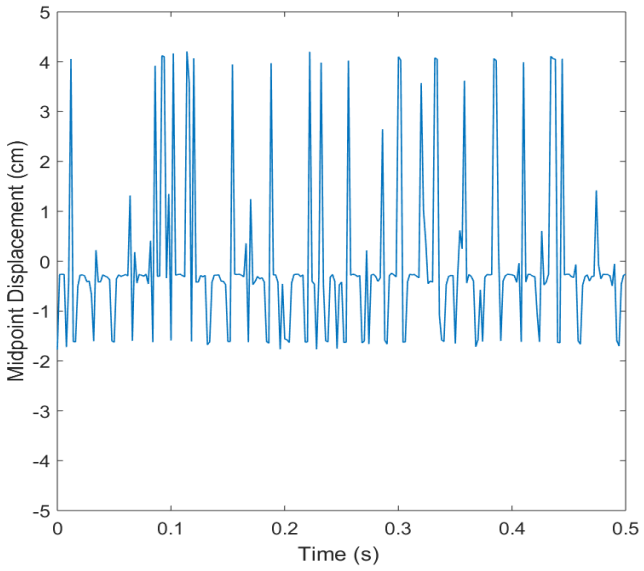

Figure 5.15: Midpoint displacement versus time for Sample 2 at the flutter speed.

For Sample 2, on the 5^{th} trial, with an air speed of 32.0 m/s, the structure failed in the form of a large crack near the clamped end. This air speed was higher than the speeds reached in the modal analysis experiments, but it is also reasonable to believe fatigue played a role in its failure. Midpoint displacement data for Sample 2 was recorded at four air speeds, as shown in Table 5.12.

Table 5.12: Maximum Midpoint Displacement for Sample 2 at Four Air Speeds.

Air Speed (m/s)	Maximum Midpoint Displacement (cm)
28.8	2.72
29.6	2.72
30.4	2.67
31.2	2.77

With the exception of the third point, the data in Table 5.12 shows that Sample 2 experiences a slight increase in maximum displacement when air speed is increased past the flutter speed. Figure 5.16 shows the midpoint displacement as a function of time for Sample 2 at the flutter speed.

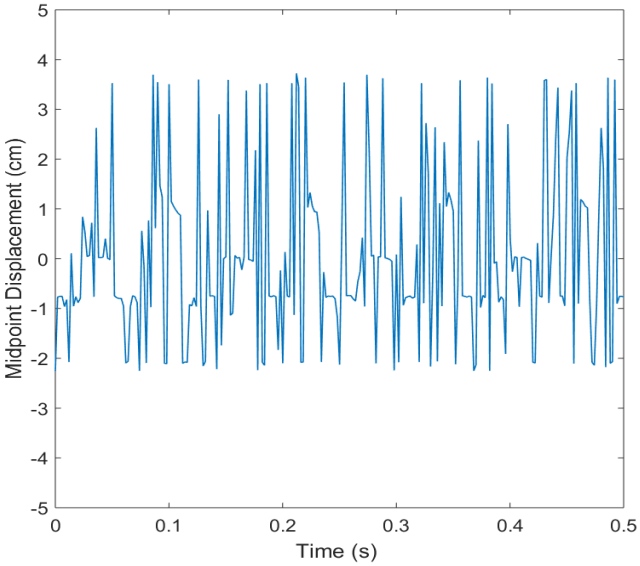

Figure 5.16: Midpoint displacement versus time for Sample 3 at the flutter speed.

The maximum displacements for Sample 3, the sample with the lowest stiffness, are shown in Table 5.13.

Table 5.13: Maximum Midpoint Displacement for Sample 3 at Six Air Speeds.

Air Speed (m/s)	Maximum Midpoint Displacement (cm)
15.5	2.40
16.2	2.46
17	2.72
17.8	3.00
18.6	3.02
19.4	3.07

Sample 3 follows the same trend as Samples 1 and 2: the maximum midpoint displacement increases as the air speed is increased beyond the flutter speed. For Sample 3, a 20.1 % increase in air speed resulted in a 22.0 % increase in maximum midpoint displacement. This shows that air speed has a more significant impact on the amplitude of the LCO than it does on the modal frequencies.

5.3 Scaling and data

In this section, the governing equation for bending displacement from the linear structure model is scaled so that the experimental results can be shown in terms of nondimensional parameters. The governing equation, where the aerodynamic loading is in terms of the Kussner doublet function, is:

$$EI\frac{\partial^4 h\left(t,y\right)}{\partial y^4}+m\frac{\partial^2 h\left(t,y\right)}{\partial t^2}=-\rho U\int_{-b}^{b}A\left(t,y,U\right)dx \tag{5.13}$$

In Equation (5.13) m is the mass of the beam per unit length, b is the half-width of the beam, and ρ is the density of the fluid. The linearized Kussner doublet function is:

$$A\left(t,y,U\right)=-\frac{1}{U}\delta\left(\frac{\partial\phi}{\partial t}\right)-\delta\left(\frac{\partial\phi}{\partial y}\right) \tag{5.14}$$

Equation (5.13) becomes:

$$EI\frac{\partial^4 h\left(t,y\right)}{\partial y^4}+m\frac{\partial^2 h\left(t,y\right)}{\partial t^2}=-\rho U\int_{-b}^{b}\left[-\frac{1}{U}\delta\left(\frac{\partial\phi}{\partial t}\right)-\delta\left(\frac{\partial\phi}{\partial y}\right)\right]dx \tag{5.15}$$

To scale the equation, define the dimensionless variables:

$$y^*=\frac{y}{L} \tag{5.16}$$

and

$$h^* = \frac{h}{L} \tag{5.17}$$

where L is the length of the beam. The nondimensional velocity is defined by:

$$U^* = \frac{U}{U_{ch}} \tag{5.18}$$

where U_{ch} is the characteristic velocity defined as:

$$U_{ch} = \frac{L}{t_{ch}} \tag{5.19}$$

and t_{ch} is a characteristic time. The nondimensional velocity potential is:

$$\phi^* = \frac{\phi}{U_{ch}L} \tag{5.20}$$

Scaling t with the characteristic time, t_{ch}, and substituting the nondimensional variables, Equation (5.13) becomes:

$$\frac{\partial^4 h^*\left(t^*, y^*\right)}{\partial y^{*4}} + \frac{mL^4}{EIt_{ch}^2}\frac{\partial^2 h^*\left(t^*, y^*\right)}{\partial t^{*2}} = -\frac{2\rho b L^4}{EIt_{ch}} U_{ch} U^* \int_{-b^*}^{b^*} A^* dx^* \tag{5.21}$$

Or,

$$\frac{\partial^4 h^*\left(t^*, y^*\right)}{\partial y^{*4}} + C\frac{\partial^2 h^*\left(t^*, y^*\right)}{\partial t^{*2}} = -BU^* \int_{-b^*}^{b^*} A^* dx^* \tag{5.22}$$

where

$$C = \frac{mL^4}{EIt_{ch}^2} \tag{5.23}$$

and

$$B = \frac{2\rho bL^4}{EIt_{ch}} U_{ch} \tag{5.24}$$

The characteristic time is determined by setting $B = 1$:

$$\frac{2\rho bL^4}{EIt_{ch}} \frac{l}{t_{ch}} = 1 \tag{5.25}$$

Thus,

$$t_{ch} = \sqrt{\frac{2b\rho L^5}{EI}} \tag{5.26}$$

The characteristic velocity becomes:

$$U_{ch} = \sqrt{\frac{EI}{2b\rho L^3}} \tag{5.27}$$

and the dimensionless velocity is:

$$U^* = U\sqrt{\frac{2b\rho L^3}{EI}} \tag{5.28}$$

For a rectangular cross-section, I is given by:

$$I = \frac{1}{12}bd^3 \tag{5.29}$$

where d is the thickness of the beam. Using Equation (5.29), U^* can be written as:

$$U^* = U\sqrt{\frac{24\rho L^3}{Ed^3}} \tag{5.30}$$

Table 5.14 shows the dimensional velocity, U, and the nondimensional velocity, U^*, for the measured values for each case.

Table 5.14: Dimensional and Nondimensional Flutter Speed.

	U (m/s)	U^*
2024-T3 Aluminum	38.3	17.6
PETG Plastic	28.0	12.8
ABS Plastic	15.5	15.1

The U^*, through its definition, is taken to be a universal constant. The variation in U^* between the aluminum and plastic cases can be attributed to the variation in the material properties of the plastics. The flutter speed in terms of U^* can be written as:

$$U = U^* \sqrt{\frac{Ed^3}{24\rho L^3}} \tag{5.31}$$

Using the U^* from the aluminum case, where the material properties are well defined, an expression for the flutter speed is:

$$U = 3.59 \sqrt{\frac{Ed^3}{\rho L^3}} \tag{5.32}$$

The expression in Equation (5.29) is a function of the structural properties, dimensions, and the density of air only. Therefore, this simple expression can be used to estimate the flutter speed for any structure provided the material properties are well known. The dimensionless frequency is defined by:

$$\omega^* = \frac{\omega}{\omega_{ch}} \tag{5.33}$$

The characteristic frequency is defined using the characteristic time:

$$\omega_{ch} = \frac{1}{t_{ch}} \tag{5.34}$$

The dimensionless frequency is:

$$\omega^* = \frac{\omega}{t_{ch}} \tag{5.35}$$

Using Equation (5.26), ω^* becomes:

$$\omega^* = \omega\sqrt{\frac{EI}{2b\rho L^5}} \tag{5.36}$$

Or, using the expression for I:

$$\omega^* = \omega\sqrt{\frac{Ed^3}{24\rho L^5}} \tag{5.37}$$

The dimensionless frequencies were calculated for each case as a function of air speed, beginning with the flutter speed. Table 5.15 shows the dimensional and nondimensional frequencies for the 2024-T3 aluminum case.

Table 5.15: Dimensional and Nondimensional Frequencies for 2024-T3 Aluminum.

U (m/s)	U^*	ω (rad/s)	ω^*
36.7	16.9	333	2374
37.5	17.2	335	2388
38.3	17.6	339	2419
39.0	17.9	341	2433
39.8	18.3	345	2464
40.6	18.7	347	2477

Treating ω^* as a constant, an expression for the dominant frequency at the flutter speed can be constructed. From Equation (5.37), ω can be written as:

$$\omega = \omega^* \sqrt{\frac{24\rho L^5}{Ed^3}} \tag{5.38}$$

Using the value of ω^* from the aluminum case, the expression for ω becomes:

$$\omega = 11,600 \sqrt{\frac{\rho L^5}{Ed^3}} \tag{5.39}$$

Equation (5.39) provides an expression to estimate the dominant frequency in LCO at the flutter speed. Figure 5.17 shows a plot of the dimensionless frequency versus air speed for 2024-T3 aluminum.

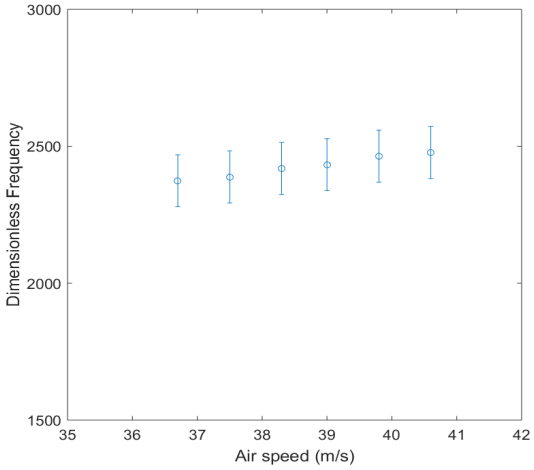

Figure 5.17: Dimensionless frequency versus air speed for 2024-T3 aluminum.

In Figure 5.17, there is a linear relation between ω^* and U with an R^2 value of 0.987, and the slope of the line from the curve fit is 27.9 s/m. This information can be used to construct a relation between the dominant frequency as a function of air speed. Because ω^* varies linearly with U:

$$\omega^* = \omega_F^* + 27.9\,(U - U_f) \tag{5.40}$$

The ω_F^* is the ω^* at the flutter speed as determined in Equation (5.39). Combining Equations (5.40) and (5.38), the frequency as a function of U can be written as:

$$\omega\,(U) = \sqrt{\frac{24\rho L^5}{Ed^3}}\,[\omega_F^* + 27.9\,(U - U_f)] \tag{5.41}$$

where U is in m/s. Or, using ω^* from Equation (5.39) and the expression for U_f from

Equation (5.30):

$$\omega\left(U\right)=\sqrt{\frac{\rho L^{5}}{Ed^{3}}}\left[11,600+137\left(U-3.45\sqrt{\frac{Ed^{3}}{\rho L^{3}}}\right)\right] \tag{5.42}$$

In Equation (5.42), U is in m/s and $\omega\left(U\right)$ is in rad/s, and the value of U^{*} used in Equation (5.10) is the one from Table 5.15 at the flutter speed. It is important to note that the expressions developed for ω in Equations (5.39) and (5.42) are based on data where an accelerometer was attached to the beam, and are therefore only intended to be approximate. Table 5.16 shows the dimensional and nondimensional frequencies for the PETG plastic case.

Table 5.16: Dimensional and Nondimensional Frequencies for PETG Plastic.

U (m/s)	U^{*}	ω (rad/s)	ω^{*}
25.9	11.8	373	4026
26.7	12.2	373	4026
27.5	12.5	373	4026
28.3	12.9	375	4049
29.1	13.3	375	4049
29.8	13.6	375	4049

Figure 5.17 shows a plot of the dimensionless frequency versus air speed for PETG plastic.

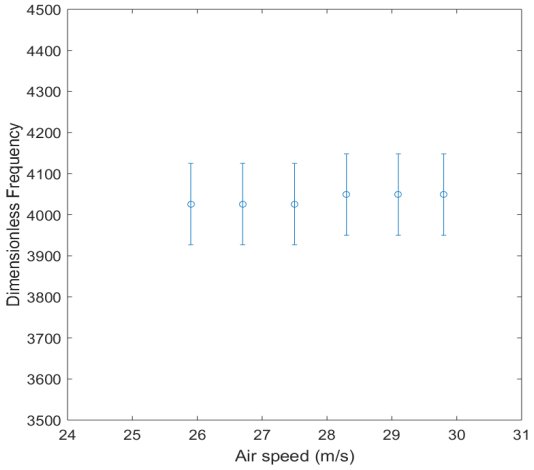

Figure 5.18: Dimensionless frequency versus air speed for PETG plastic.

In Figure 5.18 the dimensioness frequency is roughly constant with increasing air speed, which is consistent with the measured dimensional values. The dimensional and nondimensional frequencies for the ABS plastic case are shown in Table 5.17.

Table 5.17: Dimensional and Nondimensional Frequencies for ABS Plastic.

U (m/s)	U^*	ω (rad/s)	ω^*
17.3	16.8	327	1654
18	17.5	328	1664
18.8	18.2	333	1686
19.6	19.0	337	1708
20.4	19.8	344	1740
21.2	20.6	347	1759

Figure 5.19 shows a plot of the dimensionless frequency versus air speed for ABS plastic.

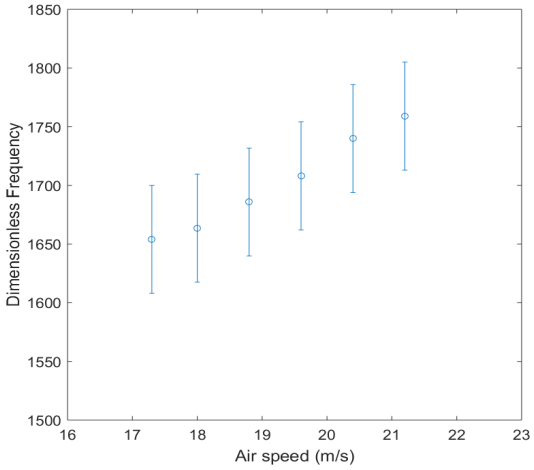

Figure 5.19: Dimensionless frequency versus air speed for ABS plastic.

In Figure 5.19, there is a linear relation between ω^* and U with an R^2 value of 0.987.

6 Discussion of results

6.1 Flutter speed

To evaluate the accuracy of the models and solution methods developed in the previous chapters, flutter speed calculations for a rectangular, beam-like structure are compared to experimental measurements. For the three configurations tested, the flutter speed was measured in a subsonic wind tunnel using the instrumentation and techniques described in Chapter 5. The uncertainty in the measured flutter speed was found to be 4.93 m/s.

The configuration used to evaluate the accuracy of the flutter speed predictions is the 2024-T3 aluminum beam, where aluminum was chosen as the material because the properties are well defined. The dimensions of the structure were chosen so that it was rigid when exposed to low speed air flow, but flexible enough so that the flutter speed can be measured in a subsonic wind tunnel. The flutter speed measurement was 38.3 ± 4.93 m/s. It is important to note that in the wind tunnel experiments, the structure was mounted to a clamp which can introduce additional flow disturbances not accounted for in the modeling. In the modeling, the flow is assumed to approach the leading edge of the structure with uniform velocity without being disturbed by any objects upstream. The additional disturbances in the air flow due to the experimental apparatus would result in a flutter speed lower than that if no disturbances were present.

First, flutter speed calculations were performed using the Balakrishnan Continuum Theory (BCT) as originally developed. For the 2024-T3 aluminum configuration, the flutter

speed obtained from the BCT was 20.3 m/s which corresponds to an underprediction of 39 % from the measured value. This prediction contains numerical error, for example from using numerical integration methods on definite integrals that cannot be evaluated analytically. More importantly, as with any mathematical modeling effort, inaccuracy is a result of simplifying assumptions.

The semi-continuum approach, which uses the fluid side solution from the BCT, along with a Galerkin method for the structure side, produced a significant improvement in the flutter speed prediction. Results for two cases using the semi-continuum approach were presented in Chapter 4: one where both the fluid and structure dynamics are modeled as linear, and the other where a nonlinear structure model is used alongside the linear fluid model. In the fully linear case the flutter speed was 50.4 m/s, which overpredicts the experimental value by 16.4%, as compared to the lower bound on the measurement. The overprediction is expected for two reasons. The first is due to the fact that the model does not account for upstream disturbances in the air flow from the experimental apparatus. An overprediction is also expected from using an Euler-Bernoulii beam model, where the result is a beam stiffer than that of other models such as the Timoshenko beam.

The semi-continuum method using the nonlinear structure model predicted a flutter speed of 48.7 m/s, which is within 11.1 % of the measured value. In this model, three modes of motion (two bending, one torsional) were coupled and the simplifying were therefore not as restrictive as the linear case. Even though two additional modes of motion were allowed, the change in the predicted flutter speed was less than 4 %. This is due to the primary mode of

bending motion being the most dominant in axial flow. In both cases (linear and nonlinear structure dynamics), the semi-continuum models are subject to numerical error.

While the semi-continuum models have been validated using the 2024 aluminum benchmark case, they were tested for two additional configurations. These samples were made of PETG and ABS plastic where the Young's modulus for each was much smaller than that of 2024-T3 aluminum. However, it is important to note that the properties for these materials are reported in ranges; in this work the average values were taken from literature. For the PETG case the flutter speed obtained from experiment was 28.0 $\pm$ 4.93 m/s. The calculated flutter speed from the BCT for this case was 32.4 m/s, which is with the range of uncertainty of the measured value. The fully linear semi-continuum model predicted a flutter speed of 30.4 m/s and the nonlinear model predicted 22.6 m/s, both of which are within the uncertainty associated with the measurement. The measured flutter speed for the ABS plastic beam was 15.5 $\pm$ 4.93 m/s. For this case, the calculated flutter speed from the BCT is 23.1 m/s, which is within 13.1 % of experimental data. The linear and nonlinear semi-continuum predicted flutter speeds of 20.6 m/s and 8.5 m/s, respectively. The linear value is within 1% of the experimental value and the nonlinear value is lower by 19.3%. An interesting observation is that in the plastic cases, which have a Young's modulus one order of magnitude smaller than aluminum, there is considerable difference between the linear and nonlinear flutter speed predictions.

6.2 Limit cycle oscillation

The objective of the first set of LCO experiments was to determine how, if at all, the frequencies of the oscillations change as the air speed is brought higher than the flutter speed. For all three configurations, it was observed that the frequencies present in the LCO at the flutter speed remained as the air speed was increased, and no higher or lower modes were excited. For the aluminum and ABS samples, there was a noticeable increase in the modal frequencies as the air speed was increased. For the aluminum case, the frequencies shifted by about 4 % as the air speed was increased to 7.9 % above the flutter speed. The ABS sample, which showed 6 frequencies in the FFT's performed on the accelerometer data, showed similar behavior. The existing peaks shifted to the right on the FFT by as much as 6.8 % for a 22.5% increase in air speed above the flutter speed. In Sample 2, the PETG plastic, the maximum increase in the modal frequency was 1.5 % for an increase in air speed of 15.1 % above the flutter speed. Although the PETG sample had a much smaller Young's modulus than the aluminum sample, the natural frequencies according to Euler-Bernoulli beam theory were higher than the other two samples.

The experiments with the high speed camera were conducted with the same goals in mind, where one key advantage was that no accelerometer was required. This results in a less intrusive experimental apparatus, because the accelerometer acts adds a point mass added to the structure. These experiments were also used to observe the shape of the structure while it was undergoing LCO. The images from these experiments show that the calculated eigenfunctions from Chapter 4 resemble the shape of the bending motion in LCO fairly well.

Using image processing techniques, the displacement of the midpoint of the structure versus time was determined. While the resulting time domain data did not produce a signal clean enough to create a meaningful FFT, it was used to observe the effect of increasing air speed on the LCO amplitude. It was found that increasing the air speed past the flutter speed had a substantial impact on the amplitude of the structure's motion. In the most flexible sample, the ABS plastic, the maximum midpoint displacement in the oscillation increased by 26.6 % for a 25.1 % increase in air speed. In the 2024-T3 aluminum case, the maximum displacement of the structure's midpoint increased by 18.0 % for a 10.1 % increase in air speed. As was the case in the modal analysis experiments, the PETG plastic sample was least affected. For an 8.3% increase in air speed, the increase in midpoint amplitude was 1.87%.

6.3 Scaling

In Chapter 5 the linear governing equation for bending was scaled and written in terms of nondimensional variables. This produced a nondimensional air speed, U^*, and a nondimensional frequency, ω^*, which were used to present the data as dimensionless values. Using the value of U^* obtained from the flutter speed measurement for 2024-T3 aluminum, an expression to estimate the flutter speed was developed. Here, U^* is taken as a universal constant which is independent of geometry and material properties, and can therefore be used to estimate the flutter speed for any configuration. While it is only meant to be an approximation, due to its incredible simplicity a result can be obtained very quickly.

The dimensionless frequency, ω^*, was calculated and plotted for versus air speed for each configuration. For the PETG plastic case, which had the highest bending stiffness, the dimensionless frequency was roughly constant with increasing air speed. This is consistent with the measured dimensional values. For the aluminum and ABS cases, it was determined that there is a linear relation between the dimensionless frequency and air speed. The R^2 on the linear curve fit was 0.987 for both cases. An expression for the frequency as a function of air speeds higher than the flutter speed, $\omega\,(U)$, was constructed using the ω^* and U^* determined from experiment. Here, it is only meant to be an approximation because the modal analysis experiments were performed on a beam with an accelerometer near the clamped end. However, the methods used to obtain this result open the door to future work.

7 Conclusions

In the most general sense, the goal of this dissertation was to connect the beauty of a mathematically rich aeroelasticity theory to the practicality of engineering calculation. One of these cannot survive without the other, and the Balakrishnan Continuum Theory (BCT) does not disappoint in providing the former. As with many mathematical modeling efforts, simplifying assumptions are made throughout the development at the expense of accuracy. This is often justified by the reduction in computational time by arriving at a simpler set of equations to solve. This is true for the BCT, where there is no costly finite element method required to obtain a result. Furthermore, the mathematics developed by the BCT were used to arrive at two physical hypotheses about aeroelasticity in axial flow. The first is that torsional motion is unconditionally stable, and the second is that the divergence speed is undefined. In this work the former could not be verified or disproven experimentally; torsional motion was observed in one experiment and not in others.

Instead of pursuing more mathematical detail within the framework of the BCT or attempting to draw physical conclusions from it, the aim of this research was to put the BCT to use for engineering purposes. The first step to doing this was to modify the stability technique so that all functions in the BCT are defined. Another task associated with implementing the BCT was to condition singular integrals so they could be evaluated using numerical integration methods. These modifications and methods were applied to the BCT, without altering the mathematics of the BCT itself, to obtain flutter speed predictions. It was found that much improvement could be made to the accuracy of the BCT predictions. The path chosen

to accomplishing this was to stray from the purely continuum mathematics, and introduce solution methods more commonly used in engineering practice.

When studying the BCT, it is immediately clear that the difficulty lies in solving the fluid side of the problem. Once this is done, in the form of a solution for the aerodynamic loading on the structure, the remaining work is much more straightforward. To avoid finite difference or series approximations, the BCT proceeds to solve the structure side of the problem by eliminating the dependence of the aerodynamic loading on the structural displacements. This is done by forming a Nuemann expansion and keeping only the first term, after which the linear differential for the bending displacement can be solved analytically. This simplification can be avoided by using a Galerkin method to solve the governing equation for the structure, while preserving the continuum solution for the fluid. In this work, this is referred to as the semi-continuum approach; it uses a continuum solution for part of the problem and a non-continuum solution for the other. Another advantage of this method is that it is not restricted to linear governing equations.

By comparing the flutter speed predictions obtained from the semi-continuum modeling to the BCT predictions and experiment, it was determined that the use of a semi-continuum method reduced the error by over a factor of two. This demonstrated that any error associated with a Galerkin method was outweighed by relieving simplifying assumptions made in the BCT. Because the semi-continuum approach sets up the system as an eigenvalue problem, and as a result produces eigenfuncitons, it can be further validated by comparing these eigenfunctions to experiment. It was found that the eigenfunctions calculated using

both linear and nonlinear structure models resembled the shape of the beam obtained from images taken by a high speed camera.

The BCT and semi-continuum methods are limited to cases where the structural displacements are very small, which is acceptable when the only quantity of interest is the flutter speed. In some applications (e.g. piezoelectric energy harvesting) the bounded motion of the structure after the flutter speed is reached, known as Limit Cycle Oscillation (LCO), can be of great importance. The modeling tools described thus far fall short in describing such motion. LCO was analyzed by experiment to determine how air speeds above the flutter speed affect the frequencies and amplitude of the oscillations. The modal analysis experiments showed that higher air speeds did not excite additional frequencies in the structure, but shifted the existing frequencies slightly higher. The experiments to determine the amplitude changes as a function of air speed used a high speed camera and image processing techniques to measure the structural displacement as a function of time. The measurements showed that substantial increases in amplitude can occur with increasing air speed.

As part of the experimental work, a scaling analysis was performed on the governing equation for bending motion to obtain a set of dimensionless parameters. This analysis was used to present the experimental results in a more useful form, and the nondimensional parameters were used to produce expressions for the flutter speed and the dominant LCO frequency as a function of air speed. While these expressions are approximate, their simplicity allows for obtaining a very rapid result. There is great deal of future work that can be done

A Numerical methods

A.1 Composite Simpson's Rule.

The formula for the Composite Simpson's Rule is:

$$\int_a^b f(x)\,dx \cong \frac{h}{3}\sum_{j=1}^{\frac{N}{2}}\left[f\left(x_{2j-2}\right)+4f\left(x_{2j-1}\right)+f\left(x_{2j}\right)\right] \tag{A.1}$$

Where N is the number of points used in the approximation, which must be an even number, and h is:

$$h = \frac{b-a}{N} \tag{A.2}$$

A.2 Newton Raphson method for a system of equations

The Newton-Raphson method for a 2×2 system of equations is as follows. For a system represented by:

$$f_1(x_1, x_2) = 0 \tag{A.3}$$

$$f_2(x_1, x_2) = 0 \tag{A.4}$$

Define the vectors:

$$\vec{x} = \begin{bmatrix} x_1 \\ \\ x_2 \end{bmatrix} \tag{A.5}$$

And

$$\vec{f}\left(\vec{x}\right) = \begin{bmatrix} f_1(x_1, x_2) \\ \\ f_2(x_1, x_2) \end{bmatrix} \tag{A.6}$$

For a system of equations the Jacobian, $\bar{\bar{J}}\left(\vec{x}\right)$, is defined by:

$$\bar{\bar{J}}\left(\vec{x}\right) = \begin{bmatrix} \frac{\partial f_1}{\partial x_1} & \frac{\partial f_1}{\partial x_2} \\ \\ \frac{\partial f_2}{\partial x_1} & \frac{\partial f_2}{\partial x_2} \end{bmatrix}$$

The updated roots $\vec{x}^{k+1}$ are given by:

$$\vec{x}^{k+1} = \vec{x}^{k} - \bar{\bar{J}}^{-1}\left(\vec{x}^{k}\right)\vec{f}\left(\vec{x}^{k}\right) \tag{A.7}$$

Where $\bar{\bar{J}}^{-1}\left(\vec{x}^{k}\right)$ is the inverse of $\bar{\bar{J}}\left(\vec{x}^{k}\right)$. If $\bar{\bar{J}}\left(\vec{x}\right)$ is a 2×2 matrix, its inverse is given by:

$$\bar{\bar{J}}^{-1}\left(\vec{x}\right) = \frac{1}{\frac{\partial f_1}{\partial x_1}\frac{\partial f_2}{\partial x_2} - \frac{\partial f_1}{\partial x_2}\frac{\partial f_2}{\partial x_1}} \begin{bmatrix} \frac{\partial f_2}{\partial x_2} & -\frac{\partial f_1}{\partial x_2} \\ -\frac{\partial f_2}{\partial x_1} & \frac{\partial f_1}{\partial x_1} \end{bmatrix} \tag{A.8}$$

The individual roots are given by:

$$\vec{x}_1^{k+1} = \vec{x}_1^{k} - \left[\frac{\partial f_1}{\partial x_1}\frac{\partial f_2}{\partial x_2} - \frac{\partial f_1}{\partial x_2}\frac{\partial f_2}{\partial x_1}\right]^{-1}\left[\frac{\partial f_2}{\partial x_2} f_1\left(x_1^k, x_2^k\right) - \frac{\partial f_1}{\partial x_2} f_2\left(x_1^k, x_2^k\right)\right] \tag{A.9}$$

And

$$\vec{x}_2^{k+1} = \vec{x}_2^{k} - \left[\frac{\partial f_1}{\partial x_1}\frac{\partial f_2}{\partial x_2} - \frac{\partial f_1}{\partial x_2}\frac{\partial f_2}{\partial x_1}\right]^{-1}\left[-\frac{\partial f_2}{\partial x_1} f_1\left(x_1^k, x_2^k\right) + \frac{\partial f_1}{\partial x_1} f_2\left(x_1^k, x_2^k\right)\right] \tag{A.10}$$

The roots are computed by iterating upon Equations (A.9) and (A.10) until sufficient convergence is obtained. Many times it is convenient to use a finite difference approximation for the derivatives in Equations (A.9) and (A.10). Using a two-point backward difference results in what is sometime's called the Secant method. These finite difference approximations are:

$$\frac{\partial f_1}{\partial x_1} = \frac{1}{\Delta x_1}\left[f_1\left(x_1, x_2\right) - f_1\left(x_1 - \Delta x_1, x_2\right)\right] \tag{A.11}$$

$$\frac{\partial f_1}{\partial x_2} = \frac{1}{\Delta x_2}\left[f_1\left(x_1, x_2\right) - f_1\left(x_1, x_2 - \Delta x_2\right)\right] \tag{A.12}$$

$$\frac{\partial f_2}{\partial x_1} = \frac{1}{\Delta x_1} \left[f_2 \left(x_1, x_2 \right) - f_2 \left(x_1 - \Delta x_1, x_2 \right) \right] \tag{A.13}$$

$$\frac{\partial f_2}{\partial x_2} = \frac{1}{\Delta x_2} \left[f_2 \left(x_1, x_2 \right) - f_2 \left(x_1, x_2 - \Delta x_2 \right) \right] \tag{A.14}$$

Where Δx_1 and Δx_2 are chosen to be sufficiently small.

A.3 Gaussian elimination

The following description closely resembles that found in Atkinson [1]. Consider the system of equations, at the step where the first row operation in forward elimination is to be performed:

$$A^{(1)}\vec{x} = \vec{b}^{(1)} \tag{A.15}$$

Where the following notation is used for the matrix $A^{(1)}$ and vector $\vec{b}^{(1)}$, , for an $n \times n$ system of equations.

$$A^{(1)} = \left[a_{ij}^{(1)}\right] \tag{A.16}$$

And

$$\vec{b}^{(1)} = \left[b_1^{(1)}, ..., b_n^{(1)}\right]^T \tag{A.17}$$

The elimination process starts by defining a row multiplier, for each row i :

$$m_{i1} = \frac{a_{i1}^{(1)}}{a_{11}^{(1)}} \tag{A.18}$$

For $i = 2, 3, \ldots, n$. The row multipliers are then used eliminate the elements below the diagonal in column 1 using the following operations:

$$a_{ij}^{(2)} = a_{ij}^{(1)} - m_{i1}a_{1j}^{(1)} \tag{A.19}$$

For $j = 2, 3, \ldots, n$. And:

$$b_{i}^{(2)} = b_{i}^{(1)} - m_{i1}b_{1}^{(1)} \tag{A.20}$$

For $i = 2, ..., n$. For an arbitrary step k , the row multiplier is:

$$m_{ik} = \frac{a_{i1}^{(k)}}{a_{11}^{(k)}} \tag{A.21}$$

For $i = k + 1, ..., n$. The corresponding row operations are:

$$a_{ij}^{(k+1)} = a_{ij}^{(k)} - m_{ik}a_{kj}^{(k)} \tag{A.22}$$

And

$$b_{i}^{(k+1)} = b_{i}^{(k)} - m_{ik}b_{k}^{(k)} \tag{A.23}$$

After n steps are performed, the forward elimination is complete and the solution for x_n is given by:

$$x_n = \frac{b_n^{(n)}}{a_{nn}^{(n)}} \tag{A.24}$$

The subsequent x_k , starting at row $k = n - 1$ are obtained using the expression:

$$x_k = \frac{1}{a_{kk}^{(n)}} \left[b_k^{(n)} - \sum_{j=k+1}^{n} a_{kj}^{(n)} x_j \right] \tag{A.25}$$

Where $k = n - 1, n - 2, \ldots, 1$. This concludes the Gaussian elimination method, but the intermediate steps provide a result that will be useful in calculating the determinant and eigenvectors. This result is the LU decomposition of the matrix A , where A is written as a product of a lower diagonal matrix L and an upper diagonal matrix U :

$$A = LU \tag{A.26}$$

After the forward elimination is completed in Gaussian elimination, the matrix $A^{(n)}$ has the form:

$$A^{(n)} = \begin{bmatrix} a_{11}^{(n)} & \ldots & \ldots & a_{1n}^{(n)} \\ 0 & \ddots & & \vdots \\ \vdots & & \ddots & \vdots \\ 0 & \ldots & 0 & a_{nn}^{(n)} \end{bmatrix} \tag{A.27}$$

The matrix in Equation (A.27) is indeed the upper diagonal matrix U . It can be shown

that the lower diagonal matrix consists of 1's on the diagonal and the row multipliers below the diagonal:

$$L = \begin{bmatrix} 1 & 0 & \dots & 0 \\ m_{21} & 1 & & \vdots \\ \vdots & & \ddots & 0 \\ m_{n1} & \dots & m_{n-1,n} & 1 \end{bmatrix} \tag{A.28}$$

Equations (A.27) and (A.28) complete the LU decomposition.

A.4 Determinant of a matrix

To calculate the determinant of the matrix A , the LU decomposition produced by Gaussian elimination can be used. Using the product rule for determinants, the determinant is:

$$\det(A) = \det(L)\det(U) \tag{A.29}$$

For an upper or lower diagonal matrix the determinant is equal to the product of the diagonal elements. Thus, $\det(L) = 1$, leading to:

$$\det(A) = \det(U) \tag{A.30}$$

Or,

$$\det(A) = \prod_{i=1}^{n} a_{ii}^{(n)} \tag{A.31}$$

A.5 Inverse of a matrix

The inverse of matrix A is calculated by performing the Gaussian elimination method n times. The matrix inverse A^{-1} can be obtained by solving the system:

$$AX = I \tag{A.32}$$

Where I is the identity matrix and the $n \times n$ x matrix solved for will be the inverse of A . Consider and written in terms of their columns:

$$X = \left[\vec{x}^{(1)}, ..., \vec{x}^{(n)}\right] \tag{A.33}$$

And

$$I = \left[\vec{e}^{(1)}, ..., \vec{e}^{(n)}\right] \tag{A.34}$$

The j^{th} column of the inverse, $\vec{x}^{(j)}$, is obtained by applying Gaussian elimination to the system:

$$A\vec{x}^{(j)} = \vec{e}^{(j)} \tag{A.35}$$

For $j = 1, \ldots, n$. The computational cost associated with computing the inverse is n times

that of the Gaussian elimination. For this reason inverting matrices is usually avoided, for example when all that is needed is the solution of a linear system.

A.6 Calculation of eigenvectors

The method used to calculate the eigenvectors is the inverse iteration method. For an eigenvalue λ_i of a matrix A , the eigenvector $\vec{x}_i$ is given by:

$$A\vec{x}_i = \lambda_i \vec{x}_i \tag{A.36}$$

The inverse iteration method begins with the LU decomposition:

$$A - \lambda I = LU \tag{A.37}$$

Combining Equations (A.36) and (A.37):

$$LU\vec{x}_i = \vec{x}_i \tag{A.38}$$

The method proceeds by using the vectors $\vec{z}^{(m)}$ and $\vec{w}^{(m+1)}$ at iteration m , defined by:

$$LU\vec{w}^{(m+1)} = \vec{z}^{(m)} \tag{A.39}$$

The inverse iteration method starts with an initial guess for the eigenvector, $\vec{z}^{(0)}$. Wilkinson [**Wilk**] recommends:

$$\vec{z}^{(0)} = L\vec{e} \tag{A.40}$$

Where

$$\vec{e} = [1, 1, ..., 1]^T \tag{A.41}$$

The updated eigenvector, $\vec{z}^{(m+1)}$, is calculated using three stages. First, a vector $\vec{y}^{(m+1)}$ is obtained from:

$$L\vec{y}^{(m+1)} = z^{(m)} \tag{A.42}$$

Next, the vector $\vec{w}^{(m+1)}$ is calculated using:

$$U\vec{w}^{(m+1)} = \vec{y}^{(m+1)} \tag{A.43}$$

Finally, the updated eigenvector is obtained from:

$$\vec{z}^{(m+1)} = \frac{\vec{w}^{(m+1)}}{\left\|\vec{w}^{(m+1)}\right\|_\infty} \tag{A.44}$$

The iterations continue until there is sufficiently small change in $\vec{z}$:

$$\left\|\vec{z}^{(m+1)} - \vec{z}^{(m)}\right\|_\infty \leq \varepsilon \tag{A.45}$$

It was generally observed that in this work no more than 10 iterations are required to obtain the eigenvector.

B Experimental data

B.1 Modal analysis data for 2024-T3 aluminum.

The following figures show the FFT diagrams for 2024-T3 aluminum obtained from the modal analysis experiments.

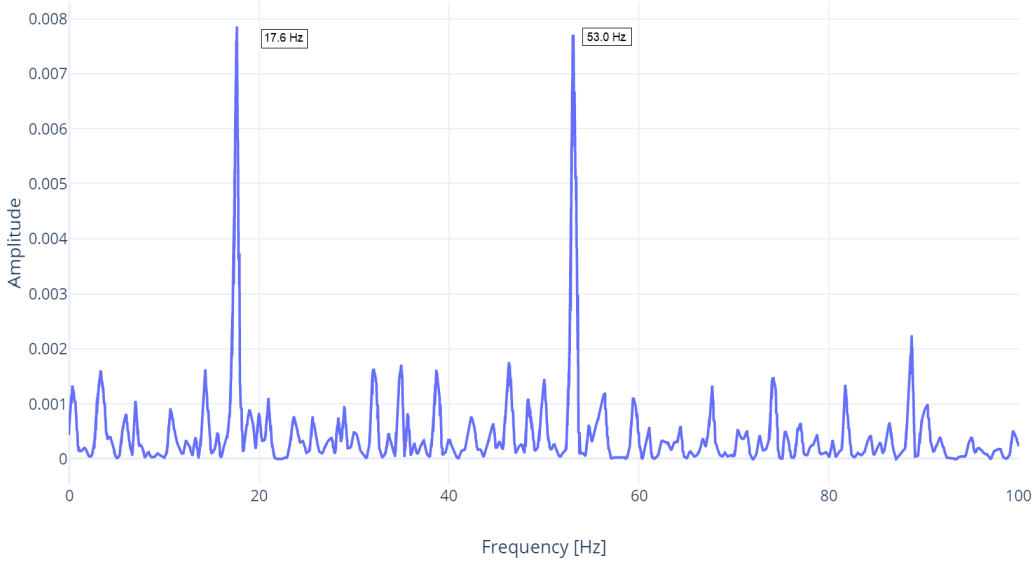

Figure B.1: FFT for 2024-T3 aluminum at U = 36.7 m/s.

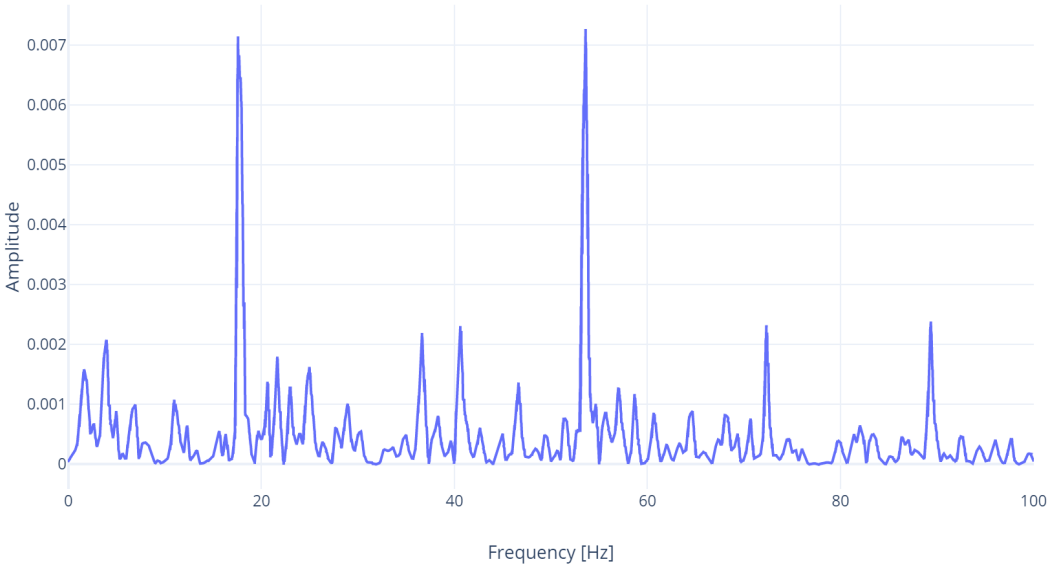

Figure B.2: FFT for 2024-T3 aluminum at U = 37.5 m/s.

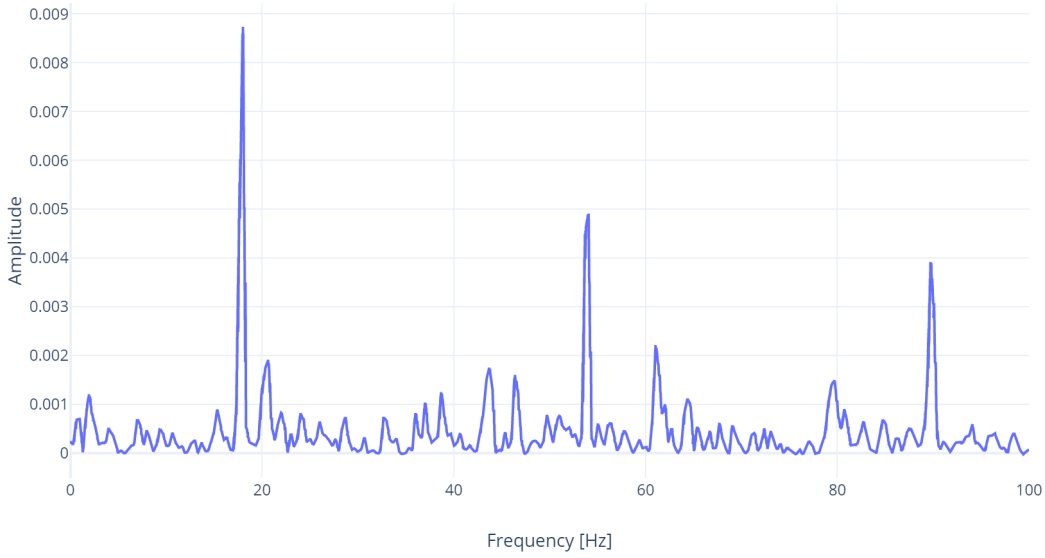

Figure B.3: FFT for 2024-T3 aluminum at U = 38.3 m/s.

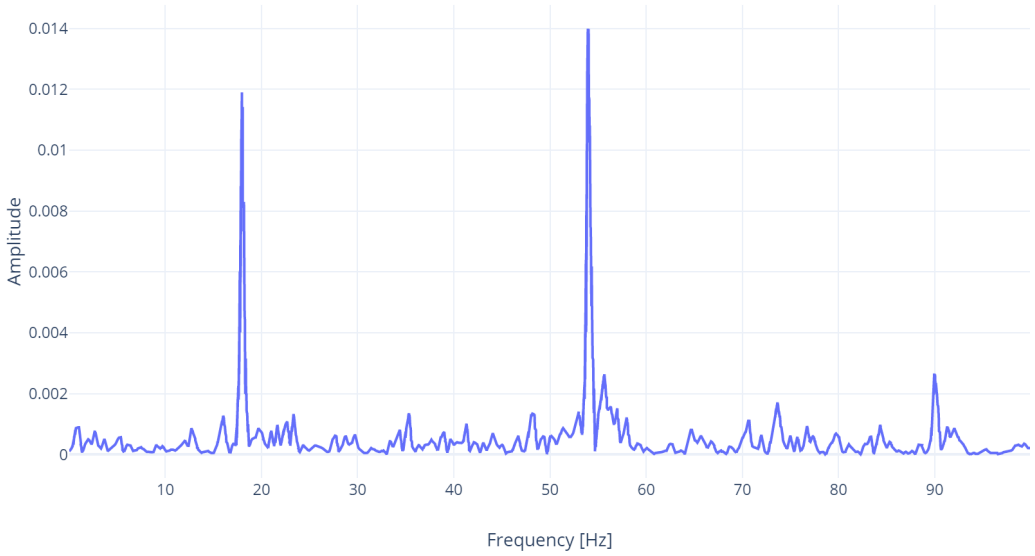

Figure B.4: FFT for 2024-T3 aluminum at U = 39.1 m/s.

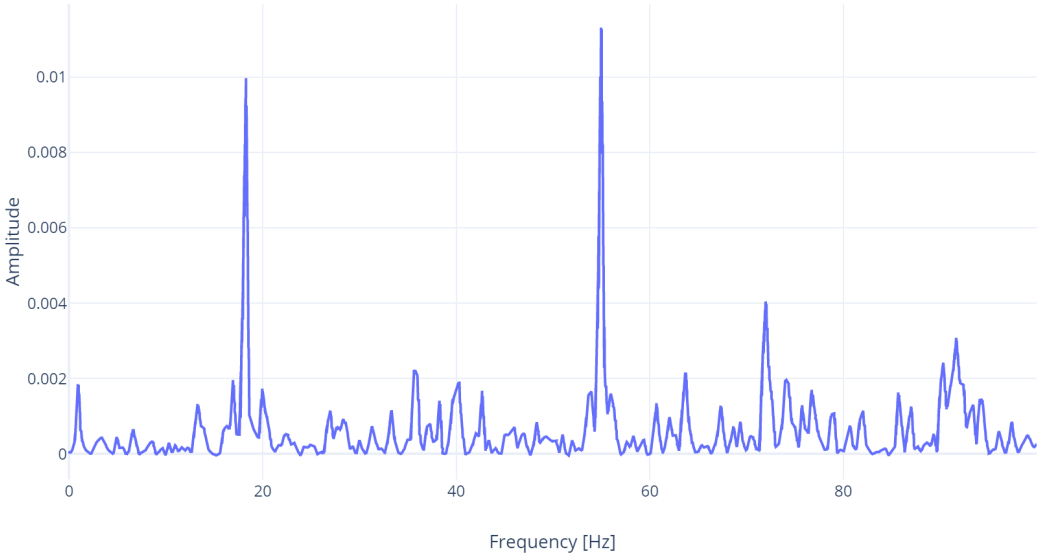

Figure B.5: FFT for 2024-T3 aluminum at U = 39.8 m/s.

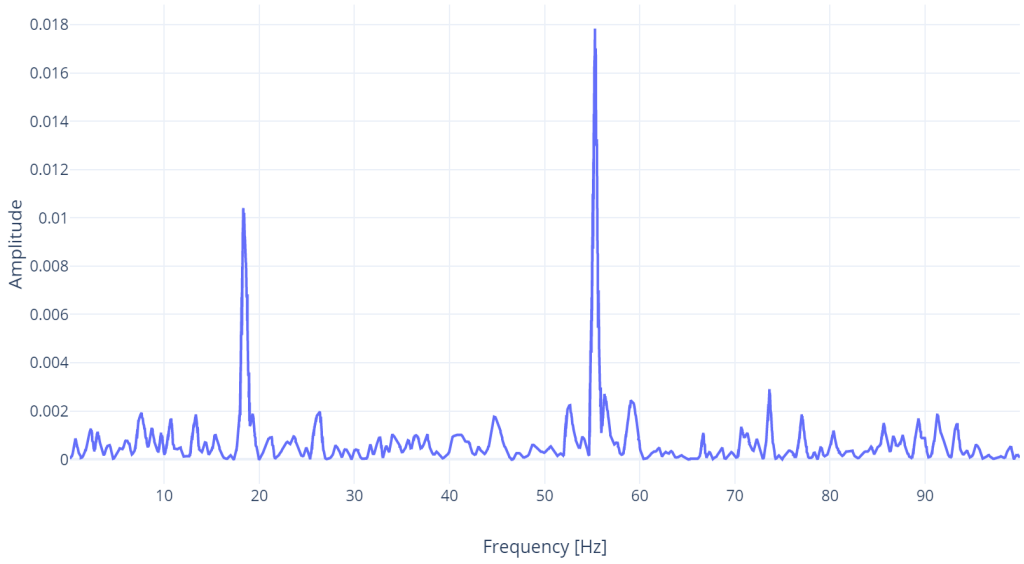

Figure B.6: FFT for 2024-T3 aluminum at U = 40.6 m/s.

B.2 Modal analysis data for ABS plastic.

The following figures show the FFT diagrams for ABS plastic obtained from the modal analysis experiments.

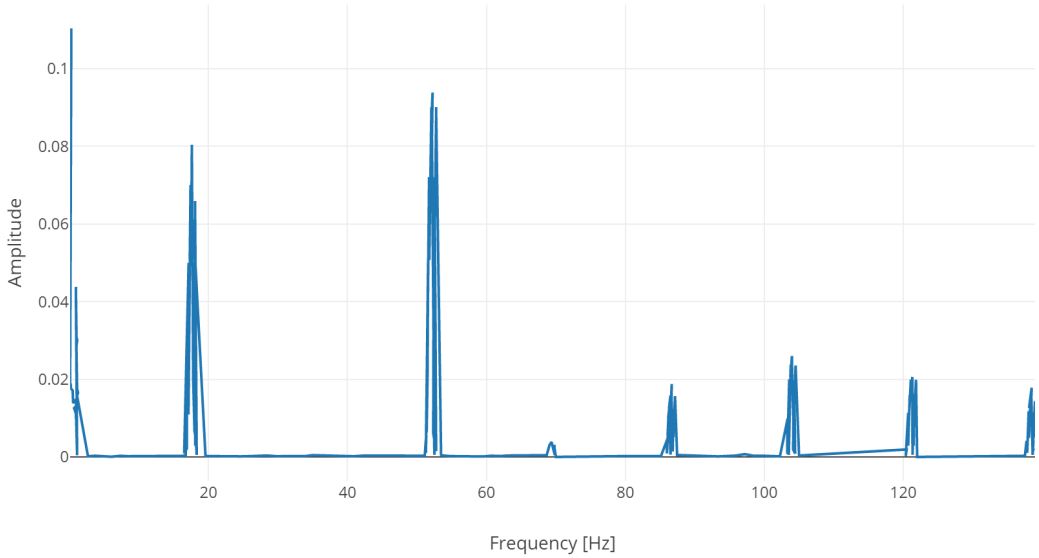

Figure B.7: FFT for ABS plastic at U = 17.3 m/s.

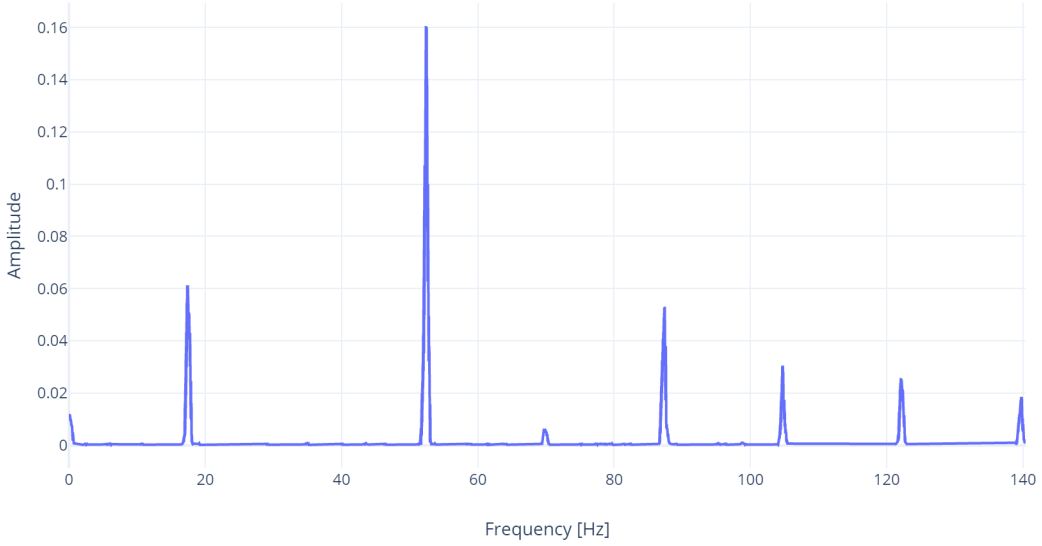

Figure B.8: FFT for ABS plastic at U = 18.0 m/s.

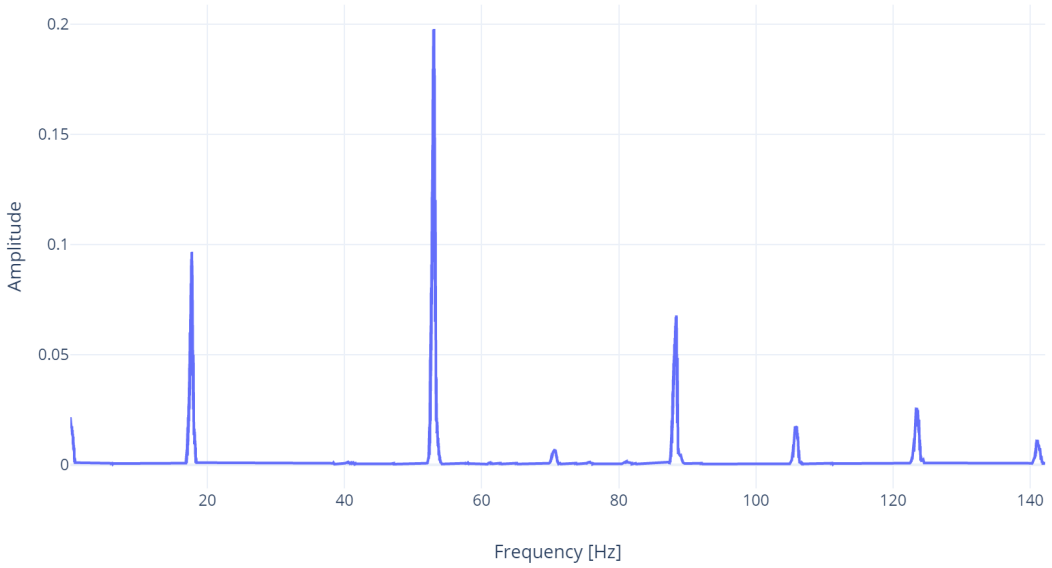

Figure B.9: FFT for ABS plastic at U = 18.8 m/s.

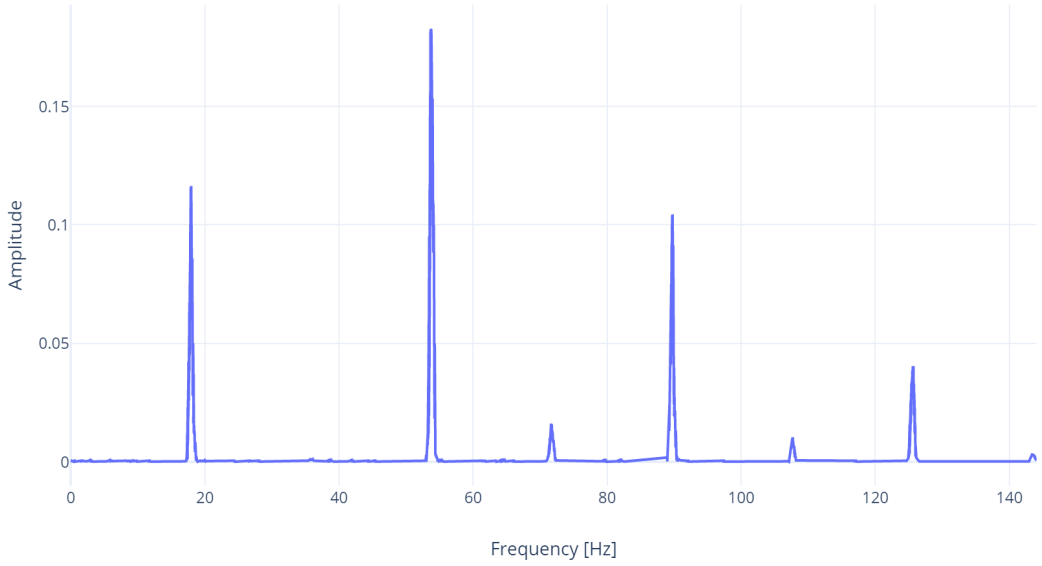

Figure B.10: FFT for ABS plastic at U = 19.6 m/s.

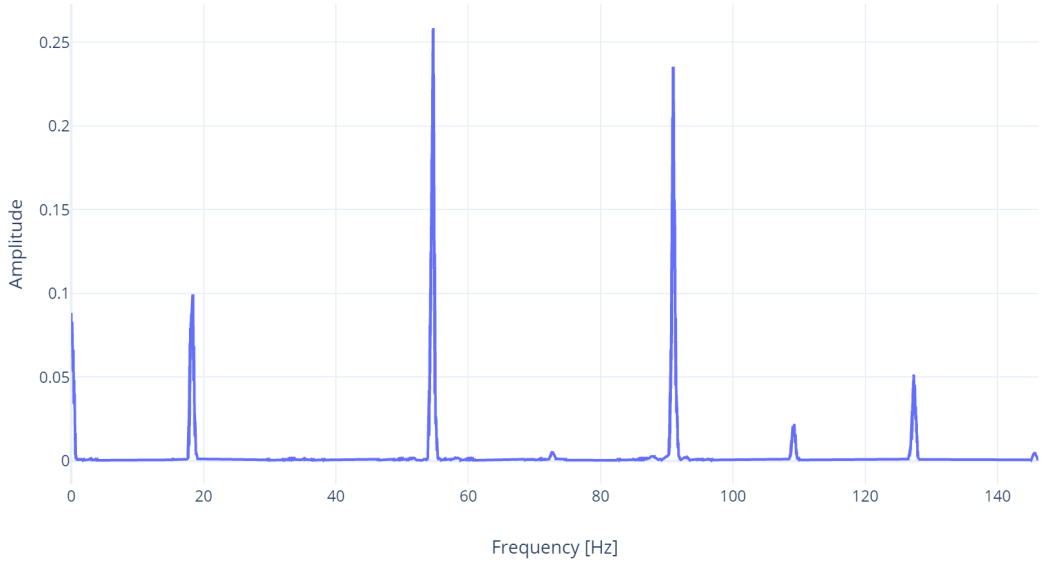

Figure B.11: FFT for ABS plastic at U = 20.4 m/s.

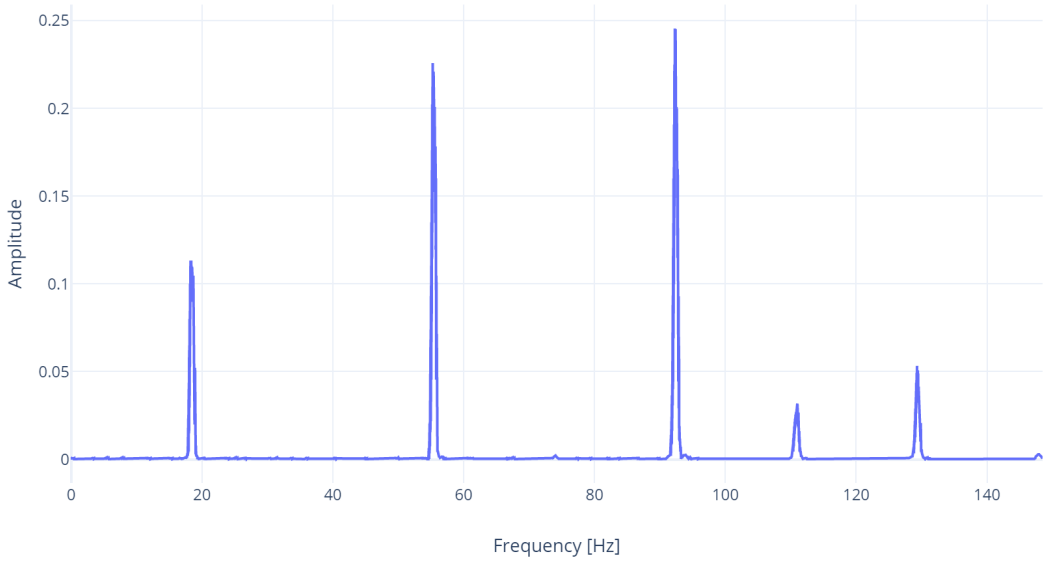

Figure B.12: FFT for ABS plastic at U = 21.2 m/s.

B.3 Modal analysis data for PETG plastic.

The following figures show the FFT diagrams for PETG plastic obtained from the modal analysis experiments.

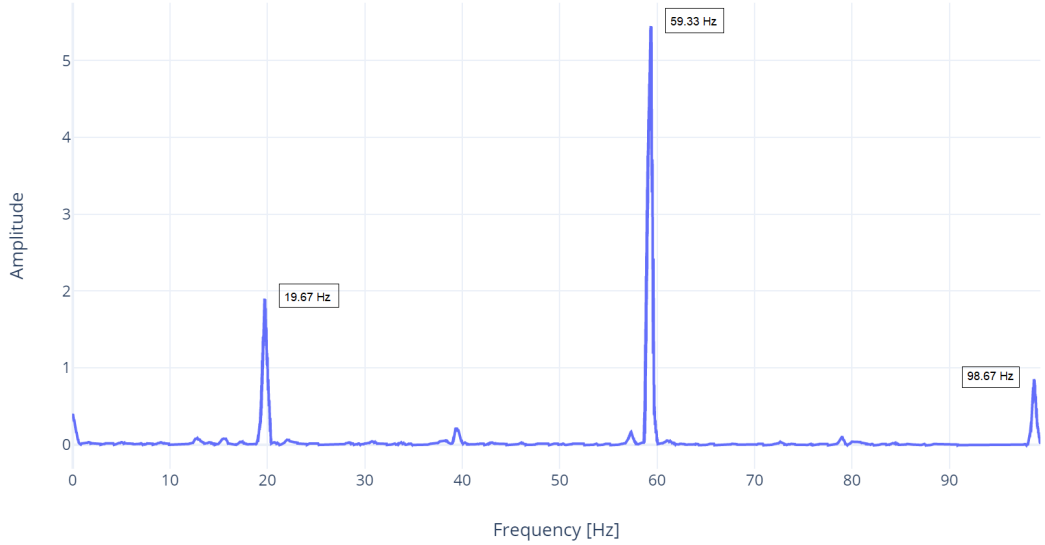

Figure B.13: FFT for PETG plastic at U = 25.9 m/s.

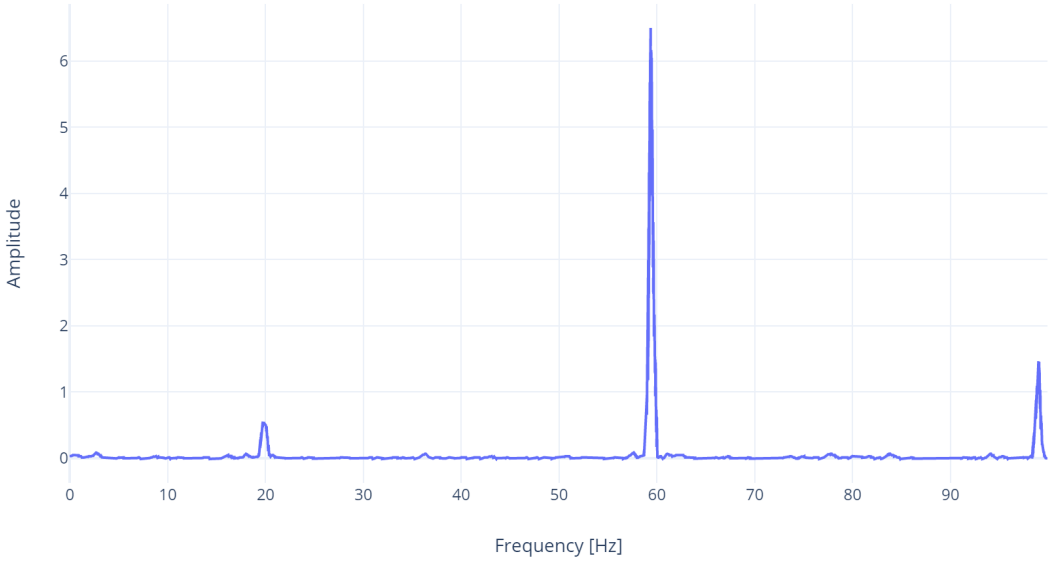

Figure B.14: FFT for PETG plastic at U = 25.9 m/s.

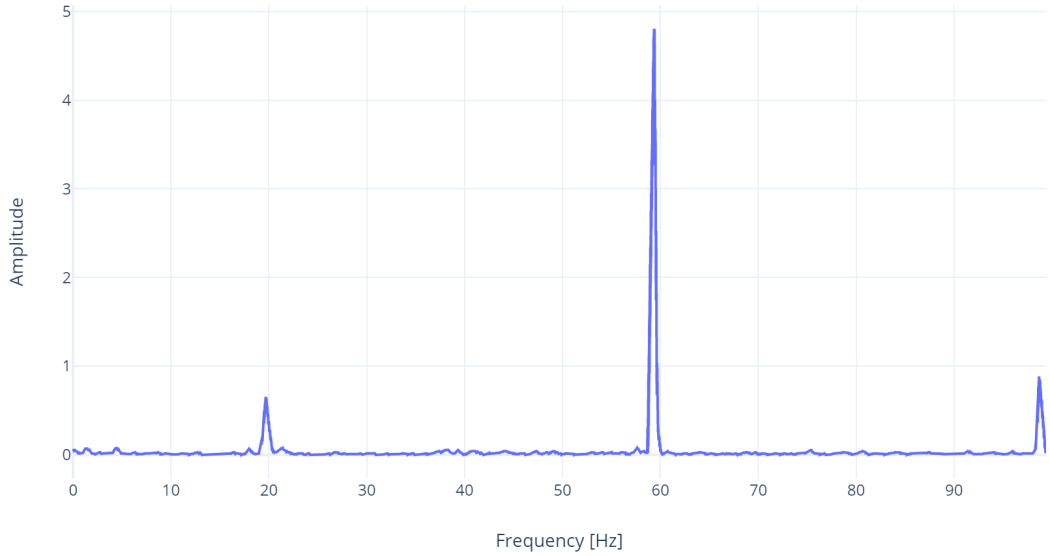

Figure B.15: FFT for PETG plastic at U = 26.7 m/s.

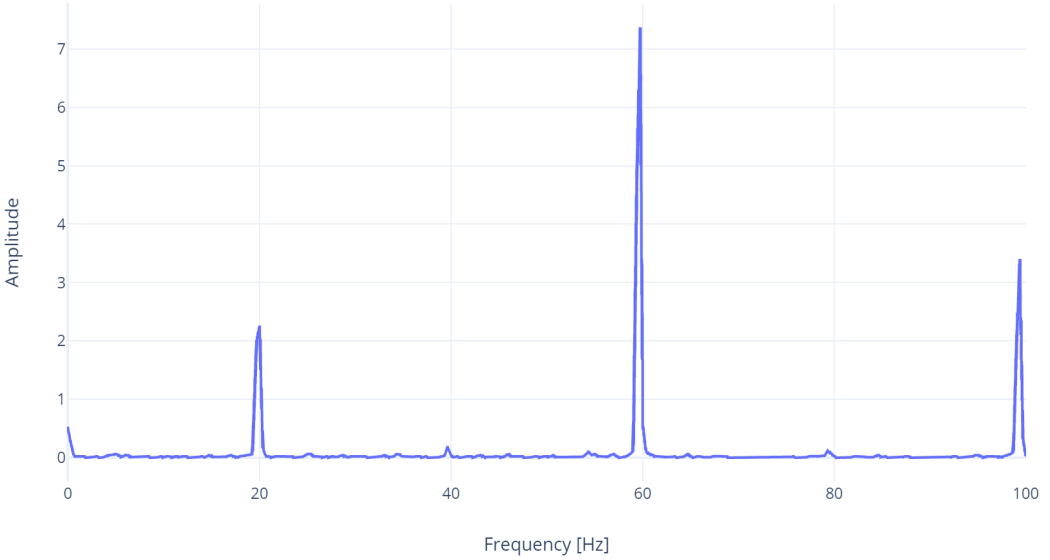

Figure B.16: FFT for PETG plastic at U = 27.5 m/s.

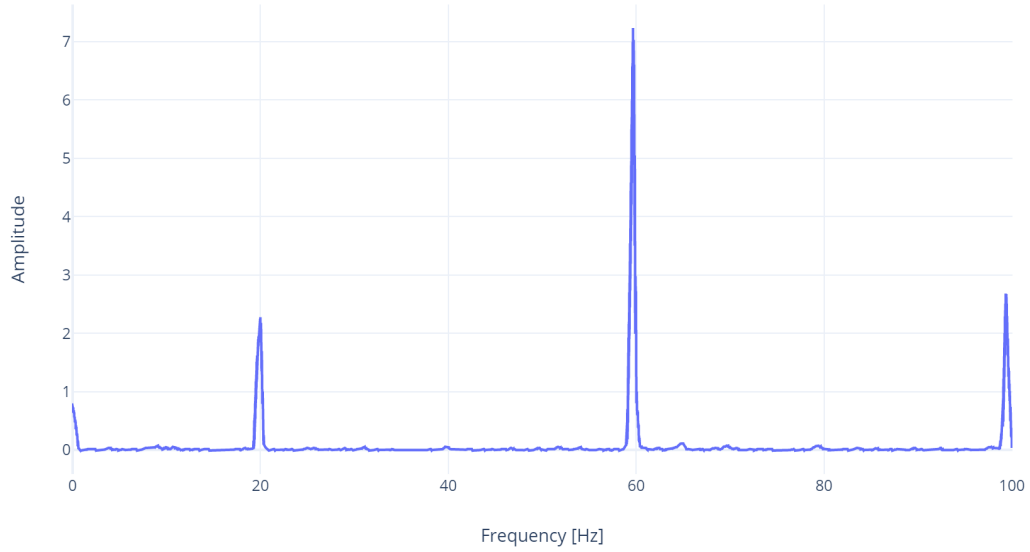

Figure B.17: FFT for PETG plastic at U = 28.3 m/s.

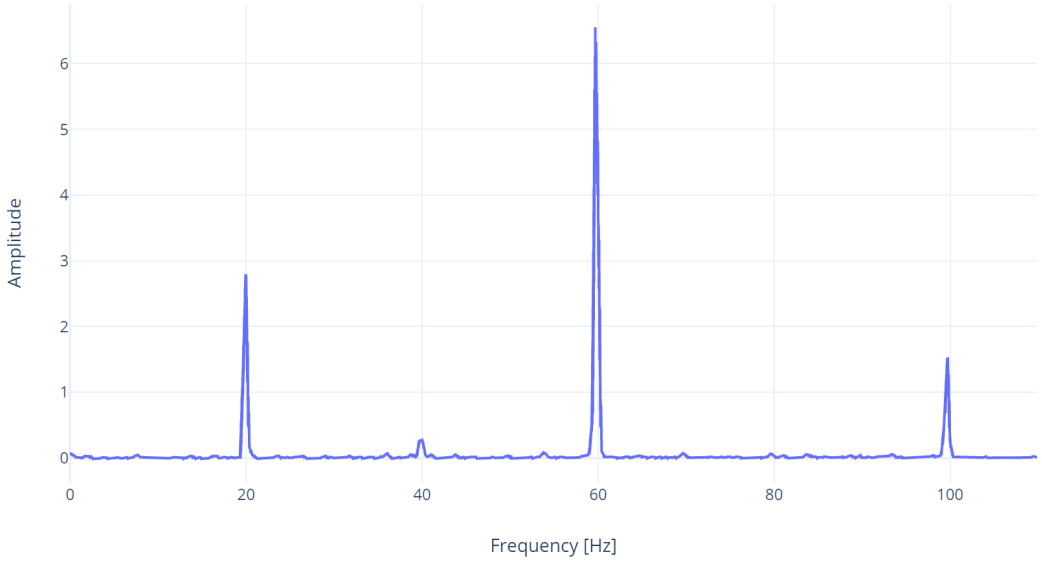

Figure B.18: FFT for PETG plastic at U = 29.1 m/s.

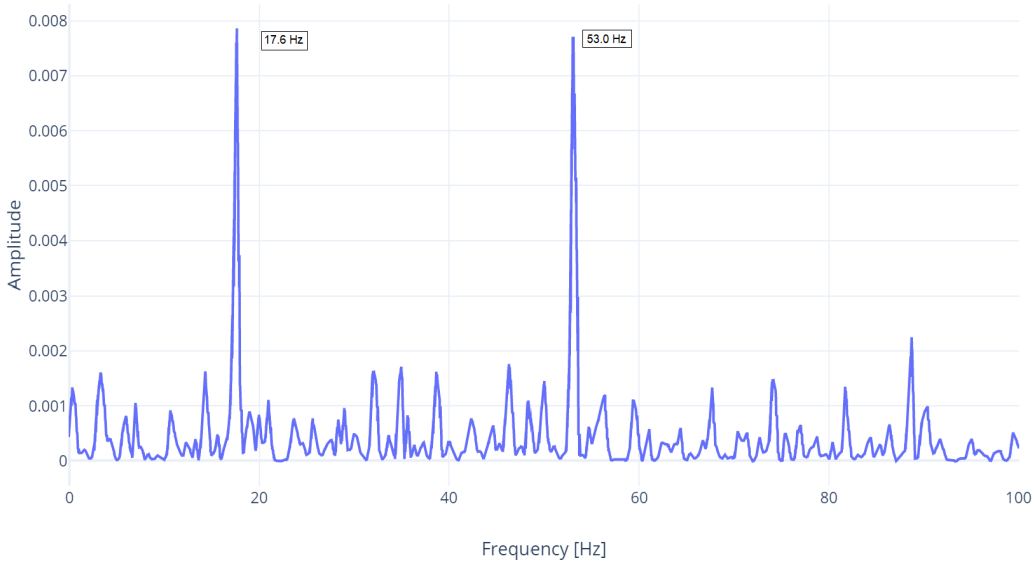

Figure B.19: FFT for PETG plastic at U = 29.8 m/s.

B.4 Image processing data for 2024-T3 aluminum.

The following figures show the midpoint displacement data for 2024-T3 aluminum obtained from the image processing program. The figures show the data from the entire time elapsed, and for a shorter duration to make the waveform more visible.

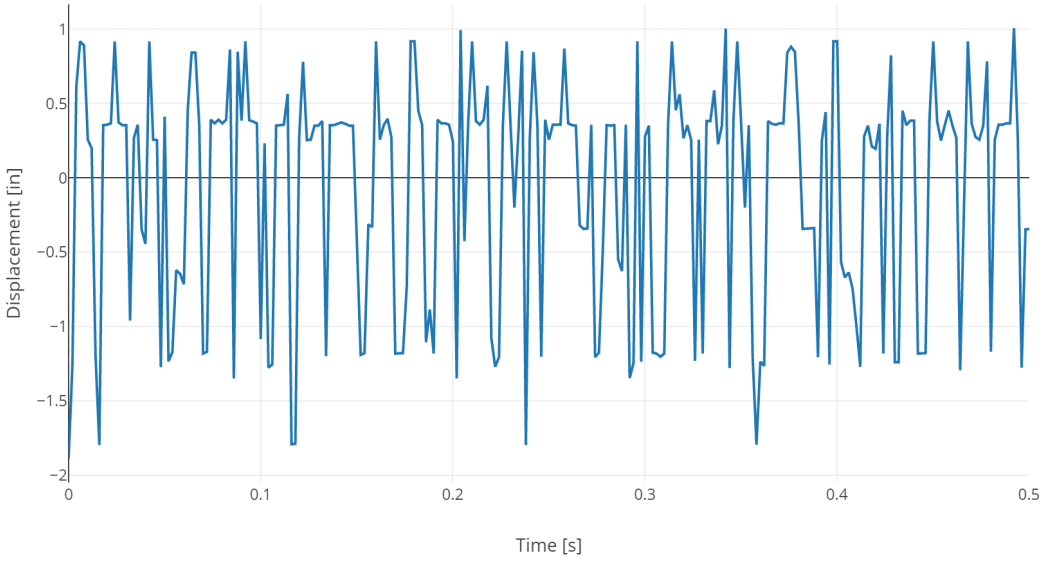

Figure B.20: Midpoint displacement versus time for U = 36.7 m/s for 0.5 seconds duration.

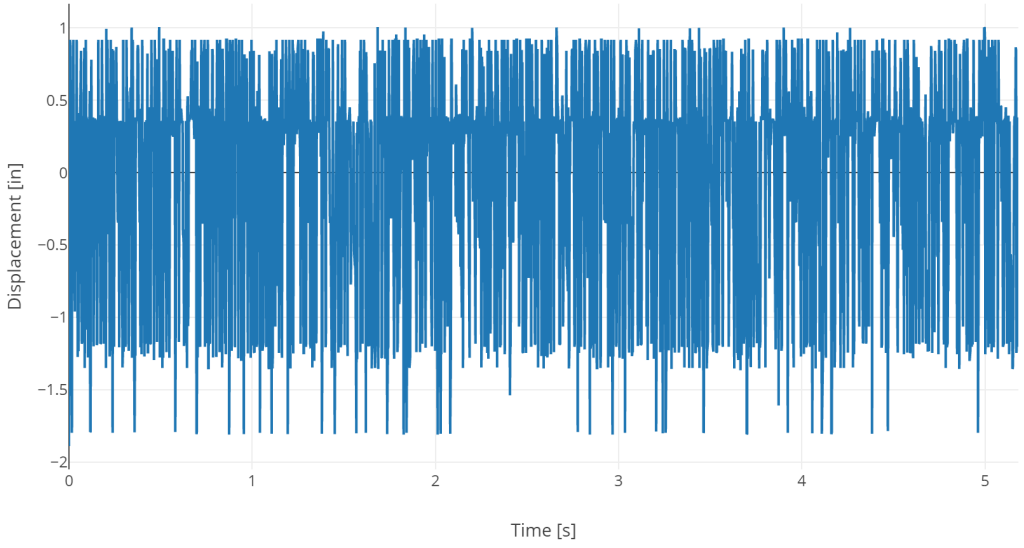

Figure B.21: Midpoint displacement versus time for U = 36.7 m/s for 5.4 seconds duration.

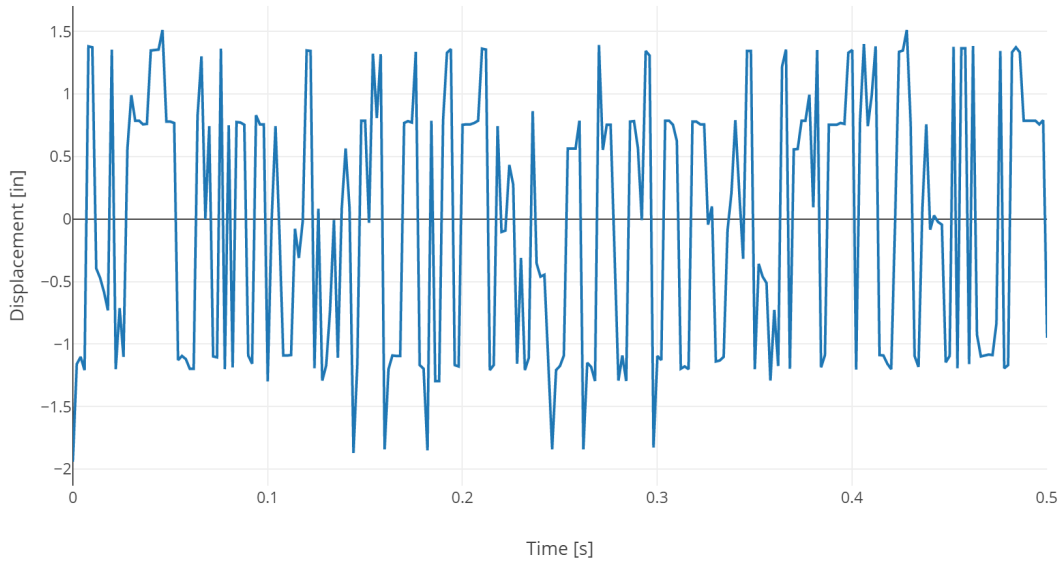

Figure B.22: Midpoint displacement versus time for U = 37.5 m/s for 0.5 seconds duration.

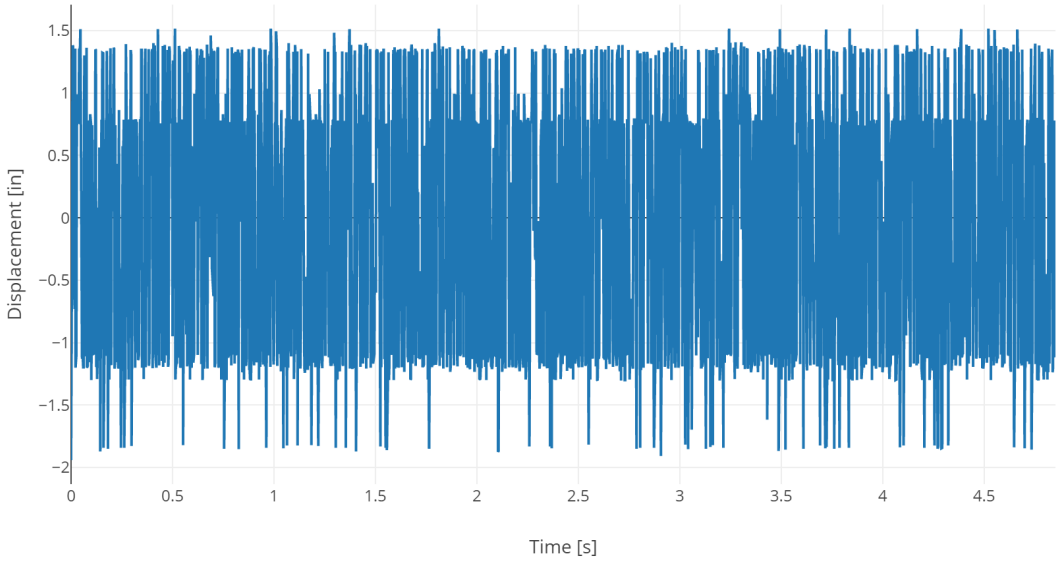

Figure B.23: Midpoint displacement versus time for U = 37.5 m/s for 5.0 seconds duration.

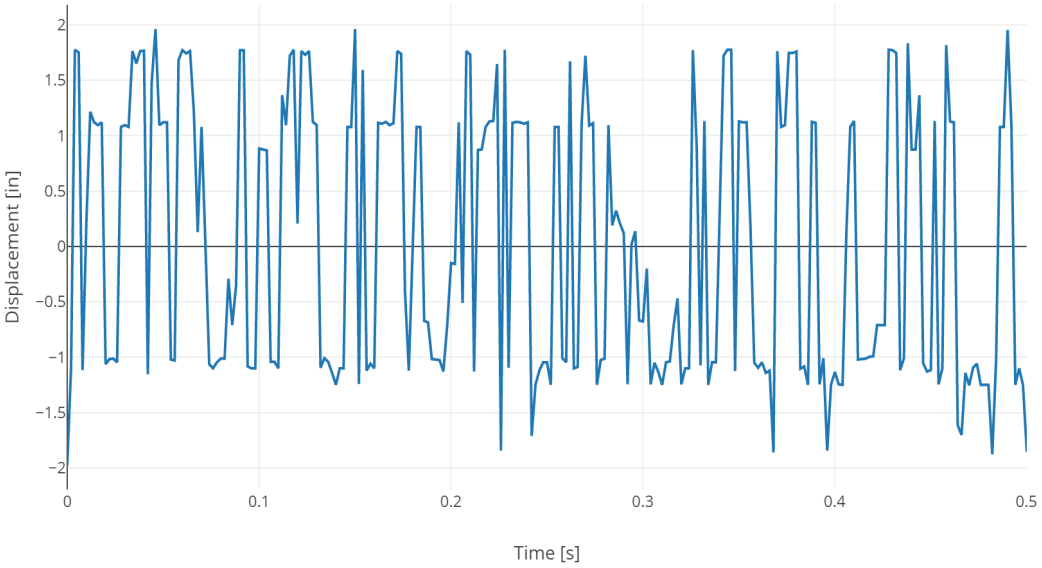

Figure B.24: Midpoint displacement versus time for U = 38.3 m/s for 0.5 seconds duration.

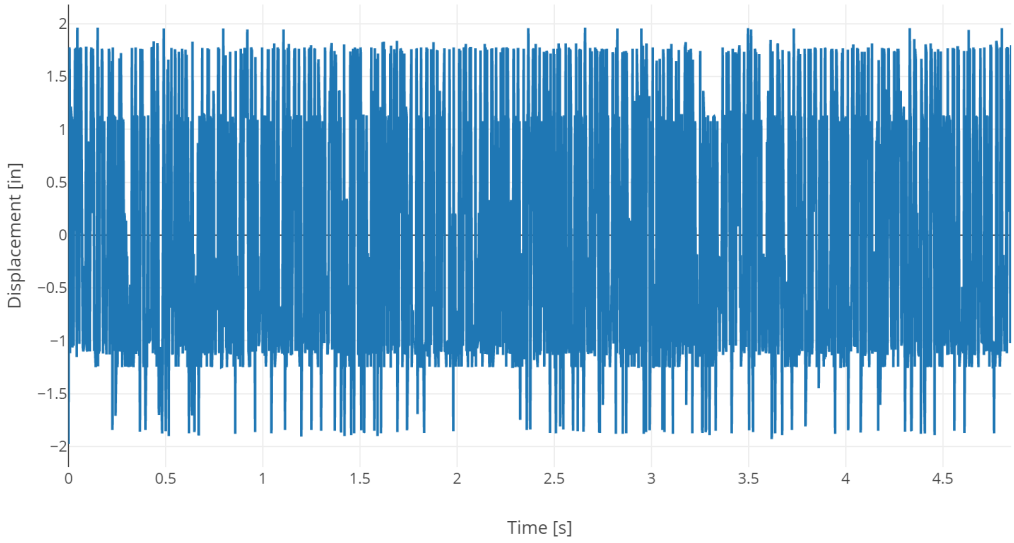

Figure B.25: Midpoint displacement versus time for U = 38.3 m/s for 5.0 seconds duration.

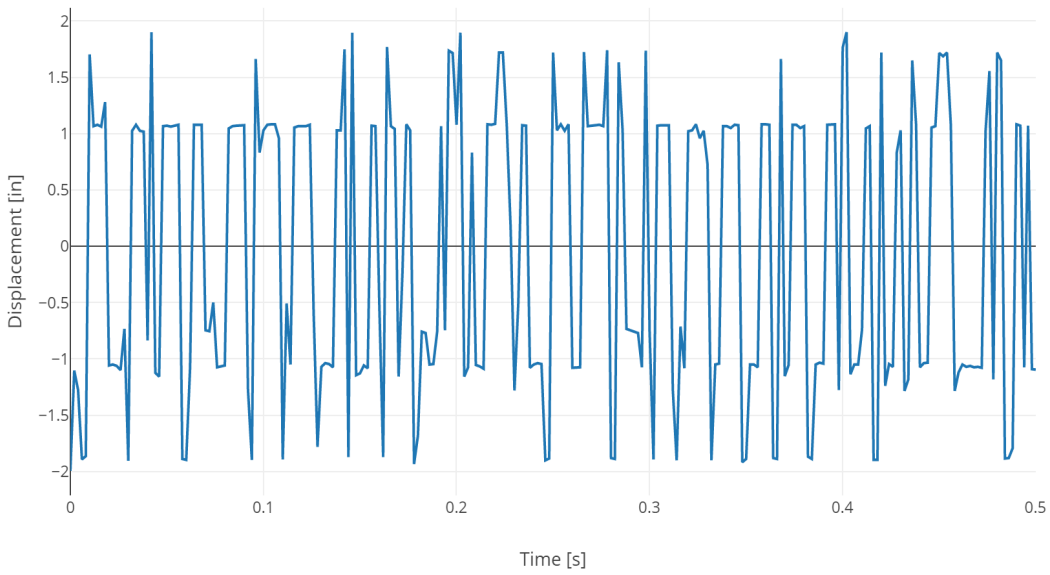

Figure B.26: Midpoint displacement versus time for U = 39.0 m/s for 0.5 seconds duration.

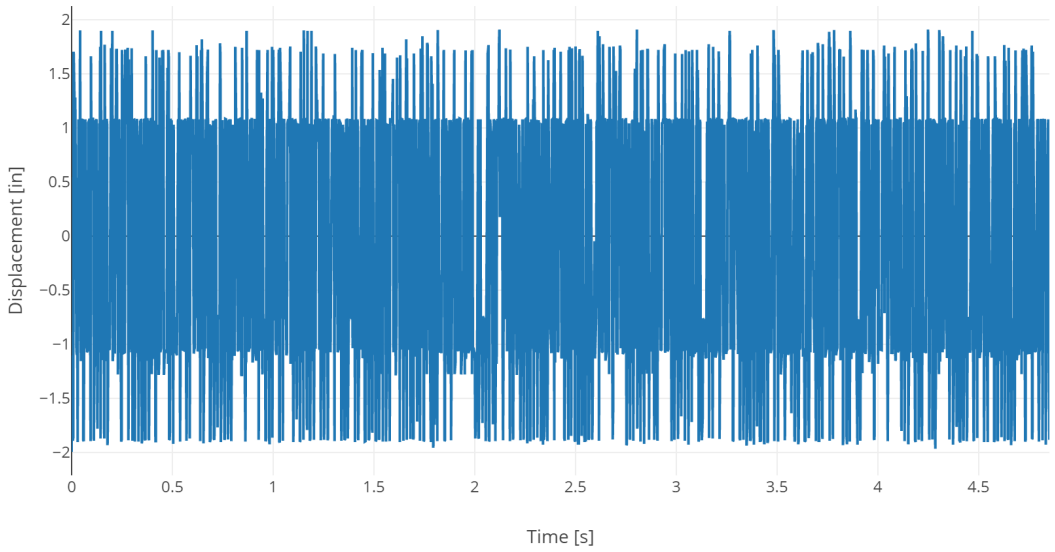

Figure B.27: Midpoint displacement versus time for U = 39.0 m/s for 5.0 seconds duration.

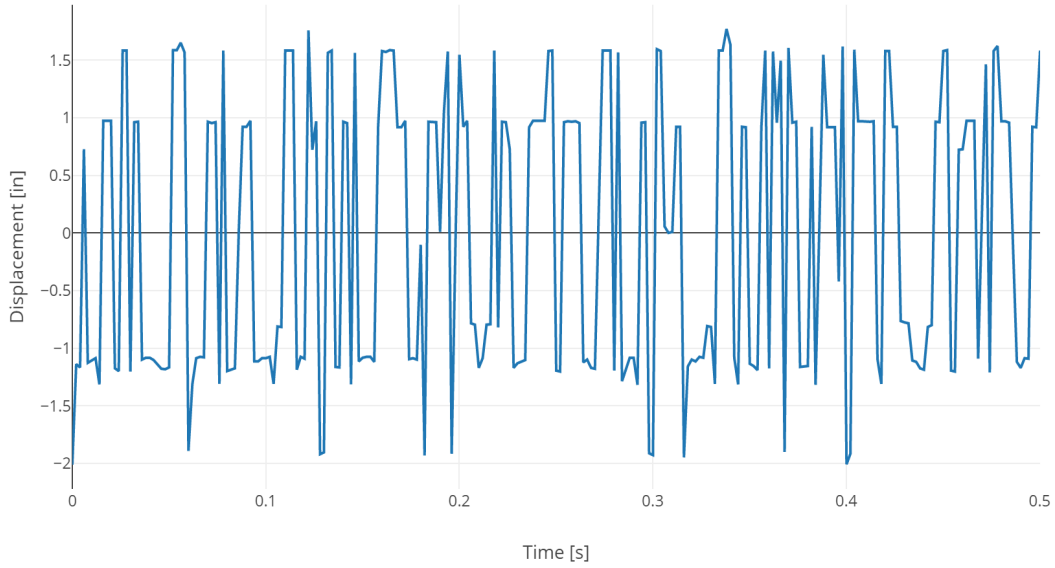

Figure B.28: Midpoint displacement versus time for U = 39.8 m/s for 0.5 seconds duration.

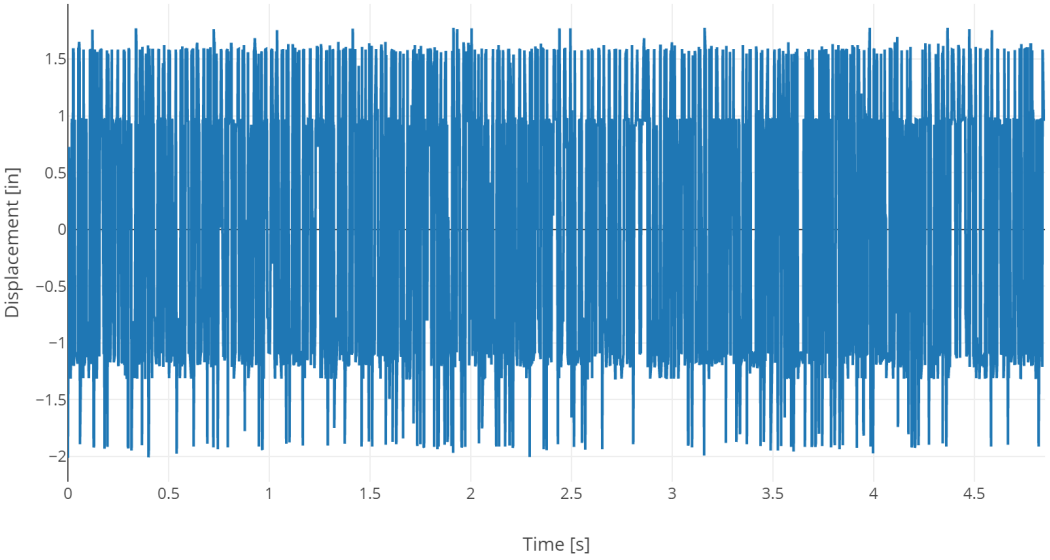

Figure B.29: Midpoint displacement versus time for U = 39.8 m/s for 5.0 seconds duration.

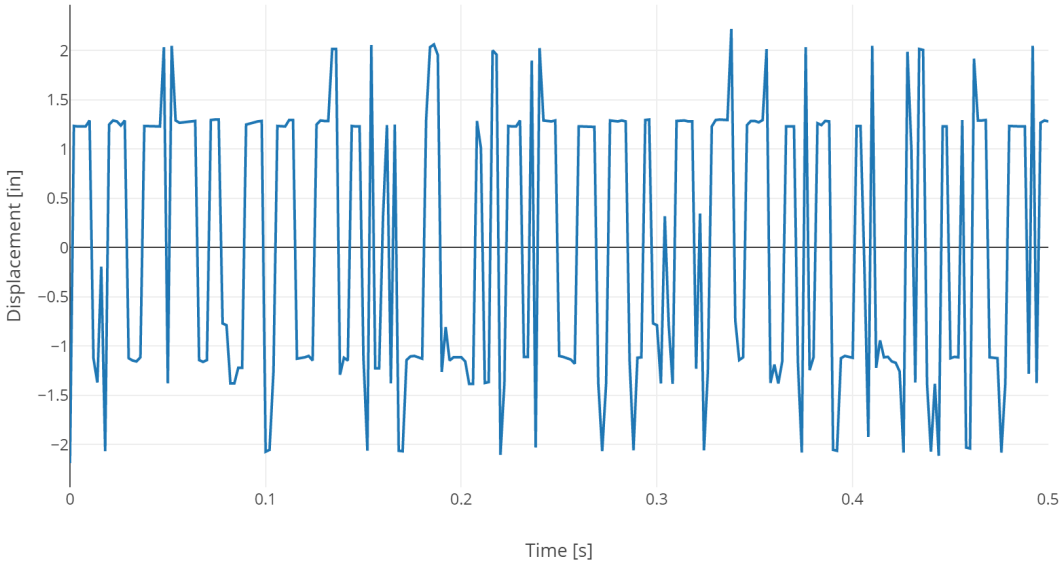

Figure B.30: Midpoint displacement versus time for U = 40.6 m/s for 0.5 seconds duration.

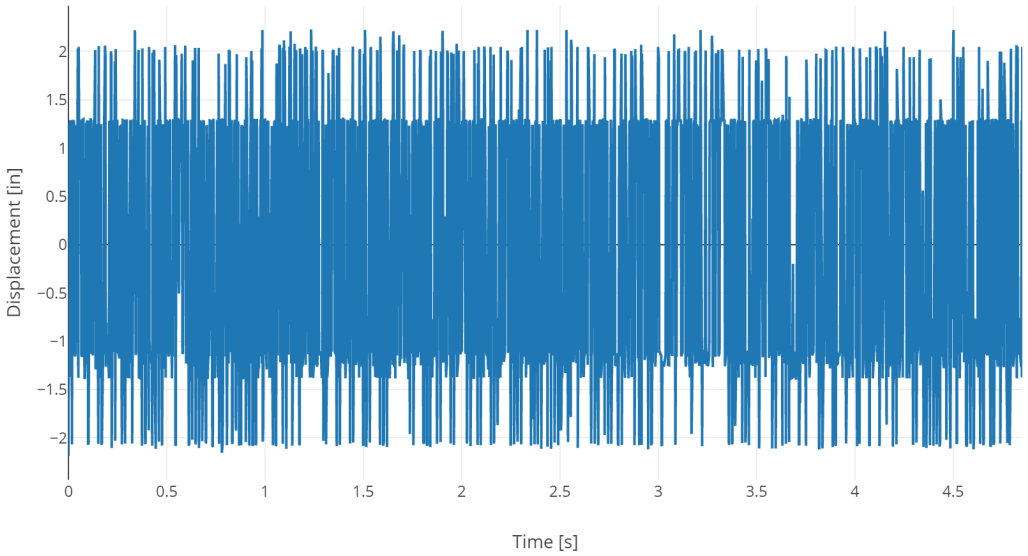

Figure B.31: Midpoint displacement versus time for U = 40.6 m/s for 5.0 seconds duration.

B.5 Image processing data for ABS plastic.

The following figures show the midpoint displacement data for ABS plastic obtained from the image processing program. The figures show the data from the entire time elapsed, and for a shorter duration to make the waveform more visible.

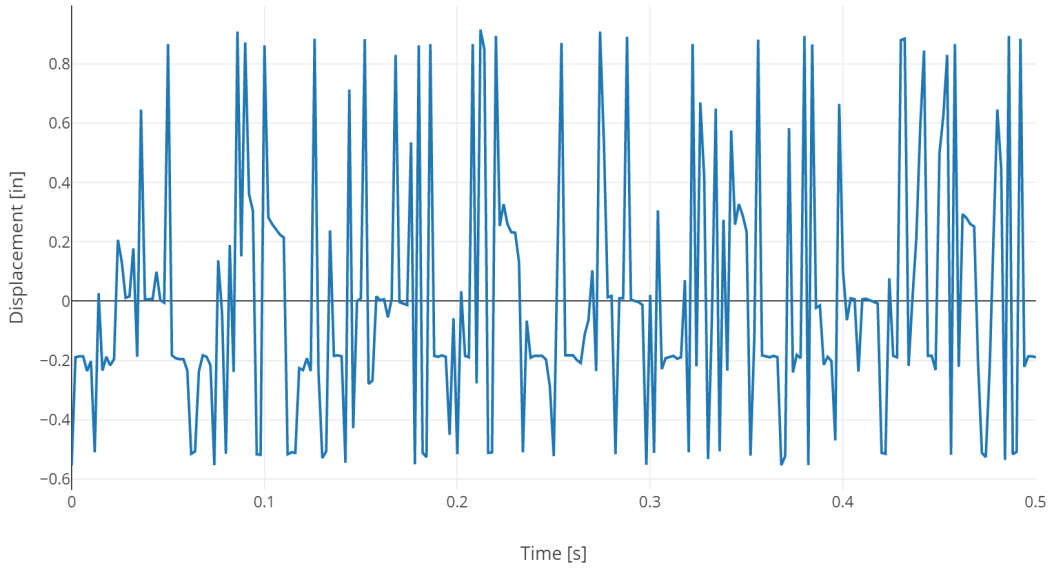

Figure B.32: Midpoint displacement versus time for U = 17.3 m/s for 0.5 seconds duration.

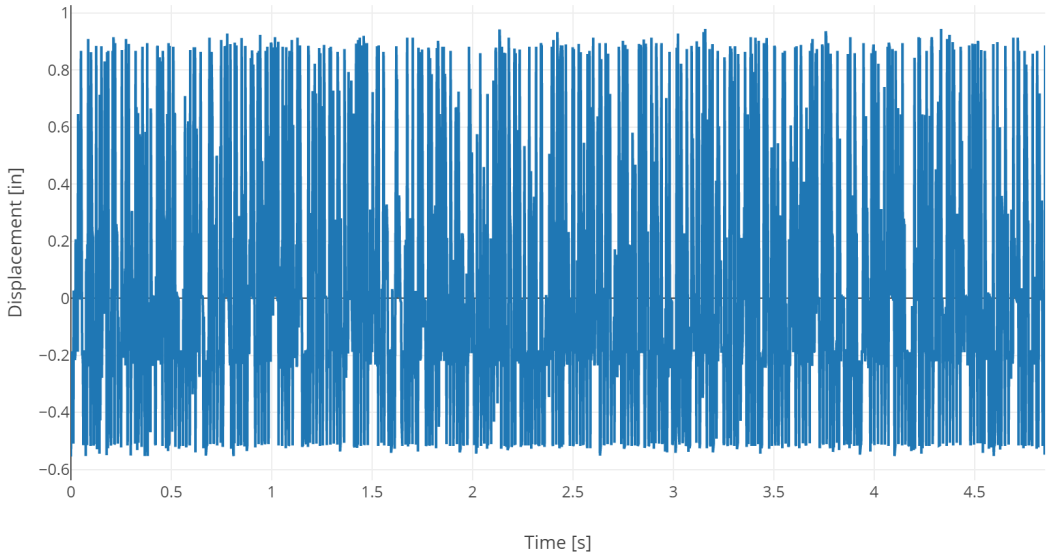

Figure B.33: Midpoint displacement versus time for U = 17.3 m/s for 5.0 seconds duration.

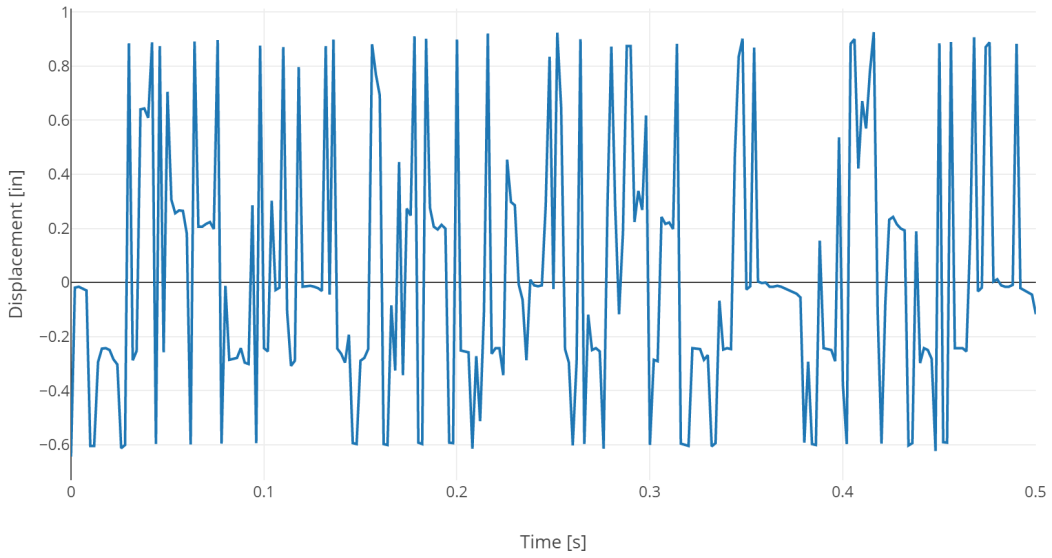

Figure B.34: Midpoint displacement versus time for U = 18.0 m/s for 0.5 seconds duration.

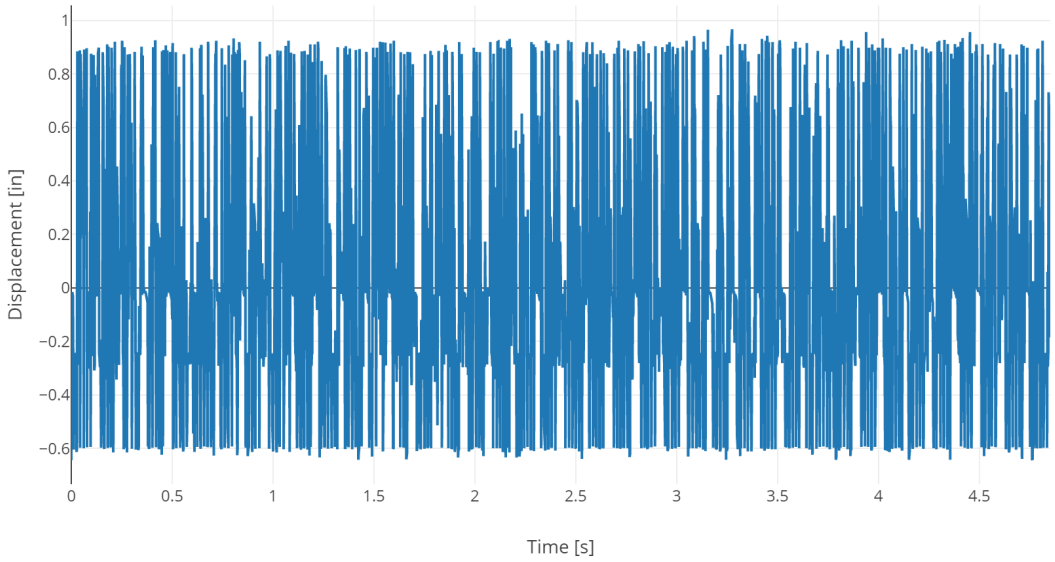

Figure B.35: Midpoint displacement versus time for U = 18.0 m/s for 5.0 seconds duration.

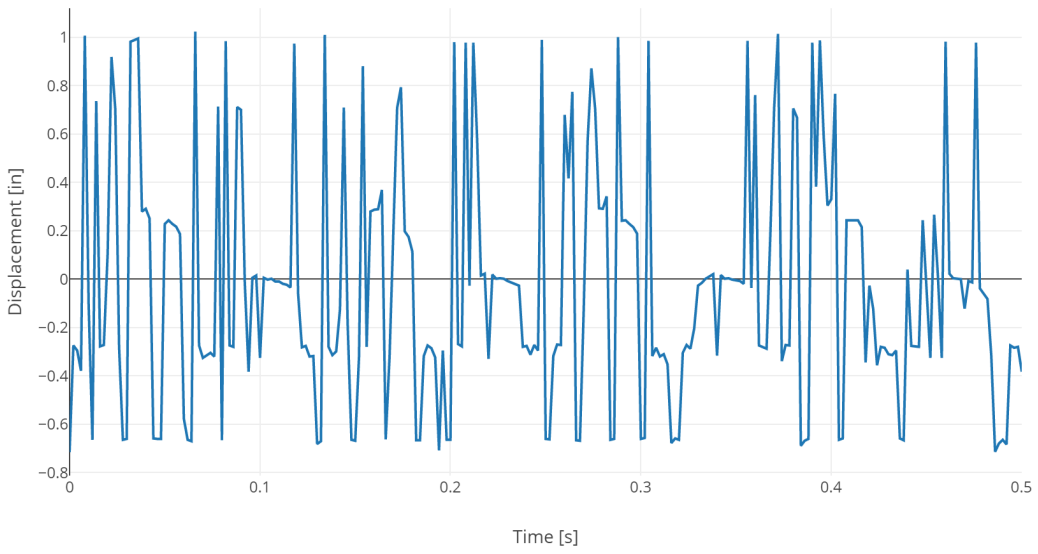

Figure B.36: Midpoint displacement versus time for U = 18.8 m/s for 0.5 seconds duration.

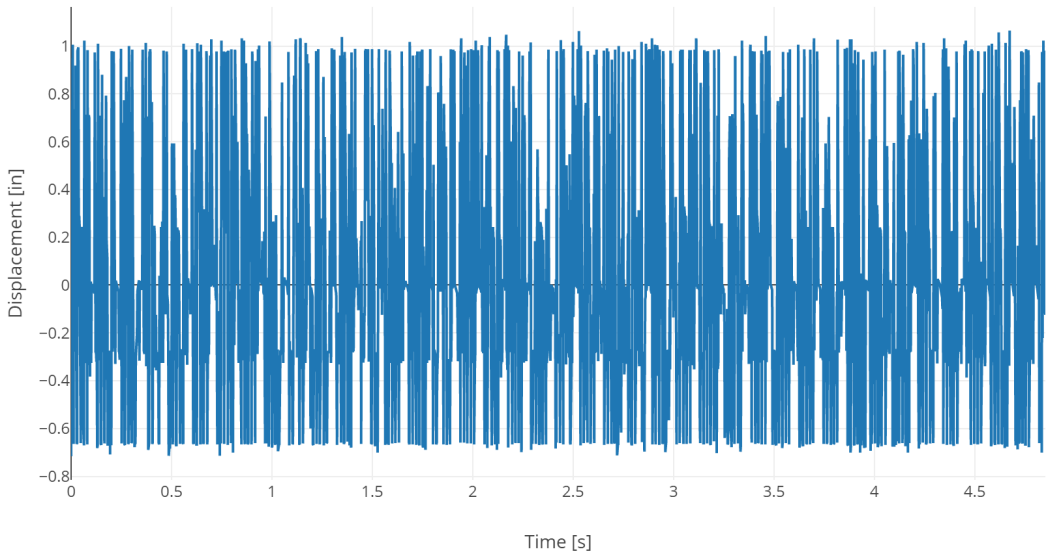

Figure B.37: Midpoint displacement versus time for U = 18.8 m/s for 5.0 seconds duration.

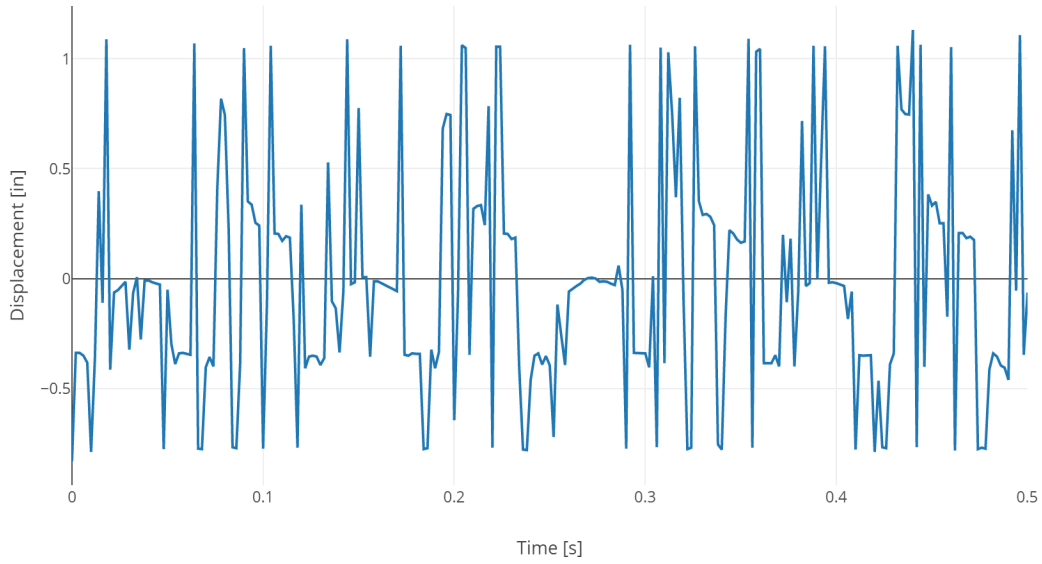

Figure B.38: Midpoint displacement versus time for U = 19.6 m/s for 0.5 seconds duration.

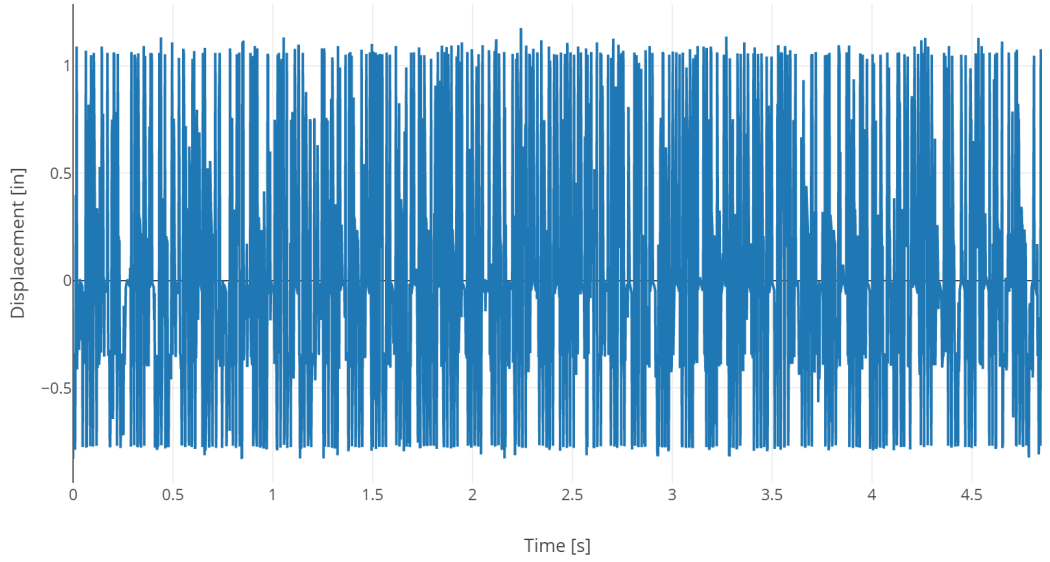

Figure B.39: Midpoint displacement versus time for U = 19.6 m/s for 5.0 seconds duration.

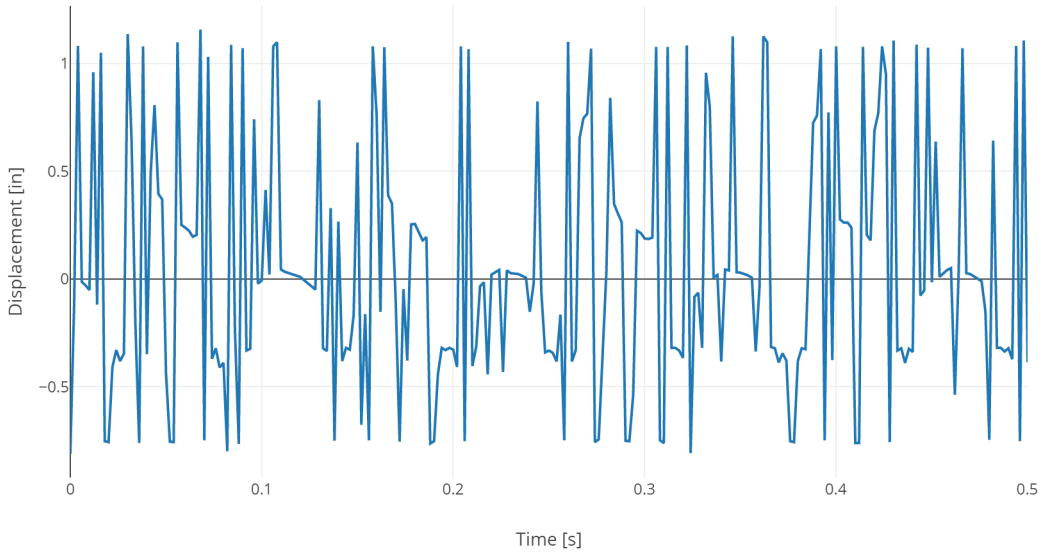

Figure B.40: Midpoint displacement versus time for U = 20.4 m/s for 0.5 seconds duration.

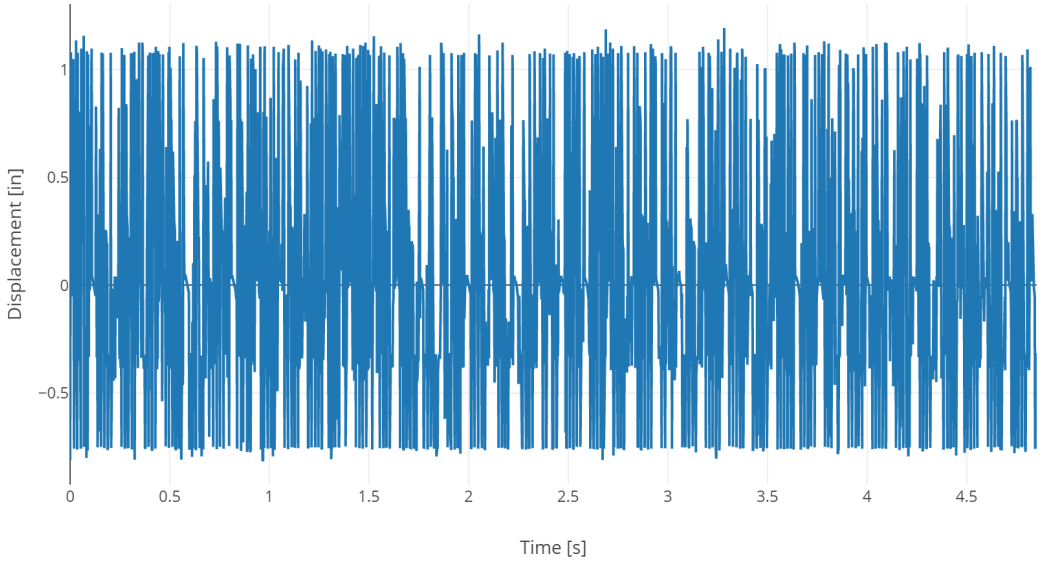

Figure B.41: Midpoint displacement versus time for U = 20.4 m/s for 5.0 seconds duration.

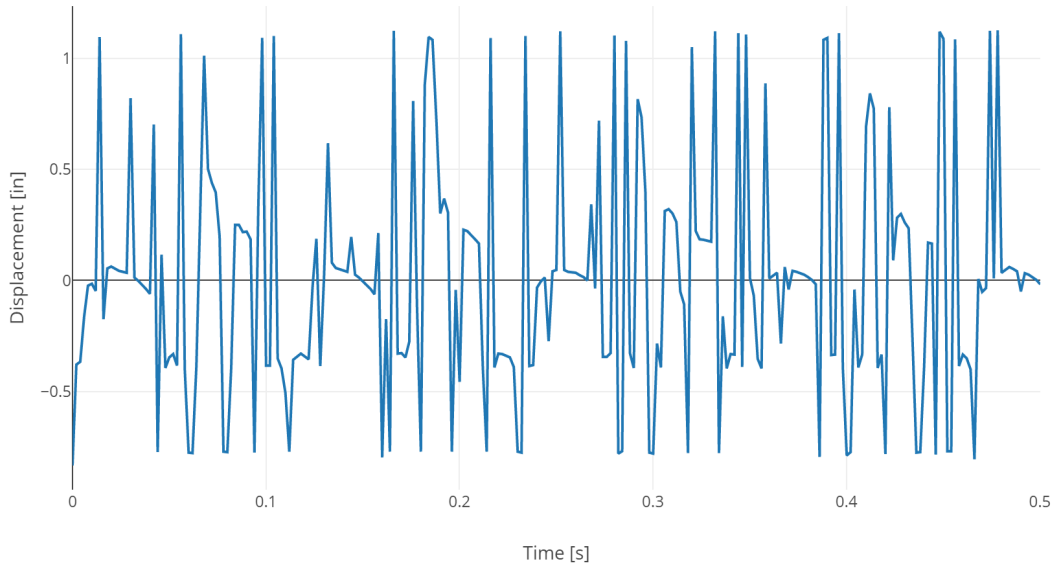

Figure B.42: Midpoint displacement versus time for U = 21.2 m/s for 0.5 seconds duration.

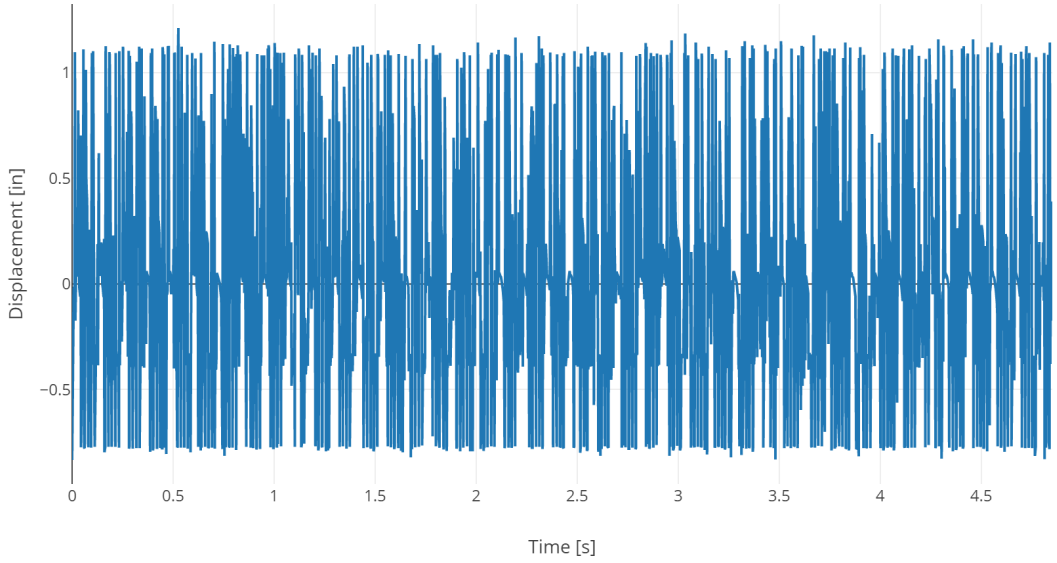

Figure B.43: Midpoint displacement versus time for U = 21.2 m/s for 5.0 seconds duration.

B.6 Image processing data for PETG plastic.

The following figures show the midpoint displacement data for PETG plastic obtained from the image processing program. The figures show the data from the entire time elapsed, and for a shorter duration to make the waveform more visible.

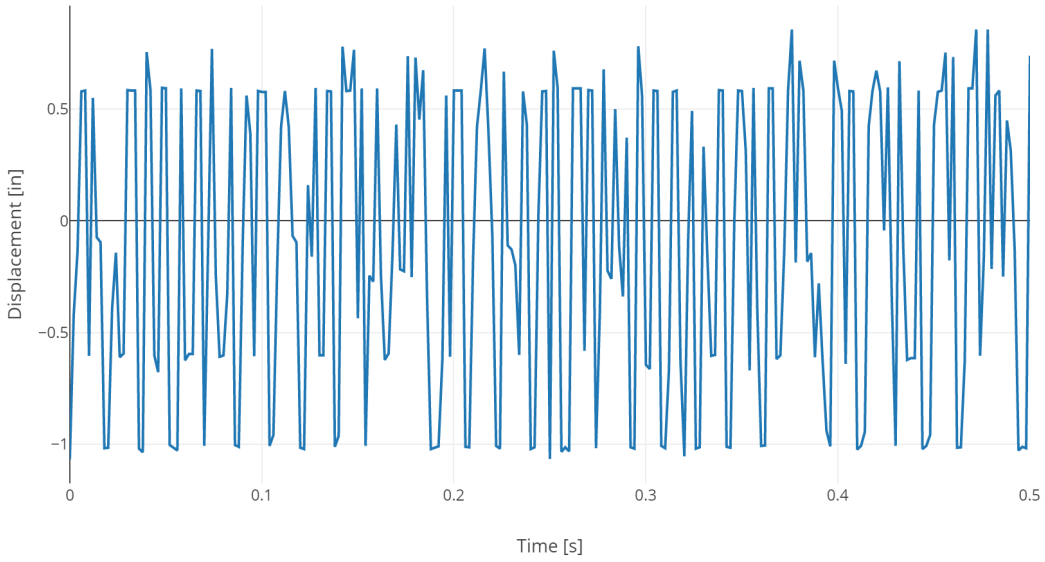

Figure B.44: Midpoint displacement versus time for U = 26.7 m/s for 0.5 seconds duration.

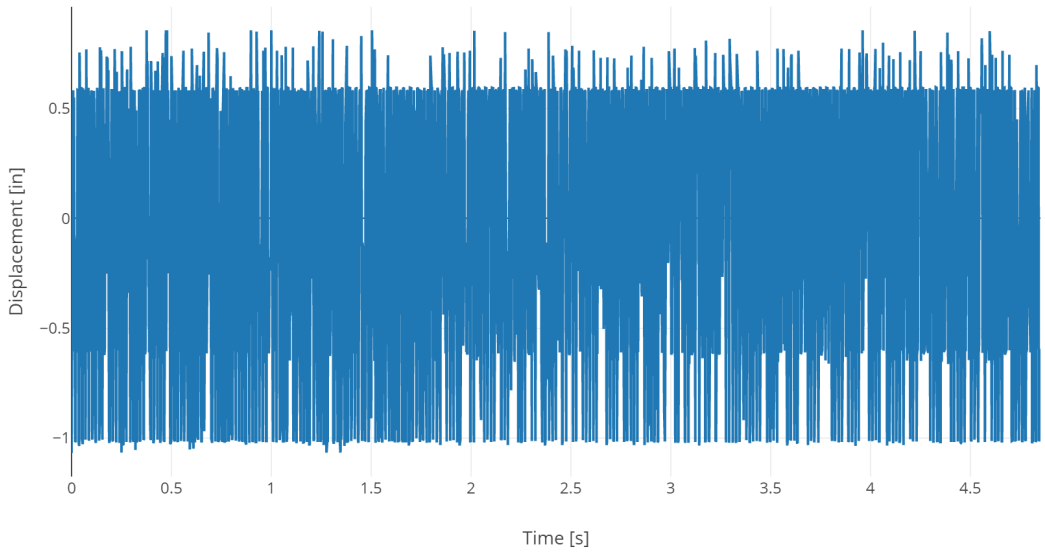

Figure B.45: Midpoint displacement versus time for U = 26.7 m/s for 5.0 seconds duration.

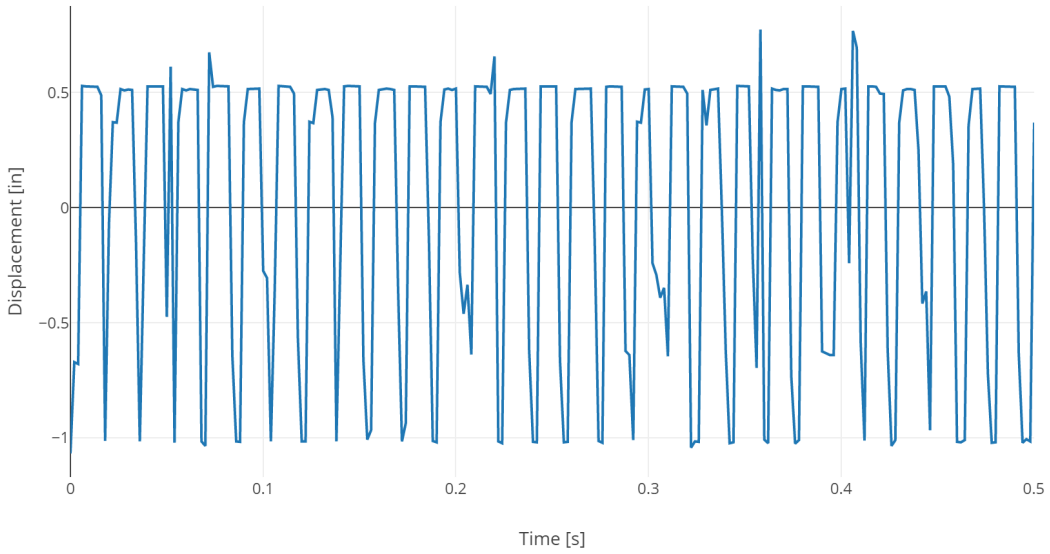

Figure B.46: Midpoint displacement versus time for U = 27.5 m/s for 0.5 seconds duration.

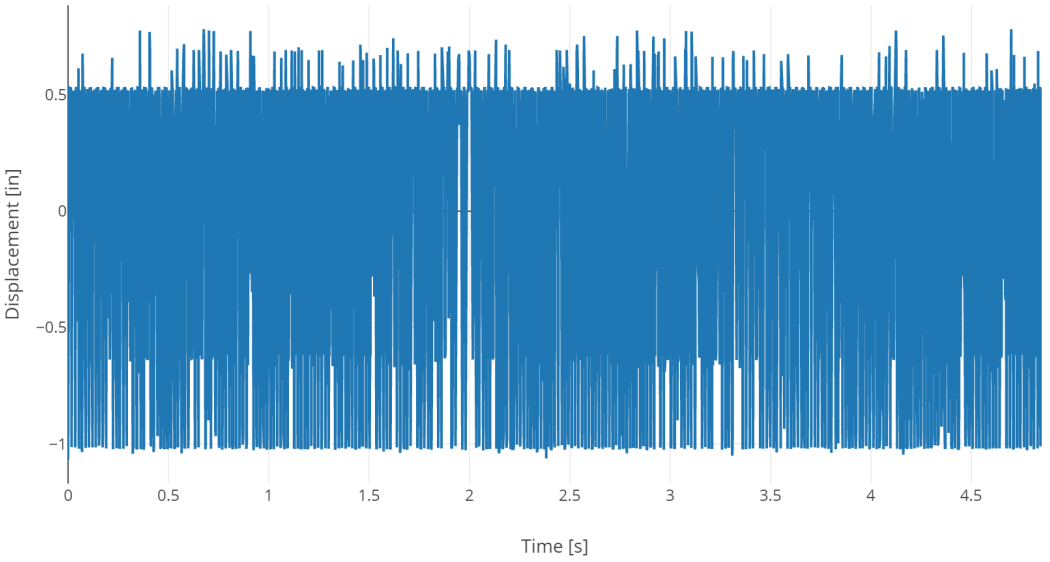

Figure B.47: Midpoint displacement versus time for U = 27.5 m/s for 5.0 seconds duration.

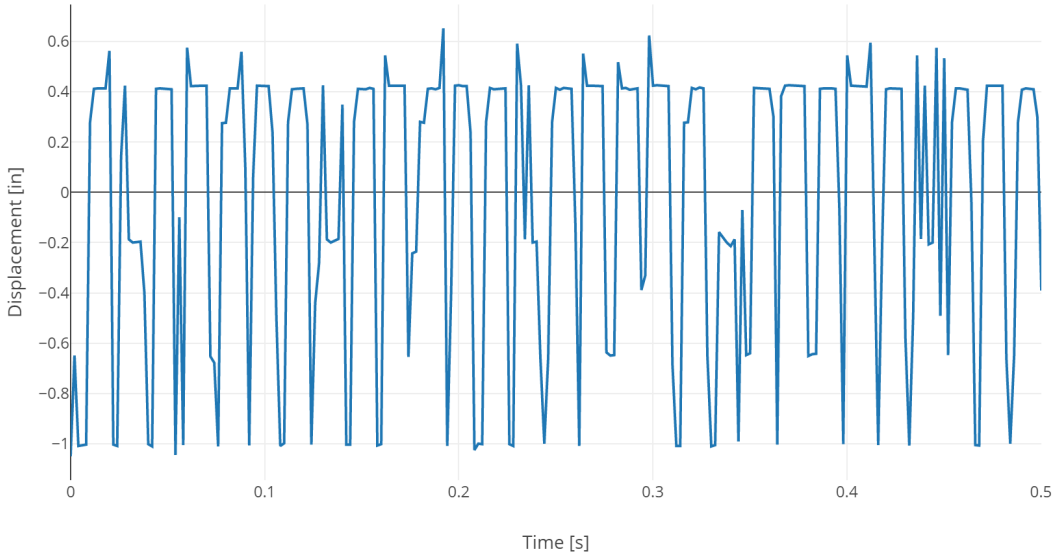

Figure B.48: Midpoint displacement versus time for U = 28.3 m/s for 0.5 seconds duration.

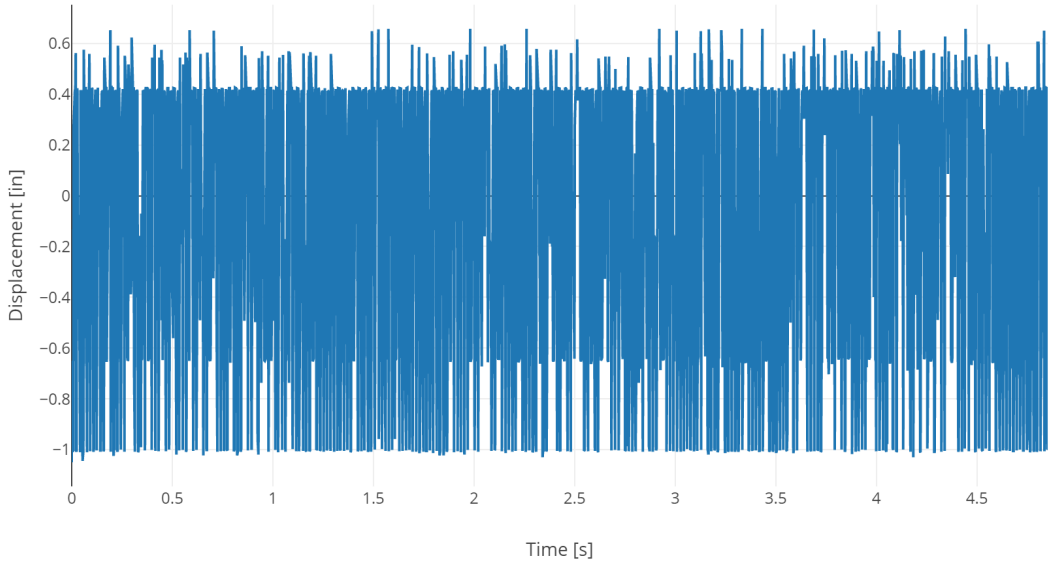

Figure B.49: Midpoint displacement versus time for U = 28.3 m/s for 5.0 seconds duration.

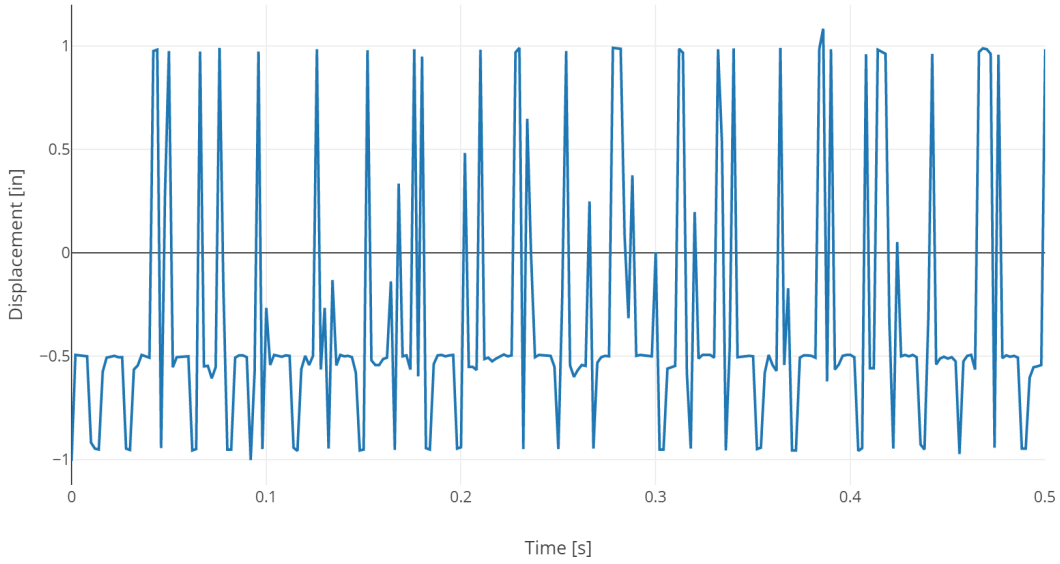

Figure B.50: Midpoint displacement versus time for U = 29.1 m/s for 0.5 seconds duration.

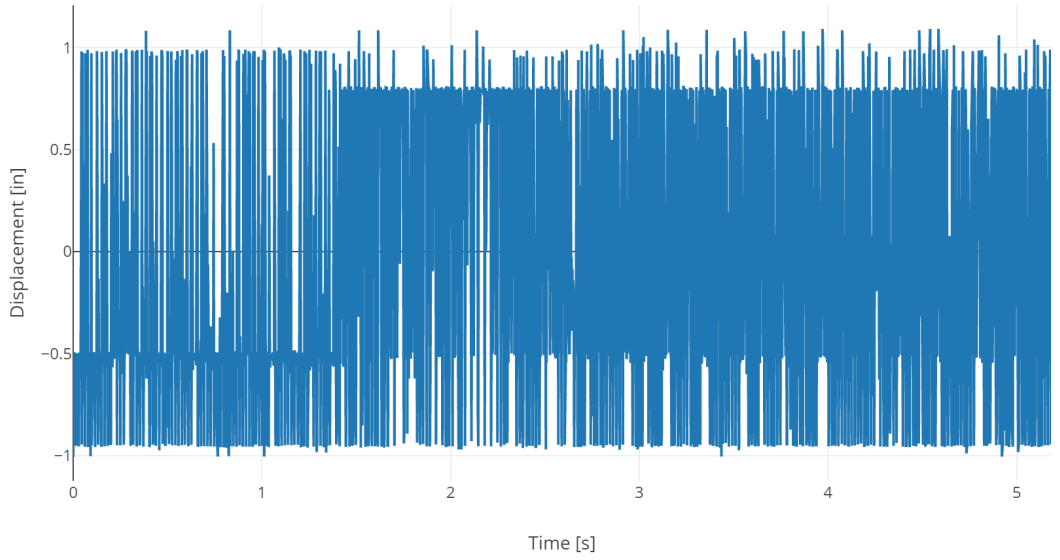

Figure B.51: Midpoint displacement versus time for U = 29.1 m/s for 5.4 seconds duration.

B.7 Uncertainty in measured frequencies for 2024-T3 aluminum.

The following tables show the calculated uncertainty values for 2024-T3 aluminum not shown in Chapter 5.

	Trial	1	2	3	4	5	6
	Air speed [m/s]	36.7	37.5	38.3	39.0	39.8	40.6
Peak 1	$\omega_{measured}$ [Hz]	17.6	17.6	18	18	18.3	18.3
	$(\delta\omega)_{\text{dim}}$ [Hz]	1.14	1.14	1.14	1.14	1.14	1.14
	$(\delta\omega_n)_{acc}$ [Hz]	0.0704	0.0704	0.072	0.072	0.0732	0.0732
	$\delta\omega_n$ [Hz]	**1.21**	**1.21**	**1.21**	**1.21**	**1.21**	**1.21**
Peak 2	$\omega_{measured}$ [Hz]	53.0	53.3	54	54.3	55.0	55.3
	$(\delta\omega)_{\text{dim}}$ [Hz]	1.91	1.91	1.91	1.91	1.91	1.91
	$(\delta\omega_n)_{acc}$ [Hz]	0.212	0.213	0.216	0.217	0.22	0.221
	$\delta\omega_n$ [Hz]	**2.12**	**2.12**	**2.13**	**2.13**	**2.13**	**2.13**

Figure B.52: Uncertainty values for 2024-T3 aluminum.

B.8 Uncertainty in measured frequencies for ABS plastic.

The following tables show the calculated uncertainty values for ABS plastic not shown in Chapter 5.

	Trial	1	2	3	4	5	6
	Air speed [m/s]	17.3	18.0	18.8	19.6	20.4	21.2
Peak 1	$\omega_{measured}$ [Hz]	17.3	17.3	17.7	18.0	18.3	18.3
	$(\delta\omega)_{dim}$ [Hz]	0.744	0.744	0.744	0.744	0.744	0.744
	$(\delta\omega_n)_{acc}$ [Hz]	0.0692	0.0692	0.0708	0.0720	0.0732	0.0732
	$\delta\omega_n$ [Hz]	**0.813**	**0.813**	**0.815**	**0.816**	**0.817**	**0.817**
Peak 2	$\omega_{measured}$ [Hz]	52	52.3	53	53.7	54.7	55.3
	$(\delta\omega)_{dim}$ [Hz]	1.25	1.25	1.25	1.25	1.25	1.25
	$(\delta\omega_n)_{acc}$ [Hz]	0.208	0.209	0.212	0.215	0.219	0.221
	$\delta\omega_n$ [Hz]	**1.46**	**1.46**	**1.46**	**1.46**	**1.47**	**1.47**
Peak 3	$\omega_{measured}$ [Hz]	86.3	87.3	88.6	89.6	91	92.3
	$(\delta\omega)_{dim}$ [Hz]	1.75	1.75	1.75	1.75	1.75	1.75
	$(\delta\omega_n)_{acc}$ [Hz]	0.345	0.349	0.354	0.358	0.364	0.369
	$\delta\omega_n$ [Hz]	**2.10**	**2.10**	**2.10**	**2.11**	**2.11**	**2.12**
Peak 4	$\omega_{measured}$ [Hz]	103.6	104.6	105.8	107.5	109.1	111
	$(\delta\omega)_{dim}$ [Hz]	2.24	2.24	2.24	2.24	2.24	2.24
	$(\delta\omega_n)_{acc}$ [Hz]	0.414	0.418	0.423	0.430	0.436	0.444
	$\delta\omega_n$ [Hz]	**2.65**	**2.66**	**2.66**	**2.67**	**2.68**	**2.68**
Peak 5	$\omega_{measured}$ [Hz]	121	122.3	123.1	125.6	127.3	129.1
	$(\delta\omega)_{dim}$ [Hz]	3.240	3.240	3.240	3.240	3.240	3.240
	$(\delta\omega_n)_{acc}$ [Hz]	0.484	0.489	0.492	0.502	0.509	0.516
	$\delta\omega_n$ [Hz]	**3.72**	**3.73**	**3.73**	**3.74**	**3.75**	**3.76**
Peak 6	$\omega_{measured}$ [Hz]	138.3	139.6	141	143.3	145.5	147.7
	$(\delta\omega)_{dim}$ [Hz]	3.74	3.74	3.74	3.74	3.74	3.74
	$(\delta\omega_n)_{acc}$ [Hz]	0.553	0.558	0.564	0.573	0.582	0.591
	$\delta\omega_n$ [Hz]	**4.29**	**4.30**	**4.30**	**4.31**	**4.32**	**4.33**

Figure B.53: Uncertainty values for ABS plastic.

B.9 Uncertainty in measured frequencies for PETG plastic.

The following tables show the calculated uncertainty values for PETG plastic not shown in Chapter 5.

	Trial	1	2	3	4	5	6
	Air speed [m/s]	25.9	26.7	27.5	28.3	29.1	29.8
Peak 1	$\omega_{measured}$ [Hz]	19.67	19.67	19.67	20	20	20
	$(\delta\omega)_{\dim}$ [Hz]	0.805	0.805	0.805	0.805	0.805	0.805
	$(\delta\omega_n)_{acc}$ [Hz]	0.0787	0.0787	0.0787	0.080	0.080	0.080
	$\delta\omega_n$ [Hz]	**0.884**	**0.884**	**0.884**	**0.885**	**0.885**	**0.885**
Peak 2	$\omega_{measured}$ [Hz]	59.33	59.33	59.33	59.67	59.67	59.67
	$(\delta\omega)_{\dim}$ [Hz]	1.35	1.35	1.35	1.35	1.35	1.35
	$(\delta\omega_n)_{acc}$ [Hz]	0.237	0.237	0.237	0.239	0.239	0.239
	$\delta\omega_n$ [Hz]	**1.59**	**1.59**	**1.59**	**1.60**	**1.60**	**1.60**
Peak 3	$\omega_{measured}$ [Hz]	98.67	98.67	98.67	99.33	99.33	99.67
	$(\delta\omega)_{\dim}$ [Hz]	1.89	1.89	1.89	1.89	1.89	1.89
	$(\delta\omega_n)_{acc}$ [Hz]	0.395	0.395	0.395	0.397	0.397	0.399
	$\delta\omega_n$ [Hz]	**2.29**	**2.29**	**2.29**	**2.29**	**2.29**	**2.29**

Figure B.54: Uncertainty values for PETG plastic.

C Galerkin coefficients from semi-continuum method.

C.1 Galerkin coefficients for linear fluid and structure dynamics.

Table C.1: Galerkin Coefficients for 2024-T3 Aluminum.

n	B_n, Real	B_n, Imaginary	n	B_n, Real	B_n, Imaginary
1	1.0000E+00	1.0000E+00	11	1.0531E-05	1.0275E-05
2	-2.9113E-01	-2.9595E-01	12	-5.8407E-07	1.1121E-06
3	2.3488E-02	4.8547E-02	13	-3.0907E-06	-3.5816E-06
4	-1.1100E-03	-9.7022E-04	14	3.8335E-06	1.4681E-05
5	-1.3920E-03	-1.8138E-03	15	-2.7128E-06	-1.9788E-06
6	1.2515E-05	5.4401E-05	16	-1.0979E-06	-2.1559E-06
7	4.0250E-04	6.5210E-04	17	-1.3529E-06	-2.1464E-07
8	-7.0667E-06	-1.0634E-05	18	1.8476E-06	6.0167E-06
9	-5.7399E-05	-7.3905E-05	19	2.3841E-06	9.3301E-06
10	5.0783E-06	8.1193E-06	20	-4.1975E-07	6.3864E-06

Table C.2: Galerkin Coefficients for PETG Plastic.

n	B_n, Real	B_n, Imaginary	n	B_n, Real	B_n, Imaginary
1	1.0000E+00	1.0000E+00	11	-8.3065E-05	4.1733E-04
2	-1.0528E-01	-2.1316E-01	12	6.9060E-03	-1.9482E-04
3	-1.4879E-02	2.6368E-02	13	4.8868E-03	-6.4265E-05
4	1.4361E-02	-2.9079E-02	14	3.6684E-03	-1.6164E-04
5	2.2118E-03	-4.9537E-02	15	2.3186E-03	7.4659E-04
6	-3.9283E-05	1.8090E-04	16	2.1558E-03	-1.9157E-04
7	-3.7978E-04	4.9775E-04	17	1.6301E-03	-4.9947E-05
8	3.7994E-05	4.8038E-05	18	1.2916E-03	2.7180E-06
9	7.7366E-04	-1.6936E-03	19	6.4210E-04	3.2476E-06
10	-4.5408E-04	1.0768E-03	20	3.4210E-04	1.2476E-06

Table C.3: Galerkin Coefficients for ABS Plastic.

n	B_n, Real	B_n, Imaginary	n	B_n, Real	B_n, Imaginary
1	1.0000E+00	5.5336E-01	11	6.2944E-06	-1.3798E-05
2	-3.0974E-02	-1.0000E+00	12	1.4381E-05	-2.1203E-03
3	8.3577E-02	7.4018E-02	13	3.1169E-05	2.9062E-04
4	-7.3367E-03	-4.7403E-02	14	-1.1741E-05	-9.1213E-05
5	-3.6565E-03	-3.9820E-02	15	9.2985E-05	1.0074E-03
6	1.4604E-04	-4.7475E-02	16	-1.2611E-05	-1.0323E-04
7	2.3644E-04	2.4786E-03	17	-2.8060E-06	2.7019E-04
8	-2.1928E-05	-1.5163E-04	18	-1.6248E-06	-2.1238E-05
9	-2.0271E-04	-2.2605E-03	19	6.4805E-06	6.2649E-05
10	8.5923E-05	6.9660E-04	20	6.9755E-06	5.2704E-05

C.2 Galerkin coefficients for linear fluid and nonlinear structure dynamics.

Table C.4: Galerkin Coefficients for 2024-T3 Aluminum.

n	B_n, Real	B_n, Imaginary	C_n, Real	C_n, Imaginary	D_n, Real	D_n, Imaginary
1	8.7852E-01	8.4557E-01	2.40E-06	5.0443E-03	-1.3261E-19	-1.8930E-16
2	-1.0000E+00	-1.0000E+00	-2.10E-06	-2.1457E-03	3.1594E-20	3.7265E-17
3	8.0597E-01	2.6049E-02	3.38E-07	-2.6126E-03	-3.4600E-21	-1.5667E-17
4	-8.2013E-02	5.5817E-03	-4.66E-07	6.6377E-03	2.5910E-21	3.3004E-18
5	-1.6078E-01	-5.7060E-02	7.36E-07	-5.0243E-03	-2.8351E-22	9.4080E-19
6	1.5986E-04	1.5477E-03	3.19E-08	4.6848E-04	-2.8642E-21	-2.2320E-18
7	1.4537E-03	7.4207E-04	1.12E-08	1.6719E-04	2.7363E-22	1.5978E-18
8	-1.9522E-04	8.9830E-05	-2.72E-08	4.0785E-04	2.6724E-22	2.1241E-19
9	-5.1632E-03	-1.2984E-03	2.40E-08	-5.4847E-04	6.0733E-22	-6.9639E-19
10	3.2928E-03	8.3727E-04	7.87E-08	1.7526E-03	-2.4179E-22	1.6333E-19

Table C.5: Galerkin Coefficients for PETG Plastic.

n	B_n, Real	B_n, Imaginary	C_n, Real	C_n, Imaginary	D_n, Real	D_n, Imaginary
1	1.0000E+00	1.0000E+00	2.02E-13	-4.4571E-13	3.3559E-26	-1.1066E-24
2	-7.9532E-01	-8.5188E-01	2.01E-13	2.4143E-13	-6.1738E-27	-2.3441E-25
3	4.3299E-02	-9.3464E-02	-6.19E-14	-2.1707E-13	-2.1173E-27	1.3074E-25
4	-4.3391E-02	1.7839E-03	-1.27E-13	-2.3158E-14	6.5909E-28	-2.7345E-26
5	-8.1649E-02	-1.5322E-01	-5.26E-14	6.3561E-14	7.1781E-28	-1.4166E-26
6	1.3557E-03	2.1086E-02	6.01E-14	7.0242E-14	2.4981E-30	3.4317E-26
7	7.7985E-04	6.4510E-04	5.17E-14	1.0220E-15	-2.0045E-28	-3.2079E-26
8	-1.0338E-04	2.9311E-04	-4.89E-15	-3.0933E-14	-6.5094E-29	4.6231E-27
9	-2.6412E-03	-4.1796E-03	-2.49E-14	-7.0160E-15	4.0077E-29	8.9323E-27
10	1.6755E-03	2.5238E-03	-8.48E-15	4.0382E-16	3.1988E-29	-1.2400E-27
11	3.4624E-04	1.2712E-03	9.58E-15	-4.00E-16	-2.01E-30	-2.21E-27
12	1.5840E-23	9.4499E-04	1.58E-23	2.00E-16	-9.08E-30	-9.24E-28

Table C.6: Galerkin Coefficients for ABS Plastic.

n	B_n, Real	B_n, Imaginary	C_n, Real	C_n, Imaginary	D_n, Real	D_n, Imaginary
1	1.0000E+00	1.0000E+00	2.71E-08	-8.5018E-05	-2.6851E-22	-2.5485E-17
2	-9.1773E-01	8.6108E-01	-3.02E-09	1.3979E-05	1.3110E-24	6.1684E-19
3	-2.1474E-01	-3.1918E-01	-3.11E-09	-4.5829E-06	4.5556E-23	-8.0926E-20
4	2.0743E-01	2.1997E-01	3.35E-10	4.2674E-07	-9.7837E-24	1.9490E-20
5	-2.5890E-02	-3.5207E-02	4.44E-10	1.7410E-06	-6.9361E-24	-3.2284E-21
6	-9.9928E-03	1.2156E-02	-2.82E-12	-1.9472E-07	2.4292E-24	-1.6485E-21
7	-3.0069E-03	1.6075E-02	-6.89E-12	-3.0698E-08	1.0459E-25	2.1286E-21
8	4.6157E-03	-9.3917E-03	1.15E-12	-2.2188E-08	-3.8899E-25	-1.5521E-21
9	-9.2667E-03	-6.9172E-03	1.57E-11	7.6000E-08	-1.1006E-25	9.0294E-22
10	-3.8321E-05	4.9334E-03	-9.51E-12	-5.4063E-08	1.7747E-25	-6.0274E-22
11	1.9812E-05	6.5918E-07	-1.52E-12	-8.41E-09	2.62E-27	4.14E-22
12	6.8960E-06	2.2789E-07	-1.89E-13	-5.16E-08	-3.78E-26	-2.33E-22
13	-4.1687E-06	2.2252E-07	-1.15E-12	3.63E-09	3.91E-26	1.35E-22
14	6.8937E-07	8.4560E-07	1.98E-208	9.22E-09	-9.20E-27	5.84E-24

References

[1] K.E. Atkinson. *An introduction to numerical analysis*. New York, NY: Wiley, 1989.

[2] A.V. Balakrishnan. *Aeroelasticity: The continuum theory*. New York, NY: Springer, 2012.

[3] A.V. Balakrishnan. "Possio Integral Equation of Aeroelasticity". In: *Journal of Aerospace Engineering* (2003).

[4] A.V. Balakrishnan. *Unpublished manuscript held at the University of Southern California.*

[5] O.O. Bendiksen. *Aeroelastic problems in turbomachines*. Technical report. NASA, 1990.

[6] O.O. Bendiksen. "Modern developments in computational aeroelasticity". In: *Journal of aerospace engineering* (2004).

[7] R.L. Bisplinghoff and H. Ashley. *Principles of aeroelasticity*. 1962.

[8] I. Chueshov, I. Lasiecka, and J.T. Webster. "Attractors for delayed, non-rotational von Karman plates with applications to flow-structure interactions without any damping". In: *Communications in Partial Differential Equations* (2014).

[9] I. Chueshov, I. Lasiecka, and J.T. Webster. "Evolution semigroups in supersonic flow-plate interactions". In: *Journal of Differential Equations* (2013).

[10] A.R. Collar. "The expanding domain of aeroelasticity". In: *Journal of the Royal Aeronautical Society* (1946).

[11] B.K. Donaldson. *Introduction to structural dynamics*. 2006.

[12] E. Dowell. *A modern course in aeroelasticity*. 2015.

[13] E. Dowell. "Experimental aeroelasticity". In: *A modern course in aeroelasticity*. 2015.

[14] J. A. Dunnmon et al. "Power extraction from aeroelastic limit cycle oscillations". In: *Journal of fluids and structures* (2011).

[15] G.A. Evans, R.C. Forbes, and J. Hyslop. "The tanh transormation for singular integrals". In: *International Journal of Computer Mathematics* (1986).

[16] M. Goland. "The flutter of a uniform cantilever wing". In: *Journal of Applied Mechanics* (1945).

[17] D.H. Hodges and G.A. Pierce. *Introduction to structural dynamics and aeroelasticity*. 2011.

[18] M. Iri, S. Moriguti, and Y. Takasawa. "On a certain quadrature formula". In: *Journal of Computational and Applied Mathematics* (1987).

[19] S. Khushnood et al. "Cross-Flow-Induced-Vibrations in Heat Exchanger Tube Bundles: A Review". In: *INTECH Open Access Publisher* (2012).

[20] S.J. Kline and F.A. McClintock. "Describing uncertanties in single-sample experiments". In: *Mechanical Engineering* (1953).

[21] I. Lasiecka and J.T. Webster. "Eliminating flutter for clamped von Karman plates immersed in subsonic flows". In: *Communications on Pure and Applied Analysis* (2014).

[22] J. Marn and I. Catton. "Flow-induced vibrations of cylindrical structures using vorticity transport equation". In: *Multidisciplinary applications of computational fluid dynamics, ASME* (1991).

[23] R. Ricketts. *Experimental Aeroelasticity History, Status and Future in Brief*. NASA Langley Research Center Hampton, Virginia, 1990.

[24] H.L. Runyan and C.E. Watkins. *Flutter of a uniform wing with arbitrarily placed mass according to a differential equation analysis and a comparison with experiment*. Technical report. National advisory committee for aeronautics, 1950.

[25] W.R. Sears. "Operational Methods in the Theory of Airfoils in Non-uniform Motion". In: *J. Franklin Institute* (1940).

[26] M.A. Shubov. "Mathematical modeling and analysis of flutter in bending-torsion coupled beams, rotating blades, and hard disk drives". In: *Journal of Aerospace Engineering* (2004).

[27] T. Theodorsen. *General theory of aerodynamic theory and the mechanism of flutter*. Technical report. National advisory committee for aeronautics, 1934.

[28] T. Theodorsen and I.E. Garrick. *Mechanism of flutter: A theoretical and experimental investigation of the flutter problem*. Technical report. National advisory committee for aeronautics, 1940.